FACULTY OF ENGINEERING AND ARCHITECTURE

Ultrafast Heating of Advanced High Strength Steels

Eliseo Hernández Durán

Doctoral dissertation submitted to obtain the academic degrees of
Doctor of Materials Engineering (UGent) and Doctor en Ciencias de la Ingeniería, Mención Ciencia e Ingeniería de los Materiales (U. de Santiago de Chile)

Supervisors

Prof. Roumen Petrov, PhD* - Prof. Felipe Castro Cerda, PhD**

* Department of Electromechanical, Systems and Metal Engineering
Faculty of Engineering and Architecture, Ghent University

** Departamento de Ingeniería Metalúrgica
Facultad de Ingeniería, Universidad de Santiago de Chile, Chile

October 2021

GHENT UNIVERSITY

UNIVERSIDAD DE SANTIAGO DE CHILE

Ultrafast Heating of Advanced High Strength Steels

Eliseo Hernández Durán

Doctoral dissertation submitted to obtain the academic degrees of

Doctor of Materials Engineering (UGent) and Doctor en Ciencias de la Ingeniería, Mención Ciencia e Ingeniería de los Materiales (U. de Santiago de Chile)

Supervisors

Prof. Roumen Petrov, PhD* - Prof. Felipe Castro Cerda, PhD**

* Department of Electromechanical, Systems and Metal Engineering
Faculty of Engineering and Architecture, Ghent University

** Departamento de Ingeniería Metalúrgica
Facultad de Ingeniería, Universidad de Santiago de Chile, Chile

October 2021

GHENT UNIVERSITY

UNIVERSIDAD DE SANTIAGO DE CHILE

ISBN 978-94-6355-533-3
NUR 971
Wettelijk depot: D/2021/10.500/81

Members of the Examination Board

Chair

Prof. Em. Hendrik Van Landeghem, PhD, Ghent University

Other members entitled to vote

Prof. Emmanuel De Moor, PhD, Colorado School of Mines, USA
Prof. Constantinos Goulas, PhD, Universiteit Twente, the Netherlands
Prof. Leo Kestens, PhD, Ghent University
Prof. Alberto Monsalve González, PhD, Universidad de Santiago de Chile, Chile
Prof. Patricia Verleysen, PhD, Ghent University

Supervisors

Prof. Roumen Petrov, PhD, Ghent University
Prof. Felipe Castro Cerda, PhD, Universidad de Santiago de Chile, Chile

This thesis is dedicated to my wife Karol

Acknowledgments

The support of Ghent University and Universidad de Santiago de Chile are gratefully acknowledged. Funding is also acknowledged from the National Agency of Research and Development (ANID) at the Chilean Ministry of Science, Technology, Knowledge and Innovation – Grant /Doctorado Nacional/ 2017–21171319.

I would like to thank and express gratitude to my promotors Prof. Dr. Roumen H. Petrov and Prof. Dr. Felipe Castro Cerda for their time, guidance and support. I would also like to thank Dr. Tanya Ros-Yanez for her valuable contribution to this project. My deepest gratitude also goes to Dr. Stella Ordoñez, who offered her support and encouraged me to keep going along the path of research.

Crucial experimental campaigns were conducted in the thermomechanical laboratories of TU Delft (the Netherlands) and OCAS (Belgium). I acknowledge the support of both institutions. I am particularly grateful to Professor Jilt Sietsma (TU Delft) and I thank the technical assistance from Hans Hofman (TU Delft) and Bart Semeese (OCAS). CRM group Belgium and Dr. Tuan Nguyen Minh are acknowledged for performing hot and cold rolling of the steels studied.

The help of the staff at Ghent University is greatly appreciated. I would especially like to thank Prof. Dr. Leo Kestens, Ilse Vercruysse and Roger Van Hecke. Prof. Dr. Patricia Verleysen (UGhent-DyMaLab) is also thanked for providing necessary facility to conduct mechanical testing. I would also like to acknowledge Dr. Vitaliy Bliznuk for performing TEM and sharing prolonged characterization sessions with me. The staff at Universidad de Santiago de Chile is also kindly thanked, Dr. Alfredo Artigas and Juana Araos were always available to help me overseas. Prof. Kestens and Prof. Verleysen, together with Prof. Emmanuel De Moor, Prof. Constantinos Goulas, and Prof. Alberto Monsalve are also thanked for serving as jury members of this thesis and providing valuable comments and suggestions.

I would like to recognize some good friends and colleagues who made my stay in Belgium one of the best experiences of my life: Ksenija, Alexandros, Sarath, Florian, Harishchandra, Edwin, Hadi, Antonio, and Luca.

Gracias a mis amigos y familia en Chile. No hay palabras suficientes para agradecer el esfuerzo de mis padres María Angela y Eliseo. Gracias por priorizar una educación de calidad para mí y para mi hermano Matías. Agradezco también el apoyo de mis suegros Luis y Sofía, y el de mi cuñado Felipe.

Last but not least, I thank my wife, Karol, for sharing my dreams and staying with me every single moment of this tough adventure. Gracias por ser mi compañera.

Summary

The development of new steel-making routes is largely driven by the current global regulations focused on reducing the CO_2 emissions generated by both, the steel industry and internal combustion engine vehicles. The majority of the efforts in this direction are focused on the development of advanced high strength steels (AHSS) that combine high strength and elongation. Until now, most of the research and technological advances of AHSS are mainly oriented towards the development of effective alloying strategies and microstructural designs, where the control is mainly on the cooling stage of the thermal treatment cycle -quenching, austempering, etc. In all these technologies the annealing part of the thermal treatment cycle is executed with heating rates between 5 and 20°C/s and the soaking times usually vary between 2 and 5 minutes. The technologies for thermal treatment that use high-speed heating sources (e.g. induction and resistance heating) are environmentally friendly and energy-saving processes that might allow to increase the capacity of the industrial continuous annealing lines by employing high and very high heating rates during the thermal treatment of AHSS. In steels, the application of high heating rates has revealed promising results, where the strength and ductility of fast heated steels are at least as good as those obtained in steel grades subjected to slow heating. The studies of low-alloy ultrafast heated (UFH) steels over the last two decades have shown a remarkable improvement in the range of 100 to 300 MPa in yield and ultimate strength, preserving or even increasing their elongation capacity. As a consequence, thinner steel sheets might be treated at a faster production rate but maintaining the strength and toughness required for designing several structural components.

There is a global trend to reduce carbon emissions by decreasing the weight of car structures and the ultrafast heating of steels is considered an advantageous approach towards the new generation of low-alloy AHSS grades. However, the requirements for combinations of strength, ductility and formability intended for several crash resistance components cannot be obtained just via fast heating followed by direct cooling to room temperature. Thus, several thermal pathways could be followed after the ultrafast heating step. This aiming to modify the microstructure and reach or surpass the mechanical requirements established in standard specifications.

Quenching & Partitioning (Q&P) and austempered transformation-induced plasticity (TRIP)-aided steel grades display outstanding strength-ductility balance accomplished by the formation of retained austenite-containing multiphase microstructures. The microstructural design of these steel grades is based on controlled transformation and chemical stabilization of austenite during low-temperature isothermal heat treatments performed after usually prolonged

annealing steps. Therefore, there are not theoretical, or even practical, restrictions for the combination of ultrafast heating and subsequent low-temperature treatments.

Driven by the potential development of optimized heat treatments, the exploratory research conducted in this PhD work focuses on the evaluation of microstructure and mechanical properties of low-alloy steels subjected to ultrafast heating annealing. The thermal treatments studied in this research were designed to gain insight into the role of ultrafast heating on the microstructural evolution and resulting mechanical response of high strength steels. Three thermal pathways are investigated in this research for producing different AHSS grades, i.e., direct quenching (DQ), quenching and partitioning (Q&P) and austempering (AT).

In this work, cold-rolled steel grades were heat-treated by applying heating rates in the range of 10 to 1000 °C/s to predetermined peak austenitization temperatures followed by defined thermal profiles. Heat treatment trials were performed in the Gleeble® thermomechanical simulator and dilatometer. The resulting microstructures were characterized via several techniques, namely optical, scanning and transmission electron microscopy, electron backscattered diffraction and X-ray diffraction. Quasi-static tensile testing was carried out on subsize dogbone samples of geometry selected according to the homogeneously treated zone obtained by Joule heating in the Gleeble® simulator.

The influence of heating rates ranging from 10 to 1000 °C/s and annealing temperatures on the microstructure and mechanical properties of two Fe-0.19C-2.0Mn-1.4Si steels with and without the addition of carbide-forming elements (Mo, Nb, and Ti) have been investigated after direct quenching. The results revealed that heating rates ≥ 100°C/s refine the parent austenitic grains in both alloys and, as expected, the presence of Nb and Ti-rich carbides and carbonitrides restricts the austenite grain growth during slow heating rate experiments. The tensile test results have shown that high heating rates do not have a significant influence on the strength of the steel microalloyed with carbide-forming elements. On the other hand, both the ultimate tensile strength (σ_{UTS}) and total elongation of the alloy without carbide-forming elements decrease at high heating rates due to the formation of bands of ferrite and martensite after cooling.

Ultrafast heating was successfully applied on an Fe-0.28C-1.91Mn-1.44Si Q&P steel with the intention of decreasing the annealing time without affecting the mechanical properties. The microstructural characterization results showed that grain refinement of the parent austenite and its transformation products occurred by increasing the heating rate from 10 °C/s to 100 °C/s, without further grain refining at 700 °C/s. The formation of fine-grained multiphase microstructures after the end of the thermal treatment accompanied by the reduction in the retained austenite carbon content suggested that local chemical heterogeneities in austenite appear upon ultrafast heating. Regardless of the prior heating rate, similar mechanical

properties and strain hardening were measured, revealing that both, the microstructure development and the extent of austenite stabilization during the quenching and partitioning stage have an important influence on the mechanical behavior of the peak annealed Q&P steels with a matrix consisting mainly of martensite.

The effect of non-conventional annealing strategies on the microstructure and related mechanical properties of austempered steels was also investigated. Multistep thermal cycling (TC) and ultrafast heating (UFH) were carried out and compared with the outcome obtained from a conventionally annealed (CA) Fe-0.28C-1.91Mn-1.44Si steel. It was found that TC and UFH strategies produce an equivalent level of microstructural refinement. Nevertheless, the microstructure obtained via TC has not led to a very significant improvement of the mechanical properties in comparison to the CA steel. On the other hand, the steel samples produced via the combination of UFH and austempering exhibit enhanced ductility without decreasing the strength compared to TC and CA, giving the best strength-ductility balance and energy absorption capacity among the studied steels. This behavior is related to the formation of a heterogeneous microstructure consisting of ferrite, bainite and retained austenite.

The microstructure and mechanical tensile properties of an Fe-0.24C-1.39Mn-1.42Si steel were evaluated after combining ultrafast heating at 500 °C/s and fast cooling to room temperature (DQ) or quenching and partitioning treatment (Q&P). Two peak temperatures were studied, annealing into the intercritical range and above the A_{C3} temperature. Bands of ferrite and a mixture of martensite, retained austenite and undissolved carbides we obtained after Intercritical annealing and direct quenching, while heating above the intercritical range produced an even distribution of allotriomorphic ferrite upon fast cooling. Q&P steel grades display an enhanced mechanical response compared to DQ steels, where yield strength, uniform elongation, and total elongation increased. The ultimate tensile strength of Q&P steels decreased compared to DQ steels annealed at the same peak temperature. However, the final strength-ductility balance of the studied Q&P steels was superior to the DQ steel grades. Moreover, considerable strength and good ductility, in the range of tensile properties tailored for the industrially produced Q&P-980MPa grade, were obtained through the combination of peak annealing above the A_{C3} temperature and Q&P. The outstanding mechanical behavior of the Q&P steels is attributed to an interplay between a sustainable TRIP effect and effective strain-stress partitioning among the microconstituents.

Samenvatting

Het ontwikkelen van nieuwe methodes om staal te produceren wordt in grote mate beïnvloed door reglementeringen omtrent het reduceren van CO_2-emissies van zowel de staalindustrie als de verbrandingsmotoren. Het merendeel van de inspanningen daarvoor is gefocust op het ontwikkelen van geavanceerd hoogsterktestaal of "advanced high strength steel (AHSS)". Deze staalsoorten bezitten zowel een hoge sterkte als een hoge ductiliteit. Veel onderzoek en technologische doorbraken omtrent AHSS zijn gericht op het ontwikkelen van legeringen en design van de microstructuur, met een hoofdzakelijk focus op de controle van de afkoelingscyclus, zoals afschrikken, austemperen, enz. Voor al deze technologieën is het gloeien of "annealing" uitgevoerd met opwarmsnelheden tussen 5 en 20°C/s en met tijden voor het gloeien of "soaking" tussen de 2 en 5 minuten. Technologieën voor warmtebehandelingen die gebruik maken van warmtebronnen om met hoge snelheid op te warmen zoals inductief warmen en opwarmen via Jouleweerstand, zijn ecologische en energiebesparende processen die de capaciteit van de continue productielijnen voor gloeien met hoge en ultra-hoge opwarmsnelheden tijdens de warmtebehandeling van AHSS kunnen doen toenemen. De toepassing van hoge opwarmsnelheden in de staalproductie heeft al veelbelovende resultaten opgeleverd, met sterktes en ductiliteit minstens even goed als staal geproduceerd aan tragere opwarmsnelheden. Onderzoek naar ultrasnel opgewarmd of "ultrafast heated (UFH)" staal in de laatste 2 decennia heeft een opmerkelijke verbetering aangetoond in het gebied van 100 tot 300 MPa voor de vloeispanning en treksterkte, met behoud of zelfs verbetering van de maximale verlenging. Bijgevolg kunnen dunnere staalplaten geproduceerd worden aan een hogere productiesnelheid met behoud van sterkte en taaiheid, hetgeen noodzakelijk is voor de ontwikkeling van verschillende structurele componenten.

Er is een globale trend om koolstofemissies te reduceren door het gewicht van de auto te verlagen. Ultrasnel opwarmen van staal kan worden gezien als een voordelige productietechniek voor de nieuwe generaties voor AHSS staalsoorten. De vereisten voor de combinatie van sterkte, ductiliteit en vervormbaarheid voor verschillende componenten voor impactweerstand kunnen echter niet gehaald worden door eenvoudigweg snel op te warmen gevolgd door afkoelen naar kamertemperatuur. Verschillende gloeicycli kunnen gevolgd worden na de ultrasnelle opwarmstap. Het doel daarbij is de microstructuur te wijzigen en zo de mechanische vereisten, nodig voor vele toepassingen, te halen of zelfs te overstijgen.

Staalsoorten gevormd door afschrikken & partitionering, ofwel "Quenching & Partitioning (Q&P)", en "transformation induced plasticity (TRIP)" staalsoorten vertonen een uitstekende sterkte-ductiliteitsbalans door de aanwezigheid van restausteniet en een meerfasige microstructuur. Het design van de microstructuur

van deze staalsoorten is gebaseerd op de gecontroleerde transformatie en de chemische stabilisatie van austeniet gedurende de isotherme warmtebehandelingen op lage temperatuur. Deze wordt meestal uitgevoerd na de eerdere gloeistappen. Daardoor zijn er theoretische noch praktische beperkingen op de combinatie van ultrasnel opwarmen gevolgd door opeenvolgende lage temperatuur warmtebehandelingen.

Met als doel het potentieel ontwikkelen van geoptimaliseerde warmtebehandelingen werd in dit doctoraatswerk gefocust op het bestuderen van de microstructuur en mechanische eigenschappen van laag gelegeerde staalsoorten onderworpen aan ultrasnelle opwarmen. De warmtebehandelingen die bestudeerd werden in dit werk werden ontworpen om inzichten te verkrijgen in de rol van ultrasnel opwarmen in de evolutie van microstructuur en de daaruit volgende mechanische respons van hoogsterktestalen. Drie warmtebehandelingstypes zijn onderzocht in dit werk om verschillende soorten AHSS te produceren: direct afschrikken of “direct quenching (DQ)”, “quenching and partitioning (Q&P)” en “austempering (AT)”.

In dit onderzoek zijn koudgewalste staalsoorten blootgesteld aan verschillende opwarmsnelheden (10 tot 1000 °C/s) tot weloverwogen piektemperatuur (in het austenitisch gebied), gevolgd door goedgedefinieerde afkoelcycli. De bestudeerde warmtebehandelingen werden uitgevoerd in de thermo-mechanische Gleeble® simulator en dilatometer. De resulterende microstructuren werden gekarakteriseerd aan de hand van verschillende technieken, namelijk optische, scanning- en transmissie(elektronen)microscopie, electron backscattered diffractie and X-stralen diffractie. Quasi-statische trektesten werden uitgevoerd op kleine proefstaven door de beperkte thermisch homogeen behandelde zone gecreëerd in de Gleeble® simulator.

Het effect van de gloeitemperaturen en opwarmsnelheden gelegen tussen 10 en 1000 °C/s op de microstructuur en de mechanische eigenschappen van 2 soorten Fe-0.2C-2.0Mn-1.4Si staal, namelijk met en zonder toevoeging van carbidevormende elementen (Mo, Nb, and Ti), zijn onderzocht na direct afschrikken (quenching). De resultaten toonden aan dat bij opwarmsnelheden ≥ 100°C/s de originele austenietkorrels in beide legeringen verfijnen. Zoals verwacht, beperkt de aanwezigheid van Nb en Ti-rijke carbides en carbonitrides de groei van de austenietkorrel bij experimenten met trage opwarmsnelheden. De trektesten toonden aan dat hoge opwarmsnelheden geen significante invloed hebben op de sterkte van het microgelegeerde staal met carbidevormende elementen. Anderzijds dalen zowel de treksterkte (σ_{UTS}) als de totale verlenging van de legering zonder carbidevormende elementen, bij hogere snelheden door de vorming van banden van ferriet en martensiet na afkoeling.

Ultrasnel opwarmen is succesvol toegepast op een Fe-0.28C-1.91Mn-1.44Si Q&P staal met als doel de tijd nodig voor de warmtebehandeling te doen dalen zonder de

mechanische eigenschappen (negatief) te beïnvloeden. De resultaten van de karakterisatie van de microstructuur toonden een korrelverfijning van het origineel austeniet en hun transformatieproducten aan door op te warmen met opwarmsnelheden tussen 10 °C/s en 100 °C/s, zonder een verdere korrelverfijning bij hogere opwarmsnelheden (700 °C/s). De vorming van fijnkorrelige multifase microstructuren na de warmtebehandeling gekoppeld met de reductie van koolstof in de restausteniet suggereert dat bij ultrasnel opwarmen lokale heterogeniteiten optreden in het austeniet. Onafhankelijk van de initiële opwarmingssnelheid werden gelijkaardige mechanische eigenschappen en rekversteviging gemeten bij gegloeide Q&P staalsoorten met een matrix van voornamelijk martensiet. Dat toont aan dat zowel de ontwikkeling van de microstructuur en de mate waarin het austeniet stabiliseert gedurende quenching en partitioning een belangrijke invloed hebben op de mechanische eigenschappen.

Het effect van niet-conventionele gloeistrategieën op de microstructuur en mechanische eigenschappen van austempered staal is onderzocht. Multistap thermal cycling (TC) en annealen via ultrasnelle opwarmen (UFH) werd uitgevoerd en vergeleken met een conventionele annealing (CA) staal, namelijk Fe-0.28C-1.91Mn-1.44Si. Er werd gevonden dat TC en UFH strategieën een gelijkaardige verfijning van de microstructuur opleverden. Echter, de microstructuur verkregen via TC leidde niet tot een significante verbetering van de mechanische eigenschappen in vergelijking met het CA staal. Anderzijds vertoonden de samples geproduceerd via de combinatie van UFH en austempering een verbeterde ductiliteit zonder verlies aan sterkte vergeleken met TC en CA, waardoor ze de beste sterkte-ductiliteitsbalans en energie-absorptievermogen vertoonden van de onderzochte staalsoorten. Dit gedrag is gelinkt aan de vorming van een heterogene microstructuur betaande uit ferriet, bainiet en restausteniet.

De microstructuur en mechanische eigenschappen van een Fe-0.24C-1.39Mn-1.42Si staal werden onderzocht na een combinatie van ultrasnel opwarmen aan 500 °C/s gevolgd door een snelle afkoeling tot kamertemperatuur (DQ) of een behandeling via quenching and partitioning (Q&P). Twee piektemperaturen werden onderzocht, namelijk gloeien tot het interkritische gebied en boven de A_{C3} temperatuur. Banden van ferriet en een mix van martensiet, restausteniet en onopgeloste carbides werden verkregen na interkritsch gloeien en direct afschrikken, terwijl opwarmen boven de interkritische zone na snel afkoelen een homogene distributie van allotriomorphisch ferriet opleverde. Q&P staalsoorten tonen verbeterde mechanische eigenschappen vergeleken met DQ staalsoorten, met een stijging van zowel de vloeispanning, de uniforme verlenging, als de totale verlenging. De treksterkte van Q&P staal verminderde vergeleken met DQ staal na blootstelling aan dezelfde piektemperatuur. De finale sterkte-ductiliteitbalans van het bestudeerde Q&P staal was echter superieur in verband met het DQ staal. Bovendien werd een goede sterkte en ductiliteit van het Q&P-980MPa staal verkregen door een

combinatie van gloeien tot boven de A_{C3} temperatuur gevolgd door Q&P. Het uitstekende mechanisch gedrag van de Q&P staalsoorten wordt verklaard door een interactie tussen een duurzaam TRIP-effect en een verdeling van rek en spanning tussen de microconstituenten.

Resumen

El desarrollo de nuevas rutas de producción de aceros está impulsado en gran medida por las regulaciones globales actuales centradas en reducir las emisiones de CO_2 generadas tanto por la industria del acero como por vehículos con motor de combustión interna. La mayoría de los esfuerzos en esta dirección se centran en el desarrollo de aceros avanzados de alta resistencia "Advanced high strength steels (AHSS)", los cuales combinan alta resistencia y ductilidad. Hasta ahora, la mayor parte de la investigación y los avances tecnológicos de AHSS están orientados principalmente al desarrollo de estrategias de diseño de aleaciones y diseños microestructurales, donde el control se encuentra principalmente en la etapa de enfriamiento del ciclo de tratamiento térmico - temple, austemperado, etc. En todas estas tecnologías la etapa de recocido del ciclo de tratamiento térmico se ejecuta con velocidades de calentamiento entre 5 y 20 °C/s y los tiempos de recocido suelen variar entre 2 y 5 minutos. Las tecnologías de tratamiento térmico que utilizan fuentes de calentamiento de alta velocidad -por ejemplo, calentamiento por inducción y por resistencia eléctrica- son procesos respetuosos con el medio ambiente y eficientes desde el punto de vista energético. Además, el uso de altas velocidades de calentamiento podría permitir aumentar la capacidad de las líneas de recocido continuo industrial durante el tratamiento térmico de AHSS. La aplicación de altas velocidades de calentamiento ha revelado resultados prometedores en tratamiento térmico de aceros, donde la resistencia y ductilidad de los aceros sometidos a calentamiento rápido son al menos tan buenas como las obtenidas en aceros sometidos a calentamiento lento. Durante las últimas dos décadas estudios en aceros de baja aleación sometidos a calentamiento ultrarrápido "Ultrafast heating (UFH)" han mostrado una mejora notable en el rango de 100 a 300 MPa en el límite elástico y resistencia a la tracción, preservando o incluso aumentando la capacidad de elongación. Como consecuencia, chapas de acero más delgadas podrían tratarse térmicamente a un ritmo de producción más rápido, pero manteniendo la resistencia y la tenacidad necesarias para el diseño de diversos componentes estructurales.

Existe una tendencia en la industria siderúrgica mundial orientada a reducir las emisiones de carbono mediante la reducción del peso de las estructuras de los automóviles, donde el tratamiento térmico mediante el calentamiento ultrarrápido de aceros se considera un enfoque ventajoso para la producción de la nueva generación de AHSS de baja aleación. Sin embargo, los requisitos de resistencia, ductilidad y conformabilidad requeridos en variados componentes de acero diseñados para la resistencia a choques no pueden ser obtenidos únicamente mediante calentamiento rápido seguido de enfriamiento directo hasta temperatura ambiente. Por lo tanto, se podrían seguir diferentes rutas de tratamiento térmico luego de la etapa de calentamiento ultrarrápido. Esto con el objetivo de modificar la

microestructura y alcanzar o superar los requisitos mecánicos establecidos en especificaciones estándar.

Aceros de temple y particionado “quenching and partitioning (Q&P)” y austemperados “austempering (AT)” presentan destacable resistencia y ductilidad obtenidas a través de la formación de microestructuras multifásicas que incluyen austenita retenida. El diseño microestructural de estos aceros se basa en la transformación controlada y la estabilización química de la austenita durante tratamientos térmicos isotérmicos de baja temperatura, los cuales son empleados luego de prolongadas etapas de recocido. Por lo tanto, no existen restricciones teóricas, ni prácticas, para la combinación de calentamiento ultrarrápido y posteriores tratamientos realizados a baja temperatura.

Impulsado por el potencial desarrollo de tratamientos térmicos optimizados, la investigación exploratoria realizada en este trabajo de doctorado se centra en la evaluación de la microestructura y las propiedades mecánicas de aceros de baja aleación sometidos a calentamiento ultrarrápido. Los tratamientos térmicos estudiados en esta investigación fueron diseñados para determinar el rol del calentamiento ultrarrápido en la evolución microestructural y la respuesta mecánica resultante de aceros de alta resistencia. En esta investigación tres vías de tratamiento térmico fueron empleadas para producir diferentes AHSS: temple “direct quench (DQ)”, temple y particionado (Q&P) y austemperado (AT).

En este trabajo aceros laminados en frío se trataron térmicamente aplicando velocidades de calentamiento en el rango de 10 a 1000 °C/s hasta temperaturas de austenitización predeterminadas, seguidas de perfiles térmicos de baja temperatura. Tratamientos térmicos fueron realizados en el simulador termomecánico Gleeble® y en dilatómetro. Las microestructuras resultantes se caracterizaron mediante varias técnicas, incluyendo microscopía óptica, microscopía electrónica de barrido y microscopía electrónica de transmisión, difracción de electrones retrodispersados y difracción de rayos X. Ensayos de tracción en régimen cuasiestático se llevaron a cabo sobre probetas de tracción diseñadas de acuerdo al tamaño de zona tratada homogéneamente en el simulador Gleeble®.

Se estudió la influencia de las velocidades de calentamiento desde 10 a 1000 ° C/s y las temperaturas pico de tratamiento térmico sobre la microestructura y propiedades mecánicas obtenidas después de enfriamiento directo (DQ) en un acero de composición base Fe-0.2C-2.0Mn-1.4Si y otro con la adición de elementos formadores de carburo (Mo, Nb y Ti). Los resultados revelaron que las velocidades de calentamiento ≥ 100 °C/s resultan en un refinamiento del tamaño de grano austenítico en ambas aleaciones y, como se esperaba, la presencia de carburos y carbonitruros de Nb y Ti restringe el crecimiento de los granos austeníticos durante los experimentos realizados a velocidades de calentamiento lenta. Los resultados de las pruebas de tracción han demostrado que las altas velocidades de calentamiento no tienen una influencia significativa en la resistencia del acero microaleado con

elementos formadores de carburo. Por otro lado, tanto la resistencia la tracción (σ_{UTS}) como la elongación total (elongación a fractura) de la aleación sin elementos formadores de carburo disminuyeron en experimentos realizados a altas velocidades de calentamiento debido a la formación de bandas de ferrita y martensita después del enfriamiento.

Calentamiento ultrarrápido se aplicó con éxito en un acero Fe-0.28C-1.91Mn-1.44Si sometido a temple y particionado (Q&P) con la intención de disminuir el tiempo de recocido sin afectar las propiedades mecánicas. Los resultados de la caracterización microestructural mostraron que el refinamiento del tamaño de grano de la austenita y sus productos de transformación ocurrió al aumentar la velocidad de calentamiento desde 10 °C/s a 100 °C/s, sin refinamiento adicional del tamaño de grano incrementando velocidad de calentamiento hasta 700 °C/s. La formación de microestructuras multifásicas de grano fino en conjunto a la reducción del contenido de carbono de la austenita retenida sugiere el desarrollo de heterogeneidades químicas a nivel local en la austenita formada durante experimentos de calentamiento ultrarrápido. Independientemente de la velocidad de calentamiento empleada, similares propiedades mecánicas y endurecimiento por deformación fueron medidos, lo que reveló que tanto el desarrollo microestructural como el grado de estabilización de la austenita durante la etapa de temple y particionado tienen una influencia importante en el comportamiento mecánico de los aceros Q&P con una matriz que consiste principalmente de martensita.

También se investigó el efecto de estrategias de recocido no convencionales sobre la microestructura y las propiedades mecánicas en el acero Fe-0.28C-1.91Mn-1.44Si sometido a austemperado. Se llevaron a cabo múltiples ciclos térmicos de calentamiento y temple “Thermal cycling (TC)” y calentamiento ultrarrápido (UFH) y los resultados fueron comparados con un acero producido mediante recocido convencional “Conventional annealing (CA)”. Se encontró que las estrategias TC y UFH producen un nivel equivalente de refinamiento microestructural. Sin embargo, la microestructura obtenida mediante TC no generó una mejora significativa de las propiedades mecánicas en comparación con el acero CA. Por otro lado, las muestras de acero producidas mediante la combinación de UFH y austemperado exhiben una ductilidad mejorada sin disminuir la resistencia en comparación con TC y CA, dando el mejor balance de resistencia-ductilidad y capacidad de absorción de energía medidos entre los aceros estudiados. Este comportamiento está relacionado con la formación de una microestructura heterogénea formada por ferrita, bainita y austenita retenida.

Se evaluó la microestructura y las propiedades mecánicas en un acero Fe-0.24C-1.39Mn-1.42Si después de combinar calentamiento ultrarrápido a 500 °C/s seguido de enfriamiento rápido a temperatura ambiente (DQ) o tratamiento de temple y particionado (Q&P). Se estudiaron dos temperaturas de tratamiento, calentamiento hasta el rango intercrítico y por encima de la temperatura A_{C3}. Bandas de ferrita y

una mezcla de martensita, austenita retenida y carburos no disueltos se obtuvieron después del recocido intercrítico y enfriamiento directo, mientras que el calentamiento por encima del rango intercrítico seguido de enfriamiento rápido produjo una distribución uniforme de ferrita alotriomórfica. Los aceros Q&P muestran una respuesta mecánica mejorada en comparación con los aceros DQ, donde se registró un aumento del límite elástico, elongación uniforme y elongación total. La resistencia a la tracción de los aceros Q&P disminuyó en comparación con los aceros DQ recocidos a la misma temperatura. Sin embargo, el balance de resistencia y ductilidad de los aceros Q&P estudiados fue superior a los aceros DQ. Además, la combinación de calentamiento por encima de la temperatura A_{C3} y Q&P resultó en una resistencia considerable y buena ductilidad, ambas en el rango de propiedades de tracción definidas para el acero Q&P-980MPa, el cual es producido industrialmente. El excelente comportamiento mecánico de los aceros Q&P es atribuido a una interacción entre un efecto TRIP sostenible y una partición efectiva de tensión-deformación entre los microconstituyentes.

List of publications

Publications in international peer-reviewed journals indexed in Science Citation Index

1. E.I. Hernandez-Duran, V. Bliznuk, T. Ros-Yanez, R. Iquilio-Abarzua, F.M. Castro-Cerda and R.H. Petrov: Improvement of the strength-ductility balance in ultrafast heated steels by combining high-temperature annealing and quenching and partitioning process. *Materials Science & Engineering A,* 827, 142045 (2021)
   https://doi.org/10.1016/j.msea.2021.142045

2. E.I. Hernandez-Duran, L. Corallo, T. Ros-Yanez, F.M. Castro-Cerda and R.H. Petrov: The effect of different annealing strategies on the microstructure development and mechanical response of austempered steels. *Metals*, 11, 1041 (2021)
   https://doi.org/10.3390/met11071041

3. E.I. Hernandez-Duran, L. Corallo, T. Ros-Yanez, F.M. Castro-Cerda and R.H. Petrov: Influence of Mo–Nb–Ti additions and peak annealing temperature on the microstructure and mechanical properties of low alloy steels after ultrafast heating process. *Materials Science & Engineering A*, 808, 140928 (2021)
   https://doi.org/10.1016/j.msea.2021.140928

4. E.I. Hernandez-Duran, T. Ros-Yanez, F.M. Castro-Cerda and R.H. Petrov: The influence of the heating rate on the microstructure and mechanical properties of a peak annealed quenched and partitioned steel. *Materials Science & Engineering A*, 797, 140061 (2020)
   https://doi.org/10.1016/j.msea.2020.140061

5. F.M. Castro-Cerda, E.I. Hernandez-Duran, T. Ros-Yanez and R.H. Petrov: Isothermal phase transformations in a low carbon steel during single and two-step partitioning. *Metallurgical and Materials Transactions A*, 51 (2020)
   https://doi.org/10.1007/s11661-020-05643-1

6. A. Banis, E.I. Hernandez-Duran, V. Bliznuk, I. Sabirov, R.H. Petrov and S. Papaefthymiou: The effect of ultra-fast heating on the microstructure, grain size and texture evolution of a commercial low-C, medium-Mn DP steel. *Metals*, 9, 877 (2019)
https://doi.org/10.3390/met9080877

7. E.I. Hernandez-Duran, R. Leiva, A. Escobar and S. Ordoñez: Effect of sub-zero treatment on the microstructure and hardness of high-chromium white cast iron. *Matéria*, 23, 02 (2018)
https://doi.org/10.1590/S1517-707620180002.0370

Conference contributions

Oral presentations

1. E.I. Hernandez-Duran, T. Ros-Yanez, F.M. Castro-Cerda and R. H. Petrov: The effect of the ultrafast heating on the microstructure and related mechanical properties of low alloy steels
Thermec 2021, Virtual conference - Vienna, June 1 - 5, 2021

2. E.I. Hernandez-Duran, T. Ros-Yanez, F.M. Castro-Cerda and R.H. Petrov: Influence of micro-alloying elements on the austenite grain size and austenite decomposition of cold-rolled low alloy steels under ultrafast heating
7th International Recrystallization and Grain Growth Conference, Belgium, August 4 - 9, 2019

3. A. Banis, E.I. Hernandez-Duran, V. Bliznuk, I. Sabirov, R.H. Petrov and S. Papaefthymiou: Effect of ultra-fast heat treatment on the texture and grain size of an industrial grade DP 600 steel
7th International Recrystallization and Grain Growth Conference, Belgium, August 4 - 9, 2019

4. E.I. Hernandez-Duran, T. Ros-Yanez, F.M. Castro-Cerda and R. H. Petrov: Third generation advanced steels via ultrafast heating
1st Scientific Congress of Postgraduate Students at Universidad de Santiago de Chile, Chile, August 20, 2019

List of symbols and abbreviations

AHSS	*Advanced high strength steels*
AT	*Austempering*
γ	*Austenite*
B	*Bainite*
θ	*Cementite*
CR	*Cold-rolled*
CA	*Conventional annealing*
DQ	*Direct quenching*
EBDS	*Electron backscattered diffraction*
F	*Ferrite*
GAIQ	*Grain average image quality*
GOS	*Grain orientation spread*
IQ	*Image quality*
KAM	*Kernel average misorientation*
M	*Martensite*
PAG	*Parent austenite grain*
P	*Pearlite*
Q&P	*Quenching and partitioning*
RD	*Rolling direction*
SEM	*Scanning electron microscopy*
TC	*Thermal cycling*
ε_{Total}	*Total elongation*
TEM	*Transmission electron microscopy*
σ_{UTS}	*Ultimate tensile strength*
UFH	*Ultrafast heating*
$\varepsilon_{Uniform}$	*Uniform elongation*
σ_{ys}	*Yield strength*

Table of contents

Chapter 1

Introduction

1.1 Advanced high strength steels

Since the 1970s, the development of advanced high strength steels (AHSS) for automotive applications has been driven by the requirements of collision safety, weight-saving and fuel efficiency of vehicles [1,2]. The necessity of combining variable levels of strength and formability/ductility in parts that compose the body-in-white of vehicles has promoted the design of different types of alloys and novel heat treatments.

Low alloy steels, including complex phase (CP), dual-phase (DP), TRIP aided ferritic-bainitic and martensitic steels belong to the "first generation" of advanced high strength steels. DP and TRIP steels are used in crash zones where energy absorption is required [3]. Martensitic steels, which exhibit tensile strengths commonly higher than 1200 MPa, are destined for structural components [4,5].

On the other hand, high alloyed austenitic steels are referred to as the "second generation" of AHSS [1,2]. The outstanding mechanical behavior of the austenitic steel grades is the result of two main strain hardening mechanisms: twinning-induced plasticity (TWIP) and transformation-induced plasticity (TRIP) [6,7]. The activation of those strengthening mechanisms results in impressive combinations of strength and ductility, achieving the properties required to design several automotive components. However, these steels might be costly due to the high alloy additions necessary to produce austenitic-based microstructures.

In Figure 1.1a, the tensile strength and total elongation combination of the first and second generation AHSS is shown. As can be observed, a gap is created between these steel grades, which is set to be filled by the emerging "third generation" of AHSS [1,2]. The mechanical behavior required for this new generation of AHSS can be achieved by carefully designed microstructures through controlled alloying and innovative thermo-mechanical pathways [8–10]. Particular attention has been given to the production of these steels since they offer comparable or even improved mechanical capabilities at lower production costs compared to the second generation of AHSS [1,2]. Retained austenite-containing high strength bainitic steels [11,12], quenched and partitioned steels [13] and medium manganese steels [14] are potential candidates towards the third generation of AHSS (Figure 1.1b) [15].

Current environmental protection measures have also targeted the steel-making process, providing the opportunity for developing and optimizing industrial

technologies that can deliver significant benefits over conventional processing methods. To this end, new rapid heating processes appear as an alternative for shortening the annealing treatments and improving the mechanical properties of AHSS.

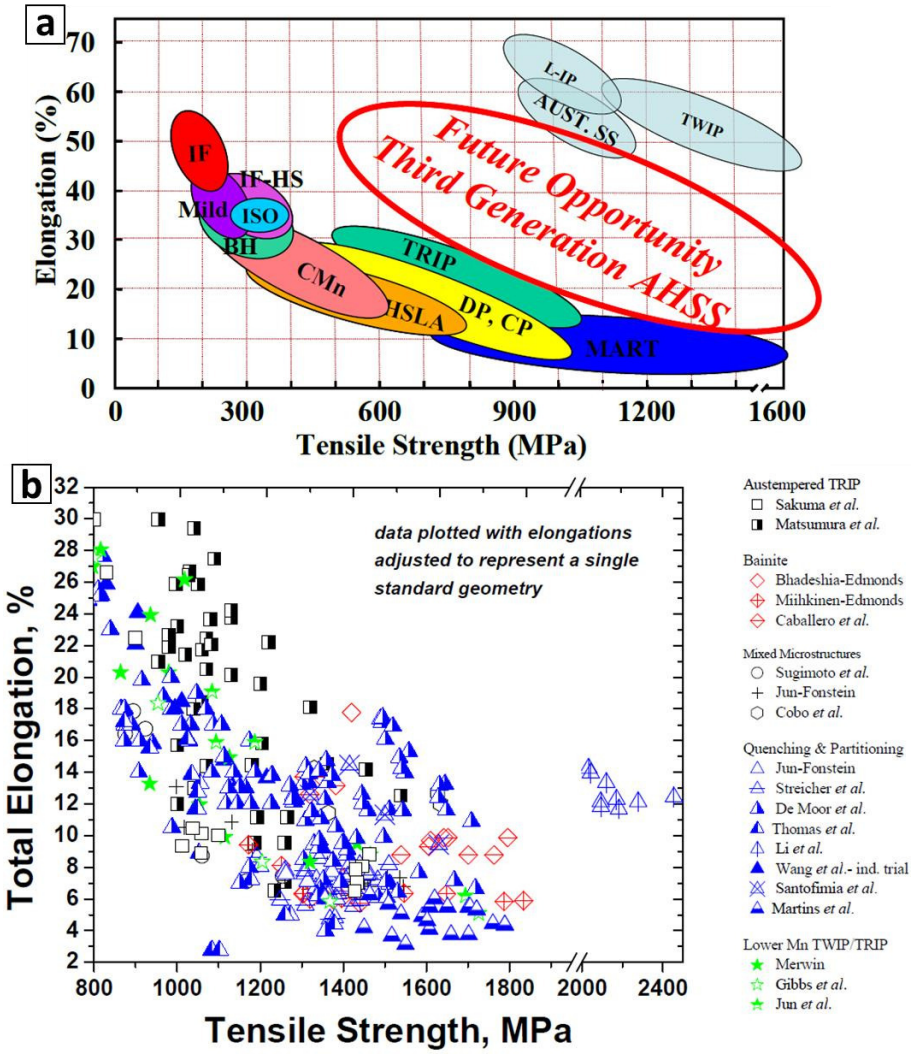

Figure 1.1: (a) Total elongation against tensile strength (MPa) chart for different classes of steel grades [2]. (b) Summary of the mechanical properties obtained in retained austenite-containing AHSS [15].

1.2 Innovative steel development towards ultrafast heating strategy

In this work, the terminology defined in [16] is adopted to identify the different heating rates studied. Heating rates up to 10 °C/s correspond to conventional heating, easily achieved in gas-fired annealing lines. Fast heating rates range from 10 to 100 °C/s, and heating rates ≥ 100 °C/s are designated as ultrafast heating (UFH). Ultrafast heating is a heat treatment strategy that employs high heating rates during the initial stage of the annealing process. This annealing approach represents an attractive route towards the new generation of steels since it leads to the development of steels with equivalent or enhanced mechanical performance compared to those obtained in conventional annealing lines. Additionally, the UFH represents an advantage for the steels industry since it increases the production speed and capacity of annealing lines coupled with high energy-cost efficiency [17].

Moreover, the development and implementation of new annealing processes based on induction heating technologies contribute to reducing the environmental impact produced by the steel-making industry [18]. Figure 1.2 presents a digital reproduction of the pilot-scale transverse flux induction heating technology developed by the FivesCeles group [18]. This technology is suitable for heat-treating of magnetic and non-magnetic steel grades, and it can reach heating rates up to 400 °C/s and peak temperatures up to 1200 °C, depending on the material and its dimensions.

The application of fast annealing technologies for developing high performance steel grades has been studied extensively. In 1988, G. F. Bobart [19] published a technical note summarizing part of the results in fast heating of steels obtained by Battelle Memorial Institute (USA) and the Electric Power Research Institute (EPRI-USA). The reported information indicates that fast heating of Al-killed steels resulted in finer grains and similar mechanical properties than those obtained in the same steel after conventional heating. Type 301, 304 and 430 stainless steel grades also showed good response in tests conducted at high heating rates, where mechanical properties were at least as good as those attained by conventional heating [19]. In 1999, O. Ivasishin and R. Teliovich reviewed the potential of the rapid heat treatment of titanium alloys and steels [20]. Beyond the well-known influence of the high heating rate on the formation of refined grain structures, Ivasishin and Teliovich highlighted the importance of the chemical heterogeneities produced upon the fast heating of steels. Those chemical heterogeneities in austenite, related to the dissolution of carbides upon heating, led to the formation of heterogeneous microstructures after cooling. The authors pointed out that those mixed microstructures could improve the mechanical performance of high strength steels. Using this approach, G. Cola developed the FlashBainite® processing [21–23], which is based on the formation of

martensitic-bainitic microstructures via the combination of ultrafast heating and fast cooling.

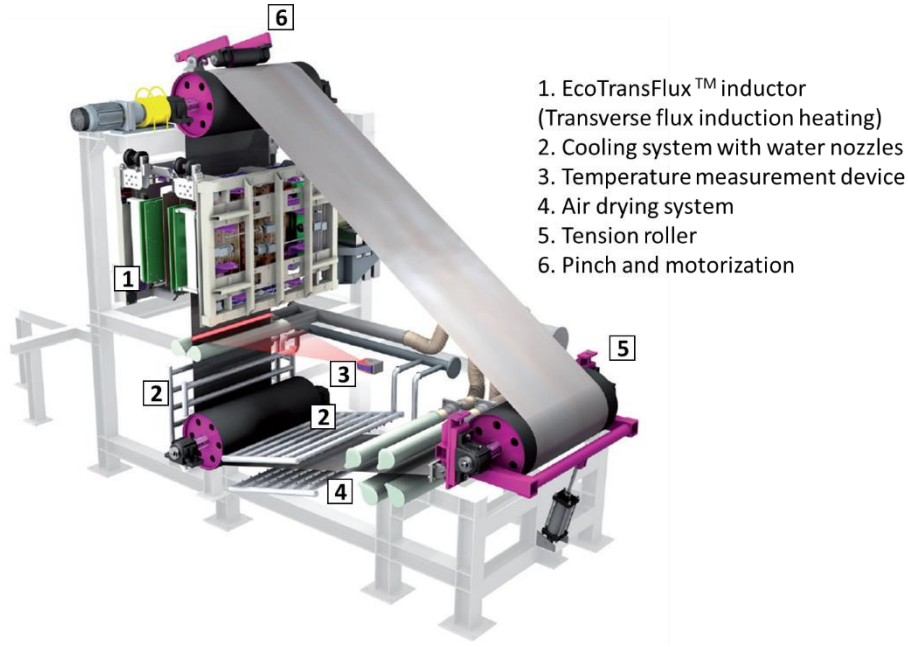

Figure 1.2: EcoTransFlux^{TM} transverse flux inductor. Close-loop fast annealing line simulator developed by FivesCeles group. Adapted from [18].

The steel grades produced through the FlashBainite® annealing process are high strength martensitic-bainitic steels with mechanical properties in the range of the advanced high strength steels. The concept behind this process is the formation of mixed microstructures in heat treatments shorter than 10 seconds (including the cooling step). Flash® heated steel grades could replace the conventional steel grades in several applications, including those that require formability. Moreover, the increased strength obtained via the combination of UFH and quench might allow the fabrication of thinner structural components while maintaining the strength level. Figure 1.3 presents prototype components made from Grade 60 steel and formable Flash® 1500 AHSS. The Flash® 1500 component is 60% lighter and 50% stronger than the one made from Grade 60 steel [21].

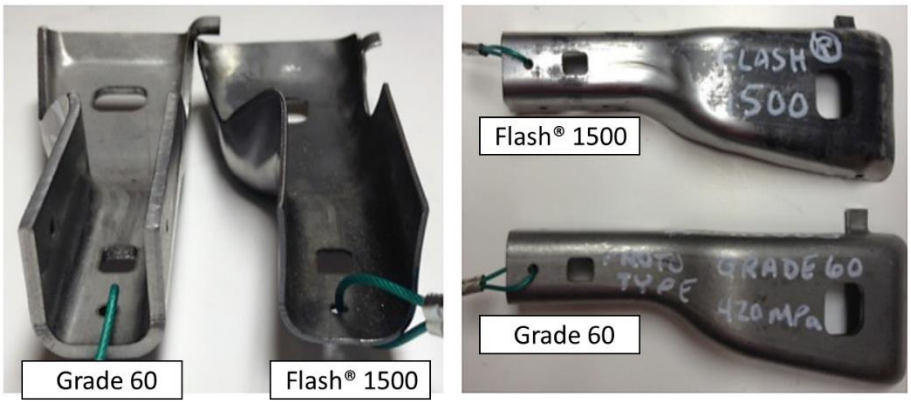

Figure 1.3: Prototype "seat track foot" annealed via Flash® processing. The component made from formable Flash®1500 steel grade is 60% lighter than the one made from Grade 60 steel. Adapted from [21].

1.3 Scope of this work

This work aims to evaluate the effect of ultrafast heating rates on the microstructure and related mechanical properties of low alloy AHSS. Thus, it is expected to assess the potential for further optimization of mechanical properties and processing routes by shortening the annealing time during heat treating of different steel grades. To fulfill this purpose, ultrafast heating rates are employed during the initial heating step in direct quenching, quenching and partitioning and austempering thermal treatments. The resulting microstructures and mechanical properties of UFH steel grades are compared to those obtained in conventionally treated steels.

References

[1] O. Bouaziz, H. Zurob, M. Huang, Driving force and logic of development of advanced high strength steels for automotive applications, Steel Res. Int. 84 (2013) 937–947. https://doi.org/10.1002/srin.201200288.

[2] D.K. Matlock, J.G. Speer, E. De Moor, Paul J. Gibbs, Recent developments in advanced high strength sheet steels for automotive applications: An overview, JESTECH. 15 (2012) 1–12.

[3] S. Oliver, T.B. Jones, G. Fourlaris, Dual phase versus TRIP strip steels: Comparison of dynamic properties for automotive crash performance, Mater. Sci. Technol. 23 (2007) 423–431. https://doi.org/10.1179/174328407X168937.

[4] A. Barani, D. Ponge, D. Raabe, Strong and Ductile Martensitic Steels for Automotive Applications, Steel Res. Int. 77 (2006) 704–711.

[5] H. Mohrbacher, Martensitic Automotive Steel Sheet - Fundamentals and Metallurgical Optimization Strategies, Adv. Mater. Res. 1063 (2015) 130–142. https://doi.org/10.4028/www.scientific.net/amr.1063.130.

[6] S. Lee, B.C. De Cooman, Effect of the intercritical annealing temperature on the mechanical properties of 10 Pct Mn multi-phase steel, Metall. Mater. Trans. A Phys. Metall. Mater. Sci. 45 (2014) 5009–5016. https://doi.org/10.1007/s11661-014-2449-0.

[7] L. Chen, Y. Zhao, X. Qin, Some aspects of high manganese twinning-induced plasticity (TWIP) steel, a review, Acta Metall. Sin. 26 (2013) 1–15. https://doi.org/10.1007/s40195-012-0501-x.

[8] J. Zhao, Z. Jiang, Thermomechanical processing of advanced high strength steels, Prog. Mater. Sci. 94 (2018) 174–242. https://doi.org/10.1016/j.pmatsci.2018.01.006.

[9] W. Bleck, F. Brühl, Y. Ma, C. Sasse, Materials and Processes for the Third-generation Advanced High-strength Steels, BHM Berg- Und Hüttenmännische Monatshefte. 164 (2019) 466–474. https://doi.org/10.1007/s00501-019-00904-y.

[10] D.K. Matlock, J.G. Speer, Processing opportunities for new advanced high-strength sheet steels, Mater. Manuf. Process. 25 (2010) 7–13. https://doi.org/10.1080/10426910903158272.

[11] D. V. Edmonds, R.C. Cochrane, Structure-property relationships in bainitic steels, Metall. Trans. A. 21 (1990) 1527–1540. https://doi.org/10.1007/BF02672567.

[12] A. Kumar, A. Singh, Mechanical properties of nanostructured bainitic steels, Materialia. 15 (2021) 101034. https://doi.org/10.1016/j.mtla.2021.101034.

[13] J.G. Speer, E. De Moor, A.J. Clarke, Critical assessment 7: Quenching and partitioning, Mater. Sci. Technol. 31 (2015) 3–9. https://doi.org/10.1179/1743284714Y.0000000628.

[14] B. Hu, H. Luo, F. Yang, H. Dong, Recent progress in medium-Mn steels made with new designing strategies, a review, J. Mater. Sci. Technol. 33 (2017) 1457–1464. https://doi.org/10.1016/j.jmst.2017.06.017.

[15] E. De Moor, J.G. Speer, D.K. Matlock, D.N. Hanlon, Effect of retained austenite on tensile behavior of AHSS revisited, Mater. Sci. Technol. Conf. Exhib. 2011, MS T'11. 1 (2011) 568–579.

[16] F. Castro-Cerda, Third Generation Advanced High Strength Steels via Ultrafast Heating, Ph. D. Thesis, Ghent University, Gent, Belgium, 2017. https://doi.org/D/2017/10.500/13.

[17] G. Griffay, M. Anderhuber, P. Klinkenberg, V. Tusset, New continuous annealing technology with high-speed induction heating followed by ultra-fast cooling. European Commission Project Contract No 7210-PR/026, 2002.

[18] FivesCeles-Group, EcoTransFlux: Transverse Flux Induction Heating Solutions. European Project LIFE09 ENV/FR/000591, 2011.

[19] G.F. Bobart, Technical note: Transverse flux induction heat treating, J. Heat Treat. 6 (1988) 47–52. https://doi.org/10.1007/BF02833163.

[20] O.M. Ivasishin, R. V. Teliovich, Potential of rapid heat treatment of titanium alloys

and steels, Mater. Sci. Eng. A. 263 (1999) 142–154. https://doi.org/10.1016/s0921-5093(98)01173-3.

[21] G.M. Cola, Replacing hot stamped, boron, and DP1000 with “room temperature formable” Flash® Bainite 1500 advanced high strength steel, ASM Int. - 28th Heat Treat. Soc. Conf. HEAT Treat. 2015. (2015) 21–28.

[22] T. Lolla, G. Cola, B. Narayanan, B. Alexandrov, S.S. Babu, Development of rapid heating and cooling (flash processing) process to produce advanced high strength steel microstructures, Mater. Sci. Technol. 27 (2011) 863–875. https://doi.org/10.1179/174328409X433813.

[23] T.R. Watkins, G. Cola, S. Babu, T. Muth, B. Shassere, H. Wang, R. Dinwiddie, Fundamental Science and Technology of Flash Processing Robustness for Advanced High Strength Steels (AHSS)-OAK RIDGE NATIONAL LABORATORY ORNL/TM-2019/1412, 2019.

Chapter 2

State of the art

This chapter reviews the microstructural evolution during the ultrafast heating of steels. Special attention is given to ferrite recrystallization and austenite formation upon fast heating. Additionally, an overview of the microstructure development and related mechanical properties in steel grades produced via a combination of UFH and different cooling paths is also presented.

2.1 Microstructural changes upon fast heating

2.1.1 Recrystallization in extra-low carbon steels

In contrast to the study of recrystallization carried out under isothermal annealing conditions [1,2], the non-isothermal (isochronal) recrystallization of cold-worked materials is analyzed via interrupted heating to different temperatures and subsequent quench in order to "freeze" the microstructural changes that happen during heating at each specific annealing temperature. Early research conducted by R. Goodenow [3] in low carbon Al-killed and rimmed steels showed that the onset of the ferrite recrystallization is shifted to higher temperatures as the heating rate increases. Combining those isochronal experiments with isothermal holding revealed that the time required to obtain a fully recrystallized microstructure decreases with increasing the annealing temperature. Increased recrystallization and grain growth rates at higher annealing temperatures are directly related to the thermally-activated nature of those solid-state reactions [4]. D. Muljono, M. Ferry and D. Dunne [4,5] stated that increasing the heating rate, in the range from 50 to 1000 °C/s, had increased the temperature of nucleation of recrystallized grains and temperature to complete recrystallization in cold rolled 0.003-0.05%C steels (Figure 2.1a). The large driving force available for nucleation at high heating rates led to the formation of a large number of recrystallized nuclei. Additionally, the time available for the growth of the newly formed recrystallized grains decreased with the increment of the heating rate, producing a refined microstructure after ultrafast heating in low and extra low carbon steels. Figure 2.1b shows the decrease in the mean recrystallized grain size with the increase of the heating rate [5]. Results from ultrafast heating of steels obtained by Reis et al. [6] in an IF Ti-alloyed steel and Senuma et al. [7] in extra-low carbon steels concur with those reported in [3–5].

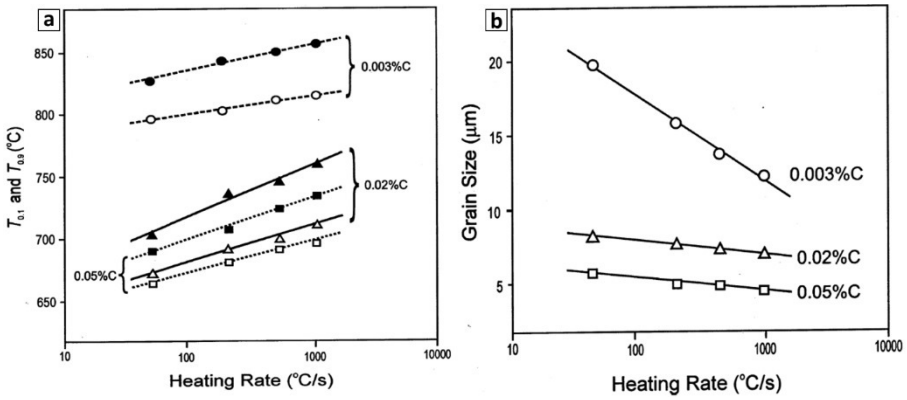

Figure 2.1: (a) Effect of the heating rate on the temperatures to start recrystallization (open symbols) and recrystallization finishing temperatures (filled symbols). (b) Effect of heating rate on recrystallized ferrite grain size. Adapted from [5].

2.1.2 Influence of the initial microstructure on austenite formation

The effect of different initial microstructures on the austenite formation upon fast heating is reviewed in this section.

i) Initial ferritic microstructure

The transformation of austenite from pure iron was found to occur via a massive mechanism [8,9]. This mechanism of austenite formation was suggested to occur in experiments performed at heating rates up to 10^6 °C/s [8]. Austenite nucleates preferentially at ferrite/ferrite grain boundaries, and the growth of the newly formed austenitic grains does not require long-range diffusion of atoms. Instead, the ferrite→austenite transformation proceeds at a high rate by an interchange of iron atoms positions at the ferrite/austenite interface. Consequently, the heating rate employed slightly affects the critical temperature of phase transformation [9].

ii) Initial pearlitic microstructure

Austenite nucleation in lamellar ferrite-cementite aggregates occurs preferably at pearlitic colony intersections in low and high heating rate experiments [8]. Then, the growth of austenite proceeds by the dissolution of ferrite and cementite lamellae. The growing of the newly formed austenite is accompanied by a marked carbon gradient that takes place due to the difference in carbon concentration between ferrite and cementite particles [10,11]. The morphology of pearlite also influences the rates of austenite nucleation and growth, and it was found that both parameters increase as the pearlite spacing decreases [10]. Additionally, as the dissolution kinetics of cementite is slower than that of ferrite, the growth of austenite can be developed by the fast consumption of ferritic lamellae. In contrast, cementite particles could remain undissolved even in slow heat treatments [10,12].

Moreover, the temperature needed to reach complete cementite dissolution increases with the heating rate due to the diffusion-controlled dissolution of cementite [13]. In this way, martensitic microstructures with embedded undissolved carbides can be obtained upon quenching. The microstructural patterns produced from those undissolved carbides resemble the initial pearlitic microstructure. Figure 2.2 shows this type of microstructural feature called “ghost pearlite” [14]. Figure 2.2a displays a martensitic matrix and lamellar cementite particles that remained undissolved after heating at 200 °C/s to 850 °C, followed by cooling at 235 °C/s [14]. Similarly, Figure 2.2b presents the microstructure produced after laser heating in an Fe-0.5C-0.8Mn-0.8Cr steel [15]. In both figures, undissolved cementite particles are highlighted by red arrows.

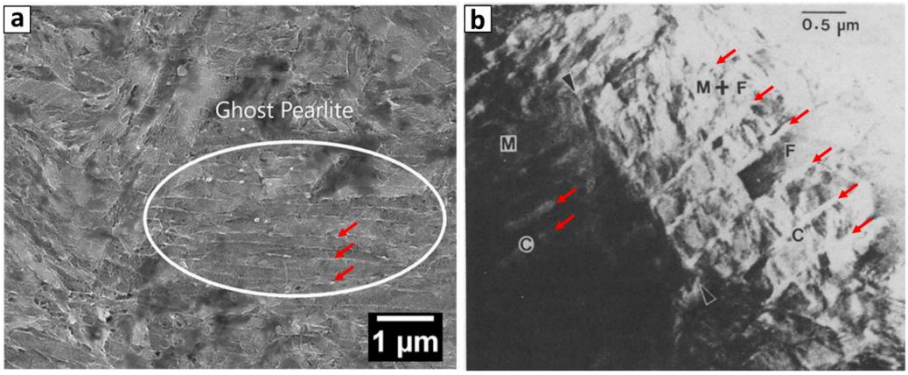

Figure 2.2: (a) SE image of ghost pearlite in a 1060 Nb steel heated at 200 °C/s to 850 °C and fast cooled to room temperature [14]. (b) STEM micrograph of an Fe-0.5C-0.8Mn-0.8Cr steel laser heat-treated [15]. M: Martensite; F: Ferrite; C: Cementite. Cementite lamellas are highlighted by red arrows.

Analogous phenomena are developed during austenite nucleation, starting from a matrix that contains spheroidized cementite particles [8,16]. Nucleation of austenite occurs at the interphase between cementite and ferrite, creating a core-shell type structure. Judd and Paxton [16] showed that spheroidized cementite particles located at ferrite grain boundaries have a strong catalytic effect on the austenite nucleation rate. They reported that the nucleation rate of austenite in cementite particles located at ferrite grain boundaries could be three to eight times faster than the nucleation rate of austenite in cementite particles located in the ferritic bulk. Figure 2.3 shows the microstructure of a spheroidized 0.77C-Fe steel pulse heated 0.02 seconds to 845 °C [17]. Martensitic rims (austenite at high temperature), surrounding undissolved spheroidized cementite particles, and the absence of martensitic features located at the ferrite-ferrite grain boundaries indicate the thermodynamically favorable nucleation of austenite at the ferrite-carbide interphase.

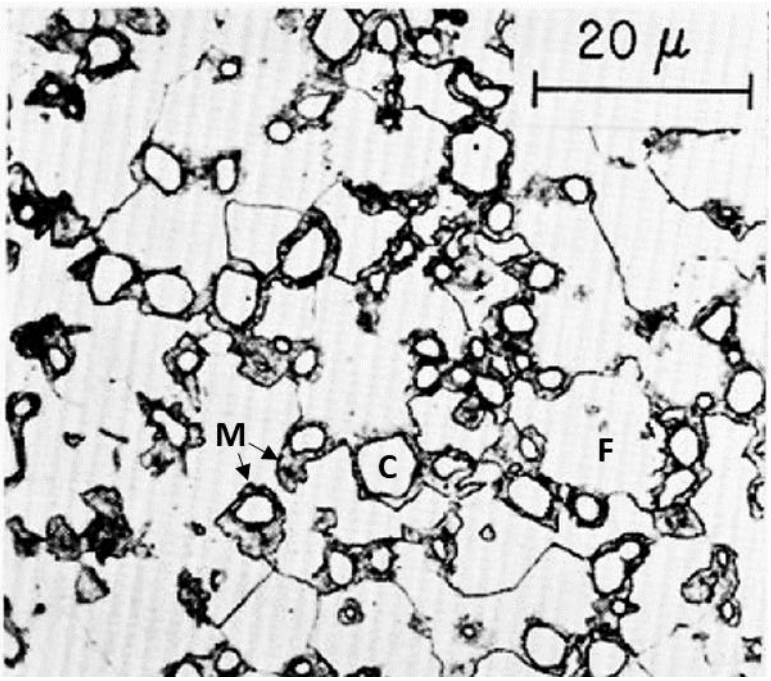

Figure 2.3: Spheroidized 0.77C-Fe steel pulse heated 0.02 seconds to 845 °C. Adapted from G. Speich et al. [17]. M: Martensite; F: Ferrite; C: Cementite.

Another relevant aspect related to austenite formation in ferrite-cementite aggregates is that carbon gradients in austenite can exist even after complete cementite dissolution, producing chemically heterogeneous parent austenite, as pointed out by Roberts and Mehl in 1947 [10].

iii) Martensitic microstructure

The formation of austenite from martensite in Fe-Ni alloys has been found to occur by a reverse martensitic mechanism of transformation [17–19]. This type of transformation leads to the generation of an austenitic microstructure with a high dislocation density, and the annealing process is accompanied by recovery and recrystallization of the reversed austenite [17,19]. The diffusionless mechanism that produces the martensite to austenite transformation in Fe-Ni alloys does not depend on the heating rate, and therefore, the critical temperatures for the martensite to austenite reversion are not affected by the prior heating rate [18]. Contrarily, it has been shown that the temperature of austenite formation in carbon-alloyed martensitic steels is heating rate dependent [18,20,21]. The behavior observed in Fe-C alloys is related to the decomposition of martensite into ferrite and carbide aggregates upon heating [18,22]. Then, once the thermodynamic conditions for austenite nucleation are reached, a diffusional type of austenite transformation occurs.

iv) Mixed Ferritic-Pearlitic (lamellar and spheroidized) and Ferritic-Martensitic microstructures

The analysis of austenite formation in hypoeutectoid steels has great importance in the microstructural design of low alloy ultrafast heated steels. The formation of austenite in mixed ferritic-pearlitic and ferritic-martensitic initial structures somehow combines the aspects indicated in Sections 2.1.2(i) to (iii)

Upon heating, the nucleation of austenite in ferritic-pearlitic steels occurs preferably at ferrite/pearlite interfaces and at the intersections between pearlitic colonies, where the surface energy is more favorable [11,12,23]. The growing of austenite is controlled by carbon diffusion with rapid consumption of the initial pearlitic regions [24–26] or martensitic islands [26]. Similarly, a diffusion-controlled process governs the dissolution of proeutectoid ferrite, whereby carbon atoms concentrated at the former austenitic regions diffuse into the newly formed austenite in contact with ferrite. This long range diffusion mechanism can be prolonged to higher temperatures, with the dissolution of ferrite following local equilibrium conditions [11]. The fraction of undissolved ferrite decreases by increasing annealing temperature and, under equilibrium conditions, ferrite is completely dissolved above the A_3 temperature [12]. Dykhuizen et al. [25] reported that the formation of austenite from ferrite could occur when carbon is available from the partially dissolved pearlitic regions. This led to a temperature range in which austenite can form from both ferrite and pearlite. Nevertheless, the rate of austenite growing through ferrite in pearlitic regions is much faster than in proeutectoid ferrite due to the shorter distances to the carbon sources, i.e., cementite particles [12,25].

A different mechanism of ferrite to austenite transformation has been observed under specific heating conditions. In fast heating experiments, austenite formation is controlled by carbon diffusion at the early stages of the process [11]. However, if a thermodynamic transient is reached upon heating, an interface-controlled mechanism can be developed during the ferrite to austenite transformation [8,11,22,27,28].

Albutt and Garber [27] reported the occurrence of a diffusionless transformation of ferrite to austenite in a 0.086%C steel heated at 2000 °C/s to 950 °C and immediately quenched. Microstructural analysis and hardness values suggested that the transformation of ferrite to austenite was developed by nucleation and growth in regions close to carbide particles [27]. Instead, a shear transformation of austenite was claimed to proceed above 910 °C, in regions far from the carbon enriched austenite. As mentioned in Section 2.1.2(i), Speich et al. [8] suggested that the transformation of ferrite to austenite occurred by a massive mechanism due to the absence of defects in the microstructure after quenching.

Observations made by Schmidt et al. [28] agree with the mechanisms previously mentioned. The authors suggested that below the T_0 temperature the formation of

austenite is controlled by long-range carbon diffusion in steels with an initial microstructure composed of ferrite and pearlite, and by interface control at temperatures above the T_0. The formation of a microstructure with distinctive morphologies after experiments performed at a heating rate of 20 °C/s was correlated to the mixed mechanisms of austenite formation occurring at carbon-rich (pearlite) and carbon-poor (ferrite) regions.

Castro-Cerda et al. [11] indicated that the transformation of austenite by diffusion control can still occur above the T_0 temperate, and the actual transition to massive-like austenite formation arises at $G^{\gamma} < G^{\alpha}$ when X_C approaches to 0. This thermodynamically defined transition was called A_m temperature [11]. Yonemura et al. also observed a massive type of ferrite to austenite transformation in an Fe-0.1C martensitic-ferritic steel heated at 10^4 °C/s [22]. The formation of austenite with comparable screw dislocation density and carbon concentration to the former ferrite suggested that austenite was formed by rearrangement of atoms at the ferrite/austenite interface [22].

As indicated in Section 2.1.1, ferrite recrystallization is shifted to higher temperatures by increasing the heating rate in Fe-C alloys [3–7]. Such a phenomenon leads to the interaction between ferrite recrystallization and austenite formation upon heating if the recrystallization is delayed to high temperatures into the temperature range of austenite nucleation. Experimental evidence [26,29–38] has shown the nucleation of austenite at ferrite/ferrite interfaces, affecting the formation of austenite upon heating and the distribution of martensite after quenching to room temperature.

The enhanced nucleation of austenite at the boundaries of the non-recrystallized ferrite and at the interfaces between recrystallized and non-recrystallized grains at temperatures just above the A_{C1} is a result of the largest driving force available for nucleation [32,38]. As the heating rate increases, the overheating resulting from the shift of the onset of austenite formation leads to a higher driving force for austenite nucleation at ferrite/carbide aggregates. However, it also favors the nucleation of austenite at ferrite/ferrite interfaces [38]. Savran et al. [12] indicated that the formation of austenite at ferrite/ferrite interfaces is a result of the rejection of carbon from ferrite-solid solution during heating. At low temperatures, the nucleation of austenite at the ferrite/ferrite interface requires carbon accumulation, and the growth of those austenitic grains will be controlled by long-range carbon diffusion. At the same time, the movement of the formed ferrite/austenite boundary depends on the carbon supply from carbon-rich regions, like prior pearlite or martensite. As a result, the growth of those austenite nuclei is very slow. This leads to the formation of grain refined austenite in intercritical annealed steels [26,29,31–38].

The banded microstructures obtained in fast heated steels result from the spatial distribution of the deformed ferritic grains and pearlite or/and martensite

[29,32,33]. Preferential nucleation and fast growth of austenite through the carbon-rich areas (pearlitic colonies or martensitic regions) create bands of martensite (austenite at high temperature) and ferrite after quenching of intercritical annealed steels. The spatial distribution of those bands generally resembles the initial cold-rolled microstructure [29,32,33,36]. Figure 2.4a shows the microstructure of an Fe-0.17C-0.74Mn ferritic-pearlitic steel cold-rolled to 80% [33]. After heating at 300 °C/s to 740 °C and water quenching with no soaking time, a banded martensitic-ferritic microstructure was produced (Figures 2.4b to 2.4c) [33]. Figure 2.4d compiles three different zones highlighted by yellow squares in Figure 2.4c. Non-recrystallized ferrite is observed between martensitic bands in Figure 2.4d(1). Figure 2.4d(2) displays an intragranular austenitic grain embedded in ferrite. The close distance to the ferrite/ferrite grain boundary suggests that the austenitic grain nucleated at the ferrite/ferrite interface and was "consumed" into ferrite due to insufficient pinning [29]. Austenitic grains located at ferritic grain boundaries are highlighted by red arrows in Figure 2.4d(3).

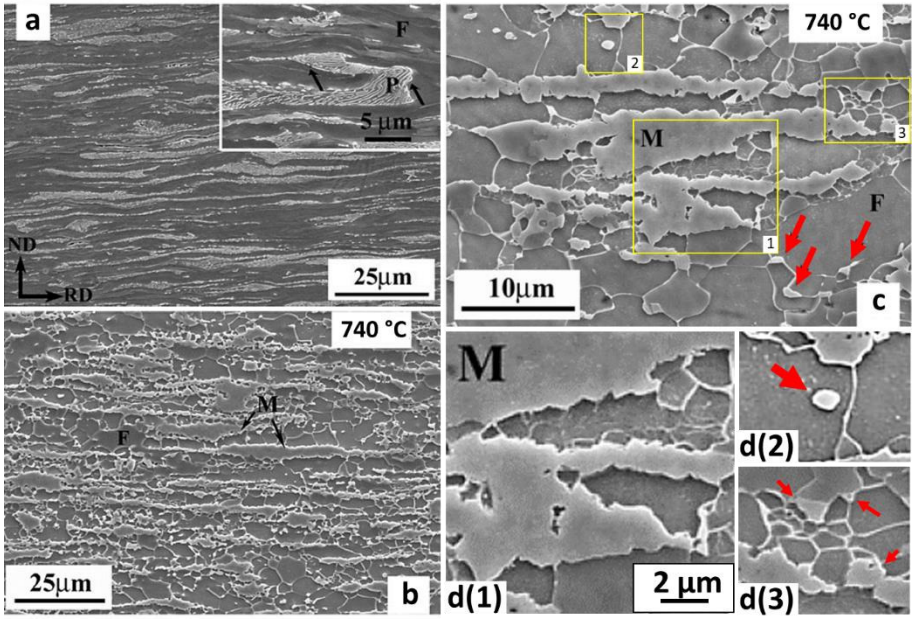

Figure 2.4: Banded ferritic-martensitic microstructure produced after ultrafast heating into the intercritical range. (a) Initial material: ferritic-pearlitic steel cold rolled to 80%. (b-c) Microstructure obtained after heating at 300 °C/s to 740 °C (1013 K) followed by water quenching. (d) Enlarged images of the yellow squares highlighted in (c). Red arrows indicated austenite grains (transformed to martensite after quenching). Adapted from [33].

It is seen that those small austenitic grains produced pinning and inhibited the grain growth of small recrystallized ferrite grains. This effect promotes the microstructural refinement of intercritical annealed DP steel [29,32,35]. Nevertheless, large recrystallized ferritic grains are observed at locations where the distance between martensitic features is large enough, producing a banded microstructure with

heterogeneous distribution of grains. Thomas and Matlock [32] evaluated the formation of banded microstructures under fast heating in an Fe-0.12C-1.40Mn-0.21Cr-0.2Mo-0.02Nb steel. They found that an even distribution of spheroidized cementite particles throughout the microstructure led to an even distribution of austenite nuclei, decreasing the degree of banding after quenching. Equiaxed distribution of martensite patches was also observed to be formed in a matrix with recrystallized ferrite, produced via slow heating (in the range of 0.3 to 2.4 °C/s) [32]. Huang et al. [36], Li et al. [31] and Karmakar et al. [39] also reported a significant variation in the spatial distribution of austenite grains (martensite after quenching) with the heating rate, changing from equiaxed to banded at slow and high heating rates, respectively.

2.1.3 The influence of the heating rate on crystallographic texture

The influence of high heating rates on the crystallographic texture of different cold-rolled steel grades has been studied extensively [6,7,34,38,40–46]. Castro-Cerda et al. [45] compared the crystallographic texture obtained in ultra-low carbon steel, produced by heating at 10 °C/s, 400 °C/s and 800 °C/s to different annealing temperatures. They reported that crystallographic components typically observed in cold-rolled ferrite are retained if the recrystallization of ferrite is not completed upon heating. Additionally, they indicated that the texture of the recrystallized ferritic grains is virtually not affected by the heating rate, where a strong ND-texture fiber of concave curvature together with a weak RD-fiber were developed.

In the evaluation of the transformation textures of an IF steel subjected to heating rates between 800 °C/s and 4500 °C/s, Reis et al. [6] observed that a texture memory effect [47,48] was produced during the ferrite→austenite→ferrite transformation. At all heating rates, fully recrystallized ferritic microstructures were obtained before ferrite to austenite transformation. After the reverse austenite→ferrite transformation, the produced texture components showed a strong match compared with the recrystallization texture observed in ferrite at the onset of the transformation.

The analysis of texture in partially recrystallized microstructures indicates that the intensity of the deformation texture becomes pronounced at high heating rates [34,40,43,44]. This is a result of the larger fraction of non-recrystallized but recovered ferrite that can be retained for a predefined annealing temperature [34,40,43,44]. It has been found that non-recrystallized ferrite also affects the transformation textures of martensite in intercritical annealed low-carbon alloy steels subjected to ultrafast heating [34,38,41–44]. Petrov et al. [34,44,49] provided evidence for austenite nucleation in a recovered ferrite matrix during the ultrafast heating of low-alloy steels. Their results [34,44,49] suggested that the texture of the newly formed austenite might be crystallographically related to the texture of the

recovered ferrite, resulting in the development of texture inheritance in martensite after quenching.

Figure 2.5 presents the texture formed after heating at 1000 °C/s in an intercritically annealed Fe-0.11C-1.87Mn-0.45Cr-0.18Mo-0.03Nb steel [38]. It can be seen that the ferrite texture remained practically unaltered compared to the initial cold-rolled material, which is the result of the low fraction of recrystallized ferrite formed upon heating (F_{Rx} ≈4.1%). On the other hand, the texture components in martensite also resemble the texture of the initial material, as evident by comparing Figure 2.5d with Figure 2.5b.

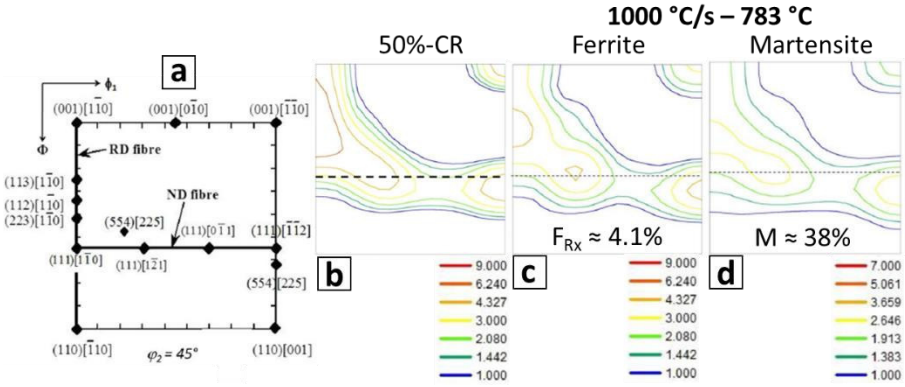

Figure 2.5: φ_2 = 45° sections of ODFs for ferrite and martensite after intercritical annealing of a cold-rolled Fe-0.11C-1.87Mn-CrMnNb steel. (a) Ideal positions of the most important BCC texture components. (b) Initial material cold rolled to 50%. Texture after hating at 1000 °C/s to 783 °C and quench: (c) Ferrite; (d) Martensite. The numbers in the lower part of figures (c) and (d) correspond to the fraction of recrystallized ferrite (F_{Rx}) and martensite (M), respectively. Adapted from [38].

This inheritance of the initial cold-rolled texture in martensite is evidence of the texture memory effect discussed elsewhere [34,38,41–44]. The negligible difference between ferritic and martensitic texture components reflects the strong incidence of the microstructural state at the onset of austenite formation on the crystallographic orientation of the transformation products in ultrafast heated steels. This leads to the opportunity of texture design in ultrafast heated steels by controlling the crystallographic orientation of the initial material before or during the annealing treatment.

2.1.4 The influence of ultrafast heating on the microstructure development

The characteristics of the parent austenite and the respective microstructures produced during cooling are greatly influenced by the selected annealing parameters. Regarding this point, two types of annealing routes can be distinguished:

- Peak annealing heat treatments: A short soaking time, in the range between 0 to 2 s, is employed once the annealing temperature is reached. Then, the sample is cooled following a predefined thermal path.
- Isothermal soaking after fast heating: In this route, a prolonged soaking time is used at a predefined annealing temperature. This strategy could lead to isothermal ferrite recrystallization (if recrystallization is partially or entirely avoided during the heating step), grain coarsening, carbide dissolution, and chemical homogenization. The rate of each mentioned reaction increases with the annealing temperature [61,62].

Rapidly heated peak annealed steels are reported to exhibit both ferritic and martensitic grain refinement [6,22,33,44,49–54]. Grain size evaluation in ultra-low carbon steels [4,5] showed that the recrystallized ferritic grain size decreases with the heating rate in the range from 50 to 1000 °C/s. Nevertheless, a saturation effect of the ferrite grain size was observed in an IF steel heated at rates beyond 1000 °C/s [6]. A similar saturation effect was found in ultrafast heated AHSS [42,51]. Castro-Cerda et al. [42], in the study of the effect of the heating rate on the microstructure of an intercritical annealed low alloy steel, reported a reduction of the average ferritic grain size diameter from ~5 µm to ~3 µm by increasing the heating rate from 10 °C/s to 400 °C/s and further refinement was not obtained by rising the prior heating rate to 800 °C/s and 1200 °C/s. Those results agree well with previous findings reported by Petrov et al. [51]. Comparable phenomenon was detected in martensitic microstructures obtained in low and medium carbon steels ultrafast heated above the intercritical range [52,55].

Moreover, the control of austenite fraction upon heating is crucial in developing intercritically annealed ultrafast heated steels. It is well established in the current literature that the increment of the heating rate leads to a shift of the critical temperatures of austenite transformation in Fe-C alloys [11,18,20,25,32,33,56,57]. As a result, a smaller fraction of austenite may be obtained by heating the steel to a predefined temperature in the intercritical range if high heating rates are applied [11,25,33,56,57]. However, it has been shown that the interaction of ferrite recrystallization, pearlite spheroidization, and austenite formation play a fundamental role in the amount of austenite produced at high heating rates. Experimental evidence suggests that austenite nucleation takes place at carbon enriched regions and at interfaces between recrystallized, recovered, and deformed ferritic grains [29]. Consequently, a larger fraction of austenite has been found in intercritically annealed steels subjected to ultrafast heating [42,58,59]. The higher driving force available for nucleation produced by overheating and the larger fraction of nucleation sites at non-recrystallized ferrite boundaries leads to the possibility of a larger fraction of austenite upon fast heating. Additionally, cementite spheroidization has been indicated as a consequence of slow hating rates [33,36,60]. The formation and growing of spheroidized particles might increase the diffusion

distance and decrease the surface area for austenite nucleation [61]. Roberts and Mehl [10] showed that the transformation of austenite from spheroidized cementite is slower than from lamellar pearlite or tempered martensite. Therefore, a similar effect is expected to occur in steels treated by continuous heating and intercritical annealing affecting the kinetics of austenite formation [36,59]. In cold-rolled steels, martensite fraction was also observed to increase with an increase in the heating rate for steels soaked for prolonged periods [36,37,62–64].

2.2 Mechanical properties obtained via a combination of ultrafast heating annealing and subsequent thermal paths

2.2.1 Directly cooled steels

Directly cooled UFH steels are steel grades produced through a simple heat treatment strategy, which combines the following steps: (i) continuous heating up to the annealing temperature, (ii) short or prolonged soaking and (iii) direct cooling.

Extensive research has been conducted in low alloy steels heated into the ferritic-austenitic range [26,42,53,64–69]. The obtained results showed that ultrafast heated steels display equivalent or improved mechanical properties than their conventional annealed counterparts. Meng et al. [67] studied the influence of the fast heating rate combined with 2 s soaking on the microstructure and mechanical properties of a commercial DP590 steel grade. Compared to the commercial steel, the UFH annealing led to an increase in ε_{Total} from 23.3% to 26.6% and σ_{UTS} from 625 MPa to 666 MPa. A similar tendency was reported by Deng et al. [69], where improved mechanical properties were obtained by increasing the heating rate from 5 °C/s to 300 °C/s in a 0.08C-0.42Si-1.83Si steel annealed at 820 °C for 60 s and water quenched. Engineering stress-strain curves obtained by Meng et al. [67] and Deng et al. [69] are presented in Figure 2.6.

Moreover, Castro-Cerda et al. [42] and Karmakar et al. [26] investigated the effect of the initial microstructure on the mechanical properties of intercritical annealed steels, showing that UFH annealing of ferritic-martensitic microstructures resulted in the best combination of strength and ductility compared with an initial ferritic-pearlitic microstructure. In general, the reported results correlated the improved mechanical properties of UFH steels to the formation of complex phase microstructures of fine grain size. The presence of non-recrystallized ferrite also contributed to the higher strength obtained in UFH steel grades [64,66].

Low alloy steels heated above the intercritical ferritic-austenitic range also display promising mechanical behavior [52,54,70,71]. The excellent combination of mechanical properties observed in steels annealed using high heating rates are also related to the formation of mixed microstructures (martensitic-bainitic) that contain a certain amount of retained austenite. Chemical heterogeneities in parent austenite

and small austenitic grains, developed during fast heating, provide favorable conditions for austenite transformation into bainite or ferrite upon fast cooling [72], leading to the formation of microstructures that are suitable for the production of AHSS [54]. Nevertheless, further work is necessary to elucidate the influence of the chemical gradients and grain size on the decomposition of austenite after the UFH step. Additionally, the complex microstructures produced after fast heating and cooling represent an important challenge for a detailed microstructural characterization [18,42,52,54,67,72,73].

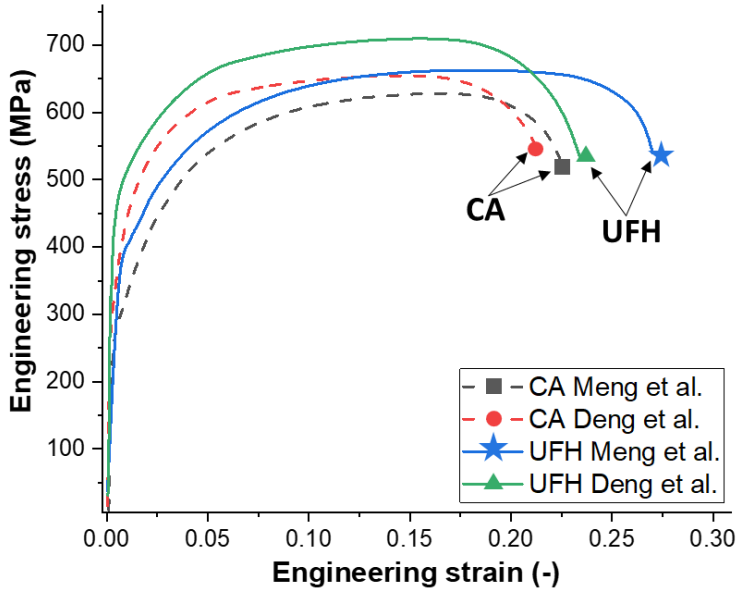

Figure 2.6: Engineering stress-strain curves of intercritical annealed steels conventionally annealed (CA) and subjected to UFH. Adapted from Meng et al. (gauge length: 80 mm; width: 20 mm; thickness: 1.5 mm) [67] and Deng et al. (gauge length: 25 mm; width: 5 mm; thickness: 1.5 mm) [69].

Regarding the formability of UFH steels, research conducted by Jaskari et al. [74,75] has shown that the ultrafast heating of ferritic stainless steels led to analogous or slightly increased R-values than the obtained in conventionally annealed steels. Similarly, Massardier et al. [46] reported that the UFH could improve the deep drawability (based on R-values calculations) of low carbon Al-killed steels through the strengthening of the {111}<uvw> texture components.

2.2.2 Steel grades produced via a combination of ultrafast heating and subsequent low-temperature isothermal treatments

The austenitization corresponds to the initial thermal step for most heat treatment of steels. Thus, there is no theoretical restriction for combining the UFH annealing and subsequent low-temperature isothermal treatments. The combination of UFH and low-temperature isothermal steps aims to develop microstructures that are not

possible to obtain just by employing high heating rates followed by direct cooling to room temperature. Low-temperature heat treatments allow to control the transformation of austenite and induce microstructural changes in the obtained microconstituents [76,77].

TRIP-aided multiphase steels have been developed using the UFH annealing prior to austempering (AT) [78,79] and quenching and partitioning (Q&P) heat treatments [41,80–82]. The results suggest that the formation of grain-refined heterogeneous microstructures composed of ferrite, bainite, martensite and retained austenite led to better mechanical performance than the obtained in bainitic [78] and martensitic TRIP-aided steels [41,82]. De Knijf et al. [41] reported an increment in $\varepsilon_{Uniform}$ of 110% and σ_{UTS} of 26% for an UFH-Q&P steel heated at 1000 °C/s compared to a conventionally annealed steel heated at 10 °C/s to 850 °C and soaked during 300 s. Dai et al. [82] have shown that after increasing the heating rate from 4 °C/s to 300 °C/s prior to the Q&P process the $\varepsilon_{Uniform}$ increased by 30% without significant influence on the σ_{UTS} value. Liu et al. [83] indicated that carbon and manganese heterogeneities presented in the initial microstructure are inherited after the UFH annealing, playing a fundamental role in the decomposition of austenite upon cooling and partitioning. Additionally, they indicated that those chemical heterogeneities could account for the improved mechanical response of the retained austenite grains [83].

2.3 Thesis outline

This chapter addressed an overview of the general aspects of ferrite recrystallization and austenite formation during ultrafast heating of steels. The mechanical properties resulting from the combination of ultrafast heating and different thermal pathways have also been reviewed. The available experimental evidence indicates that the attractive improvement of mechanical properties in UFH steels is produced by the formation of grain refined -heterogeneous- microstructures. However, the conditions for an optimal microstructural design, depending on the application, are not well understood.

Results showed that austenite transformation in pure iron proceeds via a massive mechanism. Instead, if the microstructure consists of a mixture of ferrite and carbides (cementite in pearlite or tempered martensite) the formation of austenite proceeds in steps. Firstly, by rapid dissolution of ferrite/carbides aggregates, controlled by carbon diffusion in austenite and secondly, by the dissolution of the proeutectoid ferrite. In the second case, the dissolution of ferrite can proceed either by long-range carbon diffusion or via a massive mechanism, with the former taking place at the beginning of the austenite formation process. It has been reported that the A_m temperature defines the thermodynamic threshold at which the formation of austenite changes from a diffusion-controlled to a massive mechanism. However, until now, this specific temperature has not been employed as a reference

parameter for designing UFH steels. Moreover, the influence of microalloying with carbide-forming elements on the resulting microstructures of UFH steels annealed above the A_{C3} temperature remains unexplored. Therefore, Chapter 4 deals with two steels of similar base alloy composition but one of them is additionally alloyed with Mo, Nb and Ti. Microstructures and mechanical properties of direct quenched steels, treated at heating rates ranging from 10 to 1000 °C/s up to the A_m temperature and 950 °C, are discussed in detail.

The combination of ultrafast heating and DQ, Q&P, or AT processes resulted in an improved strength-ductility balance parameter, σ_{UTS} (ultimate tensile strength) x ε_{Total} (total elongation), for low-alloy steels heated up to the intercritical range. However, the role of heterogeneous microstructures on the mechanical behavior of ultrafast heating steels remains unclear. In addition, information about the mechanical properties and microstructure of high strength steels heated up to temperatures above the intercritical range lacks in the available literature. Therefore, the effect of the heating rate on the microstructure and mechanical properties of Q&P steels annealed above the A_{C3} temperature is presented in Chapter 5. In addition, the effect of different annealing strategies, namely conventional, thermal cycling and ultrafast heating annealing, on the parent austenite grain size and resulting microstructures after austempering is discussed in Chapter 6.

With respect to the combination of ultrafast heating and Q&P treatments for creating multiphase steels, there exists a lack of understating of the influence of the partitioning step on the resulting microstructure and mechanical behavior of UFH steels. Additionally, a comparative analysis of the microstructures produced by ultrafast heating into the intercritical range and above the A_{C3} temperature has not been reported so far. Thus, Chapter 7 presents a study of the microstructure and mechanical properties of ferrite-containing UFH steels subjected to direct quenching and Q&P processes. The effects of the peak temperature and Q&P process on microstructural distribution and mechanical behavior are assessed.

Chapter 8 summarizes the main conclusions of this work and presents future work recommendations for addressing the potential of the ultrafast heating process towards the new generation of AHSS.

References

[1] P.A. Beck, Annealing of cold worked metals, Adv. Phys. 3 (1954) 245–324. https://doi.org/10.1080/00018735400101203.

[2] J.L.R. Barragan, R.A.R. Diaz, M.L. Ojeda Martinez, S. Gaona Jimenez, J.A. Juarez Islas, Effect of isothermal treatment on microstructure and mechanical properties of cold-deformed IF steel, Adv. Mater. Sci. Eng. 2019 (2019). https://doi.org/10.1155/2019/8674323.

[3] R.H. Goodenow, Recrystallization and Grain Structure in Rimmed and Aluminum-Killed Low-Carbon Steel, Trans. ASM. 59 (1966) 804–823.

[4] M. Ferry, D. Muljono, D.P. Dunne, Recrystallization Kinetics of Low and Ultra Low Carbon Steels during High-rate Annealing, ISIJ Int. 41 (2001) 1053–1060.

[5] D. Muljono, M. Ferry, D.P. Dunne, Influence of heating rate on anisothermal recrystallization in low and ultra-low carbon steels, Mater. Sci. Eng. A. 303 (2001) 90–99. https://doi.org/10.1016/S0921-5093(00)01882-7.

[6] A. Da Costa-Reis, L. Bracke, R. Petrov, W.J. Kaluba, L. Kestens, Grain Refinement and Texture Change in Interstitial Free Steels after Severe Rolling and Ultra-short Annealing, ISIJ Int. 43 (2003) 1260–1267. https://doi.org/10.2355/isijinternational.43.1260.

[7] T. Senuma, K. Kawasaki, Y. Takemoto, Recrystallization behavior and texture formation of rapidly annealed cold-rolled extralow carbon steel sheets, Mater. Trans. 47 (2006) 1769–1775. https://doi.org/10.2320/matertrans.47.1769.

[8] G. Speich, A. Szirmae, Formation of Austenite from Ferrite and Ferrite-Carbide Aggregates, Trans. Metall. Soc. AIME. 245 (1969) 1063–1074.

[9] W. Haworth, J. Gordon, The effect of rapid heating on the alpha-gamma transformation in iron, Trans. ASM. 58 (1965) 476–488.

[10] G. Roberts, F. Mehl, The mechanism and the rate of formation of austenite from ferrite-cementite aggregates, Trans. ASM. 31 (1943) 613–651.

[11] F.M. Castro Cerda, I. Sabirov, C. Goulas, J. Sietsma, A. Monsalve, R.H. Petrov, Austenite formation in 0.2% C and 0.45% C steels under conventional and ultrafast heating, Mater. Des. 116 (2017) 448–460. https://doi.org/10.1016/j.matdes.2016.12.009.

[12] V.I. Savran, Y. Leeuwen, D.N. Hanlon, C. Kwakernaak, W.G. Sloof, J. Sietsma, Microstructural features of austenite formation in C35 and C45 alloys, Metall. Mater. Trans. A Phys. Metall. Mater. Sci. 38 (2007) 946–955. https://doi.org/10.1007/s11661-007-9128-3.

[13] S.J. Lee, K.D. Clarke, A Quantitative Investigation of Cementite Dissolution Kinetics for Continuous Heating of Hypereutectoid Steel, Metall. Mater. Trans. A Phys. Metall. Mater. Sci. 46 (2015) 3917–3923. https://doi.org/10.1007/s11661-015-2995-0.

[14] R. Cryderman, D. Garrett, Z. Schlittenhart, E.J. Seo, Effects of Rapid Induction Heating on Transformations in 0.6% C Steels, J. Mater. Eng. Perform. 29 (2020) 3502–3515. https://doi.org/10.1007/s11665-020-04632-0.

[15] J.R. Bradley, S. Kim, Laser Transformation Hardening of Iron- Carbon and Iron-Carbon-Chromium Steels, Metall. Trans. A. 19A (1988) 2013–2025.

[16] R.R. Judd, H.W. Paxton, Kinetics of austenite formation from a spheroidized ferrite-carbide aggregate, Trans. Met. Soc. AIME. 242 (1968) 206–215.

[17] G. Speich, A. Szirmae, R.M. Fisher, A Laser Heating Device for Metallographic

Studies, Adv. Electron Metallogr. 6 (1966) 97–114.

[18] Y.Y. Meshkov, E. V. Pereloma, The effect of heating rate on reverse transformations in steels and Fe-Ni-based alloys, Phase Transform. Steels. 1 (2012) 581–618. https://doi.org/10.1533/9780857096104.4.581.

[19] G. Krauss, M. Cohen, Strengtening and annealing of austenite formed by reverse martensitic transformation, Trans. Metall. Soc. AIME. 224 (1962) 1212–1221.

[20] D.K. Matlock, S. Kang, E. De Moor, J.G. Speer, Applications of rapid thermal processing to advanced high strength sheet steel developments, Mater. Charact. 166 (2020) 110397. https://doi.org/10.1016/j.matchar.2020.110397.

[21] K.D. Clarke, C.J. Van Tyne, C.J. Vigil, R.E. Hackenberg, Induction hardening 5150 steel: Effects of initial microstructure and heating rate, J. Mater. Eng. Perform. 20 (2011) 161–168. https://doi.org/10.1007/s11665-010-9825-8.

[22] M. Yonemura, H. Nishibata, T. Nishiura, N. Ooura, Y. Yoshimoto, K. Fujiwara, K. Kawano, T. Terai, Y. Inubushi, I. Inoue, K. Tono, M. Yabashi, Fine microstructure formation in steel under ultrafast heating, Sci. Rep. 9 (2019) 11241. https://doi.org/10.1038/s41598-019-47668-6.

[23] S. Yabu, T. Nishibata, K. Hayashi, Analysis of Preferential Nucleation Sites for Austenite in Deformed Ferrite-pearlite Structure by Experimental and Computational Approaches, Nippon Steel Sumitomo Met. Tech. Rep. 120 (2018) 30–36.

[24] D.P. Datta, A.M. Gokhale, Austenitization kinetics of pearlite and ferrite aggregates in a low carbon steel containing 0.15 wt pct C, Metall. Trans. A. 12 (1981) 443–450. https://doi.org/10.1007/BF02648541.

[25] R.C. Dykhuizen, C. V. Robino, G.A. Knorovsky, A method for extracting phase change kinetics from dilatation for multistep transformations: Austenitizȧtion of a low carbon steel, Metall. Mater. Trans. B Process Metall. Mater. Process. Sci. 30 (1999) 107–117. https://doi.org/10.1007/s11663-999-0011-z.

[26] A. Karmakar, M. Mandal, A. Mandal, M. Basiruddin Sk, S. Mukherjee, D. Chakrabarti, Effect of Starting Microstructure on the Grain Refinement in Cold-Rolled Low-Carbon Steel During Annealing at Two Different Heating Rates, Metall. Mater. Trans. A Phys. Metall. Mater. Sci. 47 (2016) 268–281. https://doi.org/10.1007/s11661-015-3248-y.

[27] K. Albutt, S. Garber, Effect of heating rate on the elevation of the critical temperatures of low-carbon mild steel, J. Iron Steel Inst. 204 (1966) 1217–1222.

[28] E.D. Schmidt, E.B. Damm, S. Sridhar, A study of diffusion- and interface-controlled migration of the Austenite/Ferrite front during Austenitization of a case-hardenable alloy steel, Metall. Mater. Trans. A Phys. Metall. Mater. Sci. 38 (2007) 698–715. https://doi.org/10.1007/s11661-007-9208-4.

[29] C. Zheng, D. Raabe, Interaction between recrystallization and phase transformation during intercritical annealing in a cold-rolled dual-phase steel : A cellular automaton model, Acta Mater. 61 (2013) 5504–5517.

https://doi.org/10.1016/j.actamat.2013.05.040.

[30] D.Z. Yang, E.L. Brown, D.K. Matlock, G. Krauss, Ferrite Recrystallization and Austenite Formation in Cold-Rolled Intercritically Annealed Steel, Metall. Trans. A. 16A (1985) 1385–1392.

[31] P. Li, J. Li, Q. Meng, W. Hu, D. Xu, Effect of heating rate on ferrite recrystallization and austenite formation of cold-roll dual phase steel, J. Alloys Compd. 578 (2013) 320–327. https://doi.org/10.1016/j.jallcom.2013.05.226.

[32] L.S. Thomas, D.K. Matlock, Formation of Banded Microstructures with Rapid Intercritical Annealing of Cold-Rolled Sheet Steel, Metall. Mater. Trans. A Phys. Metall. Mater. Sci. 49 (2018) 4456–4473. https://doi.org/10.1007/s11661-018-4742-9.

[33] H. Azizi-Alizamini, M. Militzer, W.J. Poole, Austenite formation in plain low-carbon steels, Metall. Mater. Trans. A Phys. Metall. Mater. Sci. 42 (2011) 1544–1557. https://doi.org/10.1007/s11661-010-0551-5.

[34] R. Petrov, L. Kestens, W. Kaluba, Y. Houbaert, Recrystallization and austenite formation in a cold rolled TRIP steel during ultra fast heating, Steel Grips. 289–294 (2003).

[35] M. Bellavoine, M. Dumont, M. Dehmas, A. Stark, N. Schell, J. Drillet, V. Hébert, P. Maugis, rolled advanced high-strength steels : In situ synchrotron X-ray di ff raction and modeling, Mater. Charact. 154 (2019) 20–30. https://doi.org/10.1016/j.matchar.2019.05.020.

[36] J. Huang, W.J. Poole, M. Militzer, Austenite Formation during Intercritical Annealing, Metall. Mater. Trans. A. 35 (2004) 3363–3375. https://doi.org/10.1007/s11661-004-0173-x.

[37] Andrade-Carozzo, P.J. Jacques, Interactions between Recrystallisation and Phase Transformations during Annealing of Cold Rolled Nb-Added TRIP-Aided Steels, Thermec 2006. 543 (2007) 4649–4654. https://doi.org/10.4028/www.scientific.net/MSF.539-543.4649.

[38] F.M. Castro Cerda, L.A.I. Kestens, R.H. Petrov, “Flash” Annealing in a Cold-Rolled Low Carbon Steel Alloyed with Cr, Mn, Mo, and Nb: Part II—Anisothermal Recrystallization and Transformation Textures, Steel Res. Int. 90 (2019) 1–13. https://doi.org/10.1002/srin.201800277.

[39] A. Karmakar, M. Ghosh, D. Chakrabarti, Cold-rolling and inter-critical annealing of low-carbon steel: Effect of initial microstructure and heating-rate, Mater. Sci. Eng. A. 564 (2013) 389–399. https://doi.org/10.1016/j.msea.2012.11.109.

[40] P. Wen, J. Han, H. Luo, X. Mao, Effect of flash processing on recrystallization behavior and mechanical performance of cold-rolled IF steel, Int. J. Miner. Metall. Mater. 27 (2020) 1234–1243. https://doi.org/10.1007/s12613-020-2023-2.

[41] D. De Knijf, A. Puype, C. Föjer, R. Petrov, The influence of ultra-fast annealing prior to quenching and partitioning on the microstructure and mechanical properties, Mater. Sci. Eng. A. 627 (2015) 182–190.

https://doi.org/10.1016/j.msea.2014.12.118.

[42] F.C. Cerda, C. Goulas, I. Sabirov, S. Papaefthymiou, A. Monsalve, Microstructure, texture and mechanical properties in a low carbon steel after ultrafast heating, Mater. Sci. Eng. A. 672 (2016) 108–120. https://doi.org/10.1016/j.msea.2016.06.056.

[43] A. Banis, E.I. Hernandez-Duran, V. Bliznuk, I. Sabirov, R.H. Petrov, S. Papaefthymiou, The effect of ultra-fast heating on the microstructure, grain size and texture evolution of a commercial low-c, medium-Mn DP steel, Metals (Basel). 9 (2019). https://doi.org/10.3390/met9080877.

[44] R.H. Petrov, J. Sidor, L.A.I. Kestens, Texture formation in high strength low alloy steel reheated with ultrafast heating rates, Mater. Sci. Forum. 702–703 (2012) 798–801. https://doi.org/10.4028/www.scientific.net/MSF.702-703.798.

[45] F.M. Castro Cerda, F. Vercruysse, T.N. Minh, L. Kestens, A. Monsalve, R. Petrov, The Effect of Heating Rate on the Recrystallization Behavior in Cold Rolled Ultra Low Carbon Steel, Steel Res. Int. 88 (2017) 1–9. https://doi.org/10.1002/srin.201600351.

[46] V. Massardier, A. Ngansop, D. Fabregue, S. Cazottes, J. Merlin, Ultra-rapid intercritical annealing to improve deep drawability of low-carbon, al-killed steels, Metall. Mater. Trans. A Phys. Metall. Mater. Sci. 43 (2012) 2225–2236. https://doi.org/10.1007/s11661-012-1096-6.

[47] N. Yoshinaga, H. Inoue, K. Kawasaki, L. Kestens, B.C. De Cooman, Factors affecting texture memory appearing through α → γ → α transformation in IF steels, Mater. Trans. 48 (2007) 2036–2042. https://doi.org/10.2320/matertrans.MA200704.

[48] B. Hutchinson, L. Kestens, Origins of texture memory in steels, in: A.D. Rollett (Ed.), Appl. Texture Anal. Appl. Texture Anal. Int. Conf. Textures Mater. (ICOTOM 15), 2009: pp. 281–290.

[49] P. Roumen, S. Jurij, K. Wlodzimierz, K. Leo, Grain refinement of a cold rolled TRIP assisted steel after ultra short annealing, Mater. Sci. Forum. 715–716 (2012) 661–666. https://doi.org/10.4028/www.scientific.net/MSF.715-716.661.

[50] R.A. Grange, The rapid heat treatment of steel, Metall. Trans. 2 (1971) 65–78. https://doi.org/10.1007/BF02662639.

[51] P. Roumen, H. Farideh, S. Jurij, M. Jesus, J. Sietsma, L. Kestens, Ultra-Fast Annealing of High Strength Steel, Int. Virtual J. Mach. Technol. Mater. 8 (2012) 68–71.

[52] F.M. Castro Cerda, B. Schulz, D. Celentano, A. Monsalve, I. Sabirov, R.H. Petrov, Exploring the microstructure and tensile properties of cold-rolled low and medium carbon steels after ultrafast heating and quenching, Mater. Sci. Eng. A. 745 (2019) 509–516. https://doi.org/10.1016/j.msea.2018.12.036.

[53] M.A. Valdes-Tabernero, A. Kumar, R.H. Petrov, M.A. Monclus, J.M. Molina-Aldareguia, I. Sabirov, The sensitivity of the microstructure and properties to the peak temperature in an ultrafast heat treated low carbon-steel, Mater. Sci. Eng. A. 776 (2020) 138999. https://doi.org/10.1016/j.msea.2020.138999.

[54] T. Lolla, G. Cola, B. Narayanan, B. Alexandrov, S.S. Babu, Development of rapid

heating and cooling (flash processing) process to produce advanced high strength steel microstructures, Mater. Sci. Technol. 27 (2011) 863–875. https://doi.org/10.1179/174328409X433813.

[55] K. Banerjee, M. Militzer, M. Perez, X. Wang, Nonisothermal austenite grain growth kinetics in a microalloyed x80 linepipe steel, Metall. Mater. Trans. A Phys. Metall. Mater. Sci. 41 (2010) 3161–3172. https://doi.org/10.1007/s11661-010-0376-2.

[56] F.G. Caballero, C. Capdevila, C.G. De Andrés, An attempt to establish the variables that most directly influence the austenite formation process in steels, ISIJ Int. 43 (2003) 726–735. https://doi.org/10.2355/isijinternational.43.726.

[57] M. Kulakov, W.J. Poole, M. Militzer, The effect of the initial microstructure on recrystallization and austenite formation in a DP600 steel, Metall. Mater. Trans. A Phys. Metall. Mater. Sci. 44 (2013) 3564–3576. https://doi.org/10.1007/s11661-013-1721-z.

[58] G. Liu, J. Li, S. Zhang, J. Wang, Q. Meng, Dilatometric study on the recrystallization and austenization behavior of cold-rolled steel with different heating rates, J. Alloys Compd. 666 (2016) 309–316. https://doi.org/10.1016/j.jallcom.2016.01.137.

[59] F.M. Castro Cerda, C. Goulas, I. Sabirov, L.A.I. Kestens, R.H. Petrov, The effect of the pre-heating stage on the microstructure and texture of a cold rolled FeCMnAlSi steel under conventional and ultrafast heating, Mater. Charact. 130 (2017) 188–197. https://doi.org/10.1016/j.matchar.2017.06.010.

[60] D.Z. Yang, E.L. Brown, D.K. Matlock, G. Krauss, The formation of austenite at low intercritical annealing temperatures in a normalized 0.08C-1.45Mn-0.21Si steel, Metall. Trans. A. 16 (1985) 1523–1526. https://doi.org/10.1007/BF02658685.

[61] H.D. Alvarenga, N. Van Steenberge, J. Sietsma, H. Terryn, The Kinetics of Formation and Decomposition of Austenite in Relation to Carbide Morphology, Metall. Mater. Trans. A Phys. Metall. Mater. Sci. 48 (2017) 828–840. https://doi.org/10.1007/s11661-016-3874-z.

[62] P. Li, J. Li, Q. Meng, W. Hu, D. Xu, Effect of heating rate on nucleation and growth of austenite in cold rolled dual phase steel, Ironmak. Steelmak. 42 (2015) 81–87. https://doi.org/10.1179/1743281214Y.0000000228.

[63] H. Azizi-Alizamini, M. Militzer, W.J. Poole, Formation of ultrafine grained dual phase steels through rapid heating, ISIJ Int. 51 (2011) 958–964. https://doi.org/10.2355/isijinternational.51.958.

[64] M.A. Valdes-Tabernero, C. Celada-Casero, I. Sabirov, A. Kumar, R.H. Petrov, The effect of heating rate and soaking time on microstructure of an advanced high strength steel, Mater. Charact. 155 (2019) 109822. https://doi.org/10.1016/j.matchar.2019.109822.

[65] M.A. Valdes-Tabernero, R.H. Petrov, M.A. Monclus, J.M. Molina-Aldareguia, I. Sabirov, The effect of soaking time after ultrafast heating on the microstructure and mechanical behavior of a low carbon steel, Mater. Sci. Eng. A. 765 (2019) 138276. https://doi.org/10.1016/j.msea.2019.138276.

[66] M.A. Valdes-Tabernero, F. Vercruysse, I. Sabirov, R.H. Petrov, M.A. Monclus, J.M. Molina-Aldareguia, Effect of Ultrafast Heating on the Properties of the Microconstituents in a Low-Carbon Steel, Metall. Mater. Trans. A Phys. Metall. Mater. Sci. 49 (2018) 3145–3150. https://doi.org/10.1007/s11661-018-4658-4.

[67] Q. Meng, J. Li, H. Zheng, High-efficiency fast-heating annealing of a cold-rolled dual-phase steel, Mater. Des. 58 (2014) 194–197. https://doi.org/10.1016/j.matdes.2014.01.055.

[68] F. Vercruysse, F.M. Castro Cerda, P. Verleysen, R.H. Petrov, Behavior of ultrafast annealed advanced high strength steels under static and dynamic conditions, Mater. Sci. Eng. A. 780 (2020) 139168. https://doi.org/10.1016/j.msea.2020.139168.

[69] Y. Deng, H. Di, J. Zhang, R.D.K. Misra, Stretching the mechanical properties in a 590 MPa ferrite-martensite dual-phase steel through rapid heating, Metall. Res. Technol. 114 (2017) 1–7. https://doi.org/10.1051/metal/2017038.

[70] A. Andreiev, O. Grydin, M. Schaper, Evolution of Microstructure and Properties of Steel 22MnB5 due to Short Austenitization with Subsequent Quenching, Steel Res. Int. 87 (2016) 1733–1741. https://doi.org/10.1002/srin.201600086.

[71] J. Pedraza, R. Landa-Mejia, O. Garcia-Rincon, I. Garcia, The Effect of Rapid Heating and Fast Cooling on the Transformation Behavior and Mechanical Properties of an Advanced High Strength Steel (AHSS), Metals (Basel). 545 (2019) 1–12.

[72] A. Banis, M. Bouzouni, E. Gavalas, S. Papaefthymiou, The formation of a mixed martensitic / bainitic microstructure and the retainment of austenite in a medium-carbon steel during ultra-fast heating, Mater. Today Commun. 26 (2021) 101994. https://doi.org/10.1016/j.mtcomm.2020.101994.

[73] O.M. Ivasishin, R. V. Teliovich, Potential of rapid heat treatment of titanium alloys and steels, Mater. Sci. Eng. A. 263 (1999) 142–154. https://doi.org/10.1016/s0921-5093(98)01173-3.

[74] M. Jaskari, A. Järvenpää, P. Karjalainen, The effect of heating rate and temperature on microstructure and r-value of type 430 ferritic stainless steel, Mater. Sci. Forum. 941 MSF (2018) 364–369. https://doi.org/10.4028/www.scientific.net/MSF.941.364.

[75] M. Jaskari, A. Järvenpää, P. Karjalainen, The effect of heating rate on texture and formability of ti-nb stabilized ferritic stainless steel, Key Eng. Mater. 786 KEM (2018) 3–9. https://doi.org/10.4028/www.scientific.net/KEM.786.3.

[76] J.G. Speer, E. De Moor, A.J. Clarke, Critical assessment 7: Quenching and partitioning, Mater. Sci. Technol. 31 (2015) 3–9. https://doi.org/10.1179/1743284714Y.0000000628.

[77] S. Matas, R.F. Hehemann, The Structure of Bainite in Hypoeutectoid Steels, Trans. Metall. Soc. AIME. 221 (1961) 179–185.

[78] D. Xu, J. Li, Q. Meng, Y. Liu, P. Li, Effect of heating rate on microstructure and mechanical properties of TRIP-aided multiphase steel, J. Alloys Compd. 614 (2014)

94–101. https://doi.org/10.1016/j.jallcom.2014.06.075.

[79] D.C. Xu, Y.D. Liu, J. Li, Q.G. Meng, P. Li, Microstructure Characterization and Mechanical Properties of TRIP-aided Steel under Rapid Heating for Different Holding Time, J. Iron Steel Res. Int. 23 (2016) 138–144. https://doi.org/10.1016/S1006-706X(16)30025-5.

[80] G. Liu, S.G. Zhang, Q.G. Meng, J. Wang, J. Li, Effect of heating rate on microstructural evolution and mechanical properties of cold-rolled quenching and partitioning steel, Ironmak. Steelmak. 44 (2016) 202–209. https://doi.org/10.1080/03019233.2016.1209887.

[81] G. Liu, S. Zhang, J. Li, J. Wang, Q. Meng, Fast-heating for intercritical annealing of cold-rolled quenching and partitioning steel, Mater. Sci. Eng. A. 669 (2016) 387–395. https://doi.org/10.1016/j.msea.2016.05.106.

[82] J. Dai, Q. Meng, H. Zheng, An innovative pathway to produce high-performance quenching and partitioning steel through ultra-fast full austenitization annealing, Mater. Today Commun. 25 (2020) 101272. https://doi.org/10.1016/j.mtcomm.2020.101272.

[83] G. Liu, T. Li, Z. Yang, C. Zhang, J. Li, H. Chen, On the role of chemical heterogeneity in phase transformations and mechanical behavior of flash annealed quenching & partitioning steels, Acta Mater. 201 (2020) 266–277. https://doi.org/10.1016/j.actamat.2020.10.007.

Chapter 3

Experimental procedures

In this chapter, the materials investigated in this work are introduced. Additionally, heat treatment procedures and characterization methodologies employed in this study are described.

3.1 Materials

The chemical compositions of the steels used in this work are shown in Table 3.1.

Table 3.1: Chemical composition of the materials analyzed in this work (in wt.%).

Material	C	Mn	Si	P	S	Mo	Nb	Ti	Fe
0.2C	0.19	1.87	1.42	0.009	0.004	-	-	-	Rest
0.2CMoNbTi	0.19	1.99	1.43	0.006	0.004	0.32	0.035	0.020	Rest
0.25C	0.24	1.39	1.42	0.009	0.004	-	-	-	Rest
0.3C	0.28	1.91	1.44	0.009	0.005	-	-	-	Rest

Experimental slabs of 130 mm thickness were reheated to a temperature of 1250 °C, soaked for 30 minutes and hot rolled in multi-passes to a final thickness of 4 mm. After sandblasting, the hot-rolled plates were cold-rolled at 0.2 mm/pass to a final thickness of 1.2 mm, giving a total cold rolling reduction of 70%.

3.2 Heat treating techniques

3.2.1 Dilatometry

The dilatation or contraction in a specimen subjected to thermal changes can be measured via dilatometry [1]. Cold-rolled specimens of 10x5x1.2 mm^3 (with the longest axis parallel to RD) were heated using longitudinal flux induction heating [2] in a Bähr 805A/D push-rod dilatometer operating in quench mode. Before heating, a vacuum level of 10^{-4} mbar was reached. During cooling, a fast rate of 160 °C/s was achieved using Helium (He) gas. During dilatometric experiments, the temperature and the respective power control were controlled with one S-type thermocouple spot welded onto the central position on the tested sample surface. Details on the operation principle of the dilatometric technique can be found in Refs. [1,3,4].

In this work, the A_{C3} temperature was used as a reference parameter for designing the heat treatments of steel samples heated above the intercritical ferrite-austenite range. To that end, the A_{C3} was defined as the temperature at which 98% of austenite (determined by the lever rule method) was formed upon continuous heating. The

methodology employed is exemplified in Figure 3.1. As shown in Figure 3.1a, the extrapolations of the linear regions for the measured change in length curve were used for calculating the austenite fraction (f_γ). Figure 3.1b presents the evolution of the austenite fraction with the temperature.

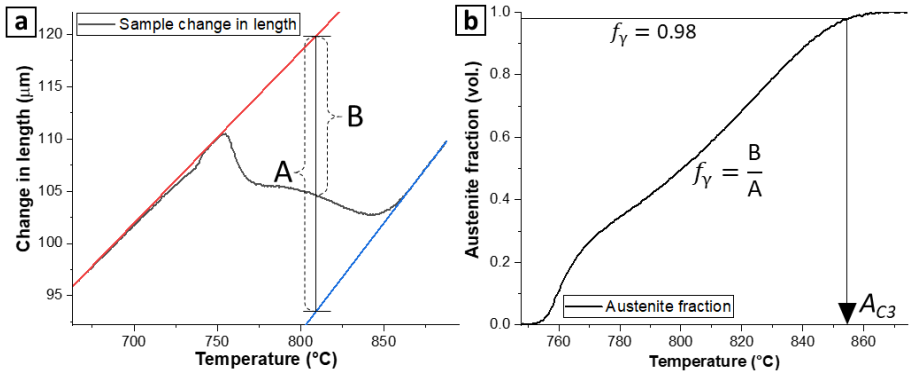

Figure 3.1: (a) Measured change in length during heating for a sample heated at 2 °C/s. (b) Volume fraction of the transformed austenite calculated from the lever rule method. Steel sample: 0.2C.

In experiments performed at heating rates higher than 300 - 350 °C/s, the heating rate declines at high temperatures. This results from the decrease in efficiency of the power supplied by the longitudinal flux induction system above the curie point of ferrite and during the formation of paramagnetic austenite. Figure 3.2 shows that the high frequency (HF) generator reaches the maximum power (100%) at elevated temperatures, giving a heating rate of ~325 °C/s above 753 °C. Nevertheless, previous evaluations of the A_{C3} evolution with the heating rate in cold-rolled low-alloy steels [5,6] indicated that the A_{C3} temperature shifts slightly when high heating rates are applied. Thomas [5], using the Gleeble® 3500 device equipped with a laser dilatometer, reported a shift of 1 to 3 °C of the A_{C3} by increasing the heating rate from 100 °C/s to 1000 °C/s in 1020, 1019M and 15B25 cold-rolled steels. Therefore, the A_{C3} temperatures determined in high heating rate experiments performed at a programmed heating rate of 500 °C/s were assumed as valid.

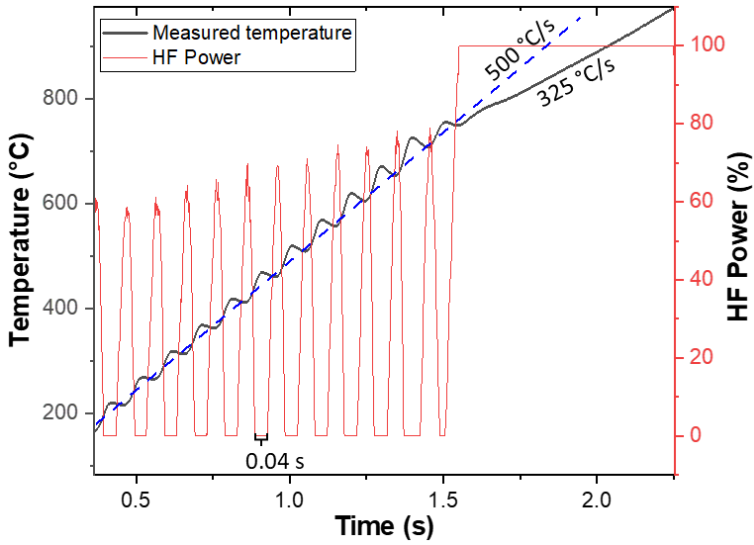

Figure 3.2: Effect of austenite formation and paramagnetic transition on the inductor power and resulting heating rate (programmed heating rate 500 °C/s). Steel sample: 0.2C.

3.2.2 Gleeble thermomechanical simulator

In this work, heat treatments were performed using the Gleeble® 1500 simulator. When the thermal mode is activated, the Gleeble® thermomechanical simulator operates using the Joule effect for heating (resistance heating). Heating rates up to 10^4 °C/s can be reached depending on the experimental setup. Samples of dimensions 90x20x1.2 mm^3 (with the longest axis parallel to RD) were clamped to the Gleeble® system using full contact copper jaws, leaving a free span of ~50 mm. During heat treating, the temperature was controlled and recorded using a K-type thermocouple spot welded at the geometrical center of each specimen. A schematic representation of the Gleeble® setup is shown in Figure 3.3. A U-shape gas gun was placed at the center of the Gleeble® setup for cooling. Samples were fast cooled at a maximum rate of 160 °C/s using compressed air. The temperature of the specimens during heating and cooling steps was recorded at a frequency of 2000 Hz.

Two different annealing routes are presented in Figure 3.4. Figure 3.4a shows a conventional annealing treatment performed at a heating rate of 10 °C/s up to 885 °C, followed by 180 seconds of soaking and fast cooling to room temperature. An example of two independent samples subjected to an -ultrafast- peak annealing treatment is displayed in Figure 3.4b. It is important to note that the samples were heat-treated following the same temperature program. In this study, samples treated at temperatures with variations greater than ±5 °C with respect to the desired heat treatment program were discarded.

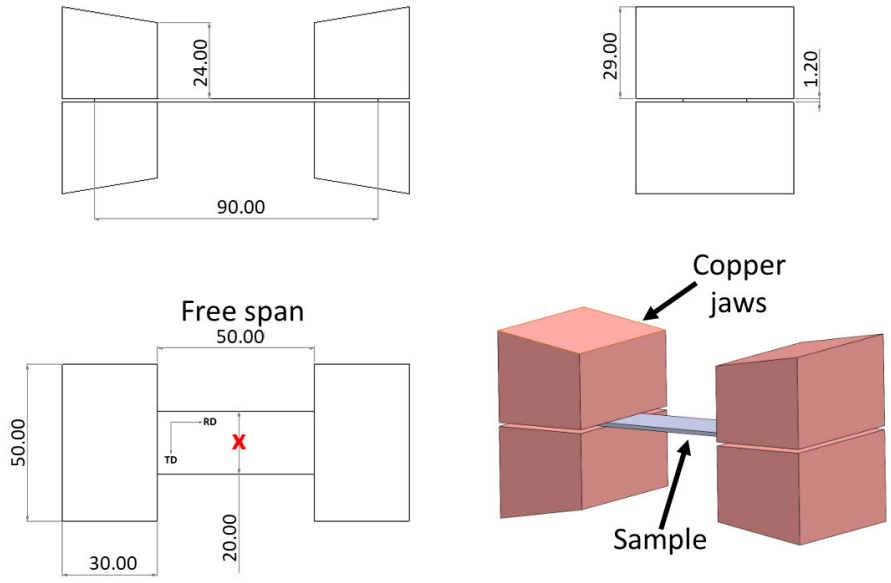

Figure 3.3: Schematic representation of the Gleeble® setup used in this work. The X on the superior view of the drawing indicates the zone where the control thermocouple is placed (dimensions in mm).

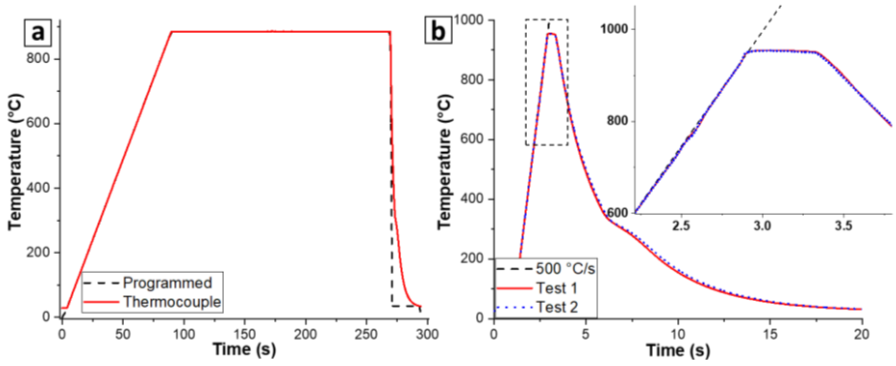

Figure 3.4: Annealing experiments carried out in the Gleeble® simulator: (a) conventional annealing treatment performed at a heating rate of 10 °C/s and (b) ultrafast peak annealing treatment performed at 500 °C/s. The temperature record of two different tests is shown in (b). The insert corresponds to the temperature profile enclosed by dashed lines.

3.3 Characterization

The resistance heating employed in the Gleeble® simulator led to a temperature gradient along the free span of the heat-treated samples. Therefore, the size of the homogeneously treated zone was determined through temperature control at various locations of the sample coupled with Vickers microhardness measurements and optical microscopy analysis as described elsewhere [7,8]. To exemplify the applied method, Figure 3.5 displays the hardness profiles obtained along the rolling

direction for two samples heated at 10 °C/s and 1000 °C/s up to 800 °C, followed by direct fast cooling. Heat-treated specimens exhibited a homogeneous zone (H-Z) of at least 12 mm.

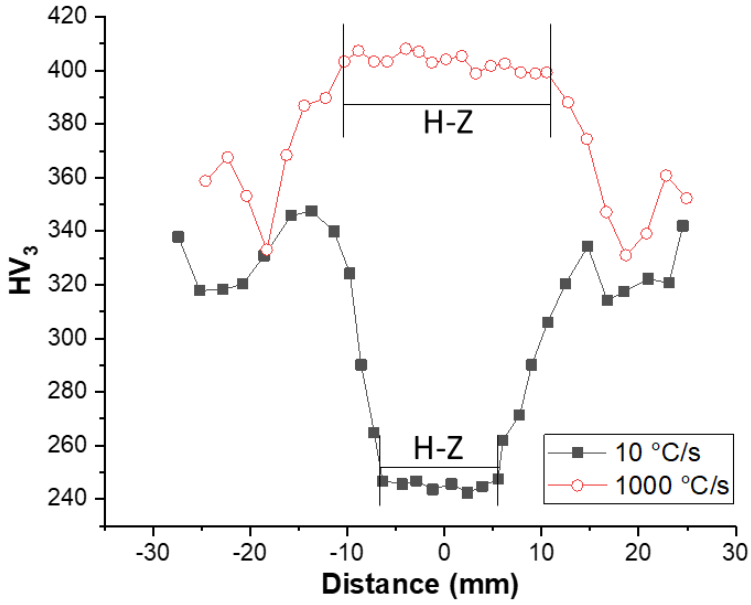

Figure 3.5: Hardness profile across the rolling direction in samples heated at 10 °C/s and 1000 °C/s up to 800 °C. H-Z denotes the homogeneously treated zone obtained in the peak annealed samples. Hardness measurements were conducted along RD on the TD-RD plane. Steel sample: 0.2CMoNbTi.

3.3.1 Optical and scanning electron microscopy

Samples for microstructural characterization and tensile testing were extracted from the homogeneously treated zone (H-Z), as schematically presented in Figure 3.6a (see the red area enclosed by dashed lines). For optical and scanning electron microscopy analyses, samples were prepared on the RD-ND plane (plane normal to the TD direction) at approximately 2 mm from where the control thermocouple was welded. Sample preparation was conducted via standard manual procedure [9], including grinding and polishing to a final polishing step with 0.25 µm fumed silica suspension (OP-S). Metallographic examinations were performed on the RD-ND plane (see Figure 3.6b). Light optical micrographs, secondary electron (SE) micrographs and EBSD scans were acquired at approximately 280 µm from the sample surface. The microstructures of the different steel grades produced in this work were revealed by chemical etching with solutions of 2% to 4% v/v HNO_3 in methanol (Nital) for 4 seconds [10]. Optical microscopy analysis (OM) was performed under bright field mode using a Keyence VHX-2000 microscope. Micrographs in secondary electron mode were captured in a scanning electron microscope (SEM)

FEI Quanta 450 FEG-SEM operating at an acceleration voltage of 15 kV and a working distance of 10 mm.

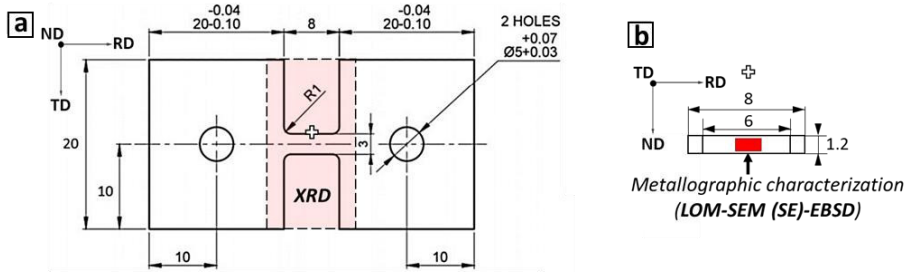

Figure 3.6: Schematic representation of the homogeneously treated zone and samples used for both microstructural and mechanical characterization (dimensions in mm). (a) Dogbone geometry and (b) area used microstructural characterizations. The area enclosed by dashed lines indicates the homogenously heat-treated zone obtained in samples treated using the Gleeble simulator. The cross next to the central region of the gauge length indicates the area used for metallographic characterization. Note that the shoulders and gauge length of the sub-size tensile sample lie within the homogeneously treated zone.

3.3.2 Electron backscattered diffraction

Electron backscatter diffraction (EBSD) analysis is used to perform a quantitative description of the microstructure and texture obtained in the studied steel grades. This technique is based on the indexation of electron backscatter patterns produced by electron beam diffraction from sets of crystallographic planes that belong to each grain captured in the studied sample [11].

Analogous to the sample preparation procedure employed for OM and SEM examinations, the sample preparation for EBSD analysis involved grinding and polishing, finishing with 0.04 µm colloidal silica suspension (OP-U) for 15 to 30 min. The EBSD measurements were performed on unetched samples using an accelerating voltage of 20 kV, beam current corresponding to an FEI spot size of 5, working distance of 14 mm and sample tilt of 70° towards the EBSD detector. Hexagonal grid scans of step sizes ranging from 50 to 150 nm were recorded using a Hikari detector operated by the EDAX-TSL OIM Data Collection v7.3 software. As mentioned in the previous section, scans were acquired on the RD-ND plane at approximately 280 µm from the sample surface.

EBSD data were post-processed using the TSL OIM Analysis v7 software. The grain definition was based on a minimum of 5 pixels per grain and a misorientation angle of 5°. Pixels with a confidence index lower than 0.1 were removed from the acquired EBSD data. After the definition of the grains, “Grain confidence index (CI) standardization” followed by “Neighbor orientation correlation” clean-up procedures were applied.

Using the EBSD technique, austenite (FCC) can be easily distinguished from ferrite, bainite, or martensite (BCC or BCT) thanks to their different crystal lattices [12].

Nevertheless, the identification of ferrite (F), martensite (M) and bainite (B) via crystal lattice criteria is challenging in heat-treated -low carbon- steels [13,14]. Tempering effects, carbon partitioning and segregation to dislocations decrease the carbon content in solid solution in martensite, reducing the degree of tetragonality of the martensitic crystal lattice [15]. Therefore, F, M, and B are commonly indexed as BCC microconstituents in EBSD measurements [11,13,14]. Figure 3.7 presents an EBSD-Phase map showing the identification of retained austenite, which is highlighted in green. Black boundaries show the Kurdjumow-Sachs orientation relationship (K-S_{OR}) between retained austenite and the BCC daughter phase.

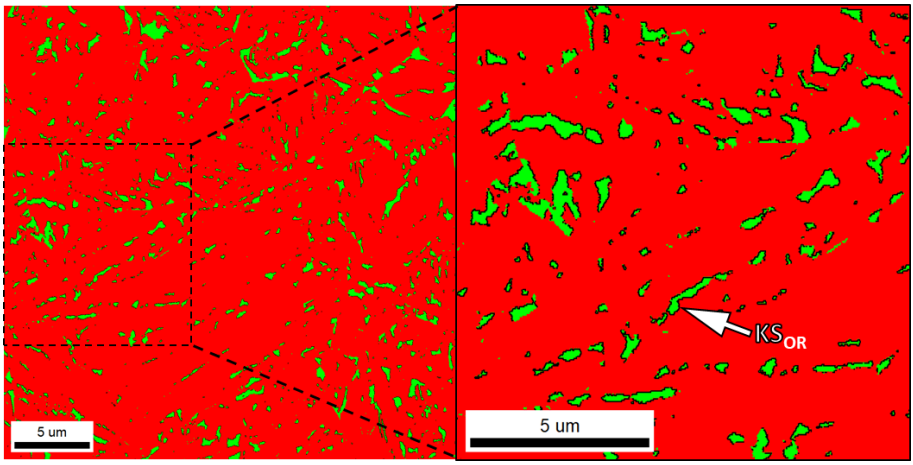

Figure 3.7: EBSD-Phase map. Retained austenite is highlighted in green. BCC microconstituents, i.e., bainite/martensite, are shown in red. Black boundaries between retained austenite and the BCC matrix show the K-S orientation relationship with a tolerance angle of 5°.

The distortion of the crystal lattices allows distinguishing martensitic and bainitic microconstituents (with high dislocation density) from ferrite via EBSD analysis. Image quality (IQ) [16] and Grain average image quality (GAIQ) [11] analyses provide an alternative for microconstituents identification and quantification via EBSD. In this work, the GAIQ criterion was employed for effective segmentation of the microstructure, identifying the ferritic and martensitic/bainitic constituents. An example of martensite and ferrite identification in a sample subjected to intercritical annealing and direct quench is presented in Figure 3.8. Figure 3.8a presents a combined EBDS IQ-GAIQ map. The respective area fraction histogram for the GAIQ values measured is shown in Figure 3.8b. Ferrite and martensite are associated with high and low GAIQ values, respectively.

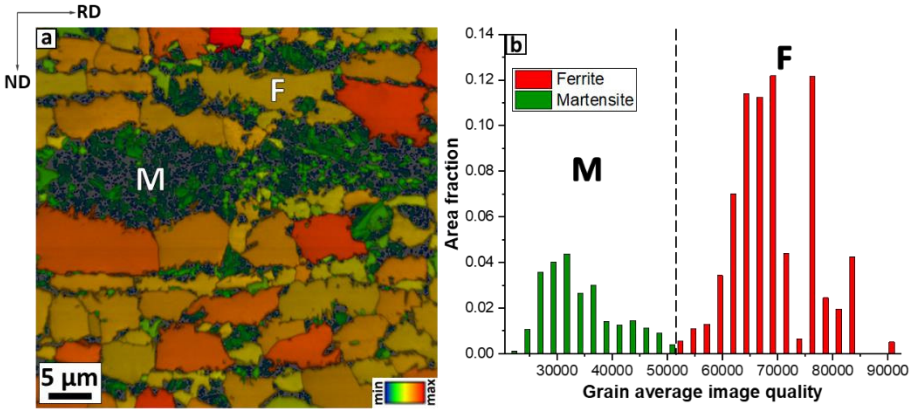

Figure 3.8: (a) Combined EBSD IQ-GAIQ maps for identification of ferrite and martensite. Color scale: GAIQ values. (b) GAIQ histogram.

Microstructural analysis based on IQ values was also applied for the identification of martensite formed after the final cooling step in samples subjected to quenching and partitioning, and austempering treatments [17,18]. As shown in Figure 3.9, martensite was found surrounded by retained austenite (γ). The region denoted as martensite (M) has a lower IQ than the bainitic matrix (B) and a different crystal lattice than retained austenite, which is highlighted in colors according to its crystal orientation. The boundary between M and γ fulfills the K-S_{OR}. The profile 1-2 presents the point-to-point misorientation and IQ values for each pixel acquired along the segment 1-2 (blue arrow).

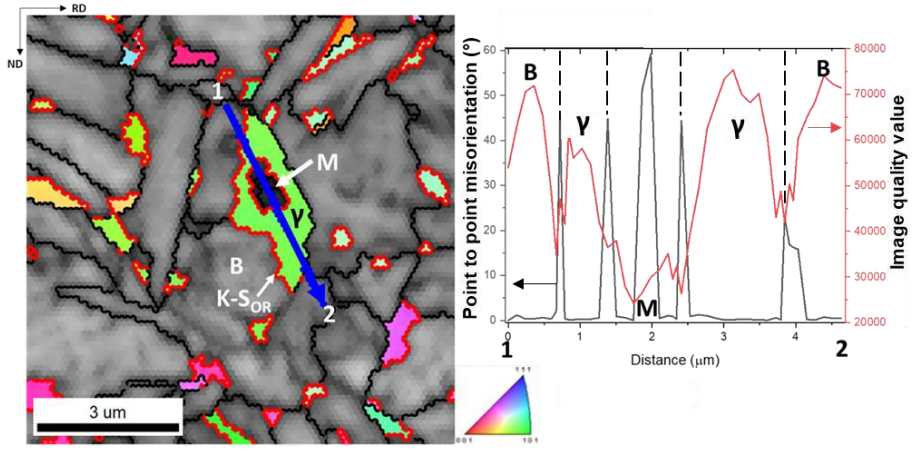

Figure 3.9: Example of martensite identification in austempered steels. Grayscale EBSD-IQ map. Retained austenite grains are highlighted according to their crystal orientation. Black and red boundaries in the EBSD-IQ map show the 5° to 65° grain boundaries and the K-S_{OR} between γ and the BCC matrix, respectively. B: Bainite, M: Martensite, γ: Retained austenite.

Additionally, the evaluation of grain orientation spread (GOS) [19] was employed for the identification of recrystallized (F_{Rx}) and non-recrystallized ferrite ($F_{N\text{-}Rx}$) in

intercritical annealed steels (Figure 3.10a). For a predefined grain with a certain number of pixels, the GOS analysis considers the misorientation angle between the orientation of a pixel and the mean orientation of the grain. The larger the misorientation, the larger the GOS value in °. In this work, grains of GOS ≥ 4° were assumed as non-recrystallized. This microstructural segmentation was corroborated using the kernel average misorientation (KAM) method [20], which provides quantitative information of the misorientation between neighbor pixels acquired via EBSD (see the 2nd neighbor KAM map presented in Figure 3.10b). The identification of $F_{N\text{-}Rx}$ is exemplified by the EBSD maps presented in Figure 3.10, whereby orange to red grains in the color-scale GOS map correspond to $F_{N\text{-}Rx}$ (Figure 3.10a).

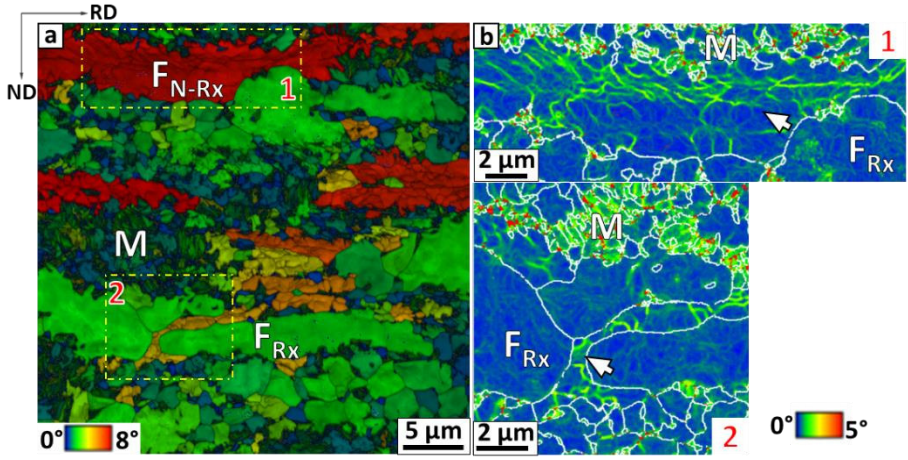

Figure 3.10: Non-recrystallized ferrite identification: (a) Combined EBSD IQ-GOS map. (b) 2nd neighbor kernel average misorientation maps for the areas 1 and 2 enclosed by dashed-dot lines in (a). Non-recrystallized ferrite grains are highlighted by white arrows in (b). White lines denote grain boundaries of misorientation angle from 15° to 63°.

The acquired EBSD scans were also used for the reconstruction of parent austenite grains (PAG). PAGs were reconstructed using the software developed by Gomes et al. [21]. This software applies two algorithms for the reconstruction of the parent austenite: (i) identification of an optimized K-S_{OR} between austenite and the "daughter" martensitic and/or bainitic constituents and (ii) reconstruction of the parent grains using a random clustering technique, which identifies groups of closely related grains according to their angular deviation from the optimized orientation relationship. The validity of the reconstruction is verified by comparing the grain boundaries of misorientation 15°-63° for the reconstructed parent austenite and prior austenite grain boundaries in the "daughter" martensitic or bainitic microstructures (before reconstruction), highlighted by plotting the 17°-47° grain misorientation [22]. Additionally, when retained austenite grains are present in the microstructure of heat-treated steels, the reconstruction is verified by evaluating the crystal orientation of the reconstructed grains and the crystal orientation of the

retained austenite grains highlighted in inverse pole figures (IPF), as shown in Figure 3.11 for a TRIP-aided bainitic steel containing 14% of γ.

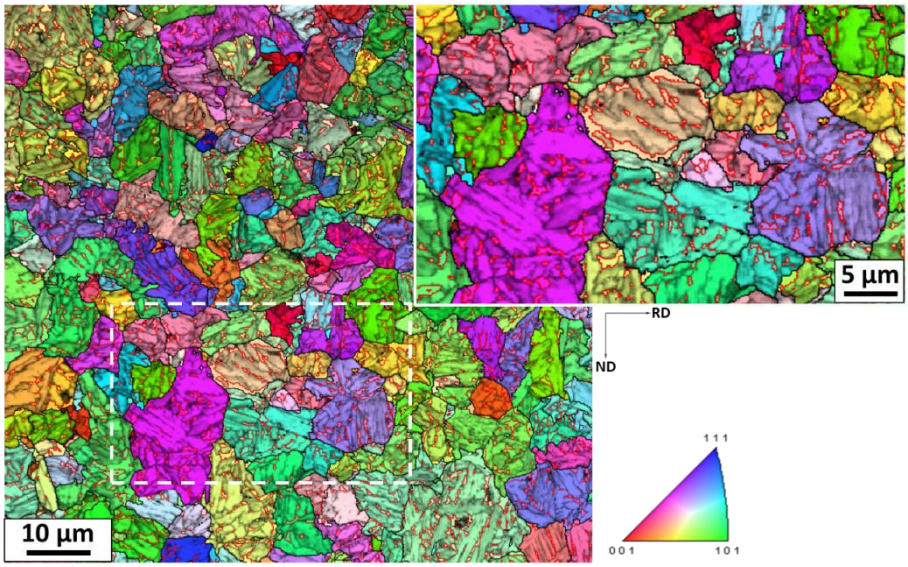

Figure 3.11: BCC IQ map combined with the IPF of the retained austenite grains and the reconstructed PAGs. Black and red boundaries denote the 15-63° misorientation for PAGs boundaries and retained austenite phase boundaries, respectively. Note the match between the orientations of the retained austenite grains and the orientations of the reconstructed grains.

3.3.3 Transmission electron microscopy

A transmission electron microscope (TEM) Jeol JEM-2200FS was used. The microscope is equipped with aberration correction of the objective lenses, column energy filter and a Jeol EDX spectrometer. During operation, an acceleration voltage of 200 kV was employed.

The sample preparation procedure for TEM consisted of grounding the samples to a thickness of 90-100 µm on the RD-TD plane. Next, discs of 3 mm diameter were cut from the grounded sample using a manual TEM disc punch system. Using a Struers Tenupol-5 for automatic electrolytic thinning of specimens, the discs were polished and thinned via precision twin-jet ion polishing with a 96 v/v% CH3COOH, 4 v/v% HClO4 solution. Once a perforation appeared in the TEM sample, the polishing step was automatically stopped by the infrared detector system incorporated in the Struers Tenupol-5.

3.3.4 X-ray diffraction

The quantifications of the fraction of retained austenite and retained austenite carbon content in heat-treated samples were estimated by means of X-ray diffraction analysis. Samples were extracted for the homogeneously treated zone

(Figure 3.6) and prepared on the RD-TD plane. A surface layer of ≈300 μm was removed by grinding, followed by repeated polishing and etching steps [23].

A Siemens Kristalloflex D5000 X-ray diffractometer equipped with Mo-K_α radiation and operating at 40 kV and 40 Am was used. The diffraction patterns were acquired over a scanned 2θ range from 25° to 45° with a step size of 0.03° per step and dwell time of 20 s. A stage rotation at 15 rpm was used. Before the X-ray diffraction data analysis, the instrumental background and $K_{\alpha 2}$ radiation were subtracted. The direct comparison method [24] was applied on the integrated intensities of the $(200)^{BCC}$, $(211)^{BCC}$, $(220)^{FCC}$ and $(311)^{FCC}$ peaks to determine the fraction of retained austenite. The average carbon content of the retained austenite was calculated from its lattice parameter according to the equation proposed by Roberts [25]:

$$a_\gamma = 3.548 + 0.044C_\gamma \quad (3.1)$$

where a_γ is the lattice parameter (in Å) and C_γ is the austenite carbon content (in wt.%).

3.3.5 Tensile testing

As indicated in Section 3.3.1, sub-size tensile specimens (Figure 3.6a) were used in this work. The geometry of the tensile samples was designed according to [26]. Tensile tests were performed in an Instron 5000 device equipped with a 50 kN load cell. A constant strain rate of 0.001 s^{-1} was imposed during testing. According to the standard ASTM E8/E8M [27], the yield strength (σ_{ys}) was defined by the conventional 0.2% engineering strain offset method, and the ultimate tensile strength (σ_{UTS}) was determined at the maximum stress level of the engineering stress v/s strain curve. The strain evolution during the tensile test was measured by 2D-digital image correlation (2D-DIC), and the acquired data was post-processed with the commercial software MatchID. The DIC technique is a non-contact -optical- technology based on tracking the displacement of a random speckle pattern applied on a sample [28], allowing an accurate measurement of local strain and extension of the gauge section of tensile samples during straining. In this study, black speckles were carefully applied in a white background to create patterns homogeneously distributed on the surface of the tensile specimens. The level of strain at each image frame captured was defined by the average displacement of multiple data points along two parallel lines (see Figure 3.12). The tensile strain was calculated from an initial gauge length of 6 mm digitally selected. It is important to note that the size of the gauge length used for the strain evaluation via DIC corresponds to the length of the reduced parallel section of the tensile sample (Figure 3.6a), i.e., L_0 = 6 mm. Uniform and total elongation were defined by the strain level at the σ_{UTS} and the maximal elongation value measured via DIC, respectively. Absorbed energy during uniaxial tensile deformation was calculated as the integrated area under the engineering stress-strain curves. Strain hardening rate was determined as the first derivative of the true stress with respect to the true strain evolution up to necking. Before differentiation

of the true stress v/s true strain values, the acquired data points were smoothed using the Locally Weighted Scatterplot Smoothing method (LOWESS).

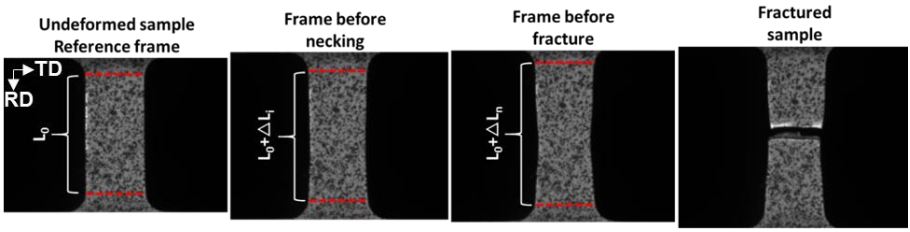

Figure 3.12: Schematic representation of the methodology employed for determining the instantaneous longitudinal strain during uniaxial tensile deformation via DIC. Undeformed sample width: 3 mm.

References

[1] ASTM-International, E228−17. Standard Test Method for Linear Thermal Expansion of Solid Materials With a Push-Rod dilatometer, Philadelphia, PA, 2017. https://doi.org/10.1520/E0228-17.

[2] R.E. Haimbaugh, Practical Induction Heat Treating, Second edi, ASM International, Ohio, 2015.

[3] T. Kop, A dilatometric study of the austenite/ferrite interphase mobility, Ph. D. Thesis, TU Delft, Delft, The Netherlands, 2000.

[4] C. Garcia de Andrés, F.G. Caballero, C. Capdevila, L.F. Alvarez, Application of dilatometric analysis to the study of solid-solid phase transformations in steels, Mater. Charact. 48 (2002) 101–111. https://doi.org/10.1016/S1044-5803(02)00259-0.

[5] L. Thomas, Effect of heating rate on intercritical annealing of low-carbon cold-rolled steel, Ph. D. Thesis, Colorado School of Mines, Golden, USA, 2015.

[6] H. Azizi-Alizamini, M. Militzer, W.J. Poole, Austenite formation in plain low-carbon steels, Metall. Mater. Trans. A Phys. Metall. Mater. Sci. 42 (2011) 1544–1557. https://doi.org/10.1007/s11661-010-0551-5.

[7] F. Castro-Cerda, Third Generation Advanced High Strength Steels via Ultrafast Heating, Ph. D. Thesis, Ghent University, Gent, Belgium, 2017. https://doi.org/D/2017/10.500/13.

[8] F. Vercruysse, F.M. Castro Cerda, P. Verleysen, R.H. Petrov, Behavior of ultrafast annealed advanced high strength steels under static and dynamic conditions, Mater. Sci. Eng. A. 780 (2020) 139168. https://doi.org/10.1016/j.msea.2020.139168.

[9] ASTM-International, ASTM E3-11. Standard Guide for Preparation of Metallographic Specimens, Philadelphia, PA, 2012. https://doi.org/10.1520/E0003-11R17.1.

[10] ASTM-International, ASTM E407-07. Standard Practice for Microetching Metals and

Alloys, Philadelphia, PA, 2016. https://doi.org/10.1520/E0407-07R15E01.2.

[11] R.H. Petrov, L.A.I. Kestens, Advanced High-Strength Steels: Electron Backscatter Diffraction (EBSD), Encycl. Iron, Steel, Their Alloy. (2015) 46–69. https://doi.org/10.1081/E-EISA-120050786.

[12] J. Michalska, B. Chmiela, Phase analysis in duplex stainless steel: comparison of EBSD and quantitative metallography methods Phase analysis in duplex stainless steel: comparison of EBSD and quantitative metallography methods, IOP Conf. Ser. Mater. Sci. Eng. (2014). https://doi.org/10.1088/1757-899X/55/1/012010.

[13] S. Zaefferer, P. Romano, F. Friedel, EBSD as a tool to identify and quantify bainite and ferrite in low-alloyed Al-TRIP steels, J. Microsc. 230 (2008) 499–508. https://doi.org/10.1111/j.1365-2818.2008.02010.x.

[14] G. Thomas, J. Speer, D. Matlock, J. Michael, Application of electron backscatter diffraction techniques to quenched and partitioned steels, Microsc. Microanal. 17 (2011) 368–373. https://doi.org/10.1017/S1431927610094432.

[15] S. Ebner, C. Suppan, A. Stark, R. Schnitzer, C. Hofer, Austenite decomposition and carbon partitioning during quenching and partitioning heat treatments studied via in-situ X-ray diffraction, Mater. Des. 178 (2019) 107862. https://doi.org/10.1016/j.matdes.2019.107862.

[16] J. Wu, P.J. Wray, C.I. Garcia, M. Hua, A.J. Deardo, T. Ebsd, Image Quality Analysis : A New Method of Characterizing Microstructures, ISIJ Int. 45 (2005) 254–262.

[17] A. Navarro-López, J. Hidalgo, J. Sietsma, M.J. Santofimia, Characterization of bainitic/martensitic structures formed in isothermal treatments below the Ms temperature, Mater. Charact. 128 (2017) 248–256. https://doi.org/10.1016/j.matchar.2017.04.007.

[18] C. Hofer, V. Bliznuk, A. Verdiere, R. Petrov, F. Winkelhofer, H. Clemens, S. Primig, Correlative microscopy of a carbide-free bainitic steel, Micron. 81 (2016) 1–7. https://doi.org/10.1016/j.micron.2015.10.008.

[19] M.A. Davinci, D. Samantaray, U. Borah, S.K. Albert, A new critical point on the stress-strain curve : Delineation of dynamic recrystallization from grain growth, Mater. Des. 116 (2017) 495–503. https://doi.org/10.1016/j.matdes.2016.12.053.

[20] T. Ogawa, N. Maruyama, N. Sugiura, N. Yoshinaga, Incomplete Recrystallization and Subsequent Microstructural Evolution during Intercritical Annealing in Cold-rolled Low, ISIJ Int. 50 (2010) 469–475.

[21] E. Gomes de Araujo, H. Pirgazi, M. Sanjari, M. Mohammadi, L.A.I. Kestens, Automated reconstruction of parent austenite phase based on the optimum orientation relationship, J. Appl. Crystallogr. 54 (2021) 569–579. https://doi.org/10.1107/S1600576721001394.

[22] N. Bernier, L. Bracke, L. Malet, S. Godet, An alternative to the crystallographic reconstruction of austenite in steels, Mater. Charact. 9 (2014) 23–32. https://doi.org/10.1016/j.matchar.2013.12.014.

[23] M. Zorgani, C. Garcia-mateo, M. Jahazi, The role of ausforming in the stability of

retained austenite in a medium-C carbide-free bainitic steel, J. Mater. Res. Technol. 9 (2020) 7762–7776. https://doi.org/10.1016/j.jmrt.2020.05.062.

[24] C.F. Jatczak, Retained austenite and its measurement by X-ray diffraction, SAE Tech. Pap. 89 (1980) 1657–1676. https://doi.org/10.4271/800426.

[25] C.S. Roberts, Effect of Carbon on the Volume Fractions and Lattice Parameters Of Retained Austenite and Martensite, J. Met. 5 (1953) 203–204. https://doi.org/10.1007/bf03397477.

[26] P. Verleysen, J. Degrieck, T. Verstraete, Influence of Specimen Geometry on Split Hopkinson Tensile Bar Tests on Sheet Materials, (2008) 587–598. https://doi.org/10.1007/s11340-008-9149-x.

[27] ASTM-International, E8/E8M-16a. Standard Test Methods for Tension Testing of Metallic Materials, Philadelphia, PA, 2020. https://doi.org/10.1520/E0008.

[28] S. Yoneyama, Y. Morimoto, Accurate Displacement Measurement by Correlation of Colored Random Patterns, JSME Int. J. Ser. A Solid Mech. Mater. Eng. 46 (2003) 178–184. https://doi.org/10.1299/jsmea.46.178.

Chapter 4

Influence of Mo-Nb-Ti additions and peak annealing temperature on the microstructure and mechanical properties of low-alloy steels after ultrafast heating process[1]

Abstract

The influence of the heating rates from 10 to 1000 °C/s and annealing temperatures on the microstructure and mechanical properties of two 0.2%C, 1.9%Mn, 1.4%Si cold-rolled steels with and without the addition of carbide-forming elements (Mo, Nb, and Ti) have been investigated. Results show that the increase of the heating rate above 100°C/s refines the parent austenitic grains in both alloys. The increment of the heating rate led to carbon heterogeneities in the austenite, which after subsequent cooling promoted the formation of a complex mixture of fine-grained constituents. As expected, at the lower heating rates the presence of Nb and Ti-rich carbides and carbonitrides controls the austenite grain growth during the annealing treatment. The tensile test results reveal that high heating rates do not have a significant influence on the tensile strength of the alloy with carbide-forming elements. On the other hand, both the ultimate tensile strength (σ_{UTS}) and total elongation of the alloy without carbide-forming elements decrease, due to the formation of bands of ferrite and high carbon martensite. However, samples treated at heating rates above 100°C/s show a combination of σ_{UTS} in the range of 1400 to 1600 MPa, and 12 to 18% of total elongation. The results suggest that the microstructure heterogeneity obtained after high heating rates, especially the ferrite content, has the major effect on the mechanical behavior of the studied steels.

4.1 Introduction

Over the last decades, the progress and research towards the third generation of advanced high strength steels (3rd gen. AHSS) have led to the development of new thermo-mechanical processes and heat treatments [1]. Among the different routes

[1] This chapter is based on the article: E.I. Hernandez-Duran, L. Corallo, T. Ros-Yanez, F.M. Castro-Cerda and R.H. Petrov. Influence of Mo-Nb-Ti additions and peak annealing temperature on the microstructure and mechanical properties of low alloy steels after ultrafast heating process. Mat. Sci. & Eng. A, 808 (2021).
https://doi.org/10.1016/j.msea.2021.140928

of steel production, the ultrafast heating (UFH) [2–7], or also called flash annealing, represents an attractive approach for the steel industry thanks to the significant time reduction of the heat treatment processes by increasing the heating rate above 100 °C/s during the annealing step. Moreover, current literature [8–11] has shown that the combination of UFH and subsequent quenching and partitioning (Q&P), can improve the mechanical properties of the low-alloy steels.

The enhanced mechanical behavior of the ultrafast annealed steels has been related to the overall grain refinement and carbon gradient through the parent austenite [12,13], which seem to be the main factors controlling the microstructure development after the peak annealing treatments with very short soaking times (0.1 to 2 seconds). It has been proposed that the formation of unique fine-grained, complex phase microstructures, as a result of the carbon heterogeneities in austenite, might lead to a wide variety of local mechanical responses, improving at the same time the overall mechanical performance. Besides, the microstructural refinement obtained via the ultrafast heating strategies suggests that conventional routes to control the grain size, as the additions of microalloying elements [14–16], could be replaced for tailoring new steel grades.

Recent studies on this topic have focused on the investigation of high heating rates for producing intercritical annealed steels [3–5,8,9,17–20] giving less attention to the mechanical behavior of fully austenitized microstructures [6,10–12], where the definition of the appropriate peak temperature could play a fundamental role on the obtained microstructure due to its influence on the non-isothermal austenitic grain growth and chemical homogenization. Regarding the peak temperature, the A_{C3} has been defined as the temperature at which the transformation from ferrite to austenite is complete during heating processes, and it has been proved that such temperature is affected by the heating rate for some specific alloys and initial microstructure [21]. Additionally, current studies on UFH of low-alloy steels carried out by Castro Cerda et al. [3,22] have proposed that the mechanism of austenite formation changes from carbon diffusion to interface controlled (massive) mechanism at the thermodynamically defined A_m temperature. At this temperature, the resulting Gibbs energy change for the transformation from ferrite to austenite is equal to 0 when the carbon content approaches to 0.

A comparative analysis of the mechanical properties obtained by designing the peak annealing heat treatments based on the A_{C3} and A_m temperatures has not been reported so far. Moreover, the evaluation of the additions of carbide forming elements on the microstructure-mechanical properties relationship of ultrafast heated steels has been studied in a limited number of works [3,20,23].

The objective of this work, therefore, is to study the influence of the heating rate on the microstructure and mechanical properties of a peak annealed low-alloy steel with and without the addition of Mo, Nb and Ti heated up to the A_m and above A_{C3} temperature.

4.2 Experimental

4.2.1 Materials and peak annealing treatments

The composition of the two steels analyzed in this study is listed in Table 4.1. The base alloy and the one with additions of Mo, Nb, and Ti will be referred through this study as 0.2C and 0.2CMoNbTi, respectively. Figure 4.1 presents the microstructure of the 0.2C (Figures 4.1a and 4.1b) and 0.2CMoNbTi (Figures 4.1c to 4.1g) steels in 70% cold-rolled condition. For alloy 0.2C, the initial microstructure consists of alternated bands of deformed ferrite (F) and pearlite (P), whereas in the alloy 0.2CMoNbTi bands of ferrite and a mixture of martensite (M) and bainite (B) were observed. Martensite is presented in the microstructure mainly as unetched blocky-like shape regions (Figures 4.1c to 4.1f), and it can be easily distinguished from the highly deformed ferrite. The darker etched regions in Figure 4.1c contain mostly bainite, which can be observed as a set of deformed parallel bainitic ferrite laths in Figures 4.1d to 4.1g. Similar bainitic morphology was observed by Hamzeh et al. [24] in a 90% cold-rolled bainitic steel. Small pearlitic regions are also distinguished in the secondary electron image of the 0.2CMoNbTi steel (Figure 4.1d). Ferrite contents of 45.5 ± 3.7% and 35.0 ± 3.9% were metallographically quantified for the 0.2C and 0.2CMoNbTi steels, respectively.

Table 4.1: Chemical composition of the studied steels (wt.%).

Alloy	C	Mn	Si	Mo	Nb	Ti	Fe
0.2C	0.19	1.87	1.42	-	-	-	Bal.
0.2CMoNbTi	0.20	1.99	1.43	0.32	0.035	0.020	Bal.

Cold-rolled samples with dimensions 10x5x1.2 mm^3 and 120x20x1.2 mm^3 were cut with the longest axis parallel to the rolling direction to perform dilatometry experiments and peak annealing treatments, respectively.

To evaluate the evolution of the A_{C3} temperature with respect to the heating rate, both steels were treated at heating rates of 10, 50, 100, 200, and 500 °C/s up to 1000 °C in a Bähr 805 A/D dilatometer. The lever rule method was applied to the temperature-change in length dilatometric curve to determine the transformed fraction of austenite. Then, the A_{C3} temperature was defined as the temperature in which 98% of austenite transformation is achieved upon continuous heating (see the insert in Figure 4.2a). The evolution of the A_{C3} with respect to the heating rate and the respective fitted curves are presented in Figure 4.2b.

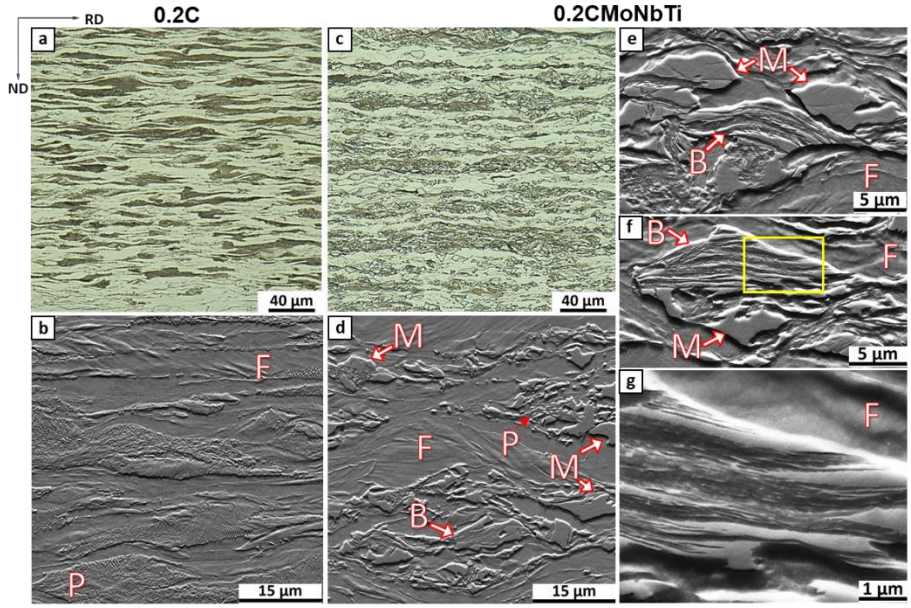

Figure 4.1: Optical and secondary electron images of the Initial 70% cold-rolled microstructure for the 0.2C (a, b) and 0.2CMoNbTi (c, d, e, f and g) steels. (e and f) High magnification images showing ferritic, martensitic, and bainitic microconstituents. (g) Enlarged image of the bainitic region highlighted by a yellow rectangle in Figure 4.1f.

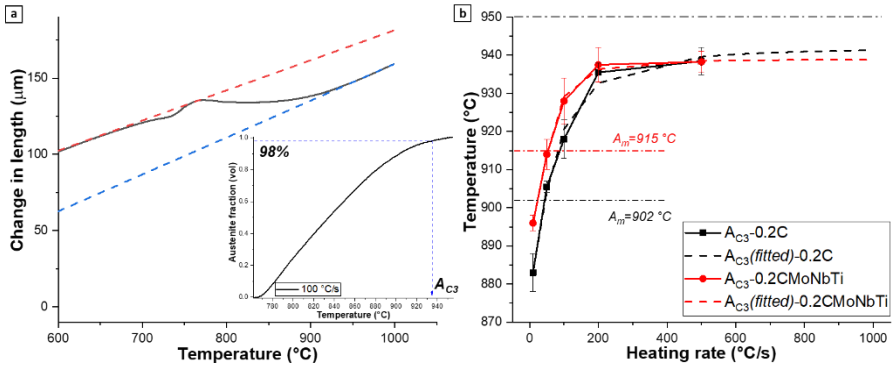

Figure 4.2: (a) Dilatometric curve of the alloy 0.2CMoNbTi heated at 100 °C/s and the respective austenite fraction v/s temperature curve. The A_{C3} temperature was determined based on 98% of austenitic transformation during heating. (b) Evolution of the A_{C3} temperature with the heating rate in the range 10 – 500 °C/s from dilatometry experiments and fitted curves up to 1000 °C/s. The horizontal dash-dot lines in Figure 4.2b correspond to the selected peak annealing temperatures.

Peak annealing treatments with heating rates of 10, 100 and 1000 °C/s were performed in a Gleeble 1500 thermomechanical simulator. Two peak temperatures were selected for microstructure analysis and mechanical testing in both steels (indicated by horizontal lines in Figure 4.2b); 950 °C based on a complete austenite transformation upon heating (i.e. peak annealing above the A_{C3}) and the respective

thermodynamically defined A_m temperature [22], which was determined using the Thermo-Calc software (database TCFE7). The heat treatment parameters used in this study are compiled in Table 4.2. The temperature profile in each thermal treatment was measured with a type K thermocouple spot-welded to the geometrical center of the samples.

Table 4.2: Peak annealing treatment parameters.

Heating rate, °C/s	Peak temperature, °C		Soaking time, s	Cooling rate, °C/s
	0.2C	0.2CMoNbTi		
10-100-1000	902 *(A_m)*	915 *(A_m)*	<0.2	160
	950			

4.2.2 Microstructural characterization

The microstructural characterization was performed using secondary electron imaging and Electron Backscatter Diffraction (EBSD) in a scanning electron microscope FEI Quanta 450 FEG-SEM. Samples for microstructure characterization were extracted at 2 mm from the geometrical center of each sample where the thermocouple was welded. The extracted samples were mechanically ground and polished following the well-established procedures for sample preparation. The specimens were chemically etched with a 2% Nital solution for ~2 s and then characterized in the SEM operating at 15 kV and a working distance of 10 mm. The EBSD analyses were performed using a voltage of 20 kV, a working distance of 14 mm, and a sample tilt of 70° towards the EBSD detector. A hexagonal scan grid with a step size of 100 nm was used in all scans and the EBSD patterns were recorded by a Hikari detector controlled with the EDAX-TSL OIM Data Collection software version 7.3. Based on an optimized Kurdjumow-Sachs [25] orientation relationship between martensite and parent austenite, the method proposed in [26] was employed for the parent austenite reconstruction from the acquired EBSD data. 5 pixels per grain and misorientation angle of 5° and 15° were selected for the grain size definition of the heat-treated samples and the corresponding reconstructed parent austenite, respectively.

A Siemens Kristalloflex D5000 x-ray diffractometer equipped with Mo-K_α operating at 40 kV and 40 mA was used to quantify the amount of retained austenite in the heat-treated samples. The diffraction patterns were acquired with a step size of 0.03° per step, dwell time of 20 s and sample rotation at 15 rpm was used to minimize the RD_TD texture effect on the quantification of the retained austenite. For the calculations, the direct comparison method [27] was used on the integrated intensities of the $(200)^{BCC}$, $(211)^{BCC}$, $(220)^{FCC}$ and $(311)^{FCC}$ peaks.

TEM analysis was performed in a Jeol JEM-2200FS, field emission transmission electron microscope. Precipitates were characterized using bright-field images (BF) and EDX analysis. The sample preparation procedure for TEM consisted in ground

the samples to 100 µm thickness followed by precision ion polishing with a 96 v/v% CH_3COOH, 4 v/v% $HClO_4$ solution.

4.2.3 Mechanical properties

Sub-sized dog-bone shape samples (see Figure 3.6a in Chapter 3: Experimental procedures) were cut from the homogeneously treated region of the specimens treated in Gleeble. The samples were tested using an Instron 5000 tensile testing machine equipped with a 50kN load cell and operating with a testing rate of 0.001 s^{-1}. The strain was measured by 2D-digital image correlation using the software MatchID. The yield strength was defined by the conventional offset method at an engineering strain value of 0.2%. By using Vickers hardness measurements was proved that the homogeneous heat-treated zone covers practically the entire gauge length of the tensile samples as described in [11].

4.3 Results

4.3.1 Microstructure

Figure 4.3 shows the microstructure of the samples after heat treatment with heating rates of 10°C/s (Figures 4.3a and 4.3b), 100°C/s (Figures 4.3c and 4.3d) and 1000 °C/s (Figures 4.3e and 4.3f). Left (Figures 4.3a, 4.3c and 4.3e) and right (Figures 4.3b, 4.3d and 4.3f) columns of images correspond to the microstructure of the samples heated up to the A_m temperature and 950 °C, respectively. As is indicated in Figure 4.3a, the left-hand side micrograph corresponds to the 0.2C steel and the right hand to the 0.2CMoNbTi steel. Table 4.3 summarizes the quantification of microconstituents obtained after heat treatment. At the A_m temperature and 950 °C all samples have a microstructure that consists of a martensitic matrix and in some cases isolated ferritic (F) grains are observed. In samples treated at 10 °C/s, acicular ferritic grains are detected at prior austenite grain boundaries for the 0.2C steel, whereas fully martensitic microstructures were obtained in the 0.2CMoNbTi steel, evidencing complete ferrite to austenite transformation before quenching. The latter is in accordance with the results obtained by dilatometry. Martensitic grains are larger in the samples heated up to 950 °C than to the A_m temperature as a result of non-isothermal austenitic grain growth.

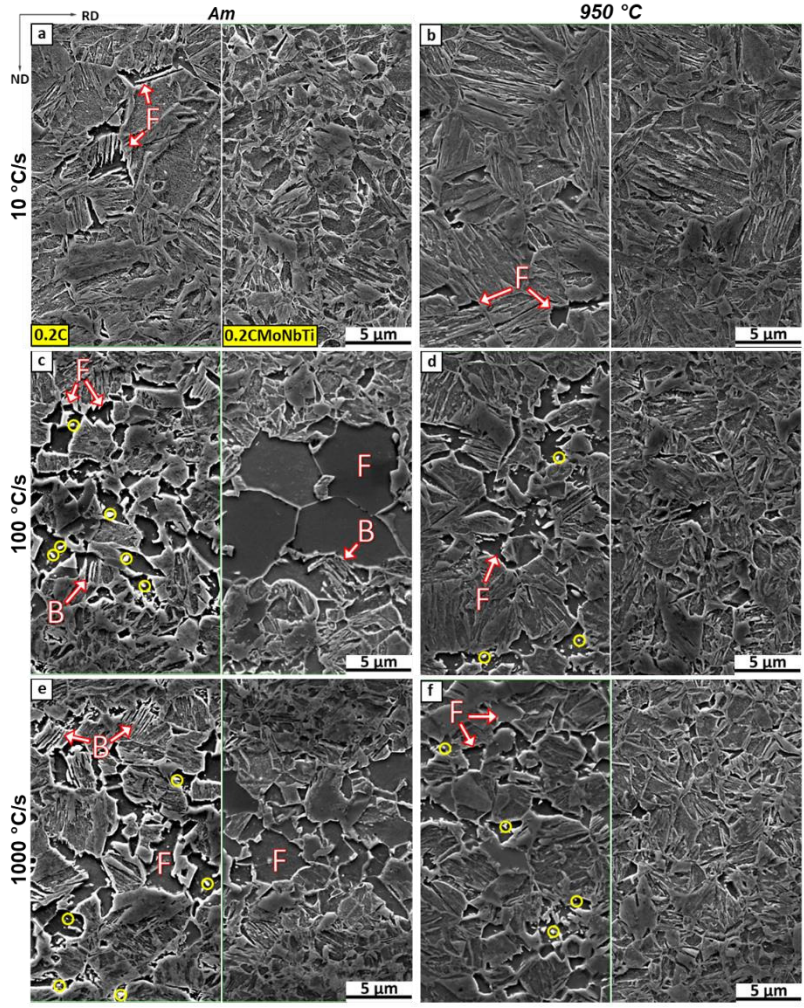

Figure 4.3: Secondary electron images illustrating the effect of the peak temperature and heating rate on the microstructure of the studied steels. The left and right images in each sub-figure correspond to 0.2C and 0.2CMoNbTi steel, respectively. The left column of images corresponds to the samples quenched from A_m temperature, whereas the right column corresponds to the samples quenched from 950 °C.

In comparison to the 0.2C steel, a finer martensitic structure is also obtained by additions of Mo, Nb and Ti. In the samples heated up to the A_m temperature (Figures 4.3a, 4.3c and 4.3e), the increase of the heating rate leads to the formation of a fine-grained mixture of martensite and ferrite, together with small fractions of bainite (B) which is detected in both steels. Fine spheroidized particles, enclosed by yellow circles, are observed in the 0.2C steel after treatment with heating rates ≥100 C/s. Those particles were also observed in the microstructure of the 0.2C steel heated at 500 °C/s to 1000 °C, followed by fast cooling (Figure 4.4a). Further TEM characterization on that sample has proved that those particles correspond to

cementite. Figure 4.4b shows two cementite particles (θ_S) and the respective indexed diffraction pattern obtained from the cementite particle highlighted by the green circle on that figure.

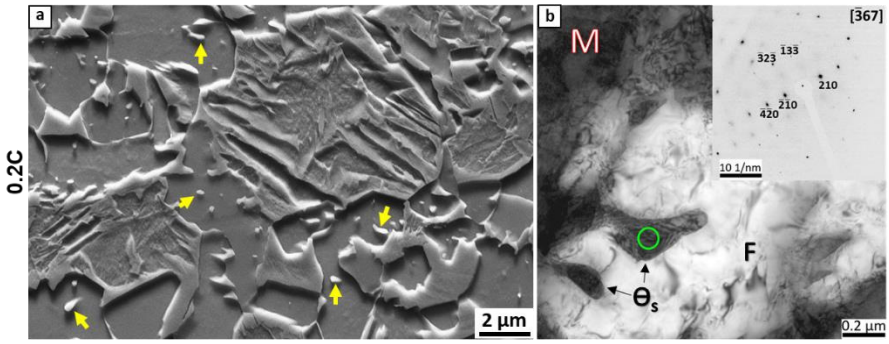

Figure 4.4: Alloy 0.2C heated at 500 °C/s to 1000 °C and quenched: (a) Secondary electron (SE) image and (b) bright field image in TEM. The indexed diffraction pattern corresponds to the spheroidized cementite particle (zone axis: [3̄67]) pointed by the green circle highlighted in (b). Yellow circles or arrows are used to highlight the undissolved cementite particles in the SE-SEM images.

After increasing the peak temperature from A_m to 950 °C the amount of ferrite in the studied steels decreases and the ferrite formation is apparently suppressed in the alloy 0.2CMoNbTi when heating rates of 100 (Figures 4.3c and 4.3d) and 1000 °C/s (Figures 4.3e and 4.3f) are used. The methodology based on the segmentation of the microstructure by using the grain average image quality values was employed to quantify the ferrite fraction from the acquired EBSD data according to the procedure explained in [28,29]. The presence of a small fraction of retained austenite (γ) was confirmed via XRD measurements, ranging from 1.9 and 4.1 % for the 0.2C steel and 0 to 2.6% in the 0.2CMoNbTi steel, respectively. The results also show that the obtained γ fraction is about 1 to 2% higher by heating up to the A_m than at 950 °C.

Table 4.3: Effect of the heating rate and peak temperature on the fraction of microconstituents (in %).

Alloy	**0.2C**					
Temperature	***Am* (902 °C)**			**950 °C**		
Heating rate, °C/s	**10**	**100**	**1000**	**10**	**100**	**1000**
Martensite	87.7	60.6	57.7	89.9	73.8	78.2
Ferrite	9.3	35.3	38.6	8.1	22.6	19.7
Retained austenite	3.0	4.1	3.7	1.9	3.6	2.1
Alloy	**0.2CMoNbTi**					
Temperature	***Am* (915 °C)**			**950 °C**		
Heating rate, °C/s	**10**	**100**	**1000**	**10**	**100**	**1000**
Martensite	97.7	90.8	86.7	99	100	100
Ferrite	0.0	9.2	13.3	0.0	<1.0	<1.0
Retained austenite	2.3	2.6	1.6	1.0	0.0	0.0

The combined greyscale image quality (IQ) and color-coded grain average image quality (GAIQ) EBSD maps for the samples heated to the A_m temperature presented in Figure 4.5 reveal that the increase of the heating rate from 10 °C/s (Figures 4.5a and 4.5b) to 1000 °C/s (Figures 4.5c and 4.5d) produces banded microstructures along the rolling direction in both alloys.

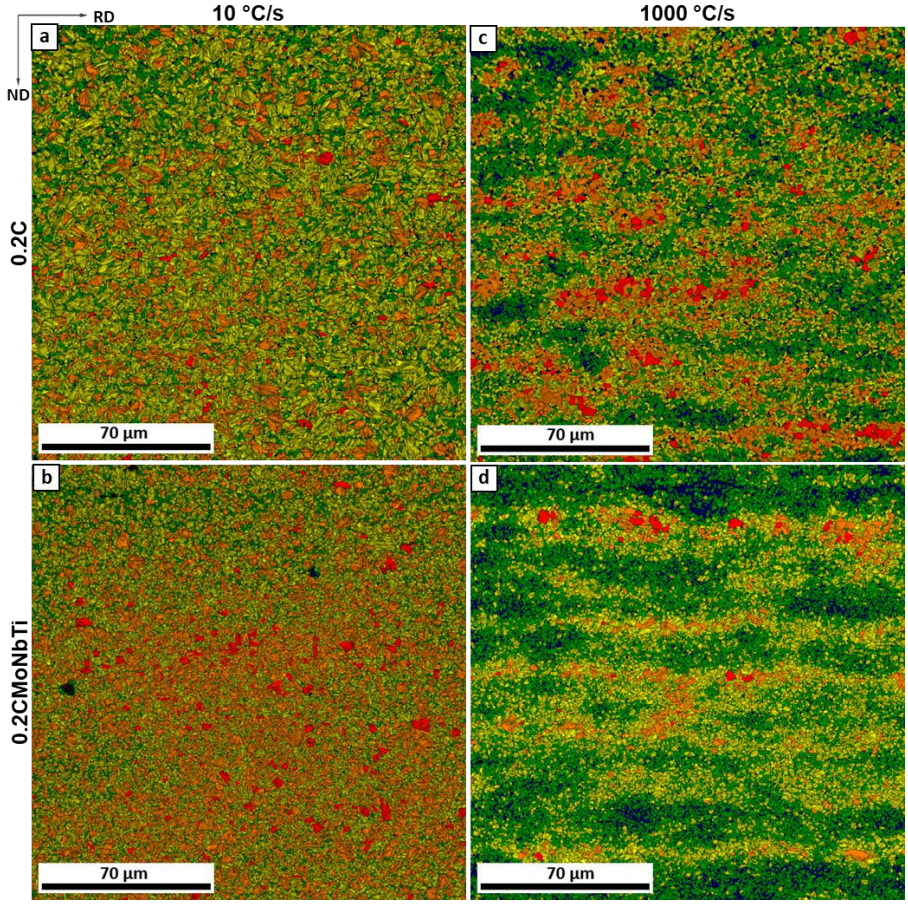

Figure 4.5: Combined EBSD Image quality and grain average image quality map of the 0.2C (a, c) and 0.2CMoNbTi (b, d) steels heated at 10 (left column) and 1000 °C/s (right column) up to the A_m temperature.

At 10 °C/s (Figures 4.5a and 4.5b) more homogeneously distributed microstructures were obtained. In the 0.2C steel (Figure 4.5a), the intense red color corresponds to ferrite grains nucleated at parent austenite grains (PAGs) boundaries and the color gradients between orange and green represent martensite (and possible bainite with slightly higher GAIQ values than martensite). For the 0.2CMoNbTi steel (Figure 4.5b), the color gradients in the IQ-GAIQ map are mainly related to local chemical heterogeneities in a fully martensitic microstructure. With the increase of the

heating rate to 1000 °C/s, the IQ-GAIQ maps of the 0.2C (Figure 4.5c) and 0.2CMoNbTi (Figure 4.5d) steels show pronounced microstructural differences, where red to orange grains and yellow to dark blue regions correspond to ferrite and martensite-bainite bands, respectively. The dark blue regions can be related to high carbon content martensite since the low IQ values measured in these zones can be associated with a highly distorted crystal lattice [12]. The microstructural analysis reveals that the banded microstructure obtained after ultrafast heating is related to the initial microstructural banding observed in the cold-rolled samples (Figure 4.1).

The ND inverse pole figures of the reconstructed parent austenitic grains (PAGs) for the alloy 0.2C and 0.2CMoNbTi heated to 950 °C are presented in Figure 4.6, giving a visual reference to the reader about the effect of the selected heating rates and microalloying additions. Black regions in Figure 4.6b and 4.6c correspond to proeutectoid ferritic grains (these grains can be observed in Figure 4.3). Ferritic grains were subtracted from the acquired EBSD data to ensure accurate reconstruction of the prior austenitic grains, based on the K-S orientation relationship between austenite and the "daughter" martensitic phase (and bainite) [25,26,30,31].

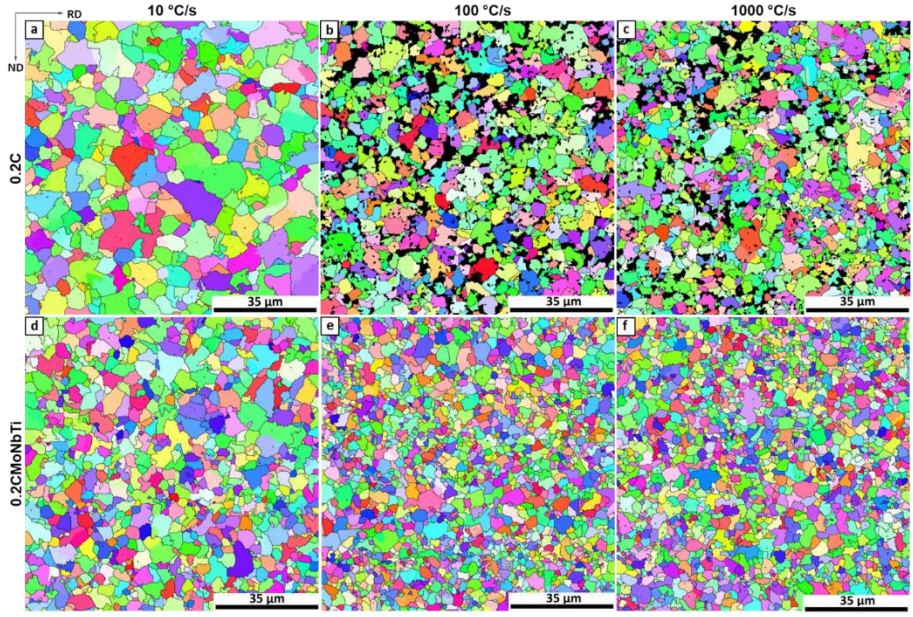

Figure 4.6: Parent austenite grains reconstruction from EBSD data for samples heated to 950 °C with heating rates of 10 (a, d), 100 (b, e) and 1000 °C/s (c, f). The upper and lower rows of images correspond to the 0.2C and 0.2CMoNb steel, respectively. The black areas correspond to non-reconstructed grains.

The increase of the heating rate from 10 to 1000 °C/s produces grain refinement in both alloys, and additions of Mo, Nb and Ti (Figures 4.6d to 4.6f) significantly contribute to the decrease of the PAGs size in the microalloyed steel with respect to

the 0.2C steel (Figures 4.6a to 4.6c). From Figure 4.6, it is clearly seen that the influence of the heating rate on the grain refinement of the parent austenite is prominent in the range 10-100 °C/s.

Figure 4.7 summarizes the effect of the heating rate and microalloying carbide-forming elements on the average PAGs size diameter (Figures 4.7a and 4.7b). The martensite block length is presented in Figure 4.7c (bainitic grains are also included in this distribution due to the difficulties on martensite-bainite selection by EBSD measurements), whereas the average ferrite grain diameter determined from the EBSD data is shown in Figure 4.7d. A circular geometry was selected to describe the parent austenite and ferrite grains, whereas an elliptical shape was used for the martensitic blocks where the major axis of the ellipse was attributed to the block length. PAGs size and martensite blocks length tend to follow the same trend, in which larger grains are obtained or at higher peak temperature or at a lower heating rate. The addition of Mo, Nb and Ti leads to finer grains in the alloy 0.2CMoNbTi than in the alloy 0.2C, but at the same time, this steel is less sensitive to the grain refinement effect obtained by increasing the heating rate.

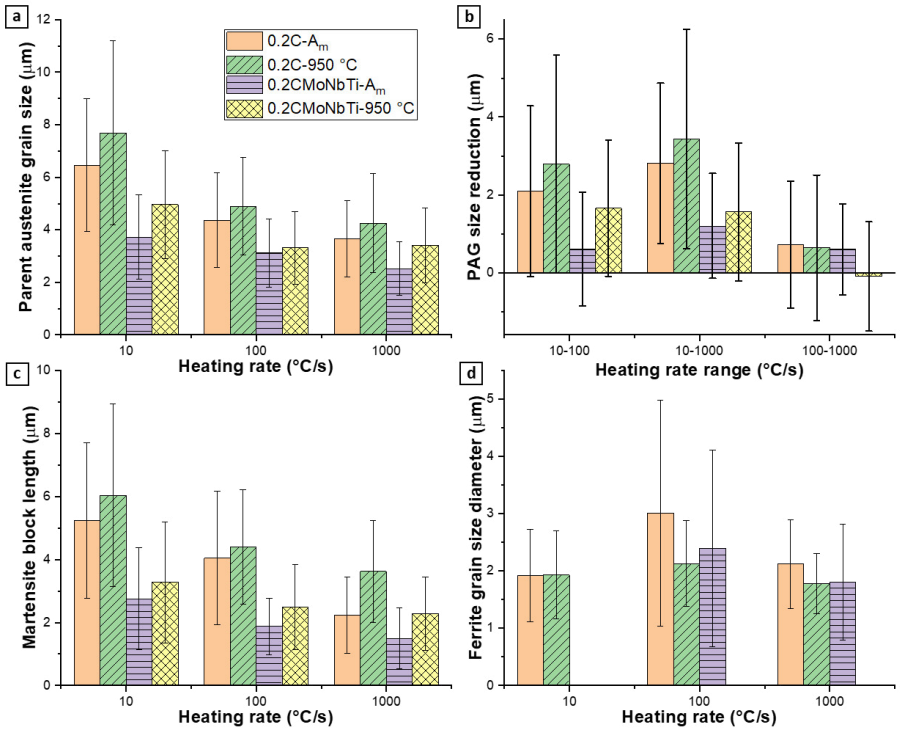

Figure 4.7: (a) Reconstructed parent austenite average grain size diameter and (b) comparison of the grain refinement effect at different heating rates and peak temperatures expressed as the difference of the reconstructed average PAG size diameter. (c) Martensite block length and (d) ferrite grain size diameter obtained for each condition.

Figure 4.7b displays the differences between the obtained average PAG size for each peak temperature and alloy in the range 10-100 °C/s, 10-1000 °C/s and 100-1000 °C/s. The increment of the heating rate from 10 to 100 °C/s has the major incidence on the average PAG size diameter. A grain size reduction of 2 and 0.5 µm after heating to A_m and 2.75 and 1.5 µm after heating to 950 °C was obtained for the 0.2C and 0.2CMoNbTi steels, respectively. A small PAGs size decrease of about 0.7 µm was reached in the samples heated at 1000 °C/s with respect to the samples treated at 100 °C/s, with exception of the 0.2CMoNbTi steel treated at 1000 °C/s to 950 °C, in which the negative value is an indication that the reconstructed PAGs do not refine when the heating rate increased. Nevertheless, a decrease of 0.2 µm in the average martensite block length (yellow column in Figure 4.7c) indicates a small refinement effect when the heating rate increases from 100 to 1000 °C/s. The obtained average ferritic grain size diameter ranged about 1.9 and 3.0 µm (Figure 4.7d).

4.3.2 Tensile properties

Representative engineering stress-strain curves for the 0.2C and the 0.2CMoNbTi steel treated at the A_m temperature and 950 °C are shown in Figure 4.8.

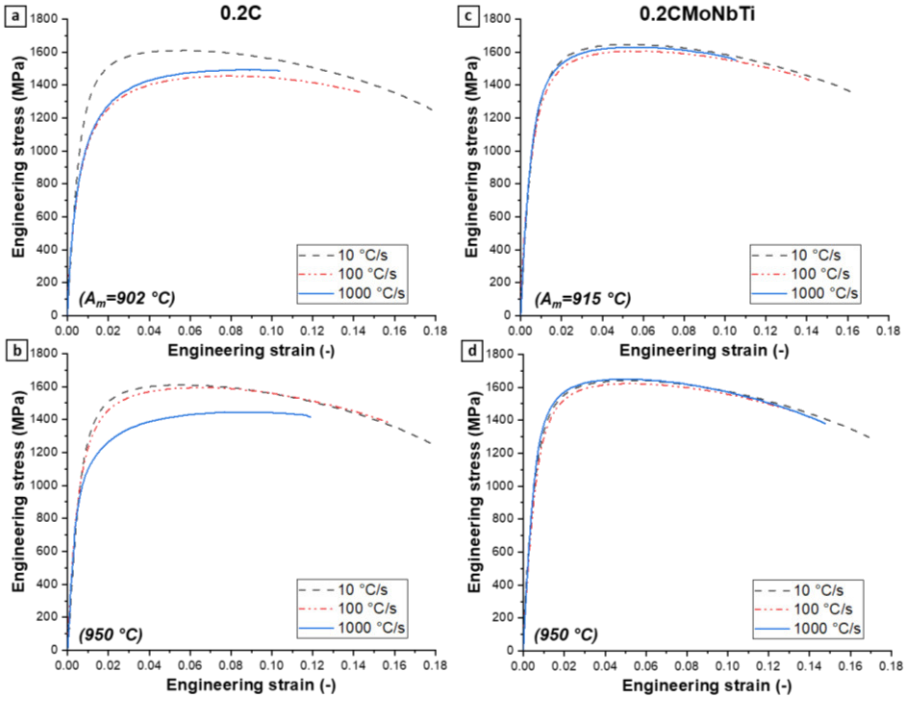

Figure 4.8: Engineering stress-strain curves of the 0.2C (a, b) and 0.2CMoNbTi (c, d) steels. The left and right-hand columns of images correspond to the 0.2C and 0.2MoNbTi, respectively. The peak annealing temperature is labeled on each image.

For comparison purposes, Figure 4.9 summarizes the obtained yield strength (σ_{ys}) (Figure 4.9a), ultimate tensile strength (σ_{UTS}) (Figure 4.9b), uniform elongation

($\varepsilon_{Uniform}$) (Figure 4.9c) and total or elongation at fracture (ε_{Total}) (Figure 4.9c) for all heat-treated samples. In the samples of the alloy 0.2C that were heated up to the A_m temperature, the σ_{ys} and σ_{UTS} decrease at high heating rates (Figure 4.9a), whereas the samples of the 0.2CMoNbTi steel show a small reduction of σ_{ys} and σ_{UTS} values when the heating rate is 100 °C/s. By increasing the peak temperature to 950 °C, the lowest σ_{ys} and σ_{UTS} were measured in the 0.2C steel samples heated at 1000 °C/s and variations in the σ_{ys} and σ_{UTS} not higher than 50 MPa were measured in the samples of the 0.2CMoNbTi steel. The analysis of the uniform elongation ($\varepsilon_{Uniform}$) (Figure 4.9c) shows that the $\varepsilon_{Uniform}$ in both 0.2C and 0.2CMoNbTi steels increases with the rise of the heating rate from 10 to 1000 °C/s for both peak temperatures, A_m and 950°C. On the other hand, the $\varepsilon_{Uniform}$ of the 0.2CMoNbTi steel varies about 5.5% for the studied conditions. Controversially, irrespectively of the peak temperature, the total elongation (Figure 4.9d) decreased continuously with the increment of the heating rate for the alloy 0.2C, while it drops when the heating rate increases from 10 to 100 °C/s in the alloy 0.2CMoNbTi, without having a further decrease in the samples treated at 1000 °C/s.

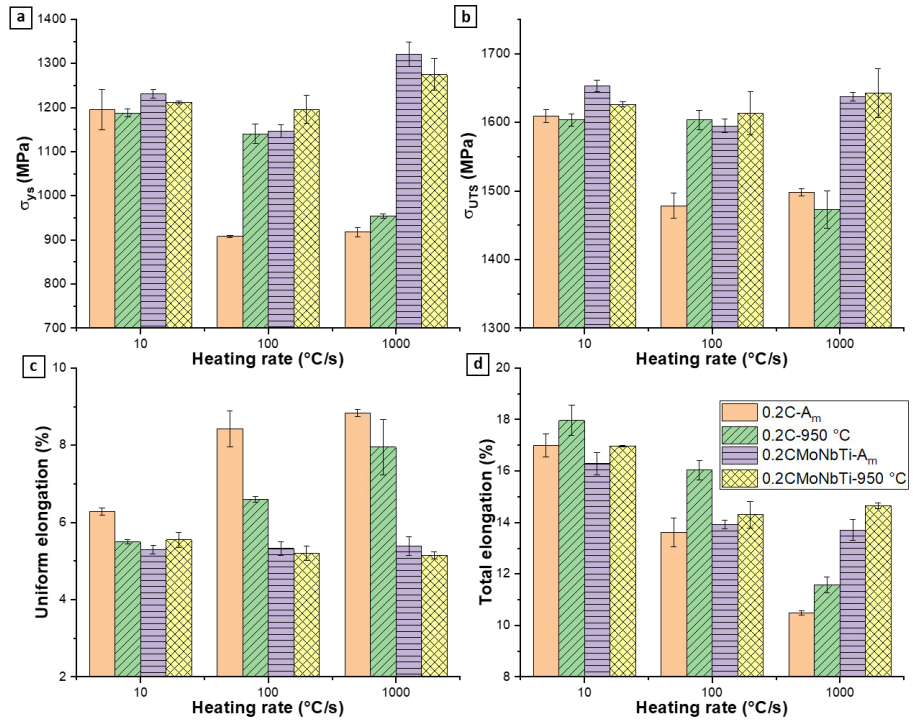

Figure 4.9: Tensile properties obtained for the studied steels produced via continuous heating up to the A_m temperature and 950 °C, followed by cooling at 160 °C/s: (a) offset yield strength, (b) ultimate tensile strength, (c) uniform elongation and (d) total elongation.

4.4 Discussions

4.4.1 The microstructures after peak annealing and quenching and the role of the initial microstructural banding

It has been reported that when low-alloy steels are rapidly heated several solid-state reactions interact [3,4,23,32] being responsible for the complex microstructures obtained after ultrafast heating. Multiple nucleation of austenite upon heating and local carbon heterogeneities seem to be the main factors controlling the microstructure development in ultrafast annealing experiments [13]. After the peak annealing treatments up to the A_m temperature and up to 950 °C, the obtained microstructures (Figures 4.3, 4.5 and Table 4.3) are composed of a martensitic matrix in both steels and the high heating rates led to the formation of banded microstructures. In ultrafast heating experiments, i.e., continuous heating at 100-1000 °C/s, the results show that martensite-ferrite microstructural banding is likely to occur when both alloys are heated up to the A_m temperature (Figure 4.5). Contrarily, the samples annealed to 950 °C displayed complete ferrite dissolution upon heating (cf. critical A_{C3} temperature in Figure 4.2b) and fully martensitic microstructures were produced in the alloy 0.2CMoNbTi after cooling at 160 °C/s, whereas ferritic grains were observed at parent austenite grain boundaries (allotriomorph ferrite morphology) in the alloy 0.2C (Figure 4.3f). Nevertheless, microstructural gradients in the martensitic matrix detected by GAIQ (Figure 4.5d), suggest that the initial microstructure also plays a fundamental role in steels ultrafast heated above the A_{C3} temperature. Figure 4.10 illustrates the microstructure evolution obtained by interrupting the heating of samples treated at 1000 °C/s to 700, 800 and 850 °C and quench for the 0.2 (Figures 4.10a to 4.10c) and 0.2CMoNbTi steel (Figures 4.10d to 4.10f). At 700 °C (Figures 4.10a and 4.10d) the microstructures consist of ferrite-perlite and tempered martensite (M_T)/bainite-ferrite for the alloys 0.2C and 0.2CMoNbTi, respectively. The major fraction of ferrite remained deformed and some recrystallized grains are observed in the microstructure. By increasing the temperature to 800 °C (Figures 4.10b and 4.10e), it can be seen that austenite (which is transformed to martensite after quenching) developed preferentially on pearlitic colonies or tempered martensite (M_T) regions and this type of microstructure is also present in samples treated at 850 °C (Figures 4.10 c and 4.10f). Moreover, a microstructural gradient is observed in Figure 4.10f, in which a light gray mixture of martensite-bainite (M/B) is obtained in front of a darker martensitic region (M), and such a microstructural distribution is consistent with the IQ-GAIQ maps presented in Figures 4.5c and 4.5d. Thus, it can be hypothesized that carbon heterogeneities in the parent austenite, but also substitutional elements segregation, as Mn and Mo, are responsible for the microstructures obtained after the proposed peak annealing treatments. Although the segregation of carbon and alloying elements was not experimentally measured in this study it is highly likely to assume that such segregation exists and it is playing a fundamental role in the microstructure

evolution. Pearlitic colonies and martensite-bainite regions act as carbon sources in the phase transformation during heating, and it is logical to expect high carbon concentration in the austenite that forms in their closest vicinity. Consequently, the phase transformation of austenite during quenching will produce high carbon martensite and/or retained austenite in the carbon enriched zones. Alternatively, the zones where the carbon content is low form carbon depleted martensite, bainite, or even ferrite, as the distance from the carbon source increases due to the limited carbon diffusion at high heating rates. This type of microstructural observation, indirectly discussed in terms of carbon gradients in the parent austenite, was early reported by Albutt and Garber [33] in a commercial rimming steel fast heated at 2000 °C/s and more recent evidence has been presented elsewhere [34], where the authors even go a step further linking the calculated carbon and alloying elements gradient around the carbon sources with the formed microstructures analyzed via EBSD and TEM. A similar effect of localized enrichment of carbon and alloying elements was observed in a flash annealed 0.32C-11.6Cr steel [35] and in a 75Cr1 steel heated at conventional rates followed by 4 min soaking [36]. In the same sources, the authors provide clear evidence for the chemical concertation profiles of carbon and the alloying elements produced by the dissolution of carbides.

Additionally, a local increment of the hardenability of the studied steels can be expected to be produced by the microchemical segregation of manganese and other substitutional elements [37–41], resulting in the banded microstructures obtained in high heating rate experiments (Figure 4.5). Such chemical segregation can be assumed as the cause of the microstructural banding observed in the initial cold-rolled samples displayed in Figure 4.1 (see the alternated layers of ferrite and perlite or ferrite and martensite-bainite for the alloys 0.2C and 0.2CMoNbTi, respectively), and similar banded microstructures were reported elsewhere [42]. Moreover, the synergic effect of Mn and Mo [43] can further increase the hardenability of the 0.2CMoNbTi steel, resulting in the formation of the martensite/bainite microconstituents observed in the initial -untreated- microstructure of this steel grade (Figures 4.1c to 4.1g).

Then, considering the hypothesis of austenite formation under negligible partitioning local equilibrium (NPLE) mode proposed by Liu et al. [44], the mixture of microconstituents M/B obtained in front of the prior pearlitic or martensitic-bainitic regions might be the result of the compositional gradients in the parent austenite that grows in contact with the proeutectoid ferrite controlled by a carbon diffusion mechanism. Such compositional gradients, together with the carbon enrichment of the parent austenite by diffusional ferrite/bainite growing during cooling, can also contribute to the stabilization of retained austenite grains (Table 4.3). A decrease of the retained austenite (RA) fraction was observed when the peak temperature increased from A_m to 950 °C in both steels, and the highest amount of γ was obtained in experiments performed at 100 °C/s. These results agree with the evidence

previously reported [4], where the fraction of the γ obtained after peak annealing experiments was related to a compromise between homogenization of carbon in the parent austenite and the rate of dissolution of cementite particles.

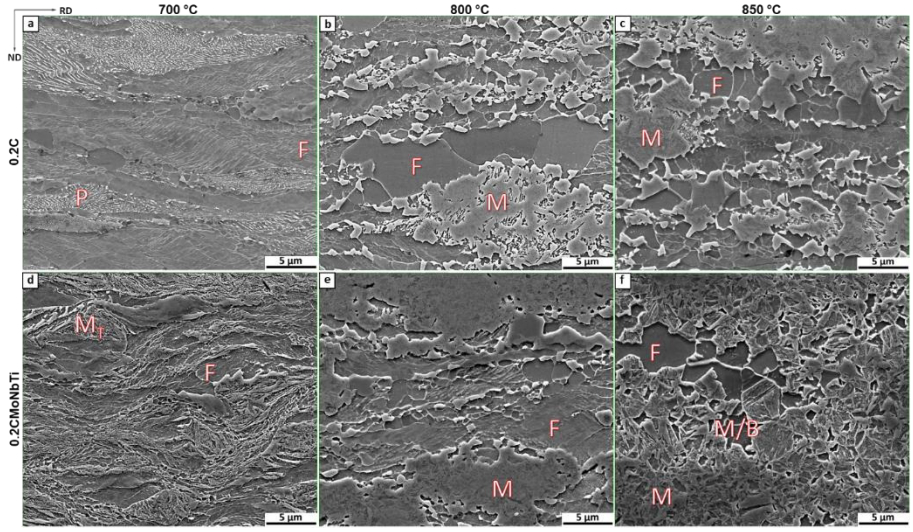

Figure 4.10: Microstructure evolution during continuous heating at 1000 °C/s to 700 °C (a, d), 800 °C (b, e) and 850 °C (c, f). The upper and lower rows of images correspond to the 0.2C and 0.2CMoNbTi steel, respectively.

Simultaneous evidence for ferrite recrystallization and formation of austenite during heating at 1000 °C/s is clearly seen in Figure 4.11. Recovered (F_{Rc}) and recrystallized (F_{Rx}) ferrite grains can easily be distinguished along ferrite bands in the 0.2CMoNbTi steel (Figure 4.11a) and in the 0.2C steel (Figure 4.11b) heated up to 772 °C and 850 °C, respectively. This microstructural characterization is in accordance with the results reported in [45–47], showing that the onset of the austenite nucleation and growth occurs through ferrite-cementite aggregates. Moreover, the formation of austenite was not detected at ferrite-ferrite grain boundaries, even when a high boundary density was available for the austenite nucleation on the F_{Rc} and F_{Rx}, as is shown in Figure 4.11b. In the presented results, austenitic grains (transformed to martensite after cooling) are always located along regions in which undissolved cementite particles (highlighted with yellow circles in Figure 4.11b and yellow arrows in Figure 4.11c) are visible at few nanometers. This supports the fact that thermodynamically, ferrite-cementite boundaries are the most favorable nucleation sites for austenite, rather than the ferrite/ferrite grain boundaries [22,45]. Instead, when the A_m temperature is reached there is no thermodynamic restriction for nucleation of austenite at ferrite-ferrite boundaries and the austenite growth might change from a carbon diffusion to an interface (massive) controlled mechanism [22]. Nevertheless, the comparative analysis of the calculated A_m and the A_{C3} temperatures obtained by dilatometry (Figure 4.2), indicates that austenite transformation was not complete upon heating when the A_m temperature was

selected as peak temperature in both steels. Thus, it can be inferred that the ferritic bands obtained in both steels annealed at A_m temperature with heating rates of 100 and 1000 °C/s (Figures 4.3c and 4.3e) are composed of both, undissolved ferrite and ferrite produced by massive transformation of austenite during cooling. In addition, ferrite can also be expected to be formed by diffusional mechanisms, which is facilitated by the decrease of the PAGs size and local chemical heterogeneities in the parent austenite [7].

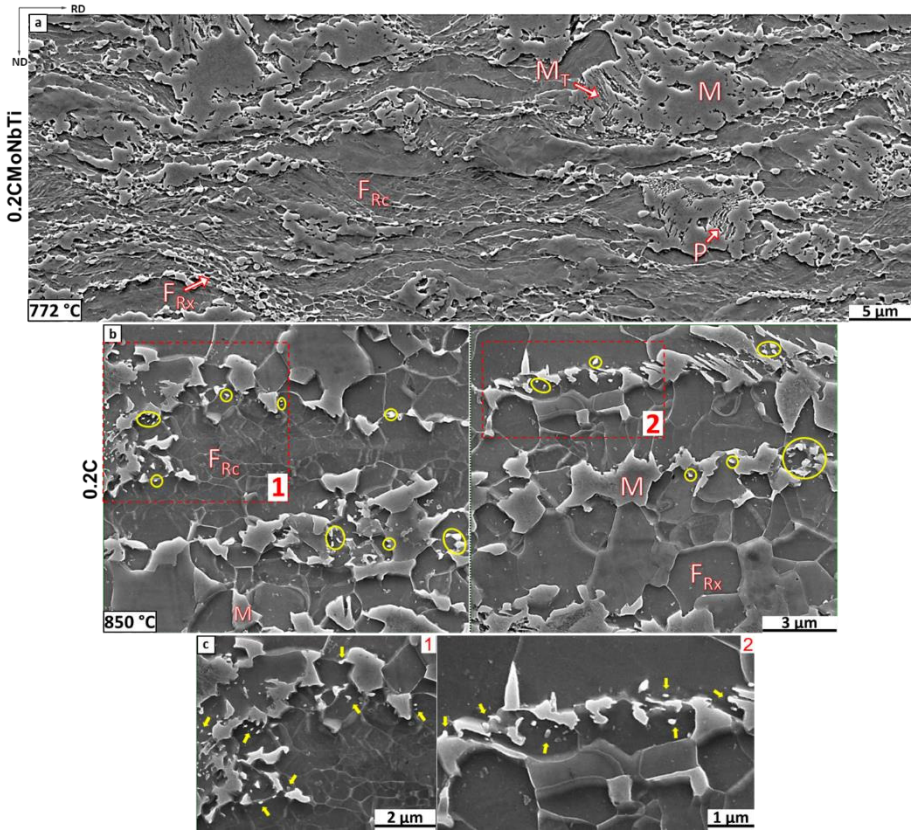

Figure 4.11: Microstructures obtained by interrupted heating at 1000 °C/s followed by cooling at 160 °C/s. a) Alloy 0.2CMoNbTi heated up to 772 °C. b) Alloy 0.2C heated up to 850 °C. c) Enlarged micrographs of the selected areas 1 and 2 enclosed by red dashed squares in Figure 4.11b. Undissolved cementite particles are enclosed by yellow circles in Figure 4.11b and pointed by yellow arrows in Figure 4.11c.

Complete austenite formation was obtained by the increase of the peak temperature to 950 °C (Figures 4.2 and 4.3). Despite the heating rate, a ferrite fraction lower than 1% was obtained in the alloy 0.2CMoNbTi and the ferrite content was increased from 10 (obtained at 10 °C/s) to ~20% (100-1000 °C/s) for the alloy 0.2C. The addition of 0.3% of Mo shows a strong influence on the hardenability of the steel 0.2CMoNbTi, in which the formation of ferrite was effectively suppressed after quenching of a fully

austenitic microstructure produced under ultrafast heating (Figures 4.3d and 4.3f). This finding provides valuable information for the alloying design and tailoring the microstructures of steels treated via ultrafast annealing process. Furthermore, the Nb microalloying might also contribute to the hardenability of the alloy 0.2CMoNbTi by solute drag effect and the influence of Nb precipitates retarding the austenite decomposition [48–50].

Eq. (4.1) [48] indicates that for a defined austenitic grain geometry (which determines the proportionality parameter K), the number of effective nucleation sites, expressed as the density of grain corners (n_n, in m^{-3}), is enlarged by a reduction of the average PAG size (d_γ, in m). Then, a larger fraction of ferrite (or bainite) can be expected to be formed in ultrafast annealing experiments due to the increment on the nucleation sites by reduction of the PAG size (Figures 4.6 and 4.7). Additionally, carbon and substitutional solute atoms depleted regions are prone to be transformed to ferrite/bainite upon quenching, increasing the chance to obtain austenite decomposition even at high cooling rates, as applied in this study (160 °C/s).

$$n_n = \frac{K}{d_\gamma^3} \tag{4.1}$$

Regarding the grain size distribution, the additions of Mo, Nb and Ti have shown to be effective in controlling the austenite grain size. PAGs and martensitic block length sizes obtained at 10 °C/s for the alloy 0.2CMoNbTi were equivalent to the values reached in the samples of the 0.2C steel heat treated by UFH at 1000 °C/s (Figures 4.7a and 4.7c). TEM analysis of the cold-rolled 0.2CMoNbTi steel revealed that fine precipitates of size 2 to 20 nm were homogeneously distributed through the microstructure (Figure 4.12a). The indexed diffraction pattern inserted in Figure 4.12a in combination with the EDX spectra presented in Figure 4.12b confirmed that those precipitates are NbC-type carbides with a cubic crystal lattice. Additionally, cubic-shaped TiNb-carbonitrides (Figure 4.12c) were also detected. In Figure 4.12d, an equilibrium phase calculation performed with Thermo-Calc indicates that ~0.043% of Nb-rich and ~0.023% of Ti-rich precipitates might be obtained in the 0.2CMoNbTi steel at room temperature. With the increase of the temperature, the calculated equilibrium fraction of Nb-rich precipitates remains nearly constant up to 970 °C and exponentially decreases to 0 at 1258 °C, instead, the fraction of Ti-rich precipitates decreases just above 1260 °C. Thus, as the precipitates are stable at the selected peak temperatures (915 and 950 °C), it can be argued that the Zener-Smith pining effect [14,16] of those thermodynamically stable Nb and Ti-rich precipitates has a strong influence on the ferrite recrystallization and austenite grain growth. Considering the kinetics of grain growth in the austenitic field under continuous heating [51], it is important to mention that when the heating rate increases, both the thermal gap between the experimentally determined A_{C3} and the peak

temperature 950 °C (Figure 4.2) and the time involved in the annealing process are considerably reduced. Thus, it is expected to obtain austenitic grain refinement under fast annealing treatments as it was discussed in [11].

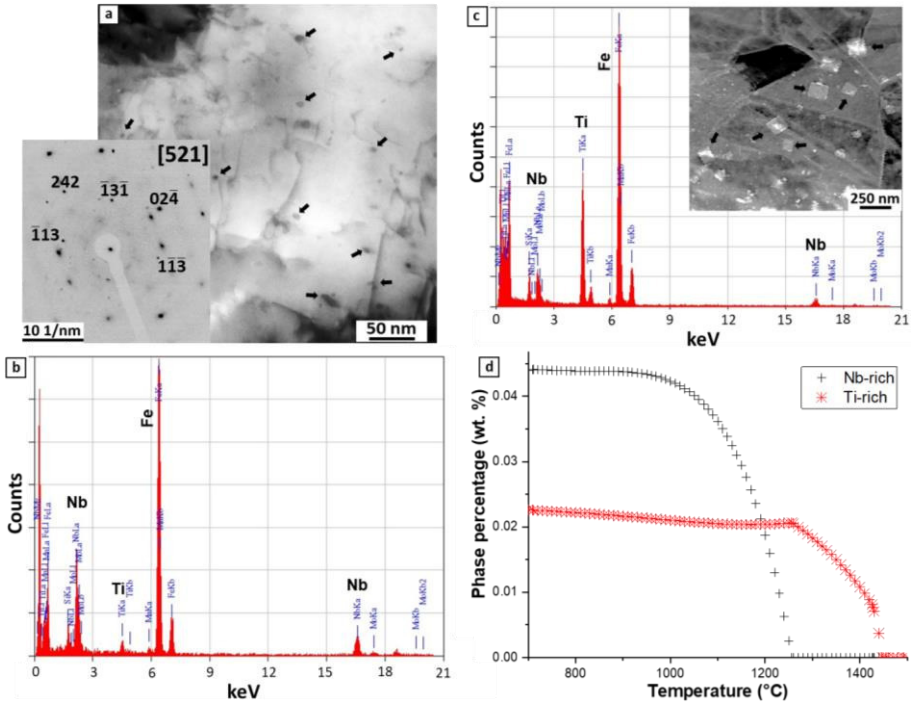

Figure 4.12: Characterization of precipitates in the alloy 0.2CMoNbTi. a) TEM bright-field (BF) image and indexed diffraction pattern of the cubic lattice NbC precipitates (zone axis: [521]). b) EDX spectra of the NbC precipitates. c) EDX spectra and BF-TEM image of the TiNb-carbonitrides. d) Equilibrium weight percentage of Nb-rich and Ti-rich precipitates as a function of the temperature calculated with Thermo-Calc. Several precipitates are pointed by black arrows in Figures 4.12a and 4.12c. The TEM characterization was performed on samples in the as-rolled condition (i.e. before ultrafast heating).

4.4.2 The effect of alloying composition and peak annealing parameters on the microstructure-mechanical properties relationship

Figures 4.8 and 4.9 summarize the mechanical properties of the 0.2C steel and 0.2CMoNbTi steel heated at 10, 100 and 1000 °C/s. In experiments performed at 10 °C/s complete austenite transformation was obtained in both steels annealed at the A_m and 950 °C (the selected peak temperatures are above the determined A_{C3}, Figure 4.2b). Both alloys display similar mechanical responses, developed by comparable microstructural characteristics and base alloy composition. Even though about ~9% of fine allotriomorph ferritic grains were obtained in the 0.2C steel, the overall mechanical behavior was governed by a martensitic matrix. The σ_{ys} of the

0.2CMoNbTi was about ~30 MPa higher than the obtained in the 0.2C steel and a similar trend is seen for the σ_{UTS} values (Figures 4.9a and 4.9b). The increment of the peak temperature causes a small reduction of both, σ_{ys} and σ_{UTS}. As the strengthening of martensite follows the Hall-Petch relationship [52,53], and this relationship has been also proved for the PAGs size [54], the small grains obtained in the alloy 0.2MoNbTi (Figure 4.7) might lead to a σ_{ys} and σ_{UTS} that are slightly higher than the ones obtained in the alloy 0.2C. Additionally, the precipitation hardening effect [15] produced by NbC nano-carbides and the absence of soft ferrite grains can explain the higher strength of the alloy 0.2CMoNbTi. On the other hand, the relatively small differences that were obtained for the $\varepsilon_{Uniform}$ and ε_{Total} values, where the ferritic grains nucleated at PAGs boundaries might contribute to the improvement of the ductility of the 0.2C steel (Figures 4.9c and 4.9d).

At heating rates ≥100 °C/s, the σ_{ys} and σ_{UTS} were lower than the ones measured at 10 °C/s for the alloy 0.2C treated at both peak temperatures (with exception of the σ_{UTS} obtained for the sample heated at 100 °C/s to 950 °C, being similar to the one obtained at 10 °C/s). Even though the ferrite fraction in the sample 0.2C annealed with a heating rate of 100 °C/s to 950 °C was higher than the one heated at 10 °C/s (Table 4.3), the measured tensile properties were similar. The reduction of the martensite grain size observed at 100 °C/s with respect to the sample heated at 10 °C/s (Figures 4.7a and 4.7c) could produce an increment in strength of the former via Hall-Petch effect. Moreover, the small ferritic grains (with an average size of 2μm) nucleated at prior grain boundaries and constrained by martensitic regions (Figures 4.3b and 4.3d) have not led to a decrease in strength, but the $\varepsilon_{Uniform}$ was slightly improved in the sample heated at 100 °C/s. The σ_{ys} and σ_{UTS} values were about 300 and 100 MPa lower than the measured for the conventionally treated samples, but at the same time, the $\varepsilon_{Uniform}$ was improved in the samples processed with high heating rates. The larger fraction of ferrite obtained in ultrafast annealing experiments than in the conventional treatment (Table 4.3) is responsible for the reduction in strength and the enhancing of the uniform elongation in the 0.2C steel. Furthermore, the presence of retained austenite grains may contribute to the increase of strain response via transformation-induced plasticity (TRIP) effect [55]. The samples heated to the A_m temperature exhibited higher $\varepsilon_{Uniform}$ than the samples treated at 950 °C due to the larger fraction of ferrite obtained after the peak annealing treatments. Nevertheless, the ε_{Total} values revealed an opposite effect, decreasing from 18% to 12% in the alloy 0.2C when the heating rate increased from 10 to 1000 °C/s. These results suggest that the formation of microstructural banding composed of ferrite and high carbon martensite (Figure 4.5) in high heating rates experiments has a detrimental effect on the ductility of the studied steels. As in Dual-Phase steels [56,57], during the initial states of straining the majority of deformation is distributed among the ferrite grains, but when the strain is transferred to the high carbon martensite regions (which in this case represent the major fraction in the microstructure for the studied steel) a brittle response is

produced, conducing to the loss of toughness and total ductility observed in the alloy 0.2C [58]. Since ferrite is present in the microstructure at PAGs boundaries or forming bands of isolated islands, its contribution to the total elongation is not like the expected to be obtained from the formation of an interconnected shell-core ferritic/martensitic microstructure [19,59].

Additionally, it is proposed that the formation of a larger fraction of bainitic ferrite could take place during the cooling of the alloy 0.2C treated at 1000 °C/s to 950 °C due to the local and micro-scale (chemical banding) chemical heterogeneities in the parent austenite, conducing in that way to the observed reduction in strength (σ_{ys} and σ_{UTS}) and increment in $\varepsilon_{Uniform}$ of this sample in comparison with the samples treated at 10 and 100 °C/s to 950 °C (Figures 4.8b, 4.9a and 4.9b).

On the other hand, the alloy 0.2CMoNbTi also exhibited a decrease of total elongation of about 17% when the heating rate increased from 10 to 100-1000 °C/s, where the microstructural banding also shows an apparent disadvantageous effect. The formation of banded microstructures might induce anisotropic flow behavior [60] producing the loss of ductility observed in samples treated by ultrafast heating. Nevertheless, the overall mechanical behavior of the alloy 0.2CMoNbTi remains practically unaltered despite the heating rate.

4.5 Conclusions

The effect of the heating rates of 10, 100 and 1000 °C/s and peak temperatures of A_m and 950 °C on the microstructure and related mechanical properties in a low-alloy steel with and without microalloying with carbide-forming elements was analyzed. The main conclusions from this study are:

- The increase in the heating rate produces parent austenite grain refinement in both steels, being prominent in the alloy 0.2C. Weak influence of the heating rate on the grain refinement was obtained in the range 100 – 1000 °C/s.
- The obtained microconstituents distribution after the proposed heat treatments is affected by both heating rate and peak temperature. At the A_m temperature, both steels show incomplete austenite transformation at heating rates of 100 and 1000 °C/s, resulting in an increase of the ferrite fraction after cooling. A decrease in the ferrite fraction was obtained rising the peak temperature to 950 °C (i.e. above the A_{C3}) due to complete ferrite to austenite transformation upon heating. The increase in the peak temperature also leads to non-isothermal austenitic grain growth.
- The initial microstructural banding has an important influence on the developed microstructure after the ultrafast heating approach. Despite the peak temperature, the formation of microstructural banding is more likely to occur at high heating rates due to preferential austenite nucleation and suppressed chemical homogenization during the annealing process.

- A less sensitive material to the influence of the heating rate was obtained by adding Mo, Nb and Ti, suppressing the ferrite formation during cooling in ultrafast heating experiments. Additional grain refinement is also achieved in the alloy 0.2CMoNbTi by the pinning effect of nano-carbides against the austenitic boundary motion. The formation of a similar distribution of microconstituents after the peak annealing treatments led to equivalent mechanical behavior in the Mo-Nb-Ti alloyed steel.
- The mechanical behavior of the samples heated at 10 °C/s is governed by the strengthening characteristics of a mainly martensitic microstructure, showing similar tensile properties in both steels due to almost the same base alloy content. At high heating rates, the decrease of σ_{ys} and σ_{UTS} values in the 0.2C steel is associated with the presence of isolated regions of ferrite in a martensitic matrix. At the same time, a global improvement in the uniform elongation is observed, whereas total elongation values do not show an improvement, being affected by the existence of brittle high carbon content martensite regions.

References

[1] J. Zhao, Z. Jiang, Thermomechanical processing of advanced high strength steels, Prog. Mater. Sci. 94 (2018) 174–242. https://doi.org/10.1016/j.pmatsci.2018.01.006.

[2] D.K. Matlock, S. Kang, E. De Moor, J.G. Speer, Applications of rapid thermal processing to advanced high strength sheet steel developments, Mater. Charact. 166 (2020) 110397. https://doi.org/10.1016/j.matchar.2020.110397.

[3] F.M. Castro Cerda, F. Vercruysse, C. Goulas, B. Schulz, R.H. Petrov, 'Flash' Annealing in a Cold-Rolled Low Carbon Steel Alloyed With Cr, Mn, Mo, and Nb: Part I - Continuous Phase Transformations, Steel Res. Int. 90 (2019) 1–11. https://doi.org/10.1002/srin.201800098.

[4] F. Vercruysse, F.M. Castro Cerda, P. Verleysen, R.H. Petrov, Behavior of ultrafast annealed advanced high strength steels under static and dynamic conditions, Mater. Sci. Eng. A. 780 (2020) 139168. https://doi.org/10.1016/j.msea.2020.139168.

[5] M.A. Valdes-Tabernero, F. Vercruysse, I. Sabirov, R.H. Petrov, M.A. Monclus, J.M. Molina-Aldareguia, Effect of Ultrafast Heating on the Properties of the Microconstituents in a Low-Carbon Steel, Metall. Mater. Trans. A Phys. Metall. Mater. Sci. 49 (2018) 3145–3150. https://doi.org/10.1007/s11661-018-4658-4.

[6] T. Lolla, G. Cola, B. Narayanan, B. Alexandrov, S.S. Babu, Development of rapid heating and cooling (flash processing) process to produce advanced high strength steel microstructures, Mater. Sci. Technol. 27 (2011) 863–875. https://doi.org/10.1179/174328409X433813.

[7] A. Banis, E.I. Hernandez-Duran, V. Bliznuk, I. Sabirov, R.H. Petrov, S. Papaefthymiou, The effect of ultra-fast heating on the microstructure, grain size and texture

evolution of a commercial low-c, medium-Mn DP steel, Metals (Basel). 9 (2019). https://doi.org/10.3390/met9080877.

[8] D. De Knijf, A. Puype, C. Föjer, R. Petrov, The influence of ultra-fast annealing prior to quenching and partitioning on the microstructure and mechanical properties, Mater. Sci. Eng. A. 627 (2015) 182–190. https://doi.org/10.1016/j.msea.2014.12.118.

[9] G. Liu, S. Zhang, J. Li, J. Wang, Q. Meng, Fast-heating for intercritical annealing of cold-rolled quenching and partitioning steel, Mater. Sci. Eng. A. 669 (2016) 387–395. https://doi.org/10.1016/j.msea.2016.05.106.

[10] J. Dai, Q. Meng, H. Zheng, An innovative pathway to produce high-performance quenching and partitioning steel through ultra-fast full austenitization annealing, Mater. Today Commun. 25 (2020) 101272. https://doi.org/10.1016/j.mtcomm.2020.101272.

[11] E.I. Hernandez-Duran, T. Ros-Yanez, F.M. Castro-Cerda, R.H. Petrov, The influence of the heating rate on the microstructure and mechanical properties of a peak annealed quenched and partitioned steel, Mater. Sci. Eng. A. 797 (2020) 140061. https://doi.org/10.1016/j.msea.2020.140061.

[12] F.M. Castro Cerda, B. Schulz, D. Celentano, A. Monsalve, I. Sabirov, R.H. Petrov, Exploring the microstructure and tensile properties of cold-rolled low and medium carbon steels after ultrafast heating and quenching, Mater. Sci. Eng. A. 745 (2019) 509–516. https://doi.org/10.1016/j.msea.2018.12.036.

[13] F. Castro-Cerda, Third Generation Advanced High Strength Steels via Ultrafast Heating, Ph. D. Thesis, Ghent University, Gent, Belgium, 2017. https://doi.org/D/2017/10.500/13.

[14] C.J. Tweed, B. Ralph, N. Hansen, The pinning by particles of low and high angle grain boundaries during grain growth, Acta Metall. 32 (1984) 1407–1414. https://doi.org/10.1016/0001-6160(84)90086-5.

[15] C. Klinkenberg, K. Hulka, W. Bleck, Niobium carbide precipitation in microalloyed steel, Steel Res. Int. 75 (2004) 744–752. https://doi.org/10.1002/srin.200405837.

[16] T.T. Gladman, D. Dulieu, Grain-Size Control in Steels, Met. Sci. 8 (1974) 167–176. https://doi.org/10.1179/msc.1974.8.1.167.

[17] M.A. Valdes-Tabernero, R.H. Petrov, M.A. Monclus, J.M. Molina-Aldareguia, I. Sabirov, The effect of soaking time after ultrafast heating on the microstructure and mechanical behavior of a low carbon steel, Mater. Sci. Eng. A. 765 (2019) 138276. https://doi.org/10.1016/j.msea.2019.138276.

[18] F.M. Castro Cerda, C. Goulas, I. Sabirov, L.A.I. Kestens, R.H. Petrov, The effect of the pre-heating stage on the microstructure and texture of a cold rolled FeCMnAlSi steel under conventional and ultrafast heating, Mater. Charact. 130 (2017) 188–197. https://doi.org/10.1016/j.matchar.2017.06.010.

[19] J. Dai, Q. Meng, H. Zheng, High-strength dual-phase steel produced through fast-heating annealing method, Results Mater. 5 (2020) 100069.

https://doi.org/10.1016/j.rinma.2020.100069.

[20] F.M. Castro Cerda, L.A.I. Kestens, R.H. Petrov, “Flash” Annealing in a Cold-Rolled Low Carbon Steel Alloyed with Cr, Mn, Mo, and Nb: Part II—Anisothermal Recrystallization and Transformation Textures, Steel Res. Int. 90 (2019) 1–13. https://doi.org/10.1002/srin.201800277.

[21] F.G. Caballero, C. Capdevila, C.G. De Andrés, An attempt to establish the variables that most directly influence the austenite formation process in steels, ISIJ Int. 43 (2003) 726–735. https://doi.org/10.2355/isijinternational.43.726.

[22] F.M. Castro Cerda, I. Sabirov, C. Goulas, J. Sietsma, A. Monsalve, R.H. Petrov, Austenite formation in 0.2% C and 0.45% C steels under conventional and ultrafast heating, Mater. Des. 116 (2017) 448–460. https://doi.org/10.1016/j.matdes.2016.12.009.

[23] L.S. Thomas, D.K. Matlock, Formation of Banded Microstructures with Rapid Intercritical Annealing of Cold-Rolled Sheet Steel, Metall. Mater. Trans. A Phys. Metall. Mater. Sci. 49 (2018) 4456–4473. https://doi.org/10.1007/s11661-018-4742-9.

[24] M. Hamzeh, A. Kermanpur, A. Najafizadeh, Fabrication of the ultrafine-grained ferrite with good resistance to grain growth and evaluation of its tensile properties, Mater. Sci. Eng. A. 593 (2014) 24–30. https://doi.org/10.1016/j.msea.2013.09.026.

[25] G. Kurdjumow, G. Sachs, Der Mechanismus der Stahlhärtung, Naturwissenschaften. 18 (1930) 534. https://doi.org/10.1007/BF01513427.

[26] E. Gomes, L.A.I. Kestens, Fully automated orientation relationship calculation and prior austenite reconstruction by random walk clustering, IOP Conf. Ser. Mater. Sci. Eng. 82 (2015) 3–7. https://doi.org/10.1088/1757-899X/82/1/012059.

[27] C.F. Jatczak, Retained austenite and its measurement by X-ray diffraction, SAE Tech. Pap. 89 (1980) 1657–1676. https://doi.org/10.4271/800426.

[28] R.H. Petrov, L.A.I. Kestens, Advanced High-Strength Steels: Electron Backscatter Diffraction (EBSD), Encycl. Iron, Steel, Their Alloy. (2015) 46–69. https://doi.org/10.1081/E-EISA-120050786.

[29] P.T. Pinard, A. Schwedt, A. Ramazani, U. Prahl, S. Richter, Characterization of dual-phase steel microstructure by combined submicrometer EBSD and EPMA carbon measurements, Microsc. Microanal. 19 (2013) 996–1006. https://doi.org/10.1017/S1431927613001554.

[30] N. Takayama, G. Miyamoto, T. Furuhara, Effects of transformation temperature on variant pairing of bainitic ferrite in low carbon steel, Acta Mater. 60 (2012) 2387–2396. https://doi.org/10.1016/j.actamat.2011.12.018.

[31] S.N. Panpurin, N.Y. Zolotorevsky, Y.F. Titovets, A.A. Zisman, E.I. Khlusova, Crystallographic features of low-carbon bainite formed under non-isothermal conditions, Mater. Sci. Forum. 762 (2013) 110–115. https://doi.org/10.4028/www.scientific.net/MSF.762.110.

[32] F.M. Castro Cerda, F. Vercruysse, T.N. Minh, L. Kestens, A. Monsalve, R. Petrov, The

Effect of Heating Rate on the Recrystallization Behavior in Cold Rolled Ultra Low Carbon Steel, Steel Res. Int. 88 (2017) 1–9. https://doi.org/10.1002/srin.201600351.

[33] K. Albutt, S. Garber, Effect of heating rate on the elevation of the critical temperatures of low-carbon mild steel, J. Iron Steel Inst. 204 (1966) 1217–1222.

[34] A. Banis, M. Bouzouni, E. Gavalas, S. Papaefthymiou, The formation of a mixed martensitic / bainitic microstructure and the retainment of austenite in a medium-carbon steel during ultra-fast heating, Mater. Today Commun. 26 (2021) 101994. https://doi.org/10.1016/j.mtcomm.2020.101994.

[35] M. Belde, H. Springer, G. Inden, D. Raabe, Multiphase microstructures via confined precipitation and dissolution of vessel phases: Example of austenite in martensitic steel, Acta Mater. 86 (2015) 1–14. https://doi.org/10.1016/j.actamat.2014.11.025.

[36] A. Verdiere, F. Castro Cerda, A. Béjar Llanes, J. Wu, L. Crebolder, R.H. Petrov, Effect of the austenitizing parameters on the microstructure and mechanical properties of 75Cr1 tool steel, Mater. Sci. Eng. A. 785 (2020). https://doi.org/10.1016/j.msea.2020.139331.

[37] F. Forouzan, L. Borasi, E. Vuorinen, F. Mücklich, Optimization of Quenching Temperature to Minimize the Micro Segregation Induced Banding Phenomena in Quenching and Partitioning (Q&P) Steels, Steel Res. Int. 90 (2019) 1–6. https://doi.org/10.1002/srin.201800281.

[38] F. HajyAkbary, J. Sietsma, R.H. Petrov, G. Miyamoto, T. Furuhara, M.J. Santofimia, A quantitative investigation of the effect of Mn segregation on microstructural properties of quenching and partitioning steels, Scr. Mater. 137 (2017) 27–30. https://doi.org/10.1016/j.scriptamat.2017.04.040.

[39] J. Hidalgo, C. Celada-Casero, M.J. Santofimia, Fracture mechanisms and microstructure in a medium Mn quenching and partitioning steel exhibiting macrosegregation, Mater. Sci. Eng. A. 754 (2019) 766–777. https://doi.org/10.1016/j.msea.2019.03.055.

[40] G. Krauss, Solidification , Segregation , and Banding in Carbon and Alloy Steels, Metall. Mater. Trans. B. 34 (2003) 781–792.

[41] S.E. Offerman, N.H. Van Dijk, M.T. Rekveldt, J. Sietsma, S. Van Der Zwaag, Pearlite band formation in hot rolled medium carbon steel, 18 (2002) 297–303. https://doi.org/10.1179/026708301225000752.

[42] F.G. Caballero, A. García-Junceda, C. Capdevila, C.G. De Andrés, Evolution of microstructural banding during the manufacturing process of dual phase steels, Mater. Trans. 47 (2006) 2269–2276. https://doi.org/10.2320/matertrans.47.2269.

[43] P. Uranga, C.S. Takehide, S.J. Yang, Molybdenum alloying in high-performance flat-rolled steel grades, Adv. Manuf. 8 (2020) 15–34. https://doi.org/10.1007/s40436-019-00285-y.

[44] G. Liu, Z. Dai, Z. Yang, C. Zhang, J. Li, H. Chen, Kinetic transitions and Mn partitioning during austenite growth from a mixture of partitioned cementite and ferrite: Role of heating rate, J. Mater. Sci. Technol. 49 (2020) 70–80.

https://doi.org/10.1016/j.jmst.2020.01.051.

[45] S. Yabu, T. Nishibata, K. Hayashi, Analysis of Preferential Nucleation Sites for Austenite in Deformed Ferrite-pearlite Structure by Experimental and Computational Approaches, Nippon Steel Sumitomo Met. Tech. Rep. 120 (2018) 30–36.

[46] J.J. Yi, I.S. Kim, H.S. Choi, Austenitization during intercritical annealing of an Fe-C-Si-Mn dual-phase steel, Metall. Trans. A. 16 (1985) 1237–1245. https://doi.org/10.1007/BF02670328.

[47] G.R. Speich, V.A. Demarest, R.L. Miller, Formation of Austenite During Intercritical Annealing of Dual-Phase Steels, Metall. Mater. Trans. A. 12 (1981) 1419–1428. https://doi.org/10.1007/BF02643686.

[48] T.A. Kop, P.G.W. Remijn, J. Sietsma, S. Van Der Zwaag, The effect of the austenitisation temperature on the transformation kinetics of an Nb-containing steel, Mater. Sci. Forum. 284–286 (1998) 193–200. https://doi.org/10.4028/www.scientific.net/msf.284-286.193.

[49] Y.J.M. Bréchet, C.R. Hutchinson, H.S. Zurob, C.W. Sinclair, Effect of Nb on ferrite recrystallization and austenite decomposition in microalloyed steels, Steel Res. Int. 78 (2007) 210–215. https://doi.org/10.1002/srin.200705882.

[50] Y. Chen, D. Zhang, Y. Liu, H. Li, D. Xu, Effect of dissolution and precipitation of Nb on the formation of acicular ferrite/bainite ferrite in low-carbon HSLA steels, Mater. Charact. 84 (2013) 232–239. https://doi.org/10.1016/j.matchar.2013.08.005.

[51] J.C. Ion, K.E. Easterling, M.F. Ashby, A second report on diagrams of microstructure and hardness for heat-affected zones in welds, Acta Metall. 32 (1984) 1949–1962. https://doi.org/10.1016/0001-6160(84)90176-7.

[52] C. Du, J.P.M. Hoefnagels, R. Vaes, M.G.D. Geers, Block and sub-block boundary strengthening in lath martensite, Scr. Mater. 116 (2016) 117–121. https://doi.org/10.1016/j.scriptamat.2016.01.043.

[53] T. Swarr, G. Krauss, The effect of structure on the deformation of as-quenched and tempered martensite in an Fe-0.2 pct C alloy, Metall. Trans. A. 7 (1976) 41–48. https://doi.org/10.1007/BF02644037.

[54] S. Morito, H. Yoshida, T. Maki, X. Huang, Effect of block size on the strength of lath martensite in low carbon steels, Mater. Sci. Eng. A. 438–440 (2006) 237–240. https://doi.org/10.1016/j.msea.2005.12.048.

[55] E. Pereloma, A. Gazder, I. Timokhina, Retained Austenite: Transformation-Induced Plasticity, Encycl. Iron, Steel, Their Alloy. (2016) 3088–3103. https://doi.org/10.1081/e-eisa-120049200.

[56] H. Ghassemi-Armaki, R. Maaß, S.P. Bhat, S. Sriram, J.R. Greer, K.S. Kumar, Deformation response of ferrite and martensite in a dual-phase steel, Acta Mater. 62 (2014) 197–211. https://doi.org/10.1016/j.actamat.2013.10.001.

[57] T. Sirinakorn, S. Wongwises, V. Uthaisangsuk, A study of local deformation and damage of dual phase steel, Mater. Des. 64 (2014) 729–742.

https://doi.org/10.1016/j.matdes.2014.08.009.

[58] M. Erdogan, The effect of new ferrite content on the tensile fracture behaviour of dual phase steels, J. Mater. Sci. 37 (2002) 3623–3630. https://doi.org/10.1023/A:1016548922555.

[59] B. Ravi Kumar, N.K. Patel, K. Mukherjee, M. Walunj, G.K. Mandal, T. Venugopalan, Ferrite channel effect on ductility and strain hardenability of ultra high strength dual phase steel, Mater. Sci. Eng. A. 685 (2017) 187–193. https://doi.org/10.1016/j.msea.2017.01.007.

[60] D. Chae, D.A. Koss, A.L. Wilson, P.R. Howell, The effect of microstructural banding on failure initiation of HY-100 steel, Metall. Mater. Trans. A Phys. Metall. Mater. Sci. 31 (2000) 995–1005. https://doi.org/10.1007/s11661-000-0041-2.

Chapter 5

Influence of the heating rate on the microstructure and mechanical properties of peak annealed quenched and partitioned steels[2]

Abstract

In this chapter an Fe-0.28C-1.91Mn-1.44Si cold-rolled steel was subjected to conventional (10 °C/s) and ultrafast (100 °C/s - 700°C/s) heating peak annealing treatments followed by quenching and partitioning (Q&P). The microstructural characterization results showed that grain refinement of the parent austenite and its decomposition products occurred with the increment of the heating rate from 10 °C/s to 100 °C/s, without further refining at 700 °C/s. The formation of complex microstructures after the end of the thermal treatment accompanied by the reduction in the retained austenite carbon content suggested that local chemical heterogeneities in austenite appear upon ultrafast heating. Regardless of the prior heating rate, similar mechanical properties and strain hardening were measured, revealing that both, the microstructure development and the extent of austenite stabilization during quenching and partitioning stage play a fundamental role in the mechanical behavior of the peak annealed Q&P steels.

5.1 Introduction

The progress in steel research proposes that the ratio performance/cost can be substantially improved by the proper design of the thermomechanical processing of low alloy steels [1]. The so-called third-generation of advanced high strength steels (AHSS) exhibits attractive combination of strength and ductility achieved by a proper designing of multiphase microstructures with excellent mechanical response [2,3]. The TRIP-assisted (transformation induced plasticity) and "quenching and partitioning" (Q&P) steel grades [4] offer a variety of microstructural combinations for tailoring the mechanical properties towards several requirements and

[2] This chapter is based on the article: E.I. Hernandez-Duran, T. Ros-Yanez, F.M. Castro-Cerda and R. H. Petrov. The influence of the heating rate on the microstructure and mechanical properties of a peak annealed quenched and partitioned steel. Mat. Sci. & Eng. A, 797 (2020). https://doi.org/10.1016/j.msea.2020.140061

applications [5,6]. The Q&P thermal cycle involves an initial annealing step at the fully austenitic or intercritical temperature range followed by quenching to a certain temperature between the M_s and M_f in order to obtain a specific fraction of martensite. Subsequently, an isothermal step denominated "partitioning" is carried out or at the quenching temperature or at a higher temperature. During the partitioning step, a carbon redistribution from the quenched martensite to the remaining, untransformed, austenite is promoted. This carbon enriched austenite is stabilized at room temperature after final cooling [7]. The typical microstructure in Q&P steel consists of a tempered carbon-depleted martensitic matrix and stabilized carbon-rich retained austenite with different morphologies –bulk (blocky) of film-like situated usually between the martensite laths. In some cases, the low carbon bulk austenite can transform to the so-called "fresh martensite" during the final cooling to room temperature which in general is considered as undesired phase, due to its possible embrittlement effect [8]. Other solid-state reactions, such as carbide precipitation and bainite formation can also be involved during the partitioning step, affecting the retained austenite fraction and the degree of carbon enrichment after the heat treatment [9]. The microstructural design and mechanical behavior of Q&P steels have been widely studied and discussed in terms of phase fraction and retained austenite stability [4,10,11], giving less attention to the influence of the microstructural refinement. Regarding the grain size, thermomechanical processing [12] and thermal cycling strategies [13] have proved that the refinement of the martensitic and austenitic grains have a beneficial effect on the carbon redistribution upon partitioning and hence, on the mechanical behavior of the Q&P steels.

Another relatively new approach towards the third generation AHSS is the ultrafast heating process, which considers the heating of the steel up to the annealing temperature at heating rates ≥100 °C/s, followed by very short (0.2 to 1.5s) soaking and subsequent quench [14,15]. The continuous annealing of low alloy, cold-rolled ferrite-pearlite steels involves several microstructural phenomena: ferrite recovery and recrystallization, cementite spheroidization, austenite nucleation and growth. The degree of interaction of such processes is markedly influenced by the heating rate [16–18]. Even though the contribution of each possible strengthening mechanisms to the overall mechanical behavior is not clear enough, the improvement in the mechanical properties of the ultrafast heated steels is reported to be due to the microstructural grain refinement and local chemical heterogeneities in the austenite that lead to the formation of a large variety of microstructural constituents upon quenching [14,19].

Due to the characteristics of both, ultrafast annealing and Q&P treatments, there are no theoretical, or even practical restrictions for their combination in a single thermal cycle, using the ultrafast heating as the first step, followed by the Q&P process. The available information regarding this specific topic has been reported by De Knijf et al. [20], Liu et al. [21,22] and Dai et al. [23]**.** Although these studies have shown that

the ultrafast heating of Q&P steels produces promising improvement of both strength and ductility compared to conventionally annealed steels, the evaluation of mechanical properties and microstructure in ferrite-free, fully austenitized, peak annealed Q&P steels is still a matter of investigation.

The current study aims to analyze the extent of influence of the prior heating rate on the microstructure development under peak annealing treatments above the intercritical range (i.e. without the presence of proeutectoid ferritic grains) and its relationship with the obtained microconstituents and mechanical behavior after the Q&P heat treatment.

5.2 Experimental

5.2.1 Initial material and heat treatments

A 70% cold-rolled low alloy steel with chemical composition shown in Table 5.1 was investigated. The as-received material is a 70% cold-rolled, 1.2 mm thickness steel with a microstructure consisting of 29% of ferrite and 69 (±3)% of pearlite (Figure 5.1). Equally distributed bands of ferrite and pearlite were found throughout the thickness of the studied material.

Table 5.1: Chemical composition of the studied steel (wt.%).

C	Mn	Si	P	S	Fe
0.28	1.91	1.44	0.009	0.005	Bal.

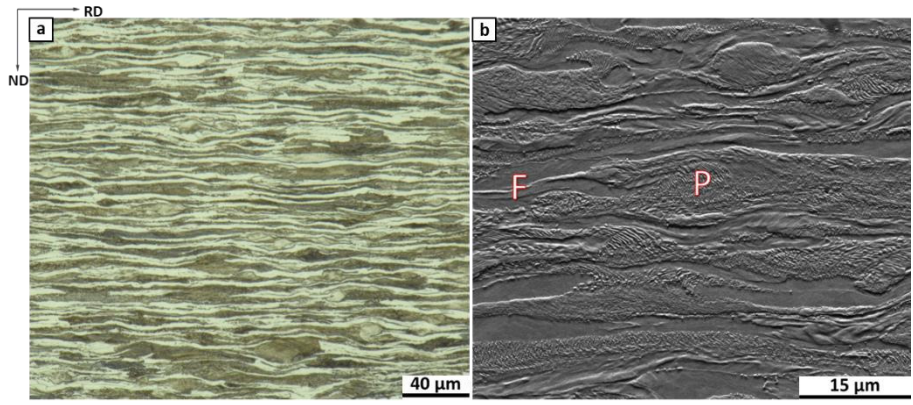

Figure 5.1: (a) Optical and (B) secondary electron (SE) micrographs of the initial condition with a total cold-rolled reduction of 70%.

Dilatometric analysis was employed for determining the quench temperature used in the Q&P treatments. Rectangular specimens of 10x5x1.2 mm^3 were heat-treated in a Bähr 805 A/D dilatometer with a heating rate of 10 °C/s up to 950 °C followed by holding at the peak temperature for 0.2 s, and then cooling to room temperature at 160 °C/s. The martensite volume fraction (Figure 5.2a) formed during the cooling step was calculated by applying the lever ruler method to the obtained

"temperature-dilatation" curve. A quench temperature of 300 °C, corresponding to a ~75% of martensite transformed fraction, was selected for designing the Q&P treatments.

The Q&P heat treatments with three different heating rates were performed using a Gleeble® thermomechanical simulator. Samples of 90 x 20 x 1.2 mm^3 were treated following the thermal treatments presented in Figure 5.2b. A fast cooling rate of 160 °C/s was selected to avoid the formation of ferrite upon quenching. The longest axis of the samples was kept parallel to the rolling direction in both, dilatometry and Gleeble® thermal treatments. The temperature profiles in each cycle were controlled with a type K thermocouple, spot-welded to the geometrical center of samples. Following the methodology presented in [24], a homogeneously treated zone of at least 12 mm length was determined by Vickers hardness measurements around the center of the Gleeble® treated specimens.

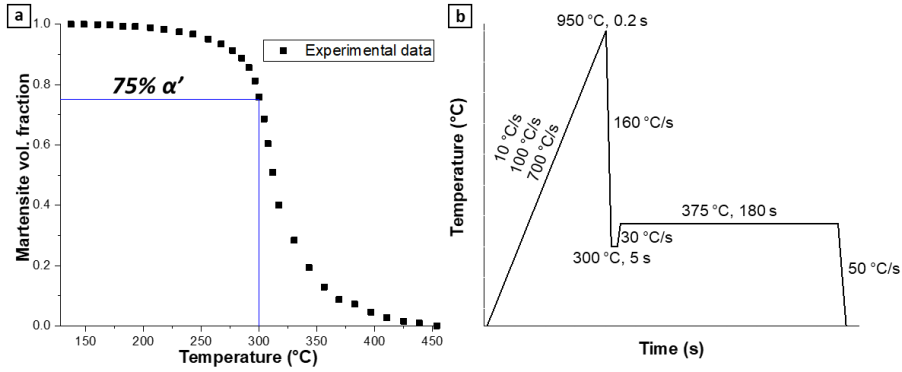

Figure 5.2: (a) Martensite transformation curve obtained during cooling to room temperature after peak annealing treatment at a heating rate of 10 °C/s up to 950 °C. (b) Schematic of the combined peak annealing Q&P heat treatments.

5.2.2 Microstructural characterization

The microstructures were characterized by scanning electron microscopy (SEM), electron backscattered diffraction (EBSD) and X-ray diffraction (XRD) techniques. Samples for metallographic characterization were prepared on the TD plane, at 2 mm from the geometrical center of each heat-treated sample following a classical grinding and polishing sequence with a final step polishing with colloidal silica suspension (OPU) of 0.04 µm. Microconstituents and phases were revealed by chemical etching with 2% nitric acid in ethanol (Nital 2%) for ~4 seconds. SEM and EBSD characterizations were performed in an FEI Quanta 450 FEG-SEM. The etched samples were studied using secondary electron image mode with the SEM operating at 15 kV and a working distance of 10 mm. The EBSD measurements were performed on unetched samples using an accelerating voltage of 20 kV, working distance of 14 mm and sample tilt of 70°. Hexagonal grid scans with step sizes of 50 and 150 nm were recorded for each sample using a Hikari detector operated by the EDAX-TSL

OIM Data Collection v7.3 software. The grain definition was based on a minimum of 5 pixels per grain and misorientation angle of 5°. Pixels with confidence index lower than 0.1 were removed from the acquired EBSD data. The parent austenitic grains (PAGs) were reconstructed from the acquired EBSD data with the method proposed by Gomes and Kestens [25]. A minimum of 7 pixels per grain and misorientation angle of 15° was selected for the PAGs definition. X-ray diffraction (XRD) analysis was performed using a Siemens Kristalloflex D5000 diffractometer equipped with Mo-K_α radiation operated at 40 kV and 40 mA to measure the retained austenite fraction and its carbon content at room temperature. For the X-ray diffraction experiments, the samples were prepared by grinding and polishing on the ND plane. The diffraction patterns were taken from the 2θ range from 25 to 45° with a step size of 0.03°, 20 seconds per step and holder rotation at 15 rpm. Before the X-ray diffraction data analysis, the instrumental background and $K_{\alpha 2}$ radiation were subtracted. The $(200)^{BCC}$, $(211)^{BCC}$, $(220)^{FCC}$ and $(311)^{FCC}$ plane reflections were used to determine the volumetric retained austenite content by the direct comparison method [26]. The retained austenite carbon content (C_γ, in wt. %) was calculated using the Roberts equation [27] (Eq. 5.1) considering the austenite lattice parameter values (a_γ, in Å) measured from the $(220)^{FCC}$ and $(311)^{FCC}$ reflection positions. Two XRD scans were performed per condition to determine the standard deviation of the measured values.

$$a_\gamma = 3.548 + 0.044 C_\gamma \quad (5.1)$$

5.2.3 Mechanical properties

An Instron 5000 tensile testing equipment with a 50kN load cell was used to evaluate the tensile properties. A constant strain rate of 0.001 s^{-1} was applied during testing. Figure 3.6a (see Chapter 3: Experimental procedures) shows the sub-size dog-bone geometry designed according to [28]. The shoulders and gauge length of the tensile specimen lie within the homogeneous heat treated zone obtained after the heat treatments. Two tensile tests were performed per condition. The yield strength was determined by the conventional 0.2% offset method. The strain obtained during the tensile test was measured by 2D-digital image correlation (2D-DIC) and the acquired data was post-processed with the commercial software MatchID. An initial gauge length of 6 mm was digitally selected to evaluate the strain evolution during uniaxial tensile testing.

5.3 Results

5.3.1 Microstructural characterization

The resulting microstructures after the combination of the peak annealing treatments with the subsequent quench to 300 °C and partition step at 375 °C for 180 s are shown in Figure 5.3. Microstructures with a tempered lath martensitic

matrix (labeled as M_T) and comparable distribution of microconstituents are present in steel samples heated at 10 °C/s (Figures 5.3a and 5.3b), 100 °C/s (Figures 5.3c and 5.3d) and 700 °C/s (Figures 5.3e and 5.3f). The green dashed lines displayed in Figures 5.3a, 5.3c and 5.3e enclosed bainitic ferrite (B) regions of size related to the parent austenitic grains (PAGs) are. Those regions are composed by sets of parallel ferritic laths and acicular ferritic grains showing oriented carbides precipitated inside them, which correspond to the microstructural description of bainite. Retained austenite (γ) grains with film (γ_F) and (γ_B) blocky-like morphologies are observed in all conditions. Samples treated at heating rates ≥100 °C/s show non-dissolved spheroidized cementite particles (θ_S) dispersed within the matrix (Figures 5.3d and 5.3f). Regions with non-etched appearance might contain fresh martensite (M_F) [29], that was obtained as result of austenite transformation during the final quenching, after the partitioning step. The increase of the heating rate shows an apparent reduction in the grain size of the microconstituents in the range 10 to 100 °C/s, without additional refinement at 700 °C/s (Figures 5.3a, 5.3c and 5.3e).

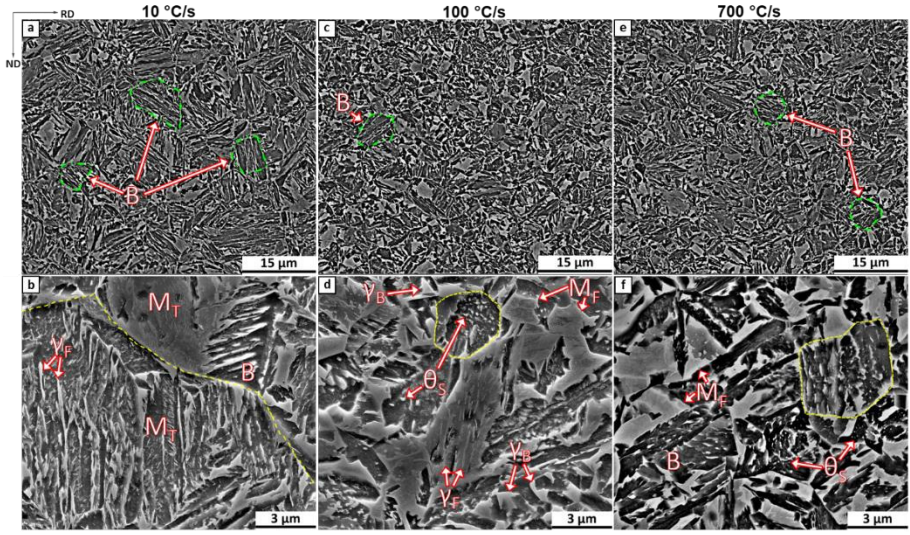

Figure 5.3: Microstructures obtained as a result of the combination of peak annealing treatments with heating rates of (a, b) 10 °C/s, (c, d) 100 °C/s and (e, f) 700 °C/s followed by quenching and partitioning step. Green dashed lines indicate bainitic ferrite regions, whereas yellow lines outline prior austenitic grains.

Due to the complex nature of the developed microstructures, in terms of microconstituents and morphologies, the evaluation of grain size distributions was performed by means of EBSD analysis. The upper row of images in Figure 5.4 shows the image quality (IQ) maps combined with ND inverse pole figures (IPF) of the retained austenite (RA) grains for samples treated at 10 °C/s (Figure 5.4a), 100 °C/s (Figure 5.4c) and 700 °C/s (Figure 5.4e) followed by Q&P. Low (5° to 15°) and high angle (15° to 63°) grain boundaries are outlined in white and black, respectively. The blue boundaries between the retained austenite grains and the transformation

products represent the Kurdjumov-Sachs (K-S) orientation relationship (with a tolerance of 5° from the ideal K-S orientation relationship). Groups of γ grains with the same color in the IPFs belong to the same PAG. The microstructural results show that γ grains with blocky morphology are more likely to be located at parent austenite grain boundaries, whereas films of γ are observed in between martensitic/bainitic blocks. Additionally, it is possible to identify M_F (fresh martensite) from the darker areas on the gray scale IQ maps, which correspond to regions with high density of lattice imperfections [9]. The ND IPF of the reconstructed parent austenite grains for each condition are presented in Figures 5.4b, 5.4d and 5.4f. The EBSD maps show that with the increase of the heating rate the BCC matrix grain size decreases and the retained austenite grains are more homogeneously distributed.

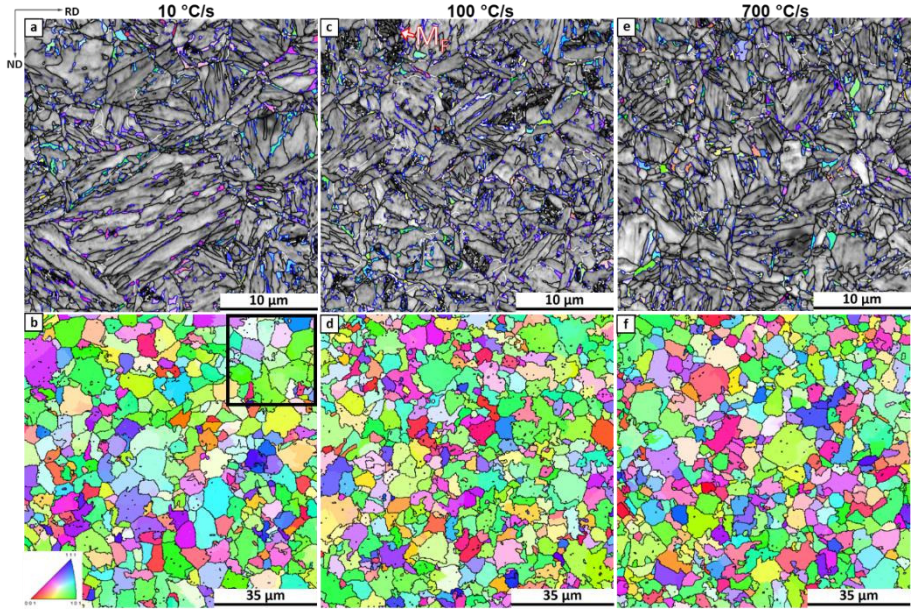

Figure 5.4: (Upper row) EBSD image quality map combined with the ND inverse pole figure of the retained austenite grains and (lower row) ND-IPF of the reconstructed parent austenite grains for the quenched and partitioned steels with previous heating rates of (a, b) 10 °C/s, (c, d) 100 °C/s and (e, f) 700 °C/s. Black lines denote high angle grain boundaries (HAGBs) with misorientation angle between 15° and 63°, whereas white lines indicate low angle grain boundaries (LAGBs) with misorientation between 5° and 15°. The blue grain boundaries in the image quality map define the Kurdjumov-Sachs orientation relationship between BCC and FCC phases. The outlined black square in Figure 5.4b illustrates the size of the area presented in the upper row of images.

The grain size characterization of the martensitic/bainitic matrix (hereinafter referred as to BCC blocks) and retained austenite has been determined by ellipses fitted to the grains due to their non-equiaxed shape, where the mayor axis of the

ellipse correspond to the grain length and the minor axis to the width. A circle geometry was used to define the parent austenite grain (PAG) size diameter.

Figure 5.5 displays the effect of the heating rate on the BCC blocks (Figures 5.5a and 5.5b), γ grains (Figures 5.5c and 5.5d) and PAGs (Figure 5.5e) size distributions. The average grain feature size for each condition is indicated by vertical lines.

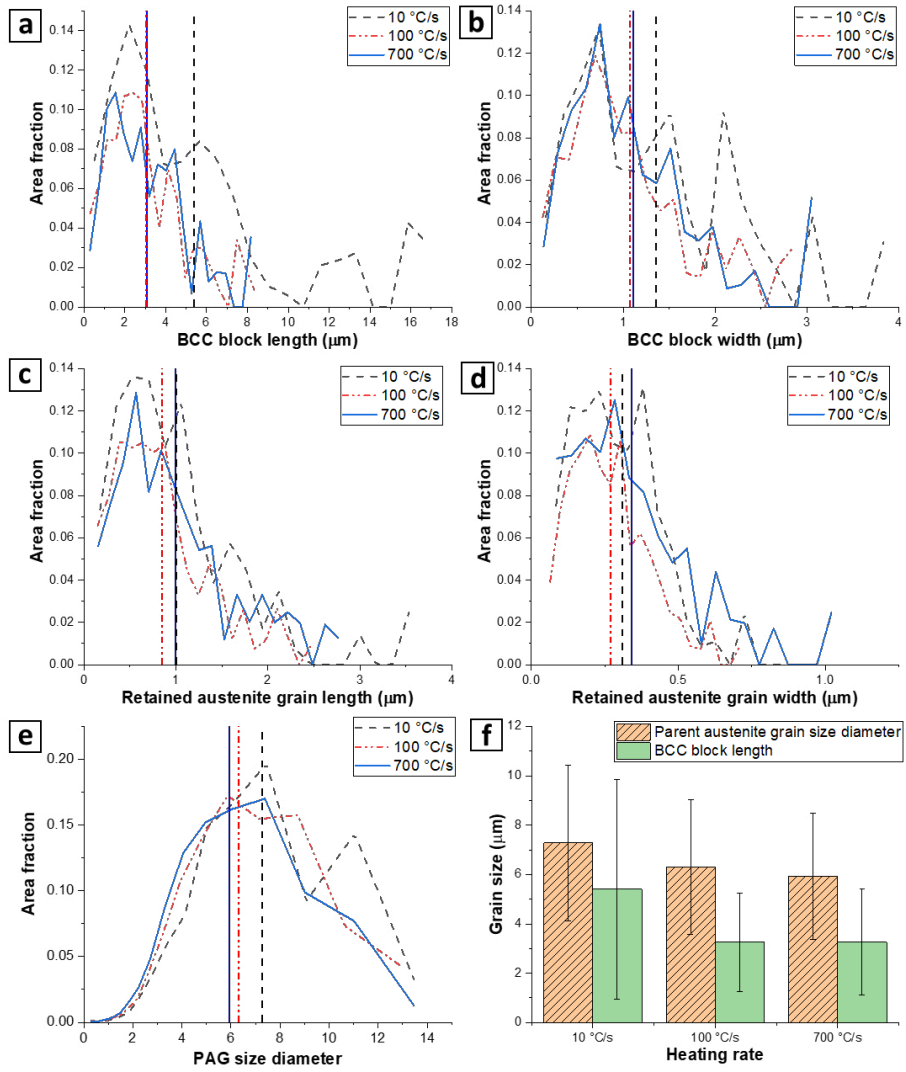

Figure 5.5: Grain size distributions obtained at 10 °C/s, 100 °C/s and 700 °C/s. BCC block (a) length and (b) width distribution. Retained austenite grain (c) length and (d) width distributions. (e) PAGs size diameter distribution. The vertical dashed lines denote the average feature size value for each distribution. (e) Average PAGs size diameter and BCC block length obtained after the proposed heat treatments. Error bars in (f) correspond to the standard deviation of the grain size distributions.

Figures 5.5a and 5.5b show that lower average BCC block length and width that are obtained after increasing the heating rate from 10 to 100 °C/s. Additionally, Figure 5.5b shows that the maximum BCC block length of 16.8 µm, which was obtained with a heating rate of 10 °C/s, is considerably reduced to 8.2 µm at heating rates of 100 °C/s and 700 °C/s and similar block length distributions were achieved in high heating rates experiments. Comparable behavior is observed for the BCC block width results (Figure 5.5c), but the size distributions obtained under ultrafast heating conditions are close to the conventional one. Compared to the microstructure after heating at 10 °C/s, a small decrease in the average BCC grain width of about 0.2 µm was obtained after ultrafast heating. The retained austenite grain size distributions (Figures 5.5c and 5.5d) do not show a significant dependence on the heating rate, reaching a minimum average length of ~0.8 µm after heating at 100 °C/s.

Figure 5.5e confirms that a more uniform distribution PAGs was obtained at high heating rates. The distribution of PAGs at 10 °C/s changes from a bimodal type, with an average grain size of ~7.3 µm, to a grain size distribution close to one maximum for the samples heated at 100 °C/s and 700 °C/s with average PAGs of 6.3 and 5.9 µm, respectively. Figure 5.5f presents a comparison between the average PAGs diameter value and the average BCC block length. As the heating rate increases, the average BCC block length value decreases following the PAGs size evolution.

The microconstituents quantification, obtained after the proposed heat treatments is presented in Table 5.2. The γ fraction was quantified via EBSD and X-ray diffraction measurements and its carbon content was calculated from the X-ray diffraction data. The observed differences in the amount of retained austenite measured by means of EBSD and XRD can be justified by the presence of fine film-like retained austenite with grain size smaller than the selected step size for the EBSD measurement (50 nm in this study) and this phenomenon has been previously reported for Q&P steels [9,13]. Thus, the value of γ obtained by XRD was used for the phase balance. The methodology proposed in [30] was employed to determine the M_F quantification from the EBSD data on the basis of grains with low grain average image quality values.

Table 5.2: Microconstituents quantification and retained austenite carbon content values (standard deviation in parenthesis).

Heating rate, °C/s	M_T Dilatometry, %	M_F EBSD, %	M_T+Bainite EBSD, %	γ EBSD, %	γ XRD, %	γ Carbon content, wt.%
10	75 (2)	3.2 (0.5)	85.1	7.1	10.9 (1.0)	1.44 (0.01)
100	-	9.0 (0.5)	76.9	9.2	12.9 (1.0)	1.35 (0.02)
700	-	2.7 (0.4)	85.6	9.3	12.9 (0.5)	1.39 (0.02)

The results show a slight 11 to 13% increment of the retained austenite fraction with the heating rate increase from 10 °C/s to 100-700 °C/s. The overall carbon content in the γ is reduced from 1.44 wt.% for the sample heated at 10 °C/s to 1.35 wt.% and 1.39 wt.% after heating at 100 and 700 °C/s, respectively. The largest volume of M_F (9%) was obtained for the sample treated at 100 °C/s, which at the same time shows the lowest value of carbon content in γ (1.35 wt.%). Moreover, by combining the phase quantification values from XRD, EBSD and dilatometry a bainite volume of ~10% was calculated for the sample treated at 10 °C/s.

5.3.2 Texture analysis

Figure 5.6 shows the calculated Orientation Distribution Function (ODF) in the φ_2 = 45° section of the Euler space for the BCC crystals of the initial condition and heat-treated samples.

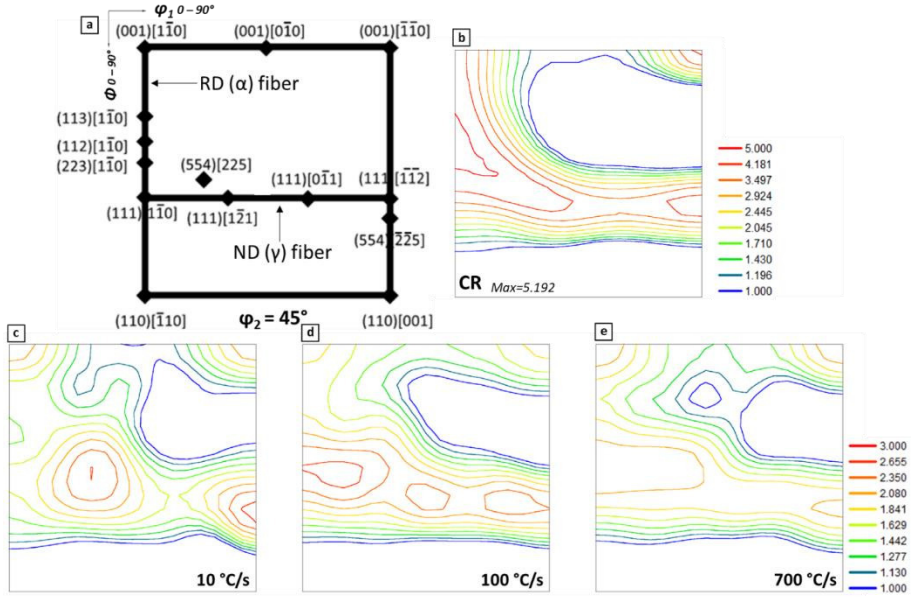

Figure 5.6: Bunge notation orientation distribution function maps (ODF) at Euler space of φ_2 = 45° (constant): (a) main orientation components for rolled BCC crystals, (b) 70% cold-rolled initial material (CR) and heat-treated specimens at (c) 10 °C/s, (d) 100 °C/s and (e) 700 °C/s followed by Q&P step. The ODFs for the heat-treated conditions are plotted with the same iso-intensity scale.

The main texture components for rolled BCC crystals are shown in Figure 5.6a. The ODF for the 70% cold-rolled ferrite-pearlite condition, CR, (Figure 5.6b) is compared with the obtained ODFs for the quenched and partitioned steel treated with heating rates of 10 °C/s (Figure 5.6c), 100 °C/s (Figure 5.6d) and 700 °C/s (Figure 5.6e). The initial cold-rolled sample displays a strong ND-RD texture fiber with maximums on the RD fiber {112}<110>, {223}<110> and ND fiber {554}<225>, {111}<121> and {111}<112> components. The rotated cube component, {001}<110>, appears but

with weaker intensity than the ND-RD components. After quenching and partitioning, the ODF of the sample heated at 10 °C/s (Figure 5.6c) shows weakening of {112}<110> and {223}<110>, and the highest intensity on the {554}<225> and {111}<112> components. With the increase of the heating rate from 10 to 700 °C/s, a progressive weakening of the (554)[225] and (111)[$1\bar{1}2$] components was developed with further recovery of the RD fiber. The acquired ODFs for the samples preheated at 100° C/s and 700 °C/s (Figures 5.6d and 5.6e) present a comparable crystallographic orientation compared to the cold-rolled condition (Figure 5.6b), but with lower intensity and the {001}<110> rotated cube components are also present.

5.3.3 Mechanical properties

The engineering stress-strain curves for the peak annealed treated quenching and partitioning steels are displayed in Figure 5.7a (a summary of the average mechanical properties is given in Table 5.3). After the peak annealing treatments followed by the quenching and partitioning process, the average offset yield strengths (σ_{ys}) and ultimate tensile strengths (σ_{UTS}) are 1106 MPa and 1378 MPa for the steel preheated at 10 °C/s, 1033 MPa and 1394 MPa for the steel heated at 100 °C/s and 1087 MPa and 1376 MPa for the steel heated at 700 °C/s steel. The σ_{ys}/σ_{UTS} varies between 0.74 and 0.80. The average uniform elongation value increases with the heating rate from 7.5 to 9.14% for the samples heated at 10 and 700 °C/s, respectively. The total elongation was similar for the produced steel grades, and it was ~20%. The calculated total absorbed energy, defined as the area under the engineering stress-strain curve, is 256 MJ/m^3, 266 MJ/m^3 and 256 MJ/m^3 for the preheated specimens at 10°C/s, 100°C/s and 700 °C/s, respectively.

Figure 5.7b shows the strain hardening rate versus true strain up to the uniform elongation value for the studied steels. Similar behavior is observed in all studied Q&P steels. The strain hardening rate curves decrease continuously with the true strain up to a strain value of ~0.3. Then, the strain hardening rate curves stabilize, decreasing at slow rate up to the onset of necking.

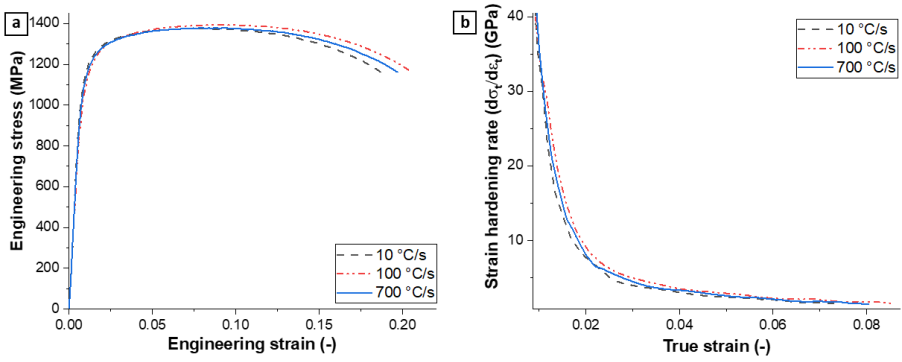

Figure 5.7: (a) Engineering tensile stress-strain curves and (b) instantaneous strain hardening exponent (n value) of the studied steels.

Table 5.3: Tensile properties (standard deviation in parenthesis).

Heating rate, °C/s	σ_{ys} , MPa	σ_{UTS}, MPa	σ_{ys}/σ_{UTS}	$\varepsilon_{Uniform}$, %	ε_{Total}, %	Absorbed energy, MJ/m³
10	1106 (2)	1378 (3)	0.80 (0.005)	7.5 (0.2)	19.9 (0.8)	256 (11)
100	1033 (2)	1394 (19)	0.74 (0.009)	8.7 (0.7)	20.2 (0.1)	266 (3)
700	1087 (5)	1376 (2)	0.79 (0.002)	9.14 (0.1)	19.9 (0.2)	256 (2)

Representative fracture topographies after the uniaxial tensile tests for the treated conditions at 10 °C/s (Figure 5.8a), 100 °C/s (Figure 5.8b) and 700 °C/s (Figure 5.8c) display a ductile type of fracture with a large fraction of microvoids. Fine fine-faceted cleavage zones (indicated by green arrows) and deep dimples are also present in the fracture surfaces.

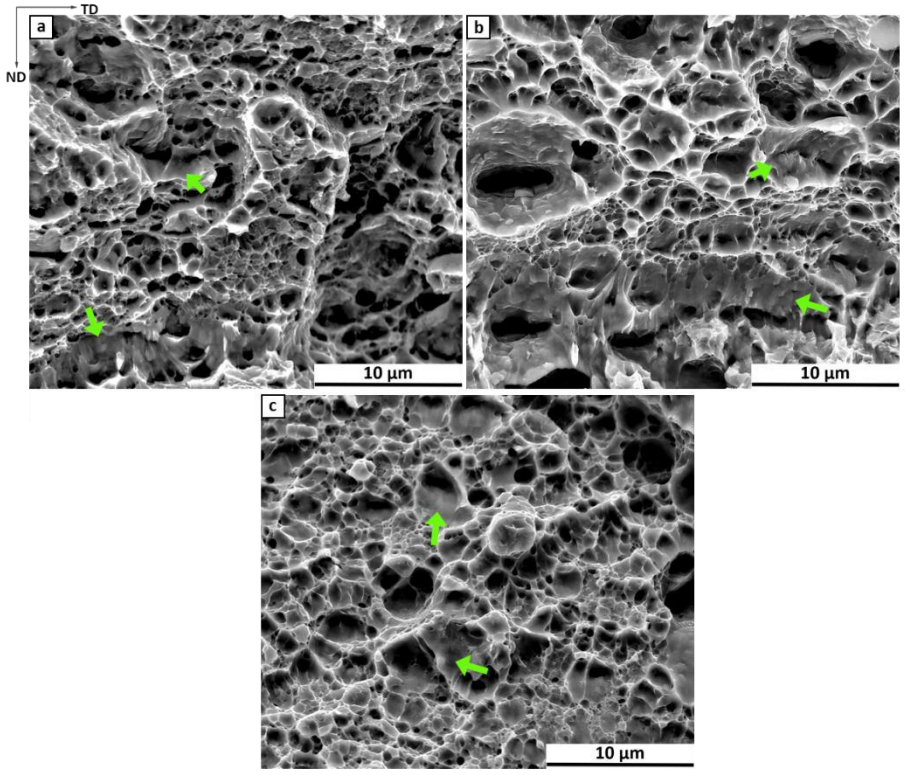

Figure 5.8: Fracture surface after uniaxial tensile test of the Q&P steels heated at (a) 10 °C/s, (b) 100 °C/s and (c) 700 °C/s. Green arrows indicate fine-faceted cleavage zones.

5.4 Discussion

5.4.1 Austenite formation during peak annealing treatment

The microstructural heterogeneity obtained at high heating rates presented in Figure 5.3 accompanied by the refinement of the parent austenite grains and its decomposition products after the peak annealing treatments (Figure 5.5) is directly linked to the mechanisms involved during austenite formation upon heating. Evidence of the microstructural state during austenite nucleation can be obtained from the crystallographic data acquired from the heat-treated samples. The texture memory effect approach [31] provides a systematic description of the F→γ→M transformation. The ODF of the initial 70% cold-rolled sample with ferrite-pearlite microstructure (Figure 5.6b) shows the typical texture components along the ND and RD fibers for cold-rolled low alloy steels [32]. As is shown in Figure 5.6c, after heating at 10 °C/s and subsequent Q&P treatment the texture components on the ND fiber are related to the presence of recrystallized ferrite at the beginning of the austenite nucleation. Due to the ferrite recrystallization during continuous heating at 10 °C/s, the {112}<110> texture component (present in the RD fiber of the initial CR condition) leads to the formation of recrystallized ferrite grains with {111}<112> texture [32]. Moreover, the occurrence of {554}<225> (and orientations on its vicinity as {332}<113>) texture is also related to the recrystallization of grains with {112}<110> texture. The {100}<011> variants present in the heat-treated samples may originate from the {110}<112> and {100}<001> austenite textures, as a result of the austenite transformation upon cooling [33].

Under ultrafast heating (Figures 5.6d and 5.6e) the resulting texture evolves to an orientation distribution similar to the initial cold-rolled state, showing a nearly straight ND fiber after heat treatment. These results suggest the formation of austenite in a non-recrystallized ferrite matrix, as it was previously reported in Refs. [17,20]. The reduction of the ODF intensity after the ultrafast annealing treatments, compared to the cold-rolled condition, is related to multiple nucleation and multiplication of the crystallographic variants –for example, 24 variants if the K-S orientation relationship is assumed for the ferrite-austenite transformation and subsequent austenite transformation to martensite [31].

The non-recrystallized (recovered or deformed) ferritic grains provide multiple nucleation sites for austenite, such as dislocation tangles, walls and shear bands [18,34]. In addition, the increase of the heating rate leads to higher A_{C1} and A_{C3} temperatures [15,16,18–20], and then the austenite formation rate is additionally boosted under ultrafast heating conditions due to the large driving force available for nucleation (larger overheating per unit time), expressed as the difference of the actual and equilibrium temperatures for austenite formation (A_1) [17], thus the density of austenite nuclei is increased.

Since proeutectoid ferrite was not detected after the peak annealing treatments for all conditions (Figure 5.3), it can be concluded that the samples were heated above the A_{C3} temperature even during high heating rates experiments. Thus, the non-isothermal austenite grain growth in the austenitic field might be restricted in high heating rates experiments due to the following reasons: (i) decrease of the thermal gap between the actual A_{C3} and the selected peak temperature with higher heating rates; (ii) constrained austenitic grain growth due the increase of the heating rate which can be described by the following equation [35,36]:

$$g^2 - g_0^2 = k_1 \int_0^{\infty} e^{-Q/RT_{(t)}} dt \qquad (5.2)$$

where g is the mean grain diameter at temperature T (which is function of the time, t), g_0 is the initial mean grain diameter, R is the gas constant, k_1 is a rate constant and Q is the activation energy for grain growth.

Furthermore, the austenitic grain boundary motion can be affected by non-dissolved cementite particles present in the microstructure of samples heated at 100 °C/s (Figure 5.3e) and 700 °C/s (Figure 5.3f). Those carbides can act by Zener pinning effect on the mobility of the austenitic boundaries at high temperature [37]. As a result, a more homogenous and fine distribution of FCC grains was reached under ultrafast heating conditions, i.e. ≥ 100 °C/s, (Figures 5.4 and 5.5). The achieved correlation between the PAGs and BCC length grains sizes presented in Figure 5.5e is in good agreement with results of previously reported data for martensitic microstructures [38,39], where was reported a decrease of the martensitic block sizes as the PAGs are refined.

5.4.2 Microstructural development by combining the ultrafast heating and Q&P processes

Considering the initial 70% cold-rolled ferrite-pearlite structure, the obtained microstructure after the ultrafast heating and very short soaking time will contain local carbon heterogeneities due to the lack of time for homogenization of the parent austenite. During the formation of austenite, the pearlitic colonies will provide higher carbon content to the newly formed austenite in their vicinity than the deformed (or partially recrystallized) ferrite grains, with nearly ~0.006 wt.% carbon content. If the extent of austenite homogenization is not enough upon quenching, as it is in ultrafast heating conditions, the austenitic grains formed at prior ferrite regions will transform to low carbon martensite (or decompose to a ferrite-bainite mixture, as it was reported in [14,23]), whereas the austenite regions near the former pearlite colonies will transform to high carbon content martensite, or even can remain partially untransformed [14]. Hence, the carbon heterogeneities in austenite obtained at high heating rates could give rise to the complex mixture of microconstituents shown in Figure 5.3. Moreover, the decrease in the retained

austenite carbon content in high heating rate experiments (Table 5.2) can be explained by the existence of the undissolved carbides in the microstructure (Figure 5.3), because they reduce the availability of carbon for austenite enrichment during the partitioning step [11], as discussed later in this section. As the rate of dissolution of cementite is a diffusion-controlled reaction [40], a higher fraction of undissolved cementite particles should be expected under ultrafast heating conditions based on the shorter time involved in the annealing process. Conversely, a slightly high amount of retained austenite was obtained at high heating rates, presumably indicative of austenite stabilization upon martensitic (displacive) transformation by parent austenite grain refinement. Figure 5.9 displays the inverse pole figure map and the {001} pole figure (PF) of the BCC grains originating within one PAG for the specimens treated at 10°C/s (Figures 5.9a and 5.9b) and 700 °C/s (Figures 5.9c and 5.9d).

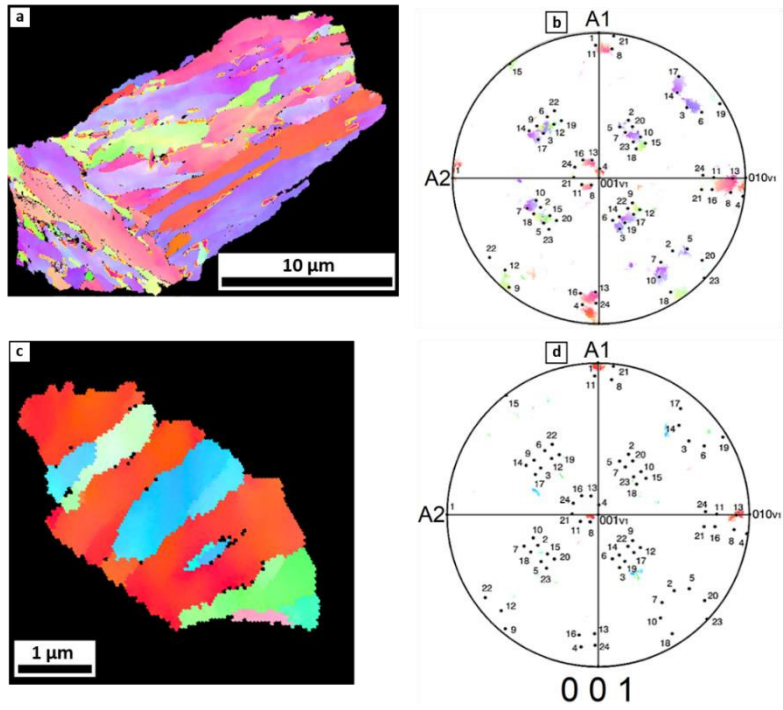

Figure 5.9: Inverse pole figure maps and {001} pole figures of the BCC blocks within one prior austenite grain for the steels heated at (a, b) 10 °C/s and (c, d) 700 °C/s. The experimental pole figures are rotated according to the theoretical K-S orientation relationship pole figure. The solid dots represent the 23 crystallographic variants with respect to variant number 1.

The experimental PF were rotated to overlap the theoretical PF of the Kurdjumov-Sachs (K-S) orientation relationship reproduced from [41]. The color related to the crystal orientation of each block in Figures 5.9a and 5.9c is highlighted on the K-S PF. From Figures 5.9a and 5.9c, it is visible that the BCC blocks are restricted to the PAG size. Groups of parallel elongated blocks form packets in the large PAG obtained at

10 °C/s, whereas the sample treated at 700 °C/s displays a more equiaxed block shape produced by the transformation of the fine-grained parent austenite. The PF for the sample heated at 10 °C/s matches with the theoretical K-S PF, in which several crystallographic variants and the three Bain groups are present (Figure 5.9b). Contrarily, few variants are observed within the fine PAG obtained at 700 °C/s (Figure 5.9c), accompanied by deviation from the theoretical variant locations of the K-S orientation relationship (Figure 5.9d). Thus, additional stabilization of the austenite can occur by reduction of the PAGs in ultrafast heating experiments due to increasing of the strain energy as a result of the restriction to the selection of multiple variants upon martensitic transformation as has been reported elsewhere [39,42].

Regarding the austenite stabilization by carbon partitioning, simulations performed by Celada-Casero et al. [13] have shown that, for a similar fraction of microconstituents, longer partitioning time is required for carbon redistribution between the coarse martensite/austenite grains compared to the fine-grained microstructures. Thus, a more effective carbon partitioning process can be accomplished through a homogeneously distributed mixture of refined microconstituents, as in the ultrafast heated steels microstructures (Figures 5.3 and 5.4). Nevertheless, Figure 5.10a illustrates the microstructural heterogeneities within a parent austenite grain of ~4 μm diameter observed in the sample heated at 100 °C/s followed by Q&P. The partial carbide dissolution and carbon gradients through the parent austenite during the high heating rate annealing allow the stabilization of high carbon austenite formed close to cementite particles upon heating. Additionally, the presence of these undissolved carbides (pointed by green dashed circles in Figure 5.10a) reduces the carbon content of the parent austenite and subsequently, the available carbon for austenite enrichment. Such a decrease in carbon also reduces the driving force for carbon redistribution from martensite to austenite during the partitioning step. The formation of a fresh martensite (M_F)/retained austenite ring-like island (pink dashed lines) within the ~4 μm PAGs is a result of the local carbon gradients through the austenite. Similar M_F/γ ring morphology were found in large PAGs [13,29] due to incomplete homogenization of carbon in austenite during the isothermal holding step. As a result, a stable high carbon layer of austenite is formed close to the initial martensite/austenite interphase and the inner region of the austenitic grain, with low carbon content, decompose to M_F upon quenching (after the partitioning step). Figure 5.10b illustrates the presence of M_F surrounded by γ in two regions of the sample treated at 100 °C/s. The upper row of images shows dark red areas in the IQ map, which is also represented by high misorientation angles in the kernel average misorientation map (KAM) (lower row). Those areas are related to the highly distorted lattice of the high-carbon martensite, M_F. The light red matrix in the IQ map correspond to carbon depleted martensite, M_T, which is represented by blue regions in the KAM map as result of the reduction in the carbon content and recovery of the BCC microstructure during the isothermal holding at 375 °C, which acts as a tempering treatment for the

first formed martensite. The KAM maps also show that the γ grains present a higher density of lattice defects near to the boundary with M_F. This local distortion is the result of the accumulation of dislocations at the interphase RA/M_F due to the strain produced by the volumetric expansion involved during the M_F transformation upon final quenching.

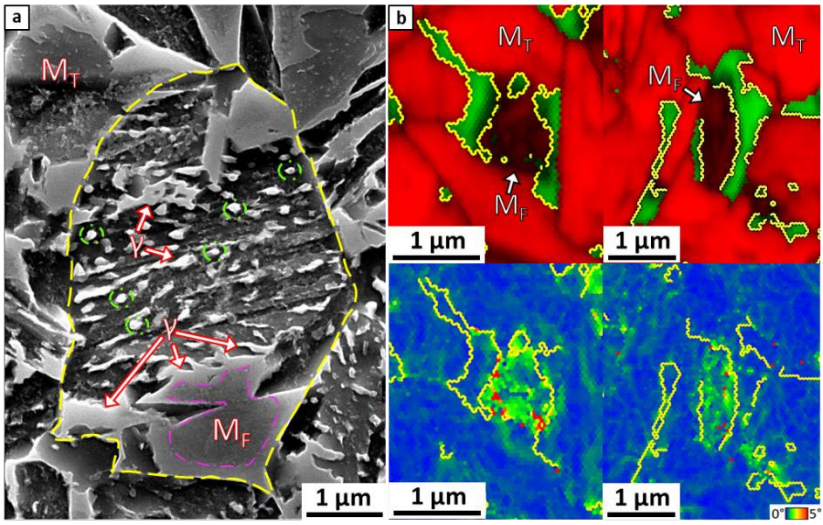

Figure 5.10: SEM and EBSD images of the sample heated at 100 °C/s followed by Q&P. (a) Heterogeneous microstructure within a single parent austenite grain. Some undissolved cementite particles are pointed by green dotted circles. The prior austenite grain and a fresh martensite island (M_F) are outlined by yellow and pink dashed lines, respectively. (b) EBSD maps: (Upper row) Image quality map combined with phase map. Red and green phases correspond to BCC and FCC, respectively. (Lower row) 1st neighbor kernel average misorientation map ranging from 0° to 5°. K-S orientation relationship between BCC and FCC is highlighted by yellow boundaries on the EBSD maps.

Although the formation of bainite during partitioning contributes to the austenite carbon enrichment [9], the analysis of the incidence of each individual microstructural feature on the retained austenite stability is not the scope of this investigation. Furthermore, chemical heterogeneities in the parent austenite might lead to different rates of bainite transformation during the partitioning step, affecting the extent of influence of this particular reaction. The microstructural quantification presented in Table 5.2 shows that the highest fraction of M_F (9%) was obtained in the sample heated at 100 °C/s, which also has the lowest carbon content in γ of 1.35 wt.%. Thus, the decomposition of austenite to bainite during the quenching and partitioning step might be responsible for the decrease in the M_F fraction and higher γ carbon content in the samples heated at 10 °C/s and 700 °C/s. From the mass balance between M_T and M_T+Bainite presented in Table 5.2, the sample heated at 10 °C/s resulted in a microstructure with ~10% of bainite produced by austenite decomposition during the partitioning step. On the other hand, it can be hypothesized that at 700 °C/s the grain refinement of the PAGs and chemical

heterogeneities in austenite might lead to the formation of low hardenability regions which can promote the formation of bainite, producing an increment of the M_T+Bainite compared to the sample treated at 100 °C/s (Table 5.2). The ferritic bands observed in the initial microstructure represent carbon-manganese depleted zones, which are prone to transform into low hardenability austenite, producing a suitable condition for austenite decomposition during the subsequent quench and partitioning step and then, decreasing the available austenite which can be transformed into M_F. Similar phenomena can be inferred from the results presented in [20], where M_F was replaced by the formation of proeutectoid ferrite in a peak annealing experiment performed at 1000 °C/s. Although the specific reason for the increase in the M_F fraction in the sample heated at 100 °C/s followed by Q&P is still a matter of investigation, the microstructural observations suggest that the influence of the refinement of the PAGs on the kinetics of austenite transformation coupled with the micro-segregation are the main factors controlling the microstructure development of ultrafast heated Q&P steels.

5.4.3 Influence of the heating rate on the mechanical properties of the peak annealed Q&P steels

In TRIP-assisted multiphase steels, such as Q&P steels, the mechanical behavior under certain stress-strain condition depends on the composition, fraction, and morphology of their microconstituents, as well as on the ability of the retained austenite to transform to martensite during straining [43]. According to the microstructural analysis, the major constituent in the microstructure of all samples is the partitioned martensite (M_T) (about 75% in the sample heated at 10 °C/s). Therefore, this microconstituent has a major role on mechanical behavior among the other phases. The highest yield strength value was obtained in the sample heated at 10 °C/s, which does not present undissolved cementite particles after heat treatment and has the highest carbon content in the retained austenite. It has been well documented [44–46] that the interstitial solid solution strengthening mechanism and the strain aging by carbon atoms have the major contribution to the mechanical behavior of the martensitic structures in steels. Thus, the increase in the carbon content in the parent austenite, by apparently complete cementite dissolution at 10 °C/s, might lead to higher yield strength by the interaction of a large fraction of carbon atoms with the dislocation structure or carbon in solid solution in the M_T and fresh martensite (M_F) formed after partitioning [47]. Moreover, a high amount of carbon in the initial martensite M_T (at 0 s partitioning) provides the possibility of forming a larger fraction of nanosized transition carbides upon partitioning, increasing the yield strength (YS) by precipitation mechanism [44,46]. On the other hand, the refinement of the BCC blocks at high heating rates should contribute to the increase in strength by grain boundary strengthening mechanism, since the yield strength of martensitic steels follows the Hall-Petch relationship with the block units size [39,46]. As the packet and block lengths are restricted to the PAGs, the

refinement of the parent austenite by ultrafast heating has a direct influence on the yield strength. Additionally, small undissolved carbides obtained under fast heating conditions can act as barriers for dislocation motion, increasing at certain degree the strength [37]. However, similar mechanical results suggest that the obtained decrease of the average grain size (PAG in ~1.4 µm and BCC block length in ~2 µm by increasing the heating rate from 10 to 700 °C/s) has a minor contribution to the strength level by comparison to the other possible active mechanisms. Evaluation of the strength values given in Table 5.3 shows that the lowest σ_{ys} and the highest σ_{UTS} values (1033 MPa and 1394 MPa, respectively) were obtained when the sample was annealed at 100 °C/s. According to the microstructural quantification (Table 5.2), this behavior is related to the highest fraction of M_F presented in that specific specimen. De Knijf et al. [8] have reported that the stresses induced by M_F to the surrounded microstructure, reduce locally the stability of the γ grains (Figure 5.10b), and then those γ grains transform to martensite at low strain resulting in a low σ_{ys} value, as in the sample heated at 100 °C/s. In the same way, the slightly high σ_{UTS} is related to the lower M_T+Bainite fraction obtained after the Q&P step.

The studied Q&P steels display similar work hardening behavior, which is consistent with the comparable fraction of microconstituents obtained after heat treatment. The observed change in the strain hardening rate is related to the contribution of the strain-induced transformation of retained austenite grains during deformation (TRIP effect) to the work hardening of the steel. Similar evolution of the strain hardening has been previously reported for fully austenitized Q&P steels [11]**.** Comparable volume fraction, size and carbon content of the γ grains obtained after the peak annealing Q&P treatments resulted in equivalent strain hardening curves, which suggest that the overall stability of the retained austenite upon deformation is similar for all heat-treated samples. Nevertheless, a slight increase of the uniform elongation value for the specimens treated at high heating rates suggests that the microstructural refinement tends to contribute towards improving the ductility of the peak annealed Q&P steels. The decrease of the BCC blocks size accompanied by a slightly increment of the γ fraction in high heating rate experiments led to a more homogeneous distribution of γ grains within the matrix (Figure 5.4), and then the strain localization is delayed as a result of uniform spreading of deformation from the γ grains to the surrounded BCC blocks during straining. Moreover, the refinement of de PAGs leads to finer BCC blocks (Figure 5.5) producing less accumulation of dislocation at grain boundaries, which in turn increased the required strain for void formation as proposed by Hanamura et al. [48]. In contrast to these results, Dai et al. [23] reported that, compared to a heating rate of 4 °C/s, the ultrafast heating of a 0.18C-1.8Mn-1.4Si Q&P steel resulted in a decrease of 80 MPa in σ_{ys} accompanied by an increase of 32% in total elongation. Those results might be related to a higher ferrite and bainite fraction produced as result of austenite decomposition during cooling, after the peak annealing process and during holding at the partitioning step. Thus, the mechanical properties of peak annealed Q&P

steels could be improved by the formation of a multiphase matrix produced by the proper control of the austenite transformation after the peak annealing step.

The different features in the fracture surfaces (Figure 5.8) are linked to the microconstituents obtained by combining continuous heating and the Q&P processes. The fracture topographies reveal that the damage behavior is governed by a ductile fracture mechanism. The formation of microvoids is mainly related to the interaction of partitioned (tempered) martensite, M_T, and the fresh martensite, M_F, in contact with retained austenite grains during deformation [29]. This interaction leads to the transformation of retained austenite into fine martensite plates, promoting void nucleation. Further ductile fracture formation can be achieved at high heating rates as a result of nucleation and coalescence of microvoids around undissolved cementite particles [46]. The presence of cleavage facets in the fracture surfaces is mainly attributed to crack propagation through brittle high carbon fresh martensite blocks and coarse block-like retained austenite grains, which transform to martensite at low strain levels [49].

5.5 Conclusions

Peak annealing experiments using heating rates of 10, 100 and 700 °C/s above the A_{C3} temperature followed by the quenching and partitioning process have been carried out on a 0.28C-1.91Mn-1.44Si cold-rolled steel with initial microstructure of ferrite and pearlite. The influence of the heating rate prior to quenching and partitioning treatment on the steel microstructure and tensile properties was analyzed.

The results show that:

- The decrease in the average BCC block size is related to the parent austenite refinement in high heating rate experiments. The increment of the heating rate from 10 °C/s to 100 °C/s reduces the average grain size of the transformation products obtained after Q&P in ~2 µm, without further refinement at a heating rate of 700 °C/s. A more homogeneous size distribution of BCC blocks was obtained at high heating rates than at 10 °C/s, accompanied by a reduction in the maximum BCC block length.
- Despite the prior heating rate, the similar work hardening behavior measured for the studied steels is a result of a comparable fraction of microconstituents and composition of the retained austenite grains after the Q&P step. Although heterogeneous and more refined microstructures were obtained under UFH than at 10 °C/s, the strain-induced transformation of retained austenite to martensite seems to determine the strain hardening behavior of the heat-treated steels through deformation.
- As compared to the steel peak annealed at 10 °C/s, the decrease of the transformation products size and the well-dispersed retained austenite grains

within the matrix of the ultrafast heated steels results in a slight improvement of the uniform elongation.

References

[1] J. Zhao, Z. Jiang, Thermomechanical processing of advanced high strength steels, Prog. Mater. Sci. 94 (2018) 174–242. https://doi.org/10.1016/j.pmatsci.2018.01.006.

[2] A. Contreras, A. López, E.J. Gutiérrez, B. Fernández, A. Salinas, R. Deaquino, A. Bedolla, R. Saldaña, I. Reyes, J. Aguilar, R. Cruz, An approach for the design of multiphase advanced high-strength steels based on the behavior of CCT diagrams simulated from the intercritical temperature range, Mater. Sci. Eng. A. 772 (2020). https://doi.org/10.1016/j.msea.2019.138708.

[3] E.A. Ariza-Echeverri, M. Masoumi, A.S. Nishikawa, D.H. Mesa, A.E. Marquez-Rossy, A.P. Tschiptschin, Development of a new generation of quench and partitioning steels: Influence of processing parameters on texture, nanoindentation, and mechanical properties, Mater. Des. 186 (2020) 108329. https://doi.org/10.1016/j.matdes.2019.108329.

[4] D. V. Edmonds, E. de Moor, D.K. Matlock, J.G. Speer, Quenching and Partitioning Steel, Encycl. Iron, Steel, Their Alloy. (2016) 2776–2793. https://doi.org/10.1081/e-eisa-120048860.

[5] B.C. De Cooman, J.G. Speer, Quench and partitioning steel: A new AHSS concept for automotive anti-intrusion applications, Steel Res. Int. 77 (2006) 634–640. https://doi.org/10.1002/srin.200606441.

[6] R.A. Stewart, J.G. Speer, B.G. Thomas, E. De Moor, A.J. Clarke, Quenching and Partitioning of Plate Steels: Partitioning Design Methodology, Metall. Mater. Trans. A Phys. Metall. Mater. Sci. 50 (2019) 4701–4713. https://doi.org/10.1007/s11661-019-05337-3.

[7] J. Speer, D.K. Matlock, B.C. De Cooman, J.G. Schroth, Carbon partitioning into austenite after martensite transformation, Acta Mater. 51 (2003) 2611–2622. https://doi.org/10.1016/S1359-6454(03)00059-4.

[8] D. De Knijf, R. Petrov, C. Föjer, L.A.I. Kestens, Effect of fresh martensite on the stability of retained austenite in quenching and partitioning steel, Mater. Sci. Eng. A. 615 (2014) 107–115. https://doi.org/10.1016/j.msea.2014.07.054.

[9] F. HajyAkbary, J. Sietsma, G. Miyamoto, T. Furuhara, M.J. Santofimia, Interaction of carbon partitioning, carbide precipitation and bainite formation during the Q&P process in a low C steel, Acta Mater. 104 (2016) 72–83. https://doi.org/10.1016/j.actamat.2015.11.032.

[10] X.C. Xiong, B. Chen, M.X. Huang, J.F. Wang, L. Wang, The effect of morphology on the stability of retained austenite in a quenched and partitioned steel, Scr. Mater. 68 (2013) 321–324. https://doi.org/10.1016/j.scriptamat.2012.11.003.

[11] E. De Moor, J.G. Speer, D.K. Matlock, J.-H. Kwak, S.-B. Lee, Effect of Carbon and Manganese on the Quenching and Partitioning Response of CMnSi Steels, ISIJ Int. 51 (2011) 137–144. https://doi.org/10.2355/isijinternational.51.137.

[12] M. Karam-Abian, A. Zarei-Hanzaki, H. Abedi, S. Ghodrat, F. Hajy-Akbary, L. Kestens, The Effect of Martensite-Austenite Constituent Characteristics on the Mechanical Behavior of Quenched-Partitioned Steel at Room Temperature, Steel Res. Int. 90 (2019) 1–8. https://doi.org/10.1002/srin.201800399.

[13] C. Celada-Casero, C. Kwakernaak, J. Sietsma, M.J. Santofimia, The influence of the austenite grain size on the microstructural development during quenching and partitioning processing of a low-carbon steel, Mater. Des. 178 (2019). https://doi.org/10.1016/j.matdes.2019.107847.

[14] F.M. Castro Cerda, B. Schulz, D. Celentano, A. Monsalve, I. Sabirov, R.H. Petrov, Exploring the microstructure and tensile properties of cold-rolled low and medium carbon steels after ultrafast heating and quenching, Mater. Sci. Eng. A. 745 (2019) 509–516. https://doi.org/10.1016/j.msea.2018.12.036.

[15] M.A. Valdes-Tabernero, C. Celada-Casero, I. Sabirov, A. Kumar, R.H. Petrov, The effect of heating rate and soaking time on microstructure of an advanced high strength steel, Mater. Charact. 155 (2019) 109822. https://doi.org/10.1016/j.matchar.2019.109822.

[16] F.M. Castro Cerda, I. Sabirov, C. Goulas, J. Sietsma, A. Monsalve, R.H. Petrov, Austenite formation in 0.2% C and 0.45% C steels under conventional and ultrafast heating, Mater. Des. 116 (2017) 448–460. https://doi.org/10.1016/j.matdes.2016.12.009.

[17] F.M. Castro Cerda, L.A.I. Kestens, R.H. Petrov, “Flash” Annealing in a Cold-Rolled Low Carbon Steel Alloyed with Cr, Mn, Mo, and Nb: Part II—Anisothermal Recrystallization and Transformation Textures, Steel Res. Int. 90 (2019) 1–13. https://doi.org/10.1002/srin.201800277.

[18] L.S. Thomas, D.K. Matlock, Formation of Banded Microstructures with Rapid Intercritical Annealing of Cold-Rolled Sheet Steel, Metall. Mater. Trans. A Phys. Metall. Mater. Sci. 49 (2018) 4456–4473. https://doi.org/10.1007/s11661-018-4742-9.

[19] T. Lolla, G. Cola, B. Narayanan, B. Alexandrov, S.S. Babu, Development of rapid heating and cooling (flash processing) process to produce advanced high strength steel microstructures, Mater. Sci. Technol. 27 (2011) 863–875. https://doi.org/10.1179/174328409X433813.

[20] D. De Knijf, A. Puype, C. Föjer, R. Petrov, The influence of ultra-fast annealing prior to quenching and partitioning on the microstructure and mechanical properties, Mater. Sci. Eng. A. 627 (2015) 182–190. https://doi.org/10.1016/j.msea.2014.12.118.

[21] G. Liu, S.G. Zhang, Q.G. Meng, J. Wang, J. Li, Effect of heating rate on microstructural evolution and mechanical properties of cold-rolled quenching and partitioning steel, Ironmak. Steelmak. 44 (2016) 202–209.

https://doi.org/10.1080/03019233.2016.1209887.

[22] G. Liu, S. Zhang, J. Li, J. Wang, Q. Meng, Fast-heating for intercritical annealing of cold-rolled quenching and partitioning steel, Mater. Sci. Eng. A. 669 (2016) 387–395. https://doi.org/10.1016/j.msea.2016.05.106.

[23] J. Dai, Q. Meng, H. Zheng, An innovative pathway to produce high-performance quenching and partitioning steel through ultra-fast full austenitization annealing, Mater. Today Commun. 25 (2020) 101272. https://doi.org/10.1016/j.mtcomm.2020.101272.

[24] F. Vercruysse, F.M. Castro Cerda, P. Verleysen, R.H. Petrov, Behavior of ultrafast annealed advanced high strength steels under static and dynamic conditions, Mater. Sci. Eng. A. 780 (2020) 139168. https://doi.org/10.1016/j.msea.2020.139168.

[25] E. Gomes, L.A.I. Kestens, Fully automated orientation relationship calculation and prior austenite reconstruction by random walk clustering, IOP Conf. Ser. Mater. Sci. Eng. 82 (2015) 3–7. https://doi.org/10.1088/1757-899X/82/1/012059.

[26] C.F. Jatczak, Retained austenite and its measurement by X-ray diffraction, SAE Tech. Pap. 89 (1980) 1657–1676. https://doi.org/10.4271/800426.

[27] C.S. Roberts, Effect of Carbon on the Volume Fractions and Lattice Parameters Of Retained Austenite and Martensite, J. Met. 5 (1953) 203–204. https://doi.org/10.1007/bf03397477.

[28] P. Verleysen, J. Degrieck, T. Verstraete, Influence of Specimen Geometry on Split Hopkinson Tensile Bar Tests on Sheet Materials, (2008) 587–598. https://doi.org/10.1007/s11340-008-9149-x.

[29] J. Hidalgo, C. Celada-Casero, M.J. Santofimia, Fracture mechanisms and microstructure in a medium Mn quenching and partitioning steel exhibiting macrosegregation, Mater. Sci. Eng. A. 754 (2019) 766–777. https://doi.org/10.1016/j.msea.2019.03.055.

[30] R.H. Petrov, L.A.I. Kestens, Advanced High-Strength Steels: Electron Backscatter Diffraction (EBSD), Encycl. Iron, Steel, Their Alloy. (2015) 46–69. https://doi.org/10.1081/E-EISA-120050786.

[31] L.S. Young, Applications of Texture Analysis Applications of Texture Analysis, John Wiley & Sons, Hoboken, NJ, 2012.

[32] M. Hölscher, D. Raabe, K. Lücke, Rolling and recrystallization textures of bcc steels, Steel Res. 62 (1991) 567–575. https://doi.org/10.1002/srin.199100451.

[33] R.K. Ray, J.J. Jonas, Transformation textures in steels, Int. Mater. Rev. 35 (1990) 1–36. https://doi.org/10.1179/095066090790324046.

[34] D.Z. Yang, E.L. Brown, D.K. Matlock, G. Krauss, Ferrite Recrystallization and Austenite Formation in Cold-Rolled Intercritically Annealed Steel, 16 (1985).

[35] S. Mishra, T. DebRoy, Non-isothermal grain growth in metals and alloys, Mater. Sci. Technol. 22 (2006) 253–278. https://doi.org/10.1179/174328406X84094.

[36] J.C. Ion, K.E. Easterling, M.F. Ashby, A second report on diagrams of microstructure and hardness for heat-affected zones in welds, Acta Metall. 32 (1984) 1949–1962. https://doi.org/10.1016/0001-6160(84)90176-7.

[37] C.J. Tweed, B. Ralph, N. Hansen, The pinning by particles of low and high angle grain boundaries during grain growth, Acta Metall. 32 (1984) 1407–1414. https://doi.org/10.1016/0001-6160(84)90086-5.

[38] T. Maki, K. Tsuzaki, I. Tamura, The Morphology of Microstructure Composed of Lath Martensites in Steels, Trans. Iron Steel Inst. Japan. 20 (1980) 207–214. https://doi.org/10.2355/isijinternational1966.20.207.

[39] Y. Matsuoka, T. Iwasaki, N. Nakada, T. Tsuchiyama, S. Takaki, Effect of Grain Size on Thermal and Mechanical Stability of Austenite in Metastable Austenitic Stainless Steel, ISIJ Int. 53 (2013) 1224–1230. https://doi.org/10.2355/isijinternational.53.1224.

[40] M. Hillert, K. Nilssson, L.-E. Torndahl, Effect of alloying elements on the formation of austenite and dissolution of cementite, J. Iron Steel Inst. 209 (1971) 49–66.

[41] S. Morito, H. Tanaka, R. Konishi, T. Furuhara, T. Maki, The morphology and crystallography of lath martensite in Fe-C alloys, Acta Mater. 51 (2003) 1789–1799. https://doi.org/10.1016/S1359-6454(02)00577-3.

[42] S. Takaki, K. Fukunaga, J. Syarif, T. Tsuchiyama, Effect of grain refinement on thermal stability of metastable austenitic steel, Mater. Trans. 45 (2004) 2245–2251. https://doi.org/10.2320/matertrans.45.2245.

[43] E. Pereloma, A. Gazder, I. Timokhina, Retained Austenite: Transformation-Induced Plasticity, Encycl. Iron, Steel, Their Alloy. (2016) 3088–3103. https://doi.org/10.1081/e-eisa-120049200.

[44] J. Chilton, P. Kelly, The strength of ferrous martensite, Acta Metall. 16 (1968) 637–656. https://doi.org/10.1016/0001-6160(68)90137-5.

[45] G. Krauss, Martensite in steel: Strength and structure, Mater. Sci. Eng. A. 273–275 (1999) 40–57. https://doi.org/10.1016/s0921-5093(99)00288-9.

[46] G. Krauss, Deformation and fracture in martensitic carbon steels tempered at low temperatures, Metall. Mater. Trans. A Phys. Metall. Mater. Sci. 32 (2001) 861–877. https://doi.org/10.1007/s11661-001-0344-y.

[47] F. HajyAkbary, J. Sietsma, G. Miyamoto, N. Kamikawa, R.H. Petrov, T. Furuhara, M.J. Santofimia, Analysis of the mechanical behavior of a 0.3C-1.6Si-3.5Mn (wt%) quenching and partitioning steel, Mater. Sci. Eng. A. 677 (2016) 505–514. https://doi.org/10.1016/j.msea.2016.09.087.

[48] T. Hanamura, S. Torizuka, S. Tamura, S. Enokida, H. Takech, Effect of Austenite Grain Size on Transformation Behavior, Microstructure and Mechanical Properties of 0.1C–5Mn Martensitic Steel, ISIJ Int. 53 (2013) 2218–2225.

[49] Z. Xiong, P.J. Jacques, A. Perlade, T. Pardoen, Ductile and intergranular brittle fracture in a two-step quenching and partitioning steel, Scr. Mater. 157 (2018) 6–9. https://doi.org/10.1016/j.scriptamat.2018.07.030.

Chapter 6

The effect of different annealing strategies on the microstructure development and mechanical response of austempered steels[3]

Abstract

This study focuses on the effect of non-conventional annealing strategies on the microstructure and related mechanical properties of austempered steels. Multistep thermal cycling (TC) and ultrafast heating (UFH) annealing were carried out and compared with the outcome obtained from a conventionally annealed (CA) Fe-0.28C-1.91Mn-1.44Si steel. After the annealing path, steel samples were fast cooled and isothermally treated at 400 °C employing the same parameters. It was found that TC and UFH strategies produce an equivalent level of microstructural refinement. Nevertheless, the obtained microstructure via TC has not led to an improvement of the mechanical properties in comparison with the CA steel. On the other hand, the steel grade produced via a combination of ultrafast heating annealing and austempering exhibits enhanced ductility without decreasing the strength level compared to TC and CA, giving the best strength-ductility balance among the studied steels. The outstanding mechanical response exhibited by the UFH steel is related to the formation of heterogeneous distribution of ferrite, bainite and retained austenite in proportions 0.09-0.78-0.14. The microstructural formation after UFH is discussed in terms of chemical heterogeneities in the parent austenite.

6.1 Introduction

A method commonly employed to achieve suitable strength-ductility balance in steels is microstructural grain refinement [1,2]. Phase transformation of austenite into micro and nanosized lath shape BCC (ferrite-martensite-bainite) sub-units can be attained via heat treatment, controlling the temperature of phase transformation [3–5]. Refinement of the parent austenite grain (PAG) size has been proved as an effective strategy towards fine-grained steel grades [2,6–8]. Among the different

[3] This chapter is based on the article: E.I. Hernandez-Duran, L. Corallo, T. Ros-Yanez, F.M. Castro-Cerda and R.H. Petrov. The effect of different annealing strategies on the microstructure development and mechanical response of austempered steels. Metals, 11, 1041 (2021).
https://doi.org/10.3390/met11071041

methods for grain refinement, the addition of microalloying elements [9] and complex thermo-mechanical treatments [10] are well-known routes to achieve a fine distribution of PAGs and improved mechanical properties in high strength steels.

On the other hand, recent trends in advanced high strength steel production account for the development of lean alloy steels with outstanding mechanical performance reached via novel and efficient heat treatments [11,12]. In order to create retained austenite containing multiphase microstructures, most of the thermo-treatments for the new generation of steels take advantage of the decomposition of austenite and carbon partitioning from bainite and/or martensite [12]. Design and study of bainitic and martensitic based TRIP steels are mainly focused on the evaluation of results obtained by manipulation of low-temperature heat treatment parameters (in the range from 200 to 500 °C), after a conventional annealing step (heating rate from 10 to 30 °C/s and soaking time at annealing temperature >60 sec).

Therefore, unconventional annealing routes could be employed to modify the initial parent austenite phase, resulting in further improvement of the mechanical response of low alloy steels subjected to low-temperature thermal paths. Results in thermal cycling annealing [6–8,13] have shown that multiple annealing and cooling steps, conducing to successive martensite-austenite transformations, are an effective route to obtain a homogeneous distribution of fine-grained PAGs, starting the cycling with a coarse martensitic microstructure.

Another promising annealing route towards the new generation of steels is the ultrafast heating (UFH) [8,14–21]. This strategy represents an optimization of the heat treatment process by employing heating rates ≥100 °C/s, reducing the annealing time from several minutes to a window of 1 to 10 s. Thanks to the development of longitudinal and transverse flux induction heating technologies, the ultrafast heating of steel strips is feasible at small and large scales [17,22,23]. Pilot-scale installations for ultrafast heating applications are reported elsewhere [22,23]. The enhanced combination of mechanical properties in lean alloyed UFH steels is developed through the formation of fine-grained heterogeneous microstructures [8,15–18,24,25]. The microstructural grain refinement reached in ultrafast heating experiments is related to several factors including (i) preferential nucleation of austenite [26,27] and interaction between ferrite recrystallization and austenite phase transformation [20,28]; (ii) pinning effect by undissolved cementite carbides [21]; (iii) restricted austenitic grain growth by the high heating rate employed [29]. Moreover, current research on this topic has confirmed that solute heterogeneities in austenite, produced due to the lack of time for homogenization during the annealing step, are responsible for the formation of a complex mixture of constituents upon cooling [15–17,24,30].

This study aims to evaluate and clarify the influence of different annealing strategies on the microstructure development and related mechanical properties of austempered bainitic steels. Annealing treatments carried out here were designed

to gain insight into the influence of different microstructural characteristics, produced via modification of the initial parent austenite, on the resulting microstructures and mechanical behavior.

6.2 Experimental

6.2.1 Material and heat treatments

A low-alloy steel with composition listed in Table 6.1 is investigated. Figure 6.1 displays the ferritic-pearlitic microstructure of the initial material after cold rolling.

Table 6.1: Chemical composition, wt.%.

C	Mn	Si	P	S	Fe
0.28	1.91	1.44	0.009	0.005	Bal.

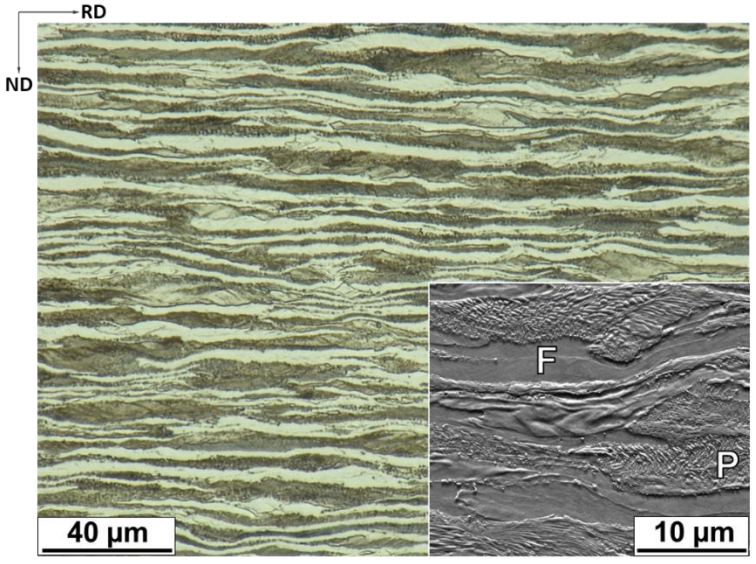

Figure 6.1: Microstructure of the as-received 70% cold-rolled steel.

The as-received material was subjected to three different annealing strategies, namely: conventional (CA), thermal cycling (TC) and ultrafast heating annealing (UFH). Throughout this manuscript, the heat-treated samples will be referred to as CA, TC and UFH based on their annealing history.

Cold-rolled samples of dimensions 10x5x1.2 mm^3 and 90x20x1.2 mm^3, with the largest axis parallel to RD, were heat-treated in a Bähr 805A/D dilatometer and in a Gleeble® 1500 thermo-mechanical simulator, respectively.

The A_{C3} temperature in each annealing treatment was estimated via dilatometric analysis employing the methodology presented in [24]. Samples treated according to the CA treatment were heated at 10 °C/s up to 885 °C, i.e. ~30 °C above the A_{C3}

(≈852 °C), and then soaked for 180 s followed by fast cooling at 160 °C/s. For TC, the first annealing step follows the same parameters as CA, and then three subsequent heating and cooling steps (cycles) were applied. The parameters of each cycle are a constant heating rate of 30 °C/s to 885 °C, soaking time of ~2 s, and cooling at 160 °C/s to room temperature (see the insert in 3a). The A_{C3} for the last annealing step (step 4) was estimated as 855 °C. The A_{C3} temperature for the samples heated at 500 °C/s in dilatometer was estimated as 892 °C. Nevertheless, this value was obtained in samples heated at 500 °C/s up to the A_{C1} temperature (767 °C), then the heating rate declined to ~380 °C/s due to the decrease in efficiency of the longitudinal flux induction heating in dilatometer above the curie point and by the formation of paramagnetic austenite. Previous evaluations of the A_{C3} evolution with the heating rate in cold-rolled low alloy steels [31,32] indicated that the A_{C3} temperature shifts slightly when high heating rates are applied. Thomas [31] reported a shift of 1 to 3 °C of the A_{C3} temperature by increasing the heating rate from 100 °C/s to 1000 °C/s in 1020, 1019M and 15B25 cold-rolled steels. Using the Gleeble® simulator, UFH samples were heated at 500 °C/s up to 925 °C, approximately 30 °C above the A_{C3} estimated by dilatometric analysis. Then, an isothermal holding step not greater than 0.3 s was employed to avoid chemical homogenization and austenitic grain growth at the annealing temperature (see the insert in Figure 6.3b). The selected cooling rate, after the annealing step, was 160 °C/s.

Figures 2a and 2b show the dilatometric curves for CA and TC obtained in samples directly cooled to room temperature and in samples isothermally held at 400 °C. The formation of martensite is clear from the expansion observed below the $M_S^{5\%}$ temperature in the dilatation-change in length v/s temperature curves (Figures 6.2a and 6.2b). In this work, the $M_S^{5\%}$ was defined as the temperature at which a 5% of the total dilatation generated by the martensitic transformation was measured by applying the lever rule method. Since it was not possible to reach a constant heating rate of 500 °C/s in the dilatometer, the M_S temperature for the sample peak annealed at 500 °C/s to 925 °C (UFH) was estimated by means of numerical differentiation of the cooling curves recorded in samples heat-treated using the Gleeble® simulator. Figure 6.2c presents the change in the slope of the cooling curve at low temperature due to the exothermic characteristics of the austenite to martensite transformation. The insert in Figure 6.2c displays the derivate of the cooling curve.

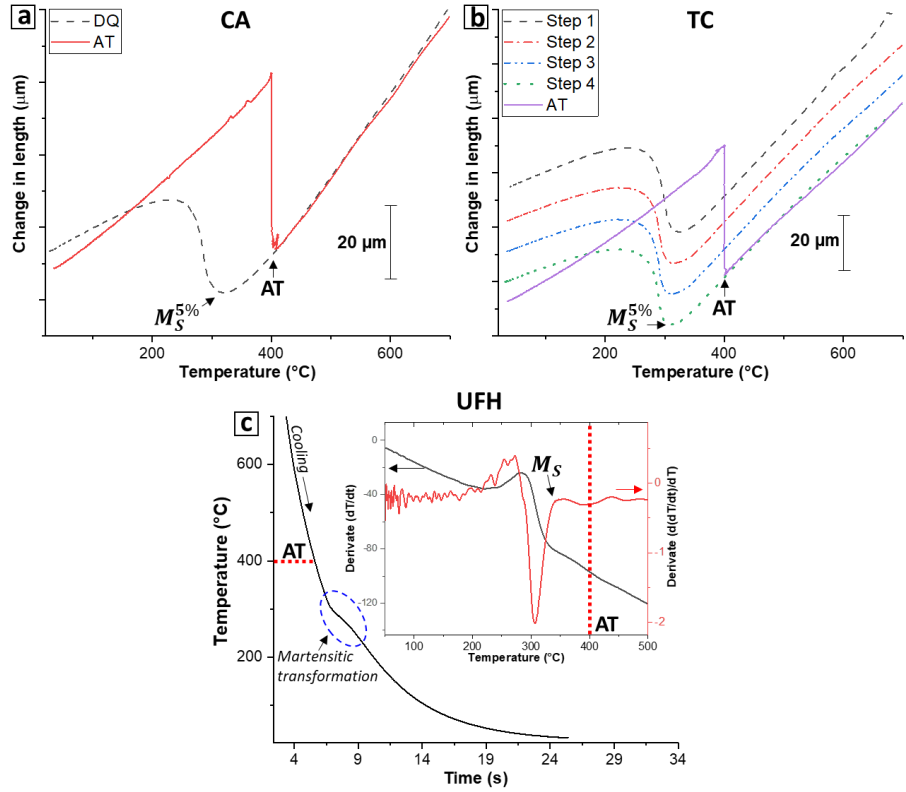

Figure 6.2: Dilatometric curves obtained during the cooling step, i.e. after the annealing treatments for samples (a) CA and (b) TC. (c) Temperature profile obtained during cooling for the ultrafast heated sample; the insert in (c) shows the estimation of the M_S temperature via differentiation of the recorded cooling curve.

M_S temperatures of 346 (±5) °C, 322 (±4) °C and 346 (±8) °C were estimated for CA, TC and UFH, respectively. The values presented in parenthesis correspond to the standard deviation of at least 2 measurements. These experimental results are in good agreement with the calculated M_S of 335 °C [33]:

$$M_s(°C) = 692 - 502C^{0.5} - 37Mn - 14Si \text{ (wt. \%)} \quad (6.1)$$

On the other hand, the dilatation measured during the isothermal step at 400 °C is to a large extent generated by the transformation of austenite to bainite (Figures 6.2a and 6.2b). Based on the dilatometric results, a set of samples were subjected to fast cooling and isothermal holding at 400 °C for 600 s to induce the stabilization of austenite via carbon redistribution during bainite formation [34]. The austempering process (AT) was performed at 400 °C to avoid the formation of martensite upon cooling. In this way, the analyses of competitive reactions typically observed in Q&P steels [35] such as carbon partitioning from martensite to austenite and/or the tempering of martensite during the isothermal step are excluded in this study.

Figures 6.3a and 6.3b display the temperature record of samples heat-treated in the Gleeble® thermomechanical simulator. The temperature was controlled using a K-type thermocouple spot welded to the geometrical center of each sample. Additionally, extra thermocouples were welded at different locations of the sample for measuring possible thermal gradients close to the control thermocouple. Depending on the experimental setup, a small homogeneously-treated zone can be obtained in samples heated by Joule effect (electric resistance heating) in the Gleeble® simulator. Then, to determine the size of this zone, Vickers hardness measurements were made along the RD direction, on the ND plane. A homogeneous zone of at least 12 mm was determined by employing this method. As schematically presented in Figure 3.6 (see Chapter 3: Experimental procedures), samples used for microstructural and mechanical characterization were extracted from the homogeneously treated zone, which is enclosed by dashed lines.

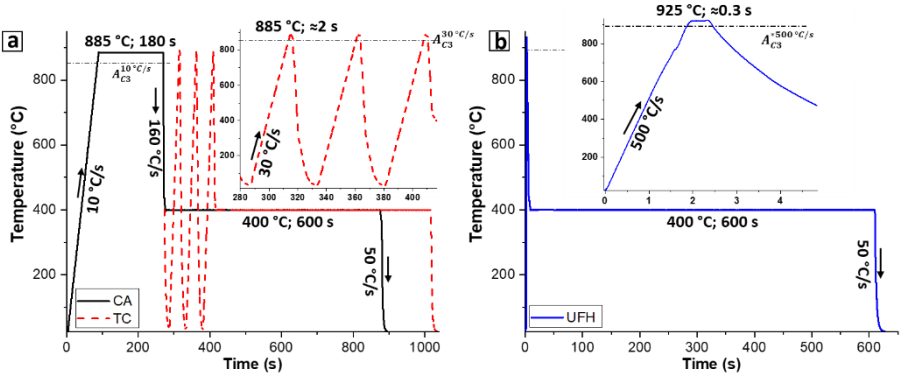

Figure 6.3: Record of the thermal treatments carried out in the Gleeble® simulator: (a) CA and TC samples; (b) UFH sample. The inserts in a and b show the actual temperature recording for the TC and UFH samples, before the austempering step. Horizontal dotted lines denote the A_{C3} temperatures estimated by dilatometry.

6.2.2 Characterization

The microstructures were characterized by means of light optical microscopy (LOM), scanning electron microscopy in secondary electron mode (SE) and electron backscattered diffraction (EBSD). Samples for microstructural characterization were extracted from the region next to the reduced section of the tensile samples. Metallographic examinations were performed on the RD-ND plane. Samples were prepared by grinding and polishing to 0.04 µm colloidal silica suspension (OP-U). LOM micrographs, SE images and EBSD scans were acquired at 280 µm from the sample surface. Image analyses via LOM and SE mode were carried out in samples pre-etched with Nital 2% (2 vol.% HNO_3 in ethanol). A scanning electron microscope FEI Quanta 450 FEG-SEM was used for microstructural characterization. SE images were acquired employing a working distance of 10 mm and an acceleration voltage of 15 kV. EBSD patterns were acquired using pixels with a hexagonal grid, step size

of 120 nm, acceleration voltage of 20 kV, working distance of 14 mm and sample pretilt of 70°. EBSD data acquisition and detector control were operated with EDAX-TSL OIM Data Collection v7.3 software. The acquired data were post-processed using TSL OIM Analysis v7 software. The minimum grain size was defined as 5 pixels per grain and grain misorientation angle of 5°.

Taking advantage of the orientation relationship between bainite and parent austenite [36], parent austenite grains (PAGs) were reconstructed from the measured EBSD data using the computer code developed by Gomes et al. [37]. PAG definition was based on 7 square pixels per grain domain and misorientation of 15°.

Quantification of the amount retained austenite (RA) and the carbon content of austenite were estimated by means of X-ray diffraction (XRD) measurements in a Siemens Kristalloflex D5000 diffractometer (Mo-kα source, operation parameters: 40 kV and 40 mA). Samples cut from the homogenously treated zone were prepared on the RD-TD plane, which is the plane normal to the ND direction (see Figure 3.6). A surface layer of ~300 μm was removed by grinding, followed by repeated polishing and etching steps. XRD patterns were acquired in the 2θ range from 25° to 45° using a step size of 0.03°, dwell time of 20 s and sample holder rotation of 15 rpm. The volume fraction of austenite was determined by the direct comparison method [37] using the integrated area of the $(200)^{BCC}$, $(211)^{BCC}$, $(220)^{FCC}$ and $(311)^{FCC}$ peaks. The retained austenite carbon content was calculated based on the relationship proposed by Roberts [38]:

$$a_\gamma = 3.548 + 0.044C_\gamma \tag{6.2}$$

where a_γ is the lattice parameter (in Å) and C_γ is the austenite carbon content (in wt.%).

6.2.3 Mechanical properties

Tensile tests were performed in an Instron 5000 device imposing a strain rate of 0.001 s^{-1}. Subsize tensile samples of geometry presented in Figure 3.6a were strained at a constant strain rate up to fracture. Two samples were tested for each austempered condition. The strain evolution during testing was locally measured by 2D-digital image correlation. Image analysis and data evaluation were processed with the Match ID software (Version 2018, MatchID, Belgium). An initial gauge length of 6 mm was digitally defined for the strain calculations. Reported yield strength values were based on the 0.2% engineering strain offset. Absorbed energy during uniaxial tensile deformation was calculated as the integrated area under the engineering stress-strain curves. Strain hardening rate was determined as the first derivative of the true stress with respect to the true strain evolution up to necking.

6.3 Results

6.3.1 Microstructures

To evaluate whether ferrite was formed upon cooling, after the annealing steps, an initial microstructural characterization was performed by means of SEM analysis on directly quenched samples (Figure 6.4). The microstructure of direct quench samples consists predominantly of a lath martensitic (M) matrix and allotriomorphic ferritic (F) grains are also distinguished (dark gray grains in Figure 6.4). Ferritic grains of about ~1 µm size are observed at parent austenite grain boundaries in CA (Figure 6.4a) and TC (Figures 6.4b and 6.4e). Widmanstätten ferrite plates (F_W) [38] were also detected in CA (Figure 6.4d). A ferrite fraction lower than 1% was obtained after fast cooling for CA, while 2.5 (±0.5)% of ferrite was quantified for TC. The UFH sample mainly consists of martensite and 8.5 (±0.4)% of ferrite with an average grain size of 1.2 (±0.5) µm (Figure 6.4c). Regions with undissolved spheroidized and lamellar cementite particles (θ) are presented in Figure 6.4f.

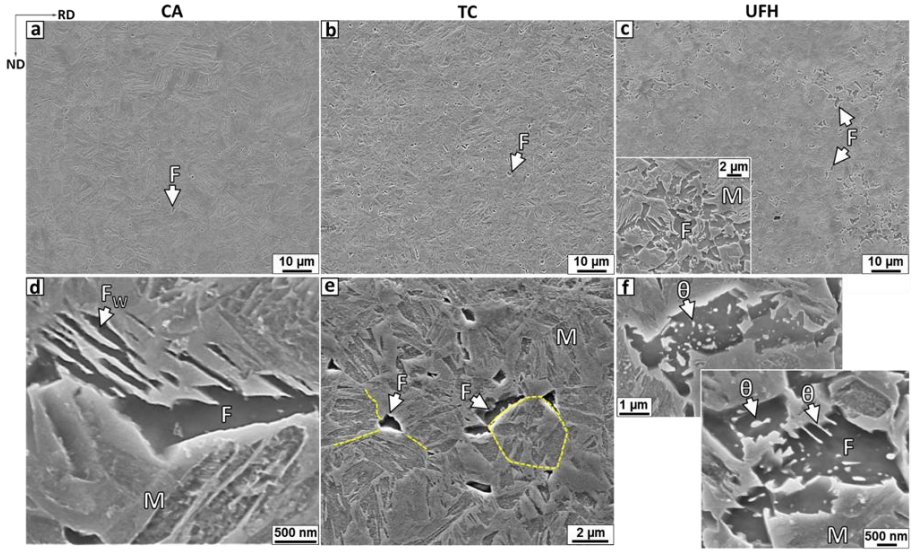

Figure 6.4: Microstructures of samples directly cooled to room temperature after the annealing step. (a-d) CA, (b-e) TC and (c-f) UFH. In (e), prior austenite grain boundaries are highlighted by dashed lines. M: Martensite; F: Ferrite; F_W: Widmanstätten ferrite; θ: Undissolved cementite particles.

Microstructures produced via a combination of the different annealing strategies and austempering at 400 °C are shown in Figure 6.5. Inverse pole figures (IPF) for the reconstructed PAGs are presented in Figures 6.5a to 6.5c. The middle row of images (Figures 6.5d to 6.5f) shows combined EBSD Image quality and phase maps, where retained austenite grains of film (γ_F) and blocky-type (γ_B) morphologies, are highlighted in green. Bainite and ferrite appear light red. Dark-red to black constituents observed in the Image Quality (IQ)-Phase maps presumably correspond

to martensite (M), produced by austenite transformation during the final cooling step [39], after the isothermal holding at 400 °C. The lattice distortion and high dislocation density in martensite decrease the diffraction pattern quality, resulting in a lower and darker IQ scale value than the obtained for the bainitic matrix [39,40]. Based on EBSD-IQ quantification, the amount of martensite was not greater than 1% for all austempered samples. Grain boundaries of misorientation angle between 5-15° and 15-65° are indicated by white and black lines, respectively.

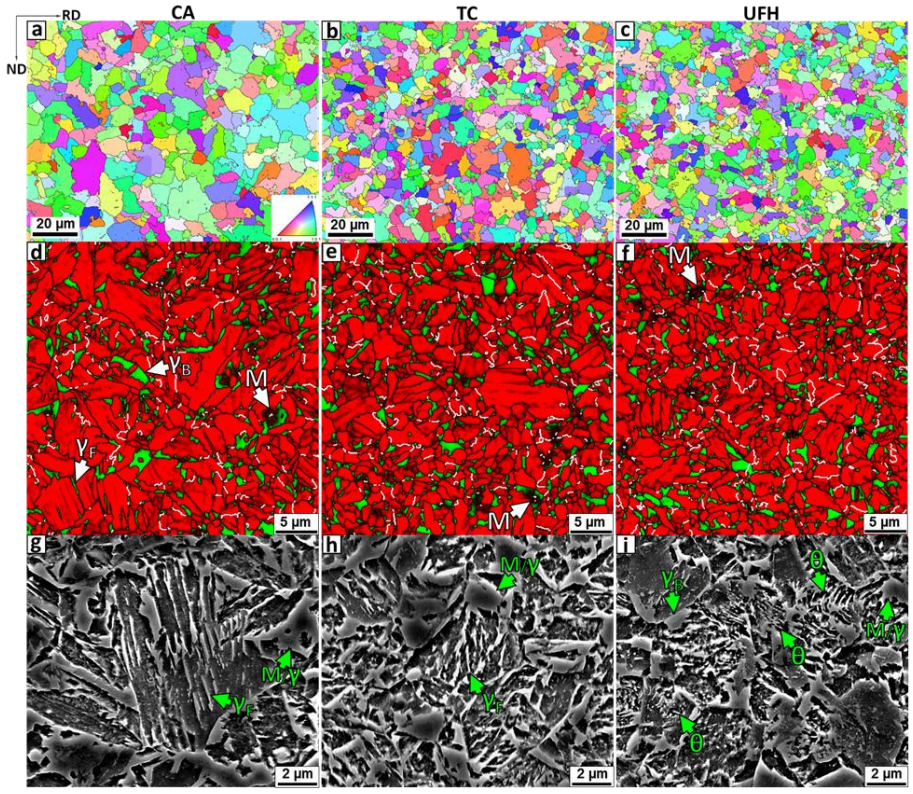

Figure 6.5: (a-d-g) CA, (b-e-h) TC and (c-f-i) UFH. Microstructures obtained after isothermal holding at 400 °C for 600 s: The first row of images presents the inverse pole figure of the reconstructed PAGs. EBDS IQ-Phase maps and secondary electron images are shown in the second and third row of images, respectively. Retained austenite grains (FCC) appear highlighted in green in the combined IQ-Phase maps, while bainite, ferrite and martensite appear red. White and black lines delineate boundaries of misorientation angle between 5-15° and 15-63°, respectively. M: Martensite; γ: Retained austenite of film (γ_F) and blocky-type (γ_B) morphologies. M/γ: martensite-retained austenite constituent; θ: undissolved cementite particles. Note that the magnification increases from the first to the third row of images.

The third row of figures (Figures 6.5g to 6.5i) displays the secondary electron micrographs of the austempered steel grades. A set of parallel bainitic blocks and films of retained austenite are observed in the CA sample (Figure 6.5g). As presented in the EBSD maps, finer microstructures resulted for the steel samples processed via

TC and UFH (Figures 6.5h and 6.5i). Islands with less etched appearance correspond to partially austenitic-martensitic constituents (M/γ) [39]. Those constituents are clearly distinguished in the EBSD IQ-Phase maps, where M is surrounded by retained austenite grains (Figures 6.5d to 6.5f). The formation of M upon the final cooling step arises due to the heterogeneous distribution of carbon in the residual austenite after bainite transformation during austempering [41–43]. In Figure 6.5i, undissolved carbides (θ) are also distinguished.

The amount of retained austenite in austempered samples was quantified via XRD as 14%, 15.3%, and 13.8% for the samples CA, TC and UFH, respectively (Table 6.2). A slightly lower fraction of γ was quantified via EBSD; this is related to non-indexed γ grains with a size smaller than the step size employed for the EBSD data acquisition [18,44].

Table 6.2: Microconstituents quantification (standard deviation).

Sample	*Bainite, %	Ferrite (SEM),%	Martensite (EBSD), %	γ (EBSD), % (0.2)	γ (XRD), % (0.5)	γ carbon content (XRD), wt. %
CA	85.0 (0.5)	<1	<1	11.9	14.0	1.36 (0.02)
TC	82.2 (0.7)	2.5 (0.5)	<1	12.5	15.3	1.33 (0.02)
UFH	77.7 (0.7)	8.5 (0.4)	<1	12.3	13.8	1.40 (0.01)

*Note: Bainite = 100-Ferrite$^{(SEM)}$-Marteniste$^{(EBSD)}$- γ $^{(XRD)}$

The grain size distributions for the austempered steels are presented in Figure 6.6. A marginal difference and equivalent grain distributions were found for samples treated via TC and UFH, while the conventional annealed steel shows larger bainitic blocks and PAGs. Average bainitic block lengths of 5.3 µm, 3.5 µm and 3.4 µm were obtained for samples CA, TC and UFH, respectively (Figure 6.6a). PAG reconstructions also revealed that thermal cycling and ultrafast heating annealing led to grain refinement of the parent austenite and similar grain distributions were obtained after these unconventional types of annealing strategies. Additionally, the narrow distribution of PAGs obtained after TC and UFH is an indication of a more homogeneous distribution of grains (Figure 6.6b). The average reconstructed PAG sizes for samples CA, TC and UFH are 8.6 µm, 5.7 µm and 5.5 µm, respectively. Both grain major axis and grain aspect ratio (minimum grain length/maximum grain length) distributions in γ are not greatly influenced by the prior annealing treatment. An average γ grain major axis between 1.5 µm and 1.8 µm was produced after the combination of the different annealing strategies and subsequent austempering (Figure 6.6c), with the largest distribution of grains for CA. Measured γ grain aspect ratio values display normal distributions with maximum and average close to 0.4, which is related to a rather elongated γ grain shape (Figure 6.6d).

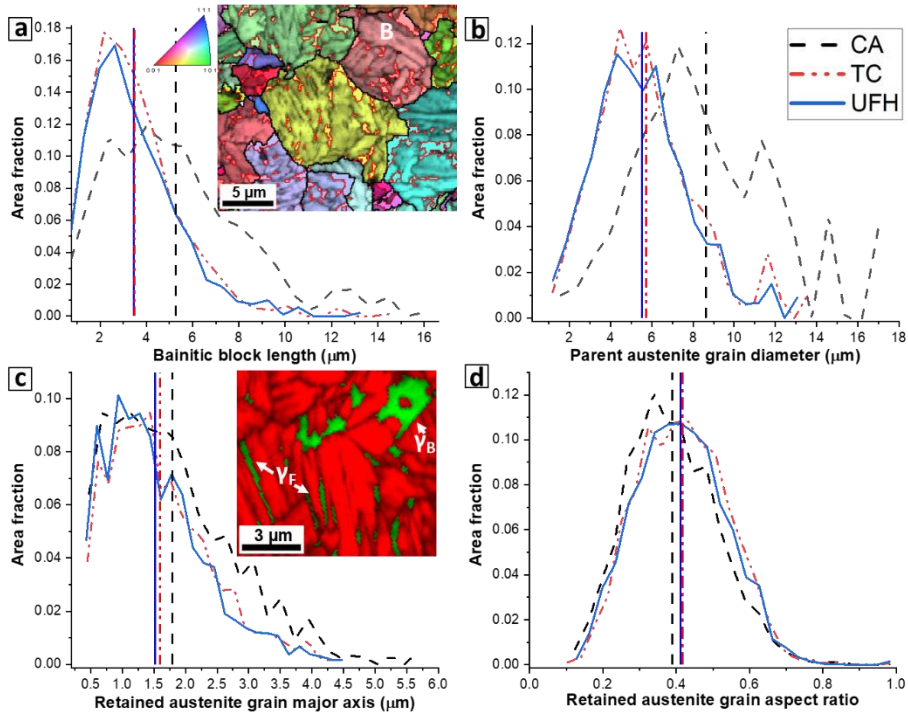

Figure 6.6: Grain size distribution: (a) Bainitic block length. (b) Reconstructed parent austenite grain size diameter. (c) Retained austenite grain major axis. (d) Retained austenite grain aspect ratio. Vertical lines denote the average value for each distribution. In (a), an IPF of reconstructed PAGs is presented together with the respective IQ map of the bainitic blocks (B) formed after austempering for the CA sample. Retained austenite grains are enclosed by red boundaries. Film (γ_F) and blocky-like (γ_B) retained austenite grains are highlighted in (c).

6.3.2 Textures

Texture analysis was carried out to elucidate the influence of the different annealing strategies on the crystallographic orientation of the transformation products in the studied steels. Figure 6.7 presents the orientation distribution functions (ODF) for the as-received cold-rolled material and austempered steels. BCC texture is presented at ϕ_2=45° section of the Euler space and the main texture components of rolled BCC-Iron (Figure 6.7a) are presented for comparison.

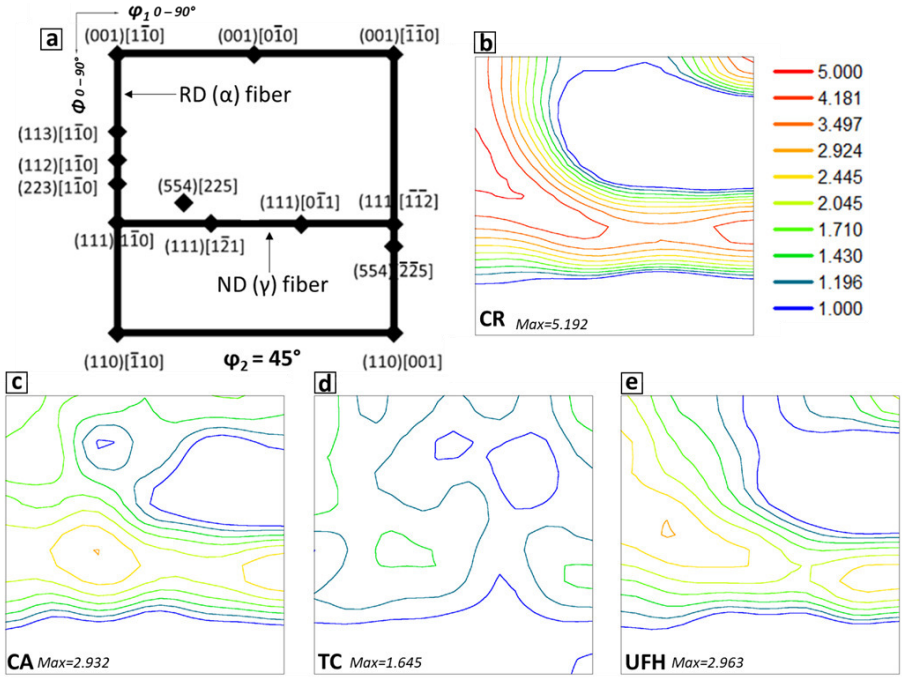

Figure 6.7: ODF at ϕ_2=45° section of the Euler space. (a) Main texture components of rolled BCC crystals. (b) 70% cold-rolled material. (c) CA. (d) TC. (e) UFH. (Scanned area 22500 μm^2).

The as-received material (CR) shows a strong ND-RD texture which is typical for cold-rolled ferritic steels [45] and the rotated cube component {001}<110> (Figure 6.7b). After conventional annealing (Figure 6.7c), the RD texture fiber disappeared and high intensity is observed along with the ND fiber, with local maxima of orientations concentrated close to the {554}<225> and {111}<112> texture components. Thermal cycling led to a maximum intensity of 1.64 multiples of random distribution (mrd) (Figure 6.7d). High intensity is observed close to ND ({554}<225>; {111}<112>) and RD ({112}<110>; {113}<110>) texture components. {001}<110> components are also distinguished after thermal cycling. Texture obtained after UFH resembles the cold-rolled texture with a strong RD-ND type of texture (Figure 6.7e). The convex curvature of the ND fiber in the CR sample is maintained in the ultrafast heated bainitic steel. At the same time, the intensities for RD-ND fibers and {001}<110> texture components are lower than the observed in CR.

6.3.3 Mechanical properties

Tensile engineering stress-strain and strain hardening rate v/s true strain curves are shown in Figures 6.8a and 6.8b, respectively. Mechanical property values are summarized in Table 6.3.

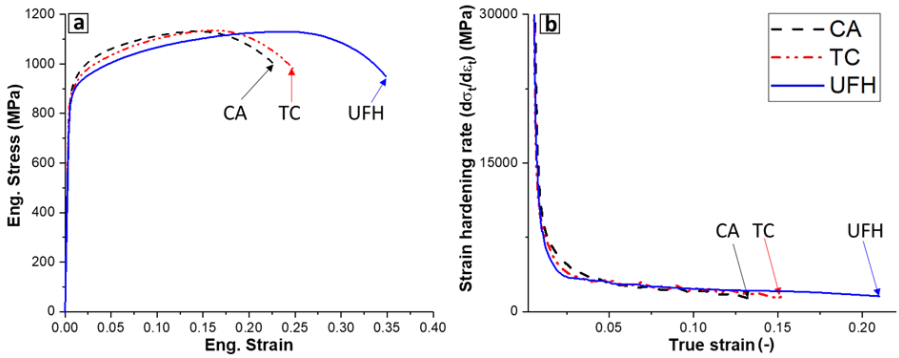

Figure 6.8: (a) Engineering stress-strain curves and (b) strain hardening rate v/s true strain curves.

Table 6.3: Mechanical properties (standard deviation).

Sample	σ_{ys}, MPa	σ_{UTS}, MPa	σ_{UTS}/σ_{ys}	$\varepsilon_{Uniform}$	ε_{Total}	Absorbed energy, MJ/m^3
CA	895 (8)	1131 (2)	1.26 (0.01)	0.14 (0.001)	0.24 (0.005)	251 (6)
TC	869 (8)	1135 (7)	1.31 (0.003)	0.16 (0.003)	0.25 (0.006)	268 (4)
UFH	862 (13)	1130 (6)	1.31 (0.003)	0.24 (0.01)	0.35 (0.004)	375 (1)

Bainitic steels produced in this study display continuous yielding and comparable values of ultimate tensile strength (σ_{UTS}). Yield strength (σ_{ys}) values of 895 MPa, 869 MPa and 862 MPa were measured for samples CA, TC and UFH, respectively. The obtained σ_{UTS} ranged from 1130 to 1135 MPa. Tensile testing, specifically the uniform ($\varepsilon_{Uniform}$) and total (ε_{Total}) elongation values, revealed a considerable difference in ductility for UFH compared to the samples CA and TC. In the CA and TC steels, $\varepsilon_{Uniform}$ and ε_{Total} are similar with values close to ~0.15 and 0.25, respectively. The sample UFH shows an $\varepsilon_{Uniform}$ and a ε_{Total} of 0.24 and 0.35, respectively. The reported difference in the elongation values represents an increment of 60% in $\varepsilon_{Uniform}$ and 40% in ε_{Total} for the sample UFH with respect to CA and TC. Absorbed energy values of 251 MJ/m^3, 268 MJ/m^3 and 375 MJ/m^3 were determined for CA, TC and UFH, respectively.

The strain hardening behavior of the studied steels is presented in Figure 6.8b. Below a true strain of 0.05, sample CA displays the highest strain hardening rate and UFH the lowest one. In the true strain range from 0.05 to 0.11, all bainitic steels present a gradual decrease of the strain hardening rate, which is extended up to a true strain of ~0.21 for the UFH sample.

6.4 Discussion

Thermal cycling and ultrafast heating produced microstructures finer than conventional annealing (Figures 6.5 and 6.6). The fine-sized PAGs and product microconstituents obtained via thermal cycling are the results of multiple reverse transformations martensite-austenite in each cycle. Consecutive nucleation of austenite at prior parent austenite and martensitic grain boundaries [6,8], like blocks and packets, together with an increase in heating rate (10 °C/s to 30 °C/s) and 2 s of holding time, resulted in refinement of the grain size in the studied TC steel. At the same time, multiple reverse transformations randomized the texture of the initial material, and localized texture components of low intensity were developed (Figure 6.7d). Multiple variant selection, related to the transformation from austenite to martensite/bainite [36] (24 variants of the K-S orientation relationship), resulted in the low intensity (multiples of random distribution) observed for the heat-treated samples in comparison with the as-received material. According to this, multiple and subsequent steps of transformation *martensite→austenite→martensite* are responsible for the weaker texture observed for TC. On the other hand, the conventional annealed sample displays a texture with higher intensity on the {554}<225> and {111}<112> components, being similar to the crystallographic texture observed in recrystallized ferrite [45,46]. The low heating rate employed during conventional annealing (i.e. 10 °C/s) leads to the recrystallization of ferrite during heating, conducing to the transformation of grains with orientations that compose the RD fiber texture (like {112}<110>) to grains with orientation close to {111}<112> and {554}<225> [45], which are the orientations observed after conventional annealing followed by austempering (Figure 6.7c). Also, {111}<112> and {001}<011> orientations components could be obtained as results of transformation from parent austenite grains with brass orientation [47]. Large PAGs and bainitic blocks for CA are the result of the slow heating rate and soaking for 180 s at the annealing temperature, where the selected annealing parameters produce both, isochronal and isothermal austenitic grain growth.

The ODF of the UFH sample (Figure 6.7e) shows that the general characteristics of the BCC texture are almost the same compared with the as-received material (Figure 6.7b). This phenomenon can be explained in terms of the texture memory effect hypothesis [46] and similar results have been previously reported for different ultrafast heated steel grades, including Q&P steels [18–20,44]. In this study, evidence of austenite formation and its interaction with non-recrystallized ferrite ($F_{N\text{-}Rx}$) during the heating process is presented. Figure 6.9 shows selected $F_{(Non\text{-}RX)}$ grains in an intercritical annealed sample heated at 500 °C/s to 800 °C, and quenched with no soaking time.

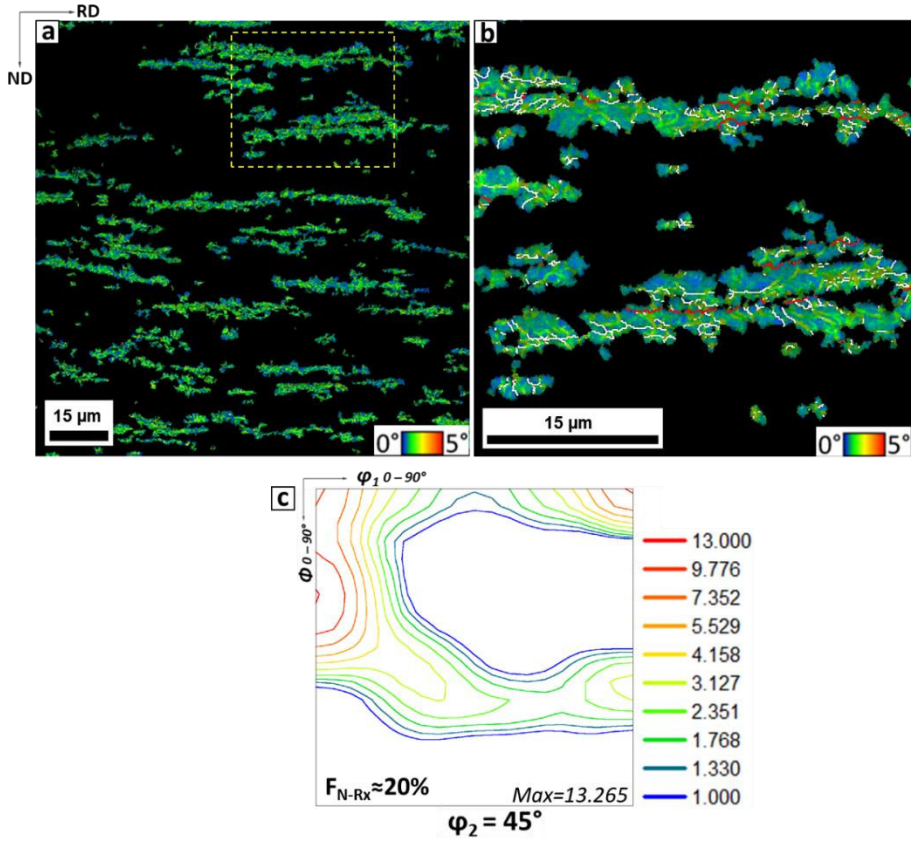

Figure 6.9: Non-recrystallized ferrite obtained in a sample heated at 500 °C/s to 800 °C followed by direct quenching: (a) 1st neighbor kernel average misorientation map. (b) Enlarged IQ-KAM map of the area enclosed by the dashed square in (a). White and red lines define boundaries with misorientation angles between 5-15° and 15-63°, respectively. (c) Orientation distribution function (scanned area 22500 µm^2).

The high misorientation observed in the 1st neighbor kernel average misorientation maps (Figures 6.9a and 6.9b) is related to a high density of dislocations in ferrite. This indicates that ferrite is in a non-recrystallized state during austenite formation. The ODF map presented in Figure 6.9c supports this observation. The ODF of the $F_{N\text{-}Rx}$ grains shows a convex curvature of the ND fiber and high intensity in the {113}<110> and {112}<110> rolling texture components. Texture characteristics of $F_{N\text{-}Rx}$ are restored after the transformation of $F_{N\text{-}Rx}$→*austenite*→*bainite* giving rise to the crystallographic orientation observed for the UFH bainitic steel (Figure 6.7e), even after heating the sample above the A_{C3} temperature. Those non-recrystallized ferritic regions provide a high density of nucleation sites for austenite [48]. Additionally, the high heating rate and undissolved carbides can effectively suppress the austenitic grain growth upon heating [18,20], resulting in the fine-grained bainitic structure produced after ultrafast heating annealing and austempering.

It is important to note that the four steps thermal cycling applied in this study, which includes heating up to the temperature range above A_{C3} followed by fast cooling, gives an equivalent grain refinement effect to the obtained through the UFH route, as presented in Figures 6.6a and 6.6b.

The microstructure produced after a predefined thermal treatment depends on the chemical and morphological characteristics of the parent austenite and subsequent thermal pathways. In this study, a fast cooling rate of 160 °C/s was employed after the initial annealing step. This approach makes possible to elucidate the characteristics of the parent austenite based on the microstructure obtained after cooling. Figure 6.10 shows the microstructure of the as-received ferritic-pearlitic steel (Figure 6.10a) together with samples CA (Figure 6.10b) and UFH (Figure 6.10c) directly cooled to room temperature (the microstructure of TC is presented in Figure 6.4b). Clear differences are observed between CA and UFH. In the UFH steel, a banded microstructure that resembles the ferritic-pearlitic bands of the as-received cold-rolled material was obtained. The insert in Figure 6.10c shows that the darker areas in the optical micrograph are mainly composed of fine-grained ferrite, as it was presented previously in Figure 6.4c. Contrarily, even distribution of microconstituents was found in CA and TC. The influence of the prior annealing strategies on the produced microstructures is exemplified using schematic continuous cooling transformation diagrams (presented in Figures 6.10d and 6.10e).

Conventional annealing produced a homogeneous parent austenite phase of rather large grain size if it is compared to the grain size distributions of TC and UFH. After cooling, a ferrite fraction lower than 1% was obtained for CA, with ferritic grains nucleated at prior austenite grain boundaries. The decrease of the PAGs size by thermal cycling annealing led to a higher amount of effective nucleation points [7], resulting in an increased number of ferritic grains obtained after cooling. The decrease of the M_S temperature is also related to the smaller PAGs produced after TC, and this phenomenon has been reported and discussed elsewhere [2,13]. On the other hand, the banded microstructure obtained after ultrafast heating and cooling is linked to the chemical heterogeneity of the parent austenite. The homogenization of manganese and carbon might be constrained during the ultrafast heating annealing [16,30,49]. This is a reason to obtain compositional gradients in the parent austenite, with regions of high and low solute concentration at prior pearlitic (high alloyed region, HA) and deformed ferritic bands (low alloyed region, LA), respectively [50,51]. During the initial stages of nucleation, austenite forms preferentially at prior pearlitic regions [26]. Additionally, austenite can also nucleate at ferrite-ferrite boundaries. Nevertheless, the growth of those nuclei will be controlled through carbon diffusion from the carbon-rich areas [48,52]. Another transformation mechanism that could operate upon fast heating is the massive growth of austenite from proeutectoid ferrite at the last stage of austenite formation [26,27].

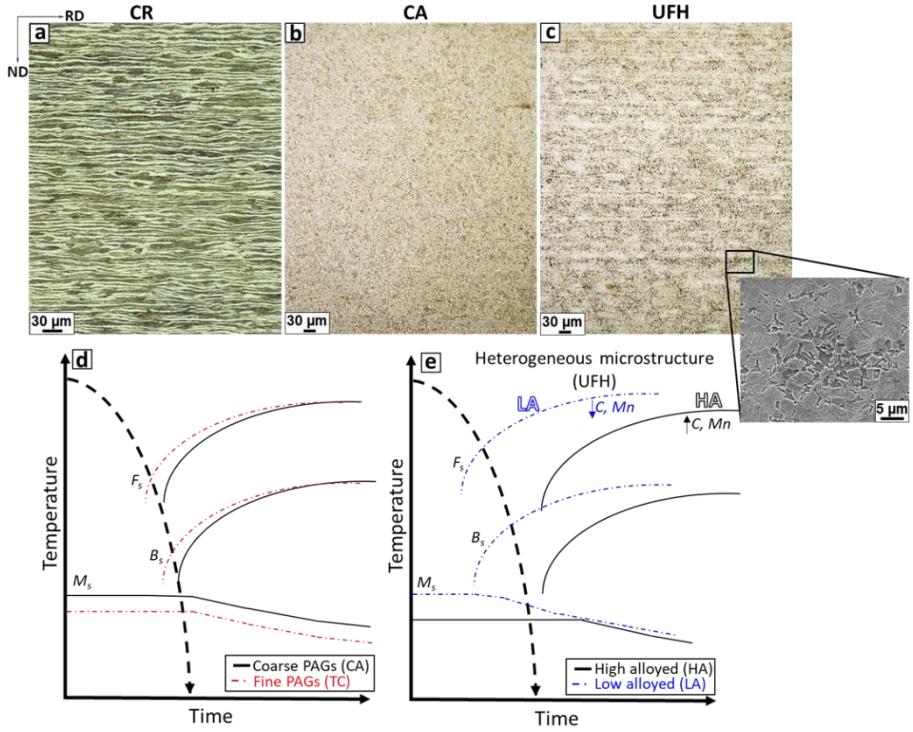

Figure 6.10: Optical micrographs for: (a) as-received material, (b) CA and (c) UFH samples. As a reference for the reader, the insert in (c) shows an enlarged micrograph of the heterogeneous microstructure obtained within the martensitic bands for the UFH sample. (d) Schematic CCT diagrams presenting the influence of the PAG size on phase transformations for CA and TC samples. (e) Chemical gradients in parent austenite produced via ultrafast heating annealing lead to different kinetic of phase transformation (local CCT diagrams) for the UFH sample. The banded microstructure produced after UFH is inherited from the initial cold-rolled material, where LA (ferritic) and HA (pearlitic) are low alloyed and high alloyed regions, respectively.

As the homogenization of carbon and the alloying elements is likely restricted by the high heating rate and short soaking time employed (<0.3 s), low and high solute regions in parent austenite will transform following different kinetics of phase transformations as presented in Figure 6.10e. The results suggest that LA regions decompose to a mixture of ferrite and possible bainite, while prior HA regions are transformed mainly to martensite due to the inhomogeneous distribution of alloying elements in austenite. These results concur with those reported for lean alloy steels subjected to ultrafast heating and fast cooling [15,49,53–55].

According to the mechanical properties, the decrease of the grain size attained via thermal cycling treatment resulted in equivalent σ_{UTS} and elongation values to the obtained in CA. These observations are in line with previous results in the influence of the PAG size and related mechanical performance of martensitic steels by Hanamura et al. [2]. The results suggest that the decrease of the average bainitic

block length from 5.3 µm (CA) to 3.5 µm (TC) and 3.4 µm (UFH) does not play a major role in the overall mechanical behavior of the studied steels. Instead, the combination of ultrafast heating and austempering produced higher uniform and total elongation, resulting in an enhanced strength-ductility balance and superior capacity of energy absorption during tensile testing.

The distribution of microconstituents and corresponding mechanical properties obtained after austempering are summarized in Figure 6.11. The results indicate that the σ_{UTS} values are insensitive to the processing history and microstructure. This observation agrees with the findings reported by Kumar et al. [56], where a saturation of the strength level was obtained in Dual-Phase steels with bainite or martensite content higher than 60%.

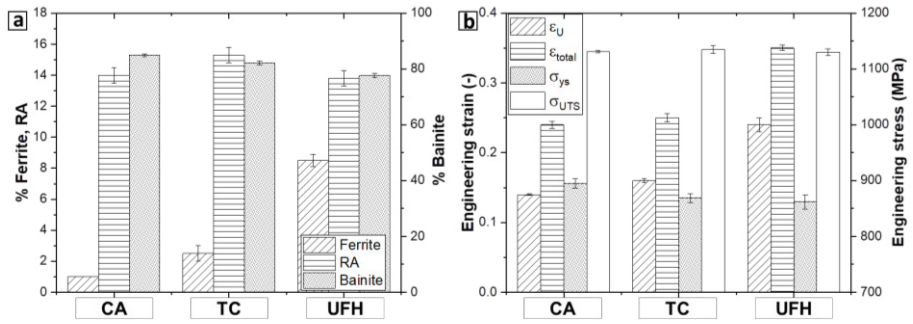

Figure 6.11: (a) Distribution of microconstituents in austempered samples (the amount of martensite is lower than 1% for all samples). RA: retained austenite. (b) Summary of the mechanical properties measured via uniaxial tensile testing. ε_U: uniform elongation; ε_{Total}: total elongation; σ_{ys}: 0.2% offset yield strength; σ_{UTS}: ultimate tensile strength.

The resulting mechanical properties obtained via the combination of UFH and austempering agree well with previous findings reported for UFH-Q&P steels [18,25], for which a promising compromise between total elongation and high strength level was found through the formation of ferrite-containing multiphase microstructures. Those results [18,25] suggested that the presence of ferrite does not affect the strength level but effectively contributes towards improving the tensile strain capacity of UFH steels.

In multiphase steels, the fraction, strength, distribution and size of each microstructural constituent define the mechanical behavior [57,58]. The strain hardening is also influenced by stress partitioning and strain accommodation between phases during deformation [59,60]. Additionally, the mechanical stability of retained austenite and its interaction with the surrounding microconstituents play a fundamental role on the strain hardening rate of TRIP-aided steels [59,61,62].

Noticeable differences in the strain hardening rates of the studied steels are observed at the initial stages of deformation, before reaching a strain value of 0.05 (Figure 6.8b). In an attempt to elucidate the potential effect of the microstructure

on the mechanical behavior, the measured strain hardening rates were analyzed by using the modified Crussard-Jaoul analysis [63,64]. Figure 6.12 shows representative plots of $\ln(d\sigma_t/d\varepsilon_t)$ vs. $\ln(\sigma_t)$ for the studied steels. Three different stages (s_{I-III}) of strain hardening are observed; true stress (ε_t) and true strain (σ_t) values at the transition of each stage are indicated in parenthesis.

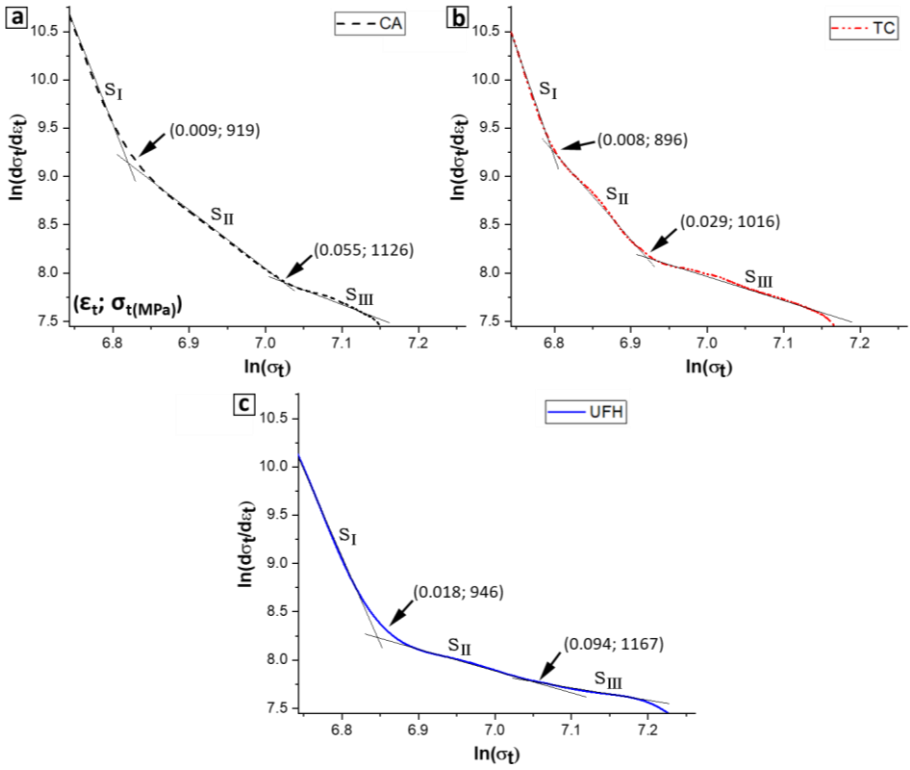

Figure 6.12: Strain hardening behavior plotted according to the modified C-J analysis in samples (a) CA, (b) TC and (c) UFH. Values indicated in parenthesis at the inflection points of the strain hardening curves correspond to the true strain and true stress, respectively (true strain; true stress).

During stage 1 (s_I), initial yielding and dislocation accumulation in bainitic regions lead to high strain hardening rates for samples CA and TC. At this stage, the accumulation of mobile dislocations at regions near to retained austenite grains takes place [65]. It is expected that the retained austenite grains that compose M/A islands are among the first to transform due to the constraining effect on strain distribution and locally higher stress levels that arise in the regions surrounding the initial martensitic zones [66]. Retained austenite grains of low mechanical stability might also transform to martensite in this stage. Stage 1 is prolonged to higher levels of stress and strain in the UFH sample due to the homogeneous deformation of soft ferritic grains, which resulted in the lowest strain hardening rate observed at the early stages of deformation [64,67]. In stage 2 (s_{II}), retained austenite grains

continuously transform to martensite due to the accumulation of strain. This transformation attenuates the strain hardening rate decreasing by inhibiting the dislocation glide process in regions where newly martensite grains were formed [65,68].

The higher strain hardening rate at the initial stages of deformation for CA and TC samples might be also influenced by a fast rate of austenite transformation upon straining. The C-J plots indicate that most of the austenite transformation proceeds quickly at low strain levels in samples CA and TC (before reaching the stress level corresponding to stage 3). This observation agrees with the results for the kinetics of austenite transformation upon straining in low alloy steels [69–71]. Instead, variations of strain hardening in the UFH sample suggest that austenite transformation is prolonged to higher levels of strain and proceeds at a slower rate than in CA and TC. This is an indication for retained austenite of higher mechanical stability, resulting in improved ductility and energy absorption capacity [70,71]. Liu et al. [16] pointed out that the chemical heterogeneities in retained austenite, generated during ultrafast heating experiments, may play a role on the mechanical behavior of multiphase ultrafast heated steels. The higher carbon and manganese concentration in austenite formed at prior pearlitic colonies may account to improve the mechanical stability of the γ grains [61,62], enhancing the ductility of the UFH steel.

During stage 3 (s_{III}), the deformation of bainite and ferrite continues. Retained austenite grains of higher mechanical stability also transform during this stage. The newly formed martensite islands act like hard particles, producing the redistribution of plastic deformation towards bainitic and ferritic constituents [68].

In addition to this analysis, it should be mentioned that the formation of the heterogeneously banded microstructure produced via UFH might lead to strain/stress gradients between ferrite, bainite and retained austenite (which transforms to martensite upon straining), producing a synergic effect that conduced to the enhancement of ductility without decreasing the strength level as reported in Refs. [72–74]. Ryu et al. demonstrated that the strain partitioning between microconstituents in low alloy steels drastically influences the stability of retained austenite [75], and this factor could be related to the higher mechanical stability indirectly evaluated for the γ grains in the UFH sample. According to the discussed results and reported mechanical properties for multiphase UFH-Q&P steels [18,25], ferrite grains could effectively contribute to the ductility by decreasing the strain localization, improving the retained austenite stability.

However, the exact quantitative analyses of the influence of the spatial distribution of microconstituents and their contribution to the mechanical behavior, coupled with the evaluation of kinetics and hardening related to the *austenite→martensite* transformation upon straining remain open for further investigation.

6.5 Conclusions

In this study, the influence of thermal cycling and ultrafast heating annealing strategies on microstructure-mechanical properties of austempered steels were evaluated and compared with a steel grade produced via a conventional annealing route. The following conclusions are addressed from the obtained results:

- Four steps thermal cycling and ultrafast heating above the A_{C3} led to finer microstructures than conventional annealing. Retained austenite grain distributions were not greatly influenced by the prior annealing treatment.
- The microstructural refinement attained via thermal cycling does not show a significant influence on the mechanical response for the studied steels.
- Ultrafast heating above the A_{C3} followed by fast cooling to room temperature produces a banded microstructure. The banded characteristics of the heat-treated material are similar to the observed in the as-received ferritic-pearlitic steel. Microstructural analysis suggested that the banded microstructure developed after heat treatment arises from local chemical heterogeneities in the parent austenite due to insufficient time for diffusion of alloying elements during the UFH process.
- In contrast to the conventional annealed sample, the grain refined-heterogeneous microstructure produced via a combination of UFH and austempering led to an increase of 40% in total elongation and 50% in energy absorbed measured under uniaxial strain to fracture.
- The enhancement of ductility for the UFH-austempered steel is reached without sacrificing the strength level. The obtained results suggest that the formation of heterogeneous microstructures via ultrafast heating annealing has a greater influence on the mechanical response than the attained level of grain refinement.

References

[1] W. Morrison, Effect of grain size on the stress-strain relationship in low-carbon steel, Trans. ASM. 59 (1966) 824–846.

[2] T. Hanamura, S. Torizuka, S. Tamura, S. Enokida, H. Takech, Effect of Austenite Grain Size on Transformation Behavior, Microstructure and Mechanical Properties of 0.1C–5Mn Martensitic Steel, ISIJ Int. 53 (2013) 2218–2225.

[3] Y. Tomita, K. Okabayashi, Heat treatment for improvement in lower temperature mechanical properties of 0.40 pct C-Cr-Mo ultrahigh strength steel, Metall. Trans. A. 14 (1983) 2387–2393. https://doi.org/10.1007/BF02663314.

[4] C. Garcia-Mateo, F.G. Caballero, T. Sourmail, M. Kuntz, J. Cornide, V. Smanio, R. Elvira, Tensile behaviour of a nanocrystalline bainitic steel containing 3wt% silicon,

Mater. Sci. Eng. A. 549 (2012) 185–192.
https://doi.org/10.1016/j.msea.2012.04.031.

[5] T. Yokota, C.G. Mateo, H.K.D.H. Bhadeshia, Formation of nanostructured steels by phase transformation, Scr. Mater. 51 (2004) 767–770.
https://doi.org/10.1016/j.scriptamat.2004.06.006.

[6] T. Furuhara, K. Kikumoto, H. Saito, T. Sekine, T. Ogawa, S. Morito, T. Maki, Phase transformation from fine-grained austenite, ISIJ Int. 48 (2008) 1038–1045.
https://doi.org/10.2355/isijinternational.48.1038.

[7] R.A. Grange, Strengthening steel by austenite grain refinemet, Trans. ASM. 59 (1966) 26–48.

[8] R.A. Grange, The rapid heat treatment of steel, Metall. Trans. 2 (1971) 65–78.
https://doi.org/10.1007/BF02662639.

[9] T.N. Baker, Microalloyed steels Microalloyed steels, Ironmak. Steelmak. 43 (2016).
https://doi.org/10.1179/1743281215Y.0000000063.

[10] B. Buchmayr, Thermomechanical Treatment of Steels – A Real Disruptive Technology Since Decades, Steel Res. Int. 87 (2017) 1–14.
https://doi.org/10.1002/srin.201700182.

[11] J. Zhao, Z. Jiang, Thermomechanical processing of advanced high strength steels, Prog. Mater. Sci. 94 (2018) 174–242.
https://doi.org/10.1016/j.pmatsci.2018.01.006.

[12] Z. Dai, H. Chen, R. Ding, Q. Lu, C. Zhang, Z. Yang, S. Van Der Zwaag, Fundamentals and application of solid-state phase transformations for advanced high strength steels containing metastable retained austenite, Mater. Sci. Eng. R. 143 (2021).
https://doi.org/10.1016/j.mser.2020.100590.

[13] C. Celada-Casero, J. Sietsma, M.J. Santofimia, The role of the austenite grain size in the martensitic transformation in low carbon steels, Mater. Des. 167 (2019).
https://doi.org/10.1016/j.matdes.2019.107625.

[14] D.K. Matlock, S. Kang, E. De Moor, J.G. Speer, Applications of rapid thermal processing to advanced high strength sheet steel developments, Mater. Charact. 166 (2020) 110397. https://doi.org/10.1016/j.matchar.2020.110397.

[15] A. Banis, M. Bouzouni, E. Gavalas, S. Papaefthymiou, The formation of a mixed martensitic / bainitic microstructure and the retainment of austenite in a medium-carbon steel during ultra-fast heating, Mater. Today Commun. 26 (2021) 101994.
https://doi.org/10.1016/j.mtcomm.2020.101994.

[16] G. Liu, T. Li, Z. Yang, C. Zhang, J. Li, H. Chen, On the role of chemical heterogeneity in phase transformations and mechanical behavior of flash annealed quenching & partitioning steels, Acta Mater. 201 (2020) 266–277.
https://doi.org/10.1016/j.actamat.2020.10.007.

[17] G.M. Cola, Replacing hot stamped, boron, and DP1000 with “room temperature formable” Flash® Bainite 1500 advanced high strength steel, ASM Int. - 28th Heat Treat. Soc. Conf. HEAT Treat. 2015. (2015) 21–28.

[18] D. De Knijf, A. Puype, C. Föjer, R. Petrov, The influence of ultra-fast annealing prior to quenching and partitioning on the microstructure and mechanical properties, Mater. Sci. Eng. A. 627 (2015) 182–190. https://doi.org/10.1016/j.msea.2014.12.118.

[19] A. Da Costa-Reis, L. Bracke, R. Petrov, W.J. Kaluba, L. Kestens, Grain Refinement and Texture Change in Interstitial Free Steels after Severe Rolling and Ultra-short Annealing, ISIJ Int. 43 (2003) 1260–1267. https://doi.org/10.2355/isijinternational.43.1260.

[20] R.H. Petrov, J. Sidor, L.A.I. Kestens, Texture formation in high strength low alloy steel reheated with ultrafast heating rates, Mater. Sci. Forum. 702–703 (2012) 798–801. https://doi.org/10.4028/www.scientific.net/MSF.702-703.798.

[21] R. Petrov, L. Kestens, W. Kaluba, Y. Houbaert, Recrystallization and austenite formation in a cold rolled TRIP steel during ultra fast heating, Steel Grips. 289–294 (2003).

[22] R.C. Hudd, L.K. Lyons, A. De Paepe, C. Stolz, J. Collins, The ultra-rapid heat treatment of low carbon strip. European Commission Project Contract No 7210-MB/818/203/819, 1998.

[23] G. Griffay, M. Anderhuber, P. Klinkenberg, V. Tusset, New continuous annealing technology with high-speed induction heating followed by ultra-fast cooling. European Commission Project Contract No 7210-PR/026, 2002.

[24] E.I. Hernandez-Duran, L. Corallo, T. Ros-Yanez, F.M. Castro-Cerda, R.H. Petrov, Influence of Mo-Nb-Ti additions and peak annealing temperature on the microstructure and mechanical properties of low alloy steels after ultrafast heating process, Mater. Sci. Eng. A. 808 (2021) 140928. https://doi.org/10.1016/j.msea.2021.140928.

[25] J. Dai, Q. Meng, H. Zheng, An innovative pathway to produce high-performance quenching and partitioning steel through ultra-fast full austenitization annealing, Mater. Today Commun. 25 (2020) 101272. https://doi.org/10.1016/j.mtcomm.2020.101272.

[26] G. Speich, A. Szirmae, Formation of Austenite from Ferrite and Ferrite-Carbide Aggregates, Trans. Metall. Soc. AIME. 245 (1969) 1063–1074.

[27] F.M. Castro Cerda, I. Sabirov, C. Goulas, J. Sietsma, A. Monsalve, R.H. Petrov, Austenite formation in 0.2% C and 0.45% C steels under conventional and ultrafast heating, Mater. Des. 116 (2017) 448–460. https://doi.org/10.1016/j.matdes.2016.12.009.

[28] L.S. Thomas, D.K. Matlock, Formation of Banded Microstructures with Rapid Intercritical Annealing of Cold-Rolled Sheet Steel, Metall. Mater. Trans. A Phys. Metall. Mater. Sci. 49 (2018) 4456–4473. https://doi.org/10.1007/s11661-018-4742-9.

[29] S. Mishra, T. DebRoy, Non-isothermal grain growth in metals and alloys, Mater. Sci. Technol. 22 (2006) 253–278. https://doi.org/10.1179/174328406X84094.

[30] G. Liu, Z. Dai, Z. Yang, C. Zhang, J. Li, H. Chen, Kinetic transitions and Mn partitioning during austenite growth from a mixture of partitioned cementite and ferrite: Role of heating rate, J. Mater. Sci. Technol. 49 (2020) 70–80. https://doi.org/10.1016/j.jmst.2020.01.051.

[31] L. Thomas, Effect of heating rate on intercritical annealing of low-carbon cold-rolled steel, Ph. D. Thesis, Colorado School of Mines, Golden, USA, 2015.

[32] H. Azizi-Alizamini, M. Militzer, W.J. Poole, Austenite formation in plain low-carbon steels, Metall. Mater. Trans. A Phys. Metall. Mater. Sci. 42 (2011) 1544–1557. https://doi.org/10.1007/s11661-010-0551-5.

[33] S. Kaar, K. Steineder, R. Schneider, D. Krizan, C. Sommitsch, New Ms-formula for exact microstructural prediction of modern 3rd generation AHSS chemistries, Scr. Mater. 200 (2021) 113923. https://doi.org/10.1016/j.scriptamat.2021.113923.

[34] S. Matas, R.F. Hehemann, The Structure of Bainite in Hypoeutectoid Steels, Trans. Metall. Soc. AIME. 221 (1961) 179–185.

[35] D.T. Pierce, D.R. Coughlin, D.L. Williamson, K.D. Clarke, A.J. Clarke, J.G. Speer, Characterization of transition carbides in quench and partitioned steel microstructures by Mossbauer spectroscopy and complementary techniques, Acta Mater. 90 (2015) 417–430. https://doi.org/10.1016/j.actamat.2015.01.024.

[36] N. Takayama, G. Miyamoto, T. Furuhara, Effects of transformation temperature on variant pairing of bainitic ferrite in low carbon steel, Acta Mater. 60 (2012) 2387–2396. https://doi.org/10.1016/j.actamat.2011.12.018.

[37] E. Gomes de Araujo, H. Pirgazi, M. Sanjari, M. Mohammadi, L.A.I. Kestens, Automated reconstruction of parent austenite phase based on the optimum orientation relationship, J. Appl. Crystallogr. 54 (2021) 569–579. https://doi.org/10.1107/S1600576721001394.

[38] Aaronson H.I., The proeutectoid ferrite and the proeutectoid cementite reactions, in: V. Zackay (Ed.), Decompos. Austenite by Diffus. Process., Interscience Publishers, Philadelphia, PA, 1960: pp. 387–546.

[39] A. Navarro-López, J. Hidalgo, J. Sietsma, M.J. Santofimia, Characterization of bainitic/martensitic structures formed in isothermal treatments below the Ms temperature, Mater. Charact. 128 (2017) 248–256. https://doi.org/10.1016/j.matchar.2017.04.007.

[40] C. Hofer, V. Bliznuk, A. Verdiere, R. Petrov, F. Winkelhofer, H. Clemens, S. Primig, Correlative microscopy of a carbide-free bainitic steel, Micron. 81 (2016) 1–7. https://doi.org/10.1016/j.micron.2015.10.008.

[41] C.P. Scott, J. Drillet, A study of the carbon distribution in retained austenite, 56 (2007) 489–492. https://doi.org/10.1016/j.scriptamat.2006.11.033.

[42] F.G. Caballero, M. Miller, C. Garcia-Mateo, Slow Bainite: an Opportunity to Determine the Carbon Content of the Bainitic Ferrite during Growth Francisca G. Caballero, Solid State Phenom. 174 (2011) 111–116. https://doi.org/10.4028/www.scientific.net/SSP.172-174.111.

[43] A.J. Clarke, J.G. Speer, M.K. Miller, R.E. Hackenberg, D. V. Edmonds, D.K. Matlock, F.C. Rizzo, K.D. Clarke, E. De Moor, Carbon partitioning to austenite from martensite or bainite during the quench and partition (Q&P) process: A critical assessment, Acta Mater. 56 (2008) 16–22. https://doi.org/10.1016/j.actamat.2007.08.051.

[44] E.I. Hernandez-Duran, T. Ros-Yanez, F.M. Castro-Cerda, R.H. Petrov, The influence of the heating rate on the microstructure and mechanical properties of a peak annealed quenched and partitioned steel, Mater. Sci. Eng. A. 797 (2020) 140061. https://doi.org/10.1016/j.msea.2020.140061.

[45] M. Hoelscher, D. Raabe, K. Lucke, Rolling and recrystallization texture in BCC steels, Steel Res. 62 (1991) 567–575.

[46] N. Yoshinaga, H. Inoue, K. Kawasaki, L. Kestens, B.C. De Cooman, Factors affecting texture memory appearing through α → γ → α transformation in IF steels, Mater. Trans. 48 (2007) 2036–2042. https://doi.org/10.2320/matertrans.MA200704.

[47] M.P. Butrón-Guillén, J.J. Jonas, R.K. Ray, Effect of austenite pancaking on texture formation in a plain carbon and A Nb microalloyed steel, Acta Metall. Mater. 42 (1994) 3615–3627. https://doi.org/10.1016/0956-7151(94)90428-6.

[48] C. Zheng, D. Raabe, Interaction between recrystallization and phase transformation during intercritical annealing in a cold-rolled dual-phase steel : A cellular automaton model, Acta Mater. 61 (2013) 5504–5517. https://doi.org/10.1016/j.actamat.2013.05.040.

[49] K. Albutt, S. Garber, Effect of heating rate on the elevation of the critical temperatures of low-carbon mild steel, J. Iron Steel Inst. 204 (1966) 1217–1222.

[50] J.D. Verhoeven, Review of microsegregation induced banding phenomena in steels, J. Mater. Eng. Perform. 9 (2000) 286–296. https://doi.org/10.1361/105994900770345935.

[51] R.A. Grange, Effect of microstructural banding in steel, Metall. Trans. 2 (1971) 417–426. https://doi.org/10.1007/BF02663328.

[52] V.I. Savran, Y. Leeuwen, D.N. Hanlon, C. Kwakernaak, W.G. Sloof, J. Sietsma, Microstructural features of austenite formation in C35 and C45 alloys, Metall. Mater. Trans. A Phys. Metall. Mater. Sci. 38 (2007) 946–955. https://doi.org/10.1007/s11661-007-9128-3.

[53] T. Lolla, G. Cola, B. Narayanan, B. Alexandrov, S.S. Babu, Development of rapid heating and cooling (flash processing) process to produce advanced high strength steel microstructures, Mater. Sci. Technol. 27 (2011) 863–875. https://doi.org/10.1179/174328409X433813.

[54] S. Sackl, M. Zuber, H. Clemens, S. Primig, Induction Tempering vs Conventional Tempering of a Heat-Treatable Steel, Metall. Mater. Trans. A. 47 (2016) 3694–3702. https://doi.org/10.1007/s11661-016-3534-3.

[55] J. Pedraza, R. Landa-Mejia, O. Garcia-Rincon, I. Garcia, The Effect of Rapid Heating and Fast Cooling on the Transformation Behavior and Mechanical Properties of an Advanced High Strength Steel (AHSS), Metals (Basel). 545 (2019) 1–12.

[56] A. Kumar, S.B. Singh, K.K. Ray, Influence of bainite/martensite-content on the tensile properties of low carbon dual-phase steels, Mater. Sci. Eng. A. 474 (2008) 270–282. https://doi.org/10.1016/j.msea.2007.05.007.

[57] K. Ismail, A. Perlade, P.J. Jacques, T. Pardoen, L. Brassart, Impact of second phase morphology and orientation on the plastic behavior of dual-phase steels, Int. J. Plast. 118 (2019) 130–146. https://doi.org/10.1016/j.ijplas.2019.02.005.

[58] A. Bhattacharyya, T. Sakaki, G.J. Weng, The Influence of Martensite Shape, Concentration, and Phase Transformation Strain on the Deformation Behavior of Stable Dual-Phase Steels, Metall. Trans. A. 24 (1993) 301–314.

[59] B.L. Ennis, E. Jimenez-melero, E.H. Atzema, M. Krugla, Metastable austenite driven work-hardening behaviour in a TRIP-assisted dual phase steel, Int. J. Plast. 88 (2017) 126–139. https://doi.org/10.1016/j.ijplas.2016.10.005.

[60] M. Calcagnotto, D. Ponge, E. Demir, D. Raabe, Orientation gradients and geometrically necessary dislocations in ultrafine grained dual-phase steels studied by 2D and 3D EBSD, Mater. Sci. Eng. A. 527 (2010) 2738–2746. https://doi.org/10.1016/j.msea.2010.01.004.

[61] E. Jimenez-Melero, N.H. van Dijk, L. Zhao, J. Sietsma, J.P. Wright, S. Van Der Zwaag, In situ synchrotron study on the interplay between martensite formation, texture evolution and load partitioning in low-alloyed TRIP steels, Mater. Sci. Eng. A. 528 (2011) 6407–6416. https://doi.org/10.1016/j.msea.2011.04.087.

[62] S. Ebner, R. Schnitzer, E. Maawad, C. Suppan, C. Hofer, Influence of partitioning parameters on the mechanical stability of austenite in a Q&P steel: A comparative in-situ study, Materialia. 15 (2021) 101033. https://doi.org/10.1016/j.mtla.2021.101033.

[63] Y. Tomita, K. Okabayashi, Tensile Stress-Strain Analysis of Cold Worked Metals and Steels and Dual-Phase Steels, Metall. Trans. A. 16 (1985) 865–872.

[64] M. Soliman, H. Palkowski, Strain Hardening Dependence on the Structure in Dual-Phase Steels, Steel Res. Int. 92 (2021) 1–15. https://doi.org/10.1002/srin.202000518.

[65] F. Alharbi, A.A. Gazder, A. Kostryzhev, B.C. De Cooman, E. V. Pereloma, The effect of processing parameters on the microstructure and mechanical properties of low-Si transformation-induced plasticity steels, J. Mater. Sci. 49 (2014) 2960–2974. https://doi.org/10.1007/s10853-013-8008-z.

[66] D. De Knijf, R. Petrov, C. Föjer, L.A.I. Kestens, Effect of fresh martensite on the stability of retained austenite in quenching and partitioning steel, Mater. Sci. Eng. A. 615 (2014) 107–115. https://doi.org/10.1016/j.msea.2014.07.054.

[67] P. Movahed, S. Kolahgar, S.P.H. Marashi, M. Pouranvari, N. Parvin, The effect of intercritical heat treatment temperature on the tensile properties and work hardening behavior of ferrite – martensite dual phase steel sheets, Mater. Sci. Eng. A. 518 (2009) 1–6. https://doi.org/10.1016/j.msea.2009.05.046.

[68] I.B. Timokhina, P.D. Hodgson, E. V Pereloma, Transmission Electron Microscopy

Characterization of the Bake-Hardening Behavior of Transformation-Induced Plasticity and Dual-Phase Steels, Metall. Mater. Trans. A. 38 (2007) 2442–2454. https://doi.org/10.1007/s11661-007-9258-7.

[69] E. Polatidis, G.N. Haidemenopoulos, D. Krizan, N. Aravas, T. Panzner, I. Papadioti, N. Casati, S. Van Petegem, H. Van Swygenhoven, The effect of stress triaxiality on the phase transformation in transformation induced plasticity steels : Experimental investigation and modelling the transformation kinetics, Mater. Sci. Eng. A. 800 (2021) 1–10. https://doi.org/10.1016/j.msea.2020.140321.

[70] E. Pereloma, A. Gazder, I. Timokhina, Retained Austenite: Transformation-Induced Plasticity, Encycl. Iron, Steel, Their Alloy. (2016) 3088–3103. https://doi.org/10.1081/e-eisa-120049200.

[71] K. Sugimoto, M. Kobayashi, S. Hashimoto, Ductility and Strain-Induced Transformation in a High-Strength Transformation-Induced Plasticity-Aided Dual-Phase Steel, Metall. Trans. A. 23 (1992) 3085–3091.

[72] H. Lyu, M. Hamid, A. Ruimi, H.M. Zbib, Stress/strain gradient plasticity model for size effects in heterogeneous nano-microstructures, Int. J. Plast. 97 (2017) 46–63. https://doi.org/10.1016/j.ijplas.2017.05.009.

[73] S.F. Hassan, H. Al-Wadei, Heterogeneous Microstructure of Low-Carbon Microalloyed Steel and Mechanical Properties, J. Mater. Eng. Perform. 29 (2020) 7045–7051. https://doi.org/10.1007/s11665-020-05217-7.

[74] X. Wu, Y. Zhu, Heterogeneous materials: a new class of materials with unprecedented mechanical properties, Mater. Res. Lett. 5 (2017) 527–532. https://doi.org/10.1080/21663831.2017.1343208.

[75] J.H. Ryu, D. Kim, S. Kim, H.K.D.H. Bhadeshia, Strain partitioning and mechanical stability of retained austenite, Scr. Mater. 63 (2010) 297–299. https://doi.org/10.1016/j.scriptamat.2010.04.020.

Chapter 7

Improvement of the strength-ductility balance in ultrafast heated steels by combining high-temperature annealing and quenching and partitioning process[4]

Abstract

The microstructure and mechanical properties of an Fe-0.24C-1.39Mn-1.42Si steel were investigated after combining ultrafast heating (UFH) at a heating rate of 500 °C/s followed by fast cooling to room temperature (DQ) or quenching and partitioning processes (Q&P). Two peak temperatures were studied, annealing into the intercritical range and above the A_{C3} temperature. After ultrafast heating and quenching, the resulting microstructures revealed that intercritical annealing led to the formation of a banded ferritic-martensitic microstructure. On the other hand, heating above the intercritical range led to an even distribution of allotriomorphic ferrite grains upon fast cooling and a complex phase microstructure, consisting mainly of martensite, was produced. Q&P steel grades exhibit an enhanced mechanical behavior compared to their DQ counterparts, where yield strength, uniform elongation, and total elongation increased after partitioning at 400 °C. The ultimate tensile strength of the Q&P steels decreased compared to the DQ steels annealed at the same peak temperature. However, the final strength-ductility balance of the studied Q&P steels was superior to the DQ steel grades. Moreover, considerable strength and improved ductility were obtained through the combination of peak annealing above the A_{C3} temperature followed by Q&P. These results are attributed to an interplay between a sustainable TRIP effect and effective strain-stress partitioning among the microconstituents resulted after the Q&P process.

[4] This chapter is based on the article: E.I. Hernandez-Duran, V. Bliznuk, T. Ros-Yanez, R. Iquilio-Abarzua, F.M. Castro-Cerda and R. H. Petrov. Improvement of the strength-ductility balance in ultrafast heated steels by combining high-temperature annealing and quenching and partitioning process. Mat. Sci. & Eng. A, 827, (2021).
https://doi.org/10.1016/j.msea.2021.142045

7.1 Introduction

Recent studies [1–8] indicated that new high strength steel grades produced by ultrafast heating and direct quenching have comparable or enhanced mechanical properties compared to conventionally heat-treated steels. Although the improvement of mechanical properties is yet not fully understood, it is attributed to the formation of grain-refined multiphase microstructures [3,4,7], produced by the interaction of several solid-state mechanisms [9–11].

The fast heating -peak annealing- treatment of steels (i.e. heat treatments with ultra-short or without soaking time at the annealing temperature) leads to the formation of small austenite grains with local heterogeneous chemical composition. Hence, a mixture of microconstituents could be obtained upon cooling due to the chemical heterogeneities in austenite [2–4,7,8]. Additionally, an increment of the austenite grain boundary density, as a result of parent austenite grain refinement under fast heating annealing, offers more sites for nucleation of ferrite or bainite during cooling in low alloy steels [2,12,13]. The beneficial effect of the formation of mixed microstructures on the mechanical properties has been previously discussed in the literature [14–17], and a similar approach is intended for the steel grades produced by rapid heat treatments [4].

Moreover, the peak annealing step corresponds to the first stage of the heat treatment pathway, being possible to combine the ultrafast heating with subsequent low-temperature treatments for tailoring the requirements of different applications and structural standards. The combined ultrafast heating plus quenching and partitioning process has shown that the mechanical properties of fast annealed steels improve compared to those obtained in conventionally annealed Q&P steels [18–23]. The enhanced mechanical performance of fast heated steels annealed up to the intercritical region [18–21] and steels heated above the A_{C3} temperature [22,23] is related to the formation of refined heterogeneous microstructures, composed of microconstituents with multiple morphologies and chemical compositions.

The evaluation of mechanical properties in Q&P steel grades subjected to conventional annealing into the intercritical and fully austenitic range has shown that the presence of proeutectoid ferrite led to higher ductilities than the obtained in fully austenitized steel grades with a matrix consisting mainly of martensite [24,25]. Yan et al. [25] reported an enhancement of the strength-ductility balance, accompanied by a decrease in the total strength, in an Fe-0.2C-1.58Si-1.55Mn steel subjected to intercritical annealing. Similarly, Wang et al. [26] and Kickinger et al. [27] studied the effect of ferrite formation after full austenitization on the mechanical properties of Q&P steels. In both studies, a slow cooling rate of 5°C/s was applied after complete austenitization to promote austenite transformation into proeutectoid ferrite. A rapid cooling rate followed the slow cooling regime to avoid

further austenite transformation before quenching the studied samples below the M_S. Such a cooling method effectively created an even distribution of ferrite grains, resulting in balanced mechanical properties in Q&P steels [27]. The heating above the A_{C3} temperature followed by austenite to ferrite transformation during cooling could be useful to modify the banded ferritic-martensitic microstructures obtained in intercritical annealed UFH steels [9,10], potentially avoiding the negative effect of microstructural banding on formability and anisotropy of mechanical properties. Moreover, a comparative analysis of the effect of fast heating into the intercritical range and above of it on the mechanical behavior of direct quenched and Q&P steels has not been thoroughly reported.

The objective of this study, therefore, is to evaluate the influence of the peak annealing temperature and the Q&P process on the microstructure and mechanical properties of a cold-rolled low alloy steel subjected to ultrafast heating. In this way, the current work attempts to gain insight into the heat treatment design of new steel grades and to understand the contribution of the microstructures in the mechanical behavior of steels produced by rapid annealing strategies.

7.2 Experimental

A 70% cold-rolled low alloy steel with composition given in Table 7.1 was studied. The microstructure of the initial cold-rolled steel consists of alternated regions of deformed ferrite and 33.7% (±3.2) of lamellar pearlite (Figure 7.1).

Table 7.1: Chemical composition of the studied steel (wt.%).

C	Mn	Si	P	S	Fe
0.24	1.39	1.42	0.009	0.004	Bal.

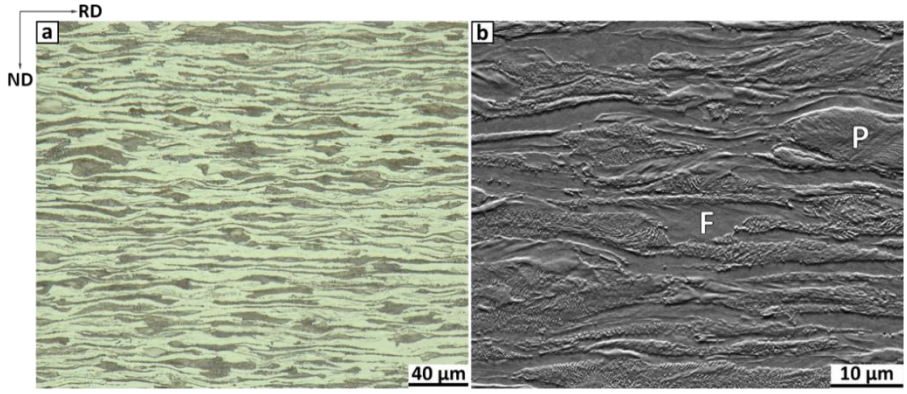

Figure 7.1: Microstructure of the initial 70% cold-rolled steel. (a) Light optical micrograph. (b) Secondary electron micrograph (SE).

Strips with dimensions of 90x20x1.2 mm^3 (length, width, and thickness, respectively) were cut along the rolling direction and heat-treated in a Gleeble® 1500 thermomechanical simulator.

Intercritically peak-annealed steel samples were produced by continuous heating up to 800 °C in order to obtain ~50% volume fraction of proeutectoid ferrite prior to fast cooling. On the other hand, the highest peak temperature employed, 940 °C, was selected for heating the samples above the intercritical range. The critical temperature, A_{C3}, was determined in samples of 10x5x1.2 mm^3 heated in a Bähr 805 A/D dilatometer, which operates using longitudinal flux induction heating. Steel samples were heated at ~500 °C/s from room temperature to 780 °C; the heating rate then declined to ~350 °C/s due to the magnetic transition of ferrite above the Curie temperature and the formation of paramagnetic austenite. Following this heating regime, the A_{C3} temperature of the studied steel was estimated as 910 °C ± 5 °C (the error of the measurement corresponds to the standard deviation of three measurements). According to the methodology presented in Ref. [28], a peak heating temperature of 940 °C, i.e. 30 °C above the determined A_{C3}, was chosen to ensure the dissolution of proeutectoid ferrite before the cooling step. Once the selected peak temperature was reached, a holding time (H.t.) not greater than 0.3 s was applied before cooling down the samples at 160 °C/s.

Figure 7.2a shows the temperature records of the heat treatments performed in the Gleeble® simulator. Through this manuscript, the steel samples are designated as AAA-BB, where AAA is the selected peak temperature (800 or 940 °C), and BB is the subsequent direct quenching (DQ) or quenching and partitioning (Q&P) process.

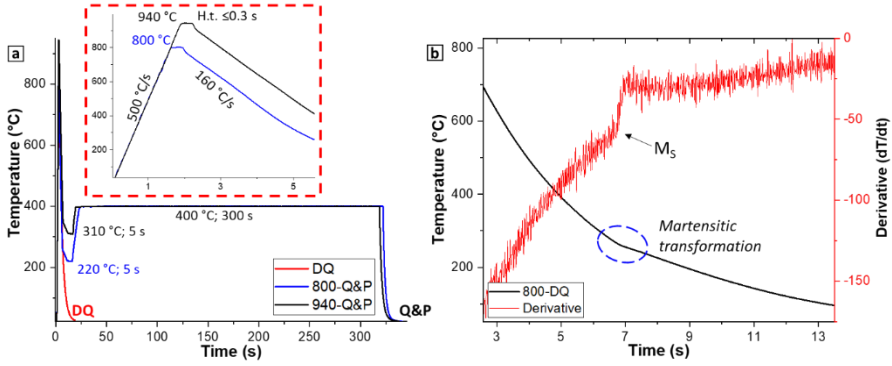

Figure 7.2: (a) Temperature profiles recorded during the combined ultrafast heating and Q&P process for the samples peak annealed at 800 and 940 °C (the red curve corresponds to the temperature profile recorded for the directly quenched samples, DQ). The insert shows the interval of time recorded between 0 and 5.5 s. (b) Estimation of the M_S temperature for the sample 800-DQ via differentiation of the cooling curve recorded in the Gleeble® thermomechanical simulator.

Before the partitioning step, Q&P steel grades peak annealed at 800 °C and 940 °C were quenched to 220 °C ± 1 °C and 310 °C ± 1 °C, respectively. These quench

temperatures were selected to obtain approximately 20% of untransformed austenite before the partitioning step. Due to the experimental limitations produced in treatments performed at high heating rates using dilatometer, the Koistinen-Marburger equation (Eq. 7.1) was employed to estimate the volume fraction of martensite (V_M) below M_S temperature for both steels [29,30]. A K parameter of 0.02 $°C^{-1}$ was selected for the martensite fraction calculation based on the results reported elsewhere [31]. The M_S temperature was determined using differentiation of the cooling curves of samples heat-treated in the Gleeble® thermomechanical simulator, as indicated in Figure 7.2b for the sample 800-DQ. M_S temperatures of 262 °C ± 4 °C and 364 °C ± 5 °C were estimated for the samples peak annealed at 800 °C and 940 °C, respectively.

$$V_M = 1 - e^{-K(M_S - T)} \quad (7.1)$$

The microstructures of the heat-treated samples were characterized by means of secondary electron imaging (SE) and electron backscattered diffraction (EBSD) in an FEI Quanta 450 FEG-SEM. EBSD scans were acquired with a step size of 0.12 µm in a hexagonal scan grid. The fractions of martensite and ferrite in the direct quenched samples were quantified by selecting grains with low and high grain average image quality (GAIQ), respectively [32]. After identifying ferrite in intercritical annealed samples, non-recrystallized ferrite grains were selected by using the grain orientation spread (GOS) criterion [33], where grains of GOS ≥ 4° were assumed as non-recrystallized.

A transmission electron microscope (Jeol JEM-2200FS) operated at 200 kV in STEM mode was used for a detailed microstructural examination of the directly quenched samples. The sample preparation procedure for TEM consisted of grounding the samples to a thickness of 90-100 µm, on the RD-TD plane. Next, using a Struers Tenupol-5 for automatic electrolytic thinning of specimens, discs of 3 mm diameter were polished and thinned via precision twin-jet ion polishing with a 96 v/v% CH_3COOH, 4 v/v% $HClO_4$ solution.

The volume fraction of retained austenite in heat-treated samples was measured using the direct comparison method [34] on X-ray diffraction patterns obtained in a Siemens Kristalloflex D5000 diffractometer equipped with Mo Kα radiation. A step size of 0.03° and a dwell time of 20 s per step were employed during the measurements.

Tensile tests were carried out on subsize dog-bone specimens of 6 mm gauge length and 3 mm width using an Instron 5000 device. Samples were tested at room temperature and at mean strain rate of 0.001 s^{-1} (crosshead speed of 0.36 mm/min). Strain until fracture was evaluated using 2D Digital Image Correlation (DIC) technique.

For more details on microstructural and mechanical characterizations (including tensile sample geometry), the reader is referred to Chapter 3: Experimental procedures.

7.3 Results

7.3.1 Microstructure after heat treatment

Figure 7.3 presents the microstructures of the samples peak annealed to 800 °C and 940 °C, followed by direct cooling to room temperature. Figures 7.3a and 7.3d show a general view of the microstructures of the samples 800-DQ and 940-DQ, respectively. The microstructure of the 800-DQ steel consists of ~45% ferrite (F), ~33% martensite (M) and ~8% retained austenite (γ). Undissolved cementite particles of lamellar (θ_L) and spheroidized (θ_S) morphologies are also observed (Figures 7.3b and 7.3c). Based on the microstructural quantification indicated above, the amount of undissolved pearlite (f_P) in the sample 800-DQ was calculated as ~12% by using the following phase balance:

$$f_P + f_{F_{Total}} + f_M + f_\gamma = 1 \tag{7.2}$$

The undissolved pearlite fraction includes regions composed of both lamellar and spheroidized cementite. However, it is important to note that the fraction of undissolved pearlite is likely overestimated due to the formation of small austenitic grains, of thickness equal to the interlamellar spacing, at the ferrite-cementite interfaces in pearlite (see the light gray patches formed within the cementite lamellae in Figure 7.3c).

Martensite (M) (austenite at high temperature) is formed preferentially at prior pearlitic regions, creating a banded structure elongated along the rolling direction (Figure 7.3a). Dark gray grains correspond to ferrite. Ultrafast heating up to 800 °C led to incomplete ferrite recrystallization and Figure 7.3b shows non-recrystallized ferrite ($F_{N\text{-}Rx}$) within martensitic bands, whereas grains of smooth surface correspond to recrystallized ferrite (F_{Rx}). As mentioned in the experimental section, F_{Rx} and $F_{N\text{-}Rx}$ grains were segmented employing the GOS method (see Figure 7.4b). After ferrite segmentation, ~10% of $F_{N\text{-}Rx}$ was quantified for the sample 800-DQ. M/γ denotes islands of unetched appearance consisting of martensite and retained austenite (Figure 7.3c).

Figures 7.3d to 7.3f display the microstructure of the sample peak annealed at 940 °C. The microstructure of the 940-DQ sample consists predominantly of ~66% martensite and ~27% ferrite. Ferritic grains are mainly located at prior austenite grain boundaries (allotriomorphic ferrite), and the degenerated ferritic plates (F_D) [35] are also distinguished in Figure 7.3f. Additionally, a microstructural rim surrounding martensite is highlighted by dashed lines in Figure 7.3f. After ultrafast heating to 940 °C, a considerably lower amount of spheroidized carbides (θ_S)

remained undissolved compared to the 800-DQ steel. The volume fraction of retained austenite after this treatment is ~6%.

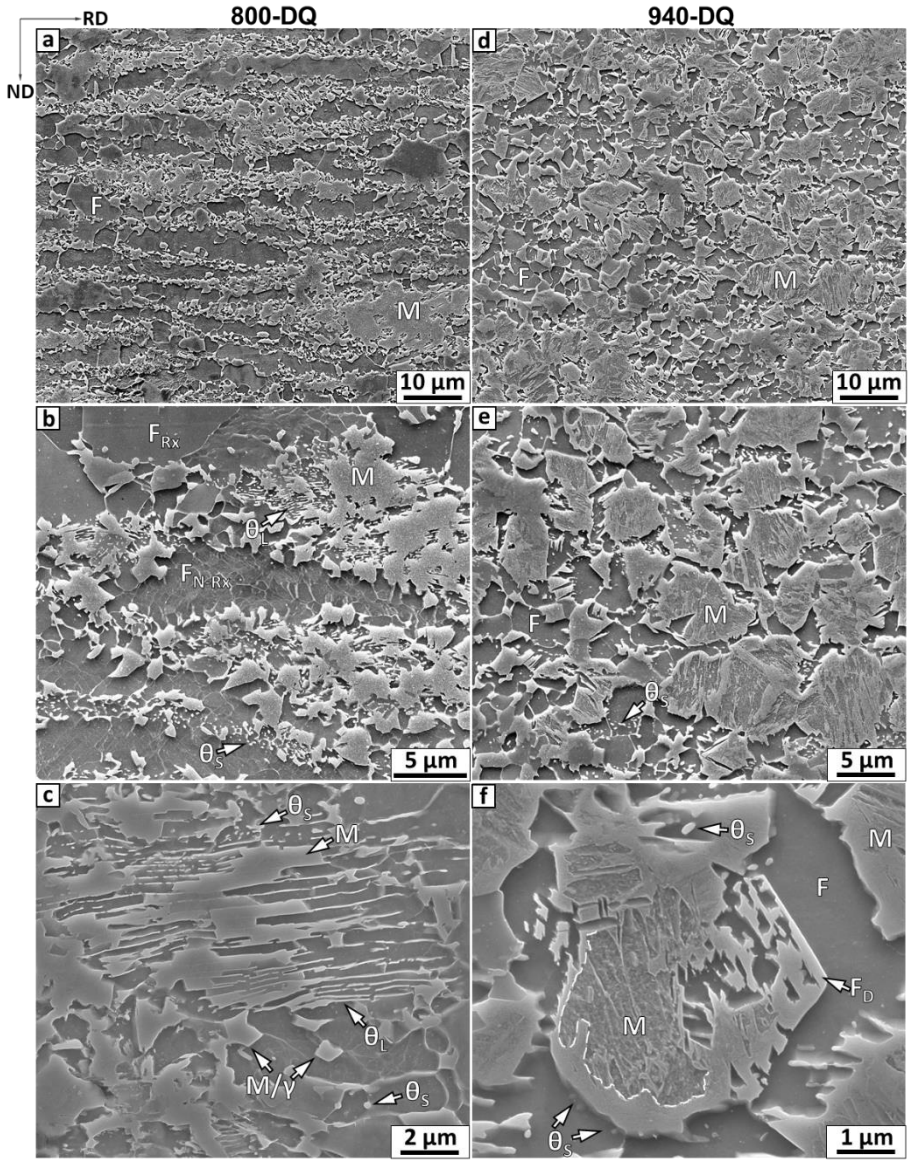

Figure 7.3: SE micrographs of the samples peak annealed at 800 °C and 940 °C, followed by direct quenching to room temperature. Samples (a-c) 800-DQ and (d-f) 940-DQ. F: Ferrite, F_{N-Rx}: Non-recrystallized ferrite, F_{Rx}: Recrystallized ferrite, F_D: Degenerated ferrite, M: Martensite, γ: Retained austenite, θ_S: Spheroidized cementite, θ_L: Lamellar cementite.

An example for identifying M, F_{Rx} and F_{N-Rx} in the sample 800-DQ is shown in Figures 7.4a to 7.4c. M grains correspond to the black to dark green grains in the combined Image Quality (IQ)-GAIQ map presented in Figure 7.4a, whereas yellow to orange

grains can be identified as ferrite. The distribution of constituents matches with the spatial distribution presented in Figures 7.3a and 7.3b, where martensitic bands are separated by ferritic regions. The GAIQ based quantification depends on the distortion of the lattice of each microstructural constituent, which is sensitive to the dislocation density [32]. The higher the lattice distortion, the lower the GAIQ value.

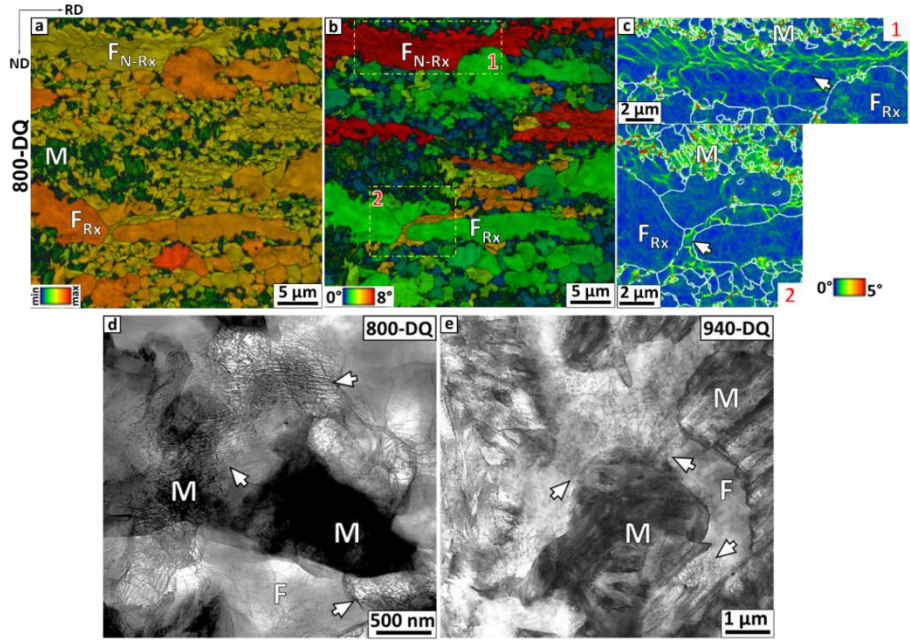

Figure 7.4: EBSD maps for the 800-DQ steel: (a) combined IQ-GAIQ map, (b) combined IQ-GOS map, and (c) enlarged 2nd neighbor KAM maps of the areas 1 and 2 enclosed by dash-dot lines in (b). STEM micrographs of ferritic and martensitic grains in direct quenched samples: (d) sample 800-DQ and (e) sample 940-DQ. White arrows indicate locations of high dislocation density in ferrite.

In comparison to Figure 7.4a, Figure 7.4b indicates that ferritic grains of lower GAIQ value display high local misorientation in GOS notation. Arrays of dislocations create low angle misorientation boundaries, increasing the misorientation angle between the acquired pixels within F_{N-Rx}. Figure 7.4c presents the 2nd neighbor kernel average misorientation (KAM) maps of the areas 1 and 2 enclosed by dash-dot lines in Figure 7.4b. The high misorientation gradients observed between neighbor pixels within F_{N-Rx} (see the arrows in Figure 7.4c) are an indirect indication of regions of high dislocation density and residual strains [36–38]. Thus, those regions correspond to non-recrystallized grains, consistent with the information obtained from the EBSD IQ-GAIQ and IQ-GOS maps. White lines in Figure 7.4c denote high angle grain boundaries of misorientation angle between 15° and 63.5° for martensite, F_{N-Rx} and F_{Rx} grains.

Moreover, the volume expansion generated by the martensitic transformation during cooling [39] produces local plastic deformation of the soft ferritic grains surrounding the newly formed martensite. As shown in Figures 7.4d and 7.4e for the samples 800-DQ and 940-DQ, respectively, the local deformation results in a high dislocation density in ferritic regions adjacent to the martensite-ferrite interphase (see the regions pointed by arrows).

The spatial distribution of constituents after combining ultrafast heating and Q&P are similar to those after direct quenching. For this reason, high magnification images are presented for the Q&P steels (Figure 7.5).

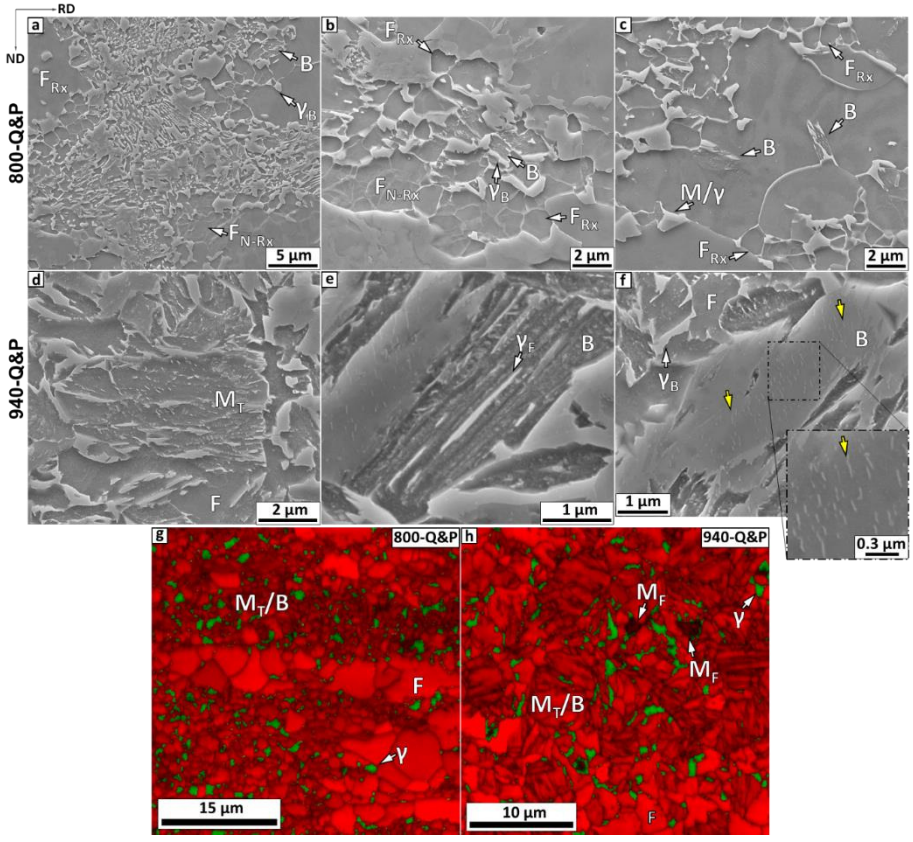

Figure 7.5: SE micrographs of the Q&P samples peak annealed at (a-c) 800 °C and (d-e) 940 °C. In (f) yellow arrows highlight carbides periodically oriented in bainite. Combined EBSD IQ-Phase maps: (g) sample 800-Q&P and (h) sample 940-Q&P. BCC and FCC phases are highlighted in red and green, respectively. F: Ferrite, F_{Rx}: Recrystallized ferrite, $F_{N\text{-}Rx}$: Non-recrystallized ferrite, M_T: Tempered martensite formed during the first quench before partitioning, M_F: Fresh martensite, B: Bainite, γ: Retained austenite with blocky (γ_B) and film (γ_F) morphologies.

The quenching and partitioning treatment led to the formation of tempered martensite (M_T) (Figure 7.5d) and bainite (B) in both steels (Figure 7.5c, 7.5d, 7.5e

and 7.5f). Figure 7.5f shows bainite with nanosized carbides (highlighted by yellow arrows) oriented periodically with respect to the main ferritic lath; this microstructural observation agrees with the morphological description for lower bainite [40]. Retained austenite grains display both film (γ_F) and blocky-like (γ_B) morphologies. Compared to the directly quench samples, the interrupted quenching and partitioning showed that the volume of retained austenite decreased to ~6% in the sample heated up to 800 °C and increased to ~9% in the 940-Q&P steel.

The microstructural contrast created after etching between darker martensitic/bainitic (M_T/B) constituents and unetched γ allows the identification of γ grains with different morphologies via SEM-SE imaging. However, larger unetched islands could also correspond to M/γ constituents. For this reason, combined EBSD IQ-Phase maps are employed for a detailed microstructural characterization.

The distribution of retained austenite grains within the microstructure of the samples 800-Q&P and 940-Q&P is presented in Figures 7.5g and 7.5h, respectively, where retained austenite grains are highlighted in green.

It is clear from the combined EBSD IQ-Phase map for the 800-Q&P steel (Figure 7.5g) that equiaxed retained austenite grains are located at prior pearlitic regions. Those regions are isolated by proeutectoid ferrite bands of higher image quality than the regions covered by M_T/B. Retained austenite grains in the sample 940-Q&P (Figure 7.5h) have a more elongated shape and can be found homogeneously distributed among the BCC microconstituents (martensite, bainite, and ferrite).

Moreover, the IQ scale in the combined EBSD IQ-Phase map allowed the identification of fresh martensite (M_F) in the sample 940-Q&P. The IQ of M_F is lower than the obtained from ferrite, bainite and tempered martensite due to the high lattice distortion produced by the high carbon content and dislocation density of this phase [23]. The fraction of fresh martensite in 940-Q&P was lower than 0.5% and, therefore, assumed as negligible in the present analysis.

The amount of bainite (f_B) in Q&P samples was calculated by balancing the microconstituents fraction:

$$f_B + f_P + f_{F_{Total}} + f_{M_{(K-M)}} + f_{RA} = 1 \tag{7.3}$$

where ($f_{M_{(K-M)}}$) is the fraction of martensite estimated using the Koistinen-Marburger equation in both steels. Ferrite fraction in Q&P samples is assumed to be the same as in DQ samples, and this has been corroborated by metallographic examinations. The same assumption was applied for the undissolved pearlite content in samples peak annealed at 800 °C.

Table 7.2 summarizes the quantification of microconstituents determined via analyses of EBSD Maps, X-ray diffraction and Eqs. 7.1 to 7.3.

Table 7.2: Percentage of microconstituents in the DQ and Q&P samples (standard deviation in parenthesis).

Sample	M	M_T[1]	B	F_{Total}	F_{Rx}[2]	$F_{N\text{-}Rx}$[2]	P[3]	γ, XRD (0.5)
800-DQ	33.26 (4.43)	-	-	45.71 (2.24)	38.42 (1.53)	10.33 (2.09)	12.35	8.30
800-Q&P	-	23.80[1]	11.81	45.71	-	-	12.35	6.33
940-DQ	65.54 (2.31)	-	-	26.65 (5.38)	-	-	-	5.49
940-Q&P	-	48.44[1]	16.24	26.65	-	-	-	8.67

Notes: [1]$f_{M_{(K-M)}}$ in Eq. (7.3). [2]Quantification of F_{Rx} and $F_{N\text{-}Rx}$ estimated using the GOS criterion. [3]f_P in Eq. (7.2)

Figure 7.6 presents the influence of the peak temperature on the grain size of the produced microconstituents. Ferritic and martensitic grains were characterized in direct quenched samples, while the retained austenite grain distributions were evaluated for the Q&P grades. The non-recrystallized ferrite grain size distribution for 800-DQ was determined by the linear interception method across sub-grain boundaries (see the $F_{N\text{-}Rx}$ in Figure 7.3b). Recrystallized ferrite, allotriomorphic ferrite (sample annealed at 940 °C), martensite block length (BL), and retained austenite grains distributions were calculated from the acquired EBSD data, where grains of size smaller than 0.36 µm (3 times the initial step size of 0.12 µm) were removed from the distributions.

Ferritic grain size diameter distributions are displayed in Figure 7.6a. The sample annealed at 800 °C shows two distinctive distributions, where the ultrafine grains with a peak located at ~0.5 µm and maximum size of ~1.7 µm correspond to non-recrystallized ferrite, whereas the recrystallized ferrite grain size ranged from 1.8 to 16 µm. In the sample annealed at 940 °C, ferritic grains obtained from austenite transformation during cooling show a grain size distribution between 0.9 and 7 µm, with a peak close to ~2 µm.

Figure 7.6b shows the martensite block length distribution for the steel grades peak annealed at 800 °C and 940 °C followed by fast cooling. The results revealed that larger blocks are obtained by increasing the peak temperature from 800 °C to 940 °C, and a similar trend is observed for the retained austenite grain major axis distributions in the Q&P steel grades (Figure 7.6c).

The martensitic blocks and retained austenite grains (Figures 7.6b and 7.6c) are smaller for samples peak annealed at 800 °C than at 940 °C. This is an indication of smaller parent austenite grains obtained by heating the samples into the intercritical range. Previous results [9–11] have shown that a high fraction of undissolved carbides and the restricted growth of austenite, controlled by the austenite/ferrite boundary migration, are effective barriers for the austenitic grain growth through the intercritical range in ultrafast heating experiments.

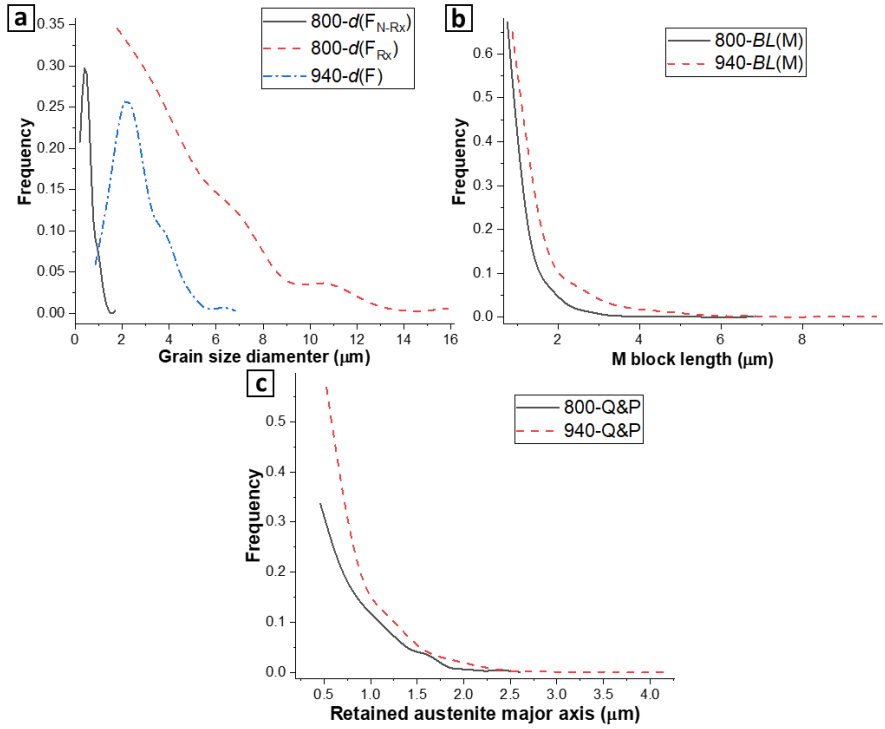

Figure 7.6: (a) Ferritic grain size diameter distribution: $d(F_{N\text{-}Rx})$: non-recrystallized ferrite, $d(F_{Rx})$: recrystallized ferrite and $d(F)$: allotriomorphic ferrite formed during cooling. (b) Martensite block length distributions: $BL(M)$. (c) Retained austenite grain major axis distributions.

7.3.2 Mechanical properties

Engineering stress-strain curves for the samples peak annealed at 800 °C and 940 °C are presented in Figures 7.7a and 7.7b, respectively. Tensile properties are summarized in Table 7.3.

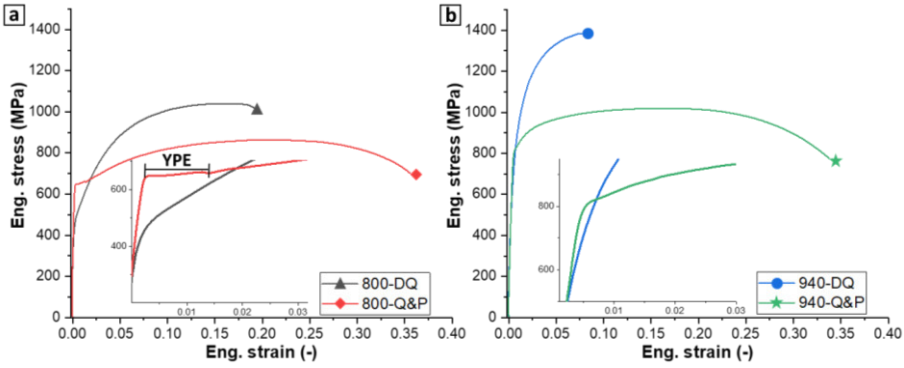

Figure 7.7: Engineering strain-stress curves of the DQ and Q&P steels: (a) samples annealed at 800 °C and (b) samples annealed at 940 °C.

Table 7.3: Tensile properties (standard deviation in parenthesis).

Sample	σ_{ys}, MPa	σ_{UTS}, MPa	σ_{ys}/σ_{UTS}	$\varepsilon_{Uniform}$	ε_{Total}	Absorbed energy, MJ/m^3
800-DQ	480.47 (9.74)	1043.85 (2.47)	0.46 (0.01)	0.16 (0.01)	0.18 (0.01)	171.16 (5.89)
800-Q&P	651.32 (7.65)	864.82 (1.17)	0.75 (0.01)	0.21 (0.01)	0.37 (0.01)	295.69 (8.92)
940-DQ	675.72 (28.13)	1355.29 (26.62)	0.50 (0.01)	-	0.09 (0.01)	102.52 (10.81)
940-Q&P	817.60 (17.30)	1027.00 (7.31)	0.80 (0.01)	0.15 (0.01)	0.33 (0.01)	318.09 (5.75)

Direct quenched samples display continuous yielding, but an incipient inflection is observed at the beginning of the plastic deformation for 800-DQ (Figure 7.7a). Compared to the DQ samples, the combination of UFH and Q&P processes led to an increase in the σ_{ys} of about ~170 MPa and ~142 MPa for the samples 800-Q&P and 940 Q&P, respectively, together with the formation of discontinuous yielding. The 800-Q&P steel exhibits a yield plateau (yield point elongation, YPE) extended up to an engineering strain of ~0.014. At the same time, the σ_{UTS} was reduced from 1044 MPa to 865 MPa and 1355 MPa to 1027 MPa after Q&P treatment for samples peak annealed at 800 °C and 940 °C, respectively. On the other hand, the uniform and total elongation of the Q&P steels increased considerably compared to the DQ samples (see Figure 7.7 and Table 7.3). This improved elongation for the Q&P steels results in a higher energy absorption capacity, expressed as the area under the engineering stress-strain curve. The absorbed energy increased by 73% and 210% replacing the DQ route by the Q&P process in samples annealed at 800 °C and 940 °C, respectively.

7.3.3 Fractography

Macroscopic and microscopic views of fractured tensile samples are presented in Figure 7.8. The figures are listed as follows: Figure (7.8a) 800-DQ, (7.8b) 800-Q&P, (7.8c) 940-DQ, and (7.8d) 940-Q&P. The first column of images shows the longitudinal section of the samples with the ND plane normal to the reader view and the rolling direction is oriented parallel to the loading direction. It is possible to see an apparent change in the macroscopic fracture characteristics of Q&P samples compared to the DQ steels. Q&P samples (Figures 7.8b and 7.8d) display a ductile type of fracture with a necked region that resembles a cup and cone. On the other hand, DQ samples (Figures 7.8a and 7.8c) show a brittle type of fracture without appreciable necking formation.

Micrographs of the fracture surfaces are presented in the second and third columns of images. The sample 800-DQ exhibits a combination of fracture mechanisms consisting of distinctive regions of cleavage and dimples (Figure 7.8a). River marks are observed within the regions fractured by cleavage. The 940-DQ steel (Figure 7.8c) displays a brittle type of fracture, which consists mainly of cleavage. Samples 800-Q&P (Figure 7.8b) and 940-Q&P (Figure 7.8d) present a quasi-cleavage type of fracture with a larger fraction of micro-voids in the former.

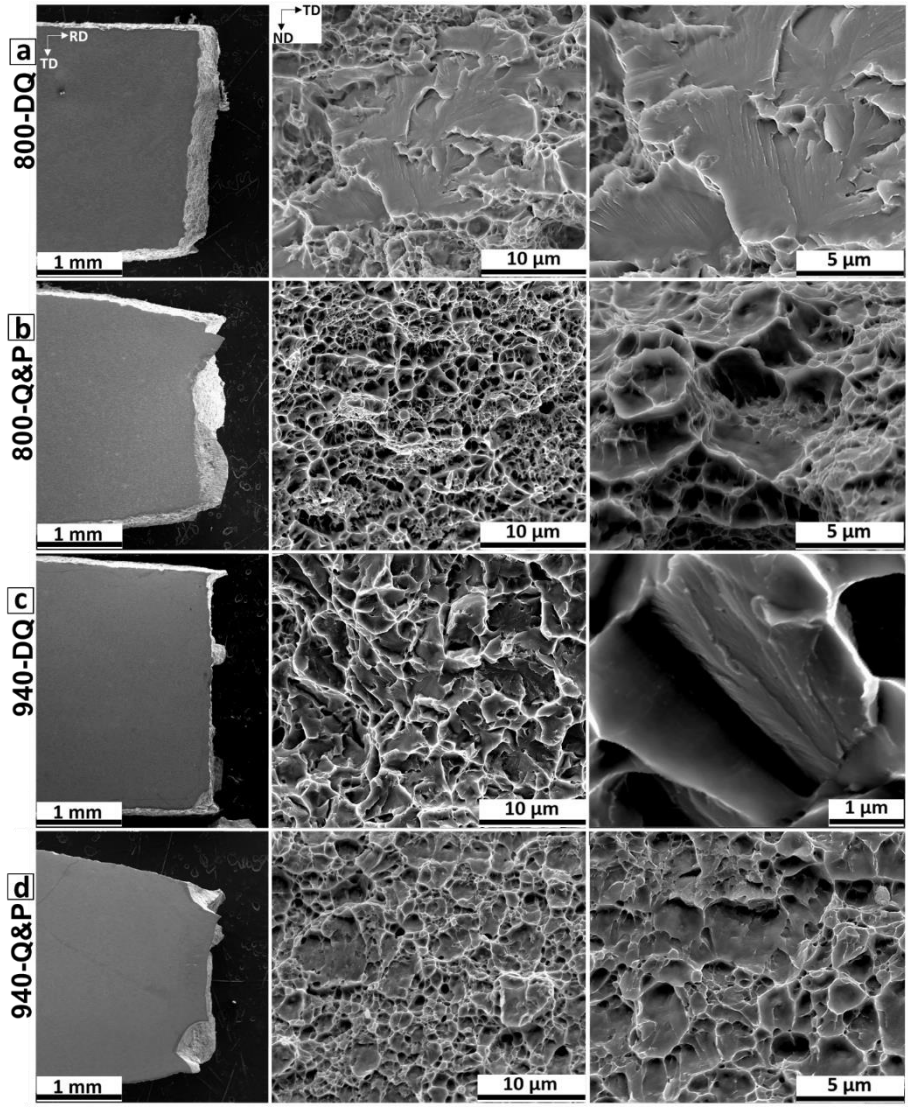

Figure 7.8: Fractography of the studied samples after tensile testing. Samples: (a) 800-DQ, (b) 800-Q&P, (c) 940-DQ and (d) 940-Q&P.

7.4 Discussion

7.4.1 The influence of the peak temperature on the obtained microstructures after ultrafast heating

Directly quenched steels heated up to 800 °C and 940 °C exhibit different distributions of microconstituents but their microstructures are mainly composed of a mixture of ferrite and martensite in different proportions.

The heterogeneous banded microstructures observed in the 800-DQ and 800-Q&P (Figures 7.3a and 7.5g) steels result from several solid-state mechanisms active during heating, including ferrite recovery and recrystallization, cementite spheroidization and dissolution, and preferential austenite formation. These observations were previously reported in the study of austenite formation during ultrafast heating of steels [9,10].

It has been demonstrated that the onset of ferrite recrystallization is shifted to higher temperatures during the ultrafast heating of low alloy steels [9–11]. Consequently, and due to the short soaking time employed at 800 °C, a partially recrystallized ferritic structure was obtained after quenching (Figures 7.3b and 7.4a to 7.4c). Hence, it can be inferred from the microstructural characterization that ferrite recrystallization and austenite formation processes overlapped during the initial heating step. The formation of heterogeneous distribution of ferritic grains for the 800-DQ steel is a consequence of this interaction (Figure 7.6a). The thickening of unpinned recrystallized ferrite grains is restricted by bands of austenite and undissolved pearlite (see Figures 7.3a, 7.3b and 7.4a to 7.4c). Additionally, as shown in Figures 7.5a to 7.5c, austenite grains formed at ferrite/ferrite interfaces impede the grain coarsening of small recrystallized ferritic grains, promoting the grain refinement of the steel grades treated via ultrafast heating into the intercritical temperature range. Recrystallized ferrite grains pinned by austenite particles were primarily found in the vicinity of prior pearlitic bands. Then, this observation suggests that carbides may serve as nucleation points for austenite at those regions, which is supported by the absence of martensitic grains at the central part of non-recrystallized ferrite grains (see Figure 7.3b). These results concur with those reported by Judd and Paxton [41], who demonstrated that spheroidized cementite particles located at ferrite grain boundaries have a strong catalytic effect on the austenite nucleation rate. Since the growth of austenite throughout the intercritical range requires carbon diffusion [42,43], the fast growth of austenite preferentially occurs along deformed pearlitic colonies, which correspond to the carbon rich areas. The spatial distribution of those pearlitic colonies resulted in a banded ferritic-martensitic microstructure after ultrafast heating and cooling. On the other hand, the growth of the austenitic grains located at ferrite/ferrite boundaries depends on the carbon supply from the carbon rich areas [42,43], leading to slow growth of those grains and further grain refinement.

The dissolution of cementite is a diffusion-controlled process [41]. Thus, compared to the 800-DQ sample, the lower fraction of undissolved carbides obtained in the 940-DQ steel can be directly related to the accelerated carbide dissolution at high temperature due to the increased rate of diffusion [41,42]. Incomplete cementite dissolution during annealing can affect the resulting microstructure as follow: it decreases the carbon in solid solution in austenite, and then lowers the hardenability in comparison to a fully homogeneous austenitic (or austenitic-ferritic) microstructure; decreases the amount of austenite formed during the annealing step; lowers average martensitic strength by reduction of the carbon content in the parent austenite; decreases the available carbon for austenite stabilization in the subsequent quenching and partitioning [24]; undissolved cementite particles may act as barriers for grain boundary motion during the annealing step via Zener pinning effect [44].

It is well known that the hardenability of steels can be controlled by two main factors: austenite composition and austenite grain size [45]. In ultrafast heated low alloy steels, the decomposition of austenite is favored by carbon and solute heterogeneities in austenite and the high amount of effective nucleation sites generated by parent austenite grain refinement [2,13,21,22]. As a result, allotriomorphic ferrite grains can be seen decorating prior austenite grain boundaries leading to an even distribution of refined ferritic grains for the 940-DQ sample (Figures 7.3d to 7.3f). The formation of multiple microconstituents within one prior austenitic grain provides indirect evidence of chemical heterogeneity in austenite formed under ultrafast heating rates (Figure 7.3f). It was found that intercritical annealing also led to a fraction of retained slightly higher than the obtained in the 940-DQ steel. Liu et al. [21] evaluated the effect of high heating rates on the microstructure of intercritical annealed low alloy steels and showed that the manganese concentration in cementite could be inherited by austenite nucleated in prior pearlitic regions. At the same time, higher carbon content is expected in those austenitic grains leading to enhanced thermal stability [46] and a higher fraction of retained austenite after direct quenching. This assumption justifies the location of retained austenite grains along bands in prior pearlitic regions for the 800-QP sample (Figure 7.5g).

Since the Q&P steels were heat-treated following the same annealing parameters applied for DQ steels, equal distributions of ferrite grains were obtained. The formation of bainitic ferrite after quenching and partitioning (Figure 7.5 and Table 7.2) indicates that austenite decomposition took place during the partitioning step. This transformation can proceed at a fast rate in low alloy steels, consuming the untransformed austenite in a short time [47]. Moreover, in the presence of martensite, the formation kinetics of bainite is accelerated and Chen et al. reported that the transformation can even proceed without incubation period [47]. The stabilization of austenite by carbon enrichment during bainitic transformation

[47,48] together with carbon partitioning from martensite to austenite [49] resulted in a higher retained austenite fraction after the Q&P process for the samples peak annealed at 940 °C. Contrarily, the formation of bainite during the partitioning step decreases the austenite fraction for the sample 800-Q&P with respect to 800-DQ. Another competitive reaction to the stabilization of austenite through carbon enrichment is the precipitation of carbides during the partitioning step [50,51]. Carbides can be observed in tempered martensite and lower bainite (Figure 7.5), decreasing to a certain extent the available carbon for austenite stabilization during the isothermal holding step at 400 °C. Additionally, carbon trapping at defects and carbon clustering [52–54] might also play a role in the incomplete carbon partitioning from martensite/bainite to austenite.

7.4.2 The relationship between microstructures and mechanical properties

The mechanical behavior of the studied steels has a direct relationship with the microstructures obtained after the combination of UFH and subsequent DQ or Q&P processes. The fraction of martensite in the 940-DQ sample (~67%) was higher than in 800-DQ (~33%). As a result, the σ_{UTS} obtained for the 940-DQ steel was the highest one in this study. The measured σ_{ys} values follow the same trend for the studied samples, including Q&P grades, the larger the initial martensite fraction, the higher the strength. This increment in strength at higher martensite fraction is accompanied by a decrease in the $\varepsilon_{Uniform}$ and ε_{Total} values, which is in agreement with previous findings reported by Speich and Miller [55] for low alloy dual-phase steels with various martensite fractions and nominal carbon contents.

The continuous yielding observed in the 940-DQ steel (Figure 7.7b) is related to the high density of free dislocations in ferrite adjacent to newly formed martensitic grains (Figure 7.4e). Contrarily, the inflection in the stress-strain curve detected at the beginning of the plastic deformation for 800-DQ (Figures 7.7a and 7.7c) could be associated with a certain degree of dislocation pinning by carbon atoms in dislocations arrays observed in non-recrystallized ferrite grains (Figures 7.4a to 7.4c). The lower fraction of martensite formed along bands for the 800-DQ steel may also induce dislocation heterogeneity in the ferritic matrix, reducing the extent of influence of the newly formed dislocations to the yield point attenuation [56].

The increment in σ_{ys} and discontinuous yielding observed for the Q&P steels indicates that the formation of Cottrell atmospheres [57] of carbon atoms around dislocations took place during the partitioning step at 400 °C. The diffusion of carbon atoms to dislocations in ferrite is favored during the partitioning step, and this static aging phenomenon has also been observed in intercritical annealed Q&P [24,58] and austempered steels [59]. Chen et al. [58] demonstrated using atom probe tomography characterization that carbon atoms segregate to dislocations in the plastically deformed ferrite adjacent to martensite during partitioning. The carbon

trapping at dislocations in ferrite enhances its yield strength, resulting in a total yield strength higher than in DQ steels. Moreover, carbon trapping can also occur at dislocations in non-recrystallized ferrite grains located far from the martensitic regions in the 800-Q&P steel, giving rise to the yield plateau (YPE) observed (Figure 7.7a). An apparent advantage of the 940-Q&P sample over the 800-Q&P steel is the attenuation of the YPE, which can be interpreted as a direct result of the higher fraction of martensite (producing a higher and homogeneous distribution of dislocations in ferrite) and the absence of non-recrystallized ferrite grains. The YPE (accompanied by localized deformation) is usually considered to be detrimental for cold forming processing, where cold stamping is one of the routes employed for the fabrication of structural components using formable Q&P steel grades [60].

In addition to the enhancement of the yield strength by carbon trapping at dislocations, the formation of carbon clusters and precipitation of nano-carbides in tempered martensite and bainite (Figure 7.5) could also contribute to an increase of the yield strength after partitioning [61].

The observed decrease of the σ_{UTS} values for Q&P samples with respect to DQ steels can be attributed to the formation of carbon depleted martensite through the precipitation of transitions carbides and carbon partitioning [51], a decrease of dislocation density in martensite [62,63], and bainitic transformation during the partitioning step [64].

In multiphase steels, the stress and strain partitioning between microconstituents with different individual strength levels lead to the development of a multistage strain hardening behavior [56,59]. The strain hardening curves of the studied steel (Figure 7.9) revealed a continuous decrease of work hardening rate with the true strain for the samples 800-DQ and 940-DQ, where the strain hardening for 940-DQ declines rapidly. Contrarily, the Q&P samples show a more sustained strain hardening decreasing, leading to enhanced ductility.

The higher ferrite fraction is responsible for the attenuated decrease of the strain hardening for the 800-DQ steel and the lower strain hardening rate at the beginning of the plastic deformation compared to the 940-DQ steel. Additionally, the transformation of austenite to martensite during straining may account for the improved strain hardening capacity observed for the 800-DQ sample, and this type of behavior has been reported by other authors for intercritical annealed dual-phase steels [65,66]. On the other hand, the higher martensite fraction and the smaller ferritic grain size obtained in the 940-DQ sample resulted in a higher strain hardening rate. It is speculated that during the initial state of straining the deformation of ferrite takes place assisted by the glide of mobile dislocations created by the martensitic transformation [65]. Then, the deformation of ferrite is rapidly constrained by the rigid martensitic grains leading to stress accumulation at the ferrite/martensite boundaries. In the last stage of straining, the simultaneous

deformation of martensite and ferrite proceeds [67], resulting in a brittle response for the 940-DQ steel.

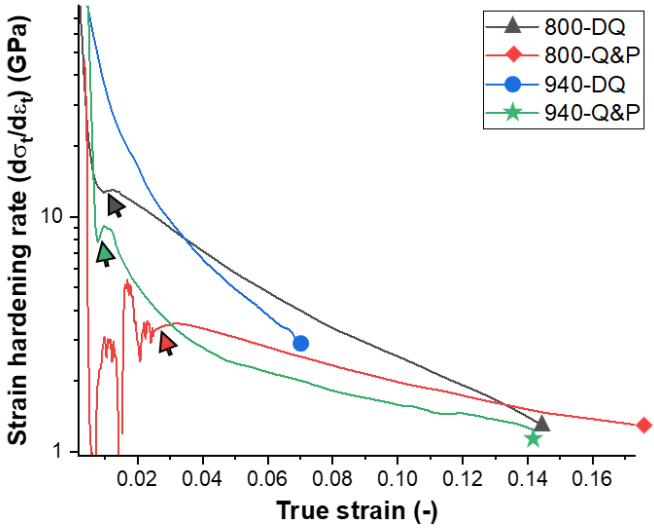

Figure 7.9: Strain hardening rate variation with the true strain. Arrows indicate an increment of the strain hardening rate at the initial stage of the plastic deformation.

Arrows in Figure 7.9 indicate a positive variation of the strain hardening rate with the true strain at the initial stage of yielding for the samples 800-DQ, 800-Q&P and 940-Q&P (the arrow for the sample 800-QP pointed the strain measured after the YPE). Matlock et al. [56] related this type of strain hardening behavior to a degree of inhomogeneous deformation on initial yielding in dual-phase steels, consistent with the pinning effect produced by carbon trapping at dislocations discussed above. Additionally, and according to the literature [59,68,69], it is suggested that the accumulation of dislocations and strain energy in retained austenite grains trigger the austenite to martensite transformation at the early stage of plastic deformation, rising the strain hardening rate [59,68]. This phase transformation creates new plastically deformed fields in the surrounding matrix, increasing the strain hardening of the deformed microconstituents [68,69]. In addition, the newly formed martensitic grains inhibit the dislocation motion process, promoting strain and stress partitioning among surrounding microconstituents. The sustainable strain hardening evolution measured above a true strain value of ~0.05 for Q&P steels might be related to a more effective and prolonged TRIP effect, giving the best strength-ductility balance for the 940-Q&P steel. Indeed, the 940-Q&P steel has nearly the same σ_{UTS} value compared to the sample 800-DQ, but the ε_{Total} was improved by almost 80%. At the same time, the larger fraction of tempered martensite in 940-Q&P conduced to higher σ_{ys} and σ_{UTS} values than in 800-Q&P.

Evidence of the retained austenite to martensite transformation upon straining at room temperature for all the studied samples is presented in Figure 7.10. Since

subsize tensile samples were used in this study, XRD patterns were obtained from an irradiated area that included both the uniformly deformed and necked regions of the fractured samples (shoulders of the tensile samples were removed before the XRD analysis). Peaks $(220)^{FCC}$ and $(311)^{FCC}$ are not detectable in fractured samples (F) for 800-DQ, 800-Q&P and 940-DQ, while a weak peak $(220)^{FCC}$ is observed for 940-Q&P, given a RA fraction lower than 1%.

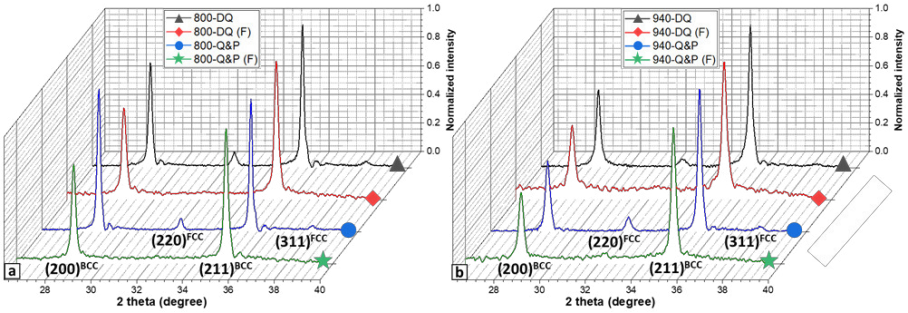

Figure 7.10: XRD patterns for the as heat-treated steels and fractured samples "(F)" after tensile testing. (a) Samples peak annealed at 800 °C. (b) Samples peak annealed at 940 °C.

As has been pointed out in Refs. [68,70], the strain partitioning between microconstituents and their individual deformation mode control the mechanical behavior of TRIP-aided steels. Thus, and considering the similar fraction of retained austenite for the as heat-treated steels, it is concluded that the formation of Cottrell atmospheres, the tempering of martensite and bainite formation play an important role in the mechanical behavior after Q&P.

Figure 7.11 shows the microstructure next to the fracture surface along the loading direction for the studied steels. Uniaxial tensile deformation resulted in more deformed microstructures for the Q&P grades (Figures 7.11c and 7.11d) than for the DQ steels (Figures 7.11a and 7.11b).

The incompatible deformation between the hard quench martensite and soft ferrite produced plastic strain localization [71], resulting in premature failure for DQ steel grades. Such a strain localization, expressed as damage, can be observed in Figures 7.11a and 7.11b, where white arrows indicate the formation of several damage features preferentially located at the interphase between ferrite and martensite. Red arrows indicate cracks in martensite. Figures 7.3d to 7.3f and 7.11b show that ferritic grains are somewhat isolated by martensitic regions in samples annealed at 940 °C. Thus, it can be said that the constrained deformation of those ferritic grains and the strain localization at ferritic/martensitic boundaries resulted in the poor ductility measured for the sample 940-DQ. Likewise, the contribution of the retained austenite grains to the ductility via the TRIP effect in the 940-DQ steels was also surpassed by the strain incompatibility produced by the large fraction of hard martensite.

On the other hand, it is clearly visible that ferritic grains are elongated along the loading direction for the Q&P steels (Figures 7.11c and 7.11d). The tempering of martensite [63] and the formation of bainite [16,17] resulted in softer microconstituents that can accommodate the external deformation, promoting the stress and strain partitioning within the microstructure. The deformation of martensitic and bainitic constituents (see the deformed M_T/B aggregates in Figures 7.11c and 7.11d) also allows the plastic deformation of the ferritic grains to larger levels of strain, resulting in greater elongation for the Q&P steel grades. Microstructural observations presented in Figure 7.11 have a close relation to the fracture surfaces presented in Figure 7.8. The change in the fracture mechanisms observed is highly influenced by the distribution of microconstituents, specially by the fraction of martensite and its state, untempered or tempered.

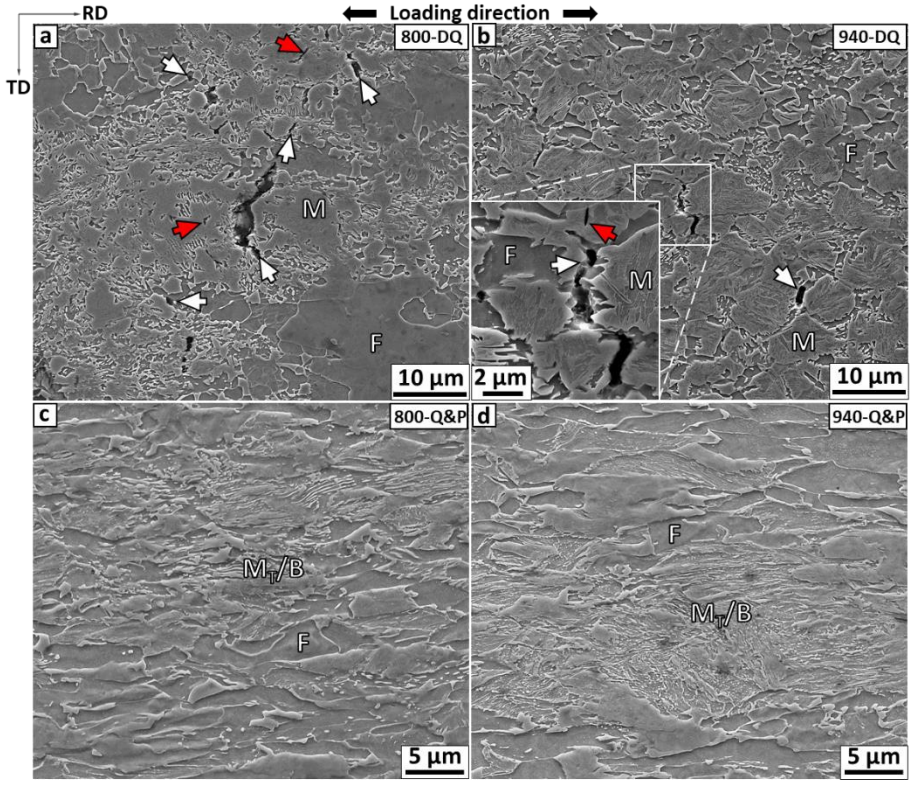

Figure 7.11: Microstructure close to the fracture surface. Samples: (a) 800-DQ, (b) 940-DQ, (c) 800-Q&P and (d) 940-Q&P. White arrows highlight damage and debonding at ferrite-martensite boundaries and red arrows indicate damage in martensite. (Distance from fractured surface 20 – 30 µm). Note: SE micrographs of the Q&P samples are shown at higher magnification for an easier observation of the deformed microconstituents.

σ_{UTS} and ε_{Total} values measured for the ultrafast heated DQ and Q&P steels are summarized in Figure 7.12 and the results are compared with those obtained in conventionally annealed Q&P steels with a partially ferritic matrix [24,26].

Additionally, the tensile properties of the industrially produced Q&P 980 MPa steel grade are included [60,72]. For comparison purposes, the total elongation values obtained by tensile testing in this study and in [26] were corrected according to the methodology proposed in the standard ISO 2256-1 [73]:

$$\varepsilon_2 = \varepsilon_1 \left(\frac{L_1\sqrt{S_2}}{L_2\sqrt{S_1}} \right)^n \quad (7.4)$$

where ε_1, $L_1$and S_1 correspond to the total elongation, gauge length and cross-section of the tested sample. ε_2 is the corrected total elongation estimated for a sample of gauge length of 50 mm (L_2) and cross-section of 12.5x1.2 mm^2 (S_2, width x thickness) according to the geometry presented in the standard ASTM E8/E8M [74]. n is a constant value equal to 0.4 for carbon and low alloy steels [73].

As presented in Figure 7.12, the strength-ductility balance obtained after combining the ultrafast heating and Q&P processes is in the range of the observed in Q&P steels processed through conventional annealing strategies. Moreover, the ultrafast heated 940-Q&P steel shows an attractive combination of mechanical properties close to the stress-strain combination tailored for the commercial Q&P 980 MPa grade. These findings provide information of great technological relevance since the ultrafast heating represents efficient producibility by shortening annealing process time from 200-500 seconds to ~2 seconds.

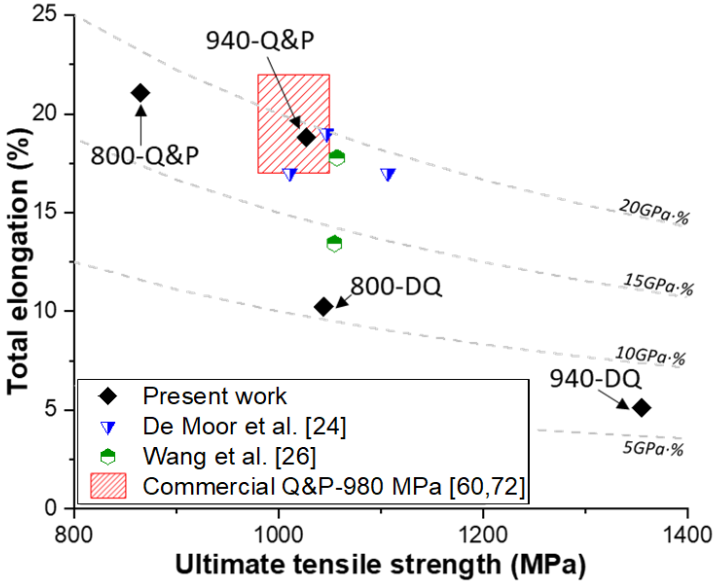

Figure 7.12: σ_{UTS} v/s ε_{Total} diagram for the studied ultrafast heated DQ and Q&P steels and conventionally annealed ferrite-containing Q&P steels. Sample geometry corrected to a gauge length of 50 mm and width of 12.5 mm according to ISO 2256-1 [73]. Reference sample geometry: ASTM E8/E8M [74], standard specimen "Sheet-Type", gauge length = 50 mm.

The development of cost-effective and environmentally friendly steel-making routes positioning the ultrafast heating as a promising approach towards the new generation of steels. The results of this work and recent studies on this subject [18–23] suggest that conventional annealing could be replaced by ultrafast heating to produce sheet steel products. Nevertheless, the evaluation of the mechanical behavior of ultrafast heated Q&P steels subjected to other testing conditions, different than quasi-static uniaxial tension, is still a matter of investigation.

7.5 Conclusions

The effect of the peak temperature on the microstructure and mechanical properties of an ultrafast heated Fe-0.24C-1.4Mn-1.4Si steel subjected to direct quenching and Q&P processes was investigated. The main conclusions from this study are summarized as follow:

- Irrespective of the peak temperature, multiphase microstructures consisting of ferrite, martensite, retained austenite and undissolved carbides were produced after the combination of ultrafast heating and fast cooling. There is an important effect of the peak temperature on the fraction of undissolved carbides and microstructural distribution.
- Bands of martensite and heterogeneous distribution of recrystallized and non-recrystallized ferritic grains were produced after ultrafast heating into the intercritical range. Instead, peak annealing above the A_{C3} temperature leads to the formation of an even distribution of ferritic grains in a matrix that consists mainly of martensite. The elevated peak temperature also contributes to a significantly larger dissolution of cementite.
- Q&P steels display discontinuous yielding accompanied by an increase in the σ_{ys}. The yield point phenomenon observed in the studied Q&P steels is related to dislocation pinning by carbon atoms and the higher ferrite fraction in the 800-Q&P steel led to the formation of yield plateau. Carbon partitioning, tempering of martensite and bainite formation during partitioning at 400 °C accounted for the decrease of ultimate tensile strength in Q&P steels compared to direct quenched steels.
- The high ductility of Q&P steels is attributed to the contribution of a sustainable TRIP effect in combination with a collaborative deformation of the ferritic, bainitic and tempered martensitic constituents. Contrarily, a brittle response was obtained for the DQ steels, where post-necking deformation was not observed during tensile testing. This behavior is the result of strain localization and damage formation at ferrite/hard-martensite grain boundaries.
- Ferrite-containing ultrafast heated Q&P steels displayed enhanced strength-ductility balance with respect to the direct quenched steel grades. Furthermore, the higher fraction of martensite and the well redistributed ferritic grains obtained through heating above the A_{C3} for the 940-Q&P steel led to an σ_{UTS}

value similar to the one measured for the 800-DQ sample, combined with almost doubled total elongation. Moreover, the attained mechanical properties for the 940-Q&P steel were in the range of the exhibited by the industrially produced Q&P 980 MPa steel grade.

According to the presented findings, there is a significant potential to improve the strength-ductility balance in low carbon -low alloyed- steels by using the ultrafast heating process. This is possible by controlling both the peak annealing temperature and the transformation of austenite upon cooling that results in fine-grained mixed microstructures. Nevertheless, further work is required to elucidate the benefits of combining the ultrafast heating and subsequent low-temperature treatments to develop new steel grades and feasible industrial technologies.

References

[1] M.A. Valdes-Tabernero, R.H. Petrov, M.A. Monclus, J.M. Molina-Aldareguia, I. Sabirov, The effect of soaking time after ultrafast heating on the microstructure and mechanical behavior of a low carbon steel, Mater. Sci. Eng. A. 765 (2019) 138276. https://doi.org/10.1016/j.msea.2019.138276.

[2] E.I. Hernandez-Duran, L. Corallo, T. Ros-Yanez, F.M. Castro-Cerda, R.H. Petrov, Influence of Mo-Nb-Ti additions and peak annealing temperature on the microstructure and mechanical properties of low alloy steels after ultrafast heating process, Mater. Sci. Eng. A. 808 (2021) 140928. https://doi.org/10.1016/j.msea.2021.140928.

[3] F.M. Castro Cerda, B. Schulz, D. Celentano, A. Monsalve, I. Sabirov, R.H. Petrov, Exploring the microstructure and tensile properties of cold-rolled low and medium carbon steels after ultrafast heating and quenching, Mater. Sci. Eng. A. 745 (2019) 509–516. https://doi.org/10.1016/j.msea.2018.12.036.

[4] T. Lolla, G. Cola, B. Narayanan, B. Alexandrov, S.S. Babu, Development of rapid heating and cooling (flash processing) process to produce advanced high strength steel microstructures, Mater. Sci. Technol. 27 (2011) 863–875. https://doi.org/10.1179/174328409X433813.

[5] F.M. Castro Cerda, L.A.I. Kestens, R.H. Petrov, “Flash” Annealing in a Cold-Rolled Low Carbon Steel Alloyed with Cr, Mn, Mo, and Nb: Part II—Anisothermal Recrystallization and Transformation Textures, Steel Res. Int. 90 (2019) 1–13. https://doi.org/10.1002/srin.201800277.

[6] D.K. Matlock, S. Kang, E. De Moor, J.G. Speer, Applications of rapid thermal processing to advanced high strength sheet steel developments, Mater. Charact. 166 (2020) 110397. https://doi.org/10.1016/j.matchar.2020.110397.

[7] Q. Meng, J. Li, H. Zheng, High-efficiency fast-heating annealing of a cold-rolled dual-phase steel, Mater. Des. 58 (2014) 194–197. https://doi.org/10.1016/j.matdes.2014.01.055.

[8] F.C. Cerda, C. Goulas, I. Sabirov, S. Papaefthymiou, A. Monsalve, Microstructure, texture and mechanical properties in a low carbon steel after ultrafast heating, Mater. Sci. Eng. A. 672 (2016) 108–120. https://doi.org/10.1016/j.msea.2016.06.056.

[9] L.S. Thomas, D.K. Matlock, Formation of Banded Microstructures with Rapid Intercritical Annealing of Cold-Rolled Sheet Steel, Metall. Mater. Trans. A Phys. Metall. Mater. Sci. 49 (2018) 4456–4473. https://doi.org/10.1007/s11661-018-4742-9.

[10] H. Azizi-Alizamini, M. Militzer, W.J. Poole, Austenite formation in plain low-carbon steels, Metall. Mater. Trans. A Phys. Metall. Mater. Sci. 42 (2011) 1544–1557. https://doi.org/10.1007/s11661-010-0551-5.

[11] J. Huang, W.J. Poole, M. Militzer, Austenite Formation during Intercritical Annealing, Metall. Mater. Trans. A. 35 (2004) 3363–3375. https://doi.org/10.1007/s11661-004-0173-x.

[12] A. Banis, E.I. Hernandez-Duran, V. Bliznuk, I. Sabirov, R.H. Petrov, S. Papaefthymiou, The effect of ultra-fast heating on the microstructure, grain size and texture evolution of a commercial low-c, medium-Mn DP steel, Metals (Basel). 9 (2019). https://doi.org/10.3390/met9080877.

[13] A. Banis, M. Bouzouni, E. Gavalas, S. Papaefthymiou, The formation of a mixed martensitic / bainitic microstructure and the retainment of austenite in a medium-carbon steel during ultra-fast heating, Mater. Today Commun. 26 (2021) 101994. https://doi.org/10.1016/j.mtcomm.2020.101994.

[14] K. Abbaszadeh, H. Saghafian, S. Kheirandish, Effect of Bainite Morphology on Mechanical Properties of the Mixed Bainite-martensite Microstructure in D6AC Steel, J. Mater. Sci. Technol. 28 (2012) 336–342. https://doi.org/10.1016/S1005-0302(12)60065-6.

[15] Y. Tomita, K. Okabayashi, Improvement in Lower Temperature Mechanical Properties of 0.40 Pct C-Ni-Cr-Mo Ultrahigh Strength Steel with the Second Phase Lower Bainite, Metall. Trans. A. 14 (1983) 485–492. https://doi.org/10.1007/BF02644225.

[16] Y. Tomita, K. Okabayashi, Modified Heat Treatment for Lower Temperature Improvement of the Mechanical Properties of Two Ultrahigh Strength Low Alloy Steels, Metall. Trans. A. 16 (1985) 83–91. https://doi.org/10.1007/BF02656715.

[17] T.V.L. Rao, S.N. Dikshit, G. Malakondaiah, P.R. Rao, On mixed upper bainite-martensite in an AISI 4330 steel exhibiting an uncommonly improved strength-toughness combination, Scr. Metall. Mater. 24 (1990) 1323–1328. https://doi.org/10.1016/0956-716X(90)90350-P.

[18] D. De Knijf, A. Puype, C. Föjer, R. Petrov, The influence of ultra-fast annealing prior to quenching and partitioning on the microstructure and mechanical properties, Mater. Sci. Eng. A. 627 (2015) 182–190. https://doi.org/10.1016/j.msea.2014.12.118.

[19] G. Liu, S.G. Zhang, Q.G. Meng, J. Wang, J. Li, Effect of heating rate on microstructural evolution and mechanical properties of cold-rolled quenching and partitioning steel, Ironmak. Steelmak. 44 (2016) 202–209. https://doi.org/10.1080/03019233.2016.1209887.

[20] G. Liu, S. Zhang, J. Li, J. Wang, Q. Meng, Fast-heating for intercritical annealing of cold-rolled quenching and partitioning steel, Mater. Sci. Eng. A. 669 (2016) 387–395. https://doi.org/10.1016/j.msea.2016.05.106.

[21] G. Liu, T. Li, Z. Yang, C. Zhang, J. Li, H. Chen, On the role of chemical heterogeneity in phase transformations and mechanical behavior of flash annealed quenching &

partitioning steels, Acta Mater. 201 (2020) 266–277. https://doi.org/10.1016/j.actamat.2020.10.007.

[22] J. Dai, Q. Meng, H. Zheng, An innovative pathway to produce high-performance quenching and partitioning steel through ultra-fast full austenitization annealing, Mater. Today Commun. 25 (2020) 101272. https://doi.org/10.1016/j.mtcomm.2020.101272.

[23] E.I. Hernandez-Duran, T. Ros-Yanez, F.M. Castro-Cerda, R.H. Petrov, The influence of the heating rate on the microstructure and mechanical properties of a peak annealed quenched and partitioned steel, Mater. Sci. Eng. A. 797 (2020) 140061. https://doi.org/10.1016/j.msea.2020.140061.

[24] E. De Moor, J.G. Speer, D.K. Matlock, J.H. Kwak, S.B. Lee, Effect of carbon and manganese on the quenching and partitioning response of CMnSi steels, ISIJ Int. 51 (2011) 137–144. https://doi.org/10.2355/isijinternational.51.137.

[25] S. Yan, X. Liu, W.J. Liu, T. Liang, B. Zhang, L. Liu, Y. Zhao, Comparative study on microstructure and mechanical properties of a C-Mn-Si steel treated by quenching and partitioning (Q&P) processes after a full and intercritical austenitization, Mater. Sci. Eng. A. 684 (2017) 261–269. https://doi.org/10.1016/j.msea.2016.12.026.

[26] X. Wang, L. Liu, R.D. Liu, M.X. Huang, Benefits of Intercritical Annealing in Quenching and Partitioning Steel, Metall. Mater. Trans. A Phys. Metall. Mater. Sci. 49 (2018) 1460–1464. https://doi.org/10.1007/s11661-018-4559-6.

[27] C. Kickinger, C. Suppan, T. Hebesberger, R. Schnitzer, C. Hofer, Microstructure and mechanical properties of partially ferritic Q&P steels, Mater. Sci. Eng. A. 815 (2021) 141296. https://doi.org/10.1016/j.msea.2021.141296.

[28] E. Hernandez-Duran, L. Corallo, T. Ros-Yanez, F. Castro-Cerda, R.H. Petrov, The Effect of Different Annealing Strategies on the Microstructure Development and Mechanical Response of Austempered Steels, Metals (Basel). 1041 (2021) 1–20. https://doi.org/10.3390/met11071041.

[29] D.P. Koistinen, R.E. Marburger, A general equation prescribing the extent of the austenite-martensite transformation in pure iron-carbon alloys and plain carbon steels, Acta Metall. 7 (1959) 59–60. https://doi.org/10.1016/0001-6160(59)90170-1.

[30] D. V. Edmonds, K. He, F.C. Rizzo, B.C. De Cooman, D.K. Matlock, J.G. Speer, Quenching and partitioning martensite-A novel steel heat treatment, Mater. Sci. Eng. A. 438–440 (2006) 25–34. https://doi.org/10.1016/j.msea.2006.02.133.

[31] C. Celada-Casero, J. Sietsma, M.J. Santofimia, The role of the austenite grain size in the martensitic transformation in low carbon steels, Mater. Des. 167 (2019). https://doi.org/10.1016/j.matdes.2019.107625.

[32] R.H. Petrov, L.A.I. Kestens, Advanced High-Strength Steels: Electron Backscatter Diffraction (EBSD), Encycl. Iron, Steel, Their Alloy. (2015) 46–69. https://doi.org/10.1081/E-EISA-120050786.

[33] M.A. Davinci, D. Samantaray, U. Borah, S.K. Albert, A new critical point on the stress-strain curve : Delineation of dynamic recrystallization from grain growth, Mater. Des. 116 (2017) 495–503. https://doi.org/10.1016/j.matdes.2016.12.053.

[34] C.F. Jatczak, Retained austenite and its measurement by X-ray diffraction, SAE Tech. Pap. 89 (1980) 1657–1676. https://doi.org/10.4271/800426.

[35] Aaronson H.I., The proeutectoid ferrite and the proeutectoid cementite reactions, in: V. Zackay (Ed.), Decompos. Austenite by Diffus. Process., Interscience Publishers, Philadelphia, PA, 1960: pp. 387–546.

[36] W. Hsu, L. Chang, P. Sun, N. Ho, P. Kao, I. Hsiao, Correlation between Recrystallization Texture and Heterogeneities in Deformed Structure of an Electrical Steel by Electron Back-scatter Diffraction, ISIJ Int. 55 (2015) 2212–2216. https://doi.org/10.2355/isijinternational.ISIJINT-2015-159.

[37] N. Allain-bonasso, F. Wagner, S. Berbenni, D.P. Field, A study of the heterogeneity of plastic deformation in IF steel by EBSD, Mater. Sci. Eng. A. 548 (2012) 56–63. https://doi.org/10.1016/j.msea.2012.03.068.

[38] M. Calcagnotto, D. Ponge, E. Demir, D. Raabe, Orientation gradients and geometrically necessary dislocations in ultrafine grained dual-phase steels studied by 2D and 3D EBSD, Mater. Sci. Eng. A. 527 (2010) 2738–2746. https://doi.org/10.1016/j.msea.2010.01.004.

[39] J.M. Moyer, G.S. Ansell, The Volume Expansion Accompanying the Martensite Transformation in Iron-Carbon Alloys, Metall. Trans. A. 6 (1975) 1785–1791. https://doi.org/10.1007/BF02642308.

[40] G. Spanos, H.S. Fang, H.I. Aaronson, A mechanism for the formation of lower bainite, Metall. Trans. A. 21 (1990) 1381–1390. https://doi.org/10.1007/BF02672558.

[41] R.R. Judd, H.W. Paxton, Kinetics of austenite formation from a spheroidized ferrite-carbide aggregate, Trans. Met. Soc. AIME. 242 (1968) 206–215.

[42] G.R. Speich, V.A. Demarest, R.L. Miller, Formation of Austenite During Intercritical Annealing of Dual-Phase Steels, Metall. Mater. Trans. A. 12 (1981) 1419–1428. https://doi.org/10.1007/BF02643686.

[43] V.I. Savran, Y. Leeuwen, D.N. Hanlon, C. Kwakernaak, W.G. Sloof, J. Sietsma, Microstructural features of austenite formation in C35 and C45 alloys, Metall. Mater. Trans. A Phys. Metall. Mater. Sci. 38 (2007) 946–955. https://doi.org/10.1007/s11661-007-9128-3.

[44] C. Smith, Grains, Phases, and Interfaces—an Interpretation of Microstructure, Trans. AIME. 175 (1948) 15–51.

[45] E. Davenport, E. Bain, General relations between grain-size and hardenability and the normality of steels, ASM Trans. Q. 22 (1934) 879–921.

[46] M. Belde, H. Springer, G. Inden, D. Raabe, Multiphase microstructures via confined precipitation and dissolution of vessel phases: Example of austenite in martensitic steel, Acta Mater. 86 (2015) 1–14. https://doi.org/10.1016/j.actamat.2014.11.025.

[47] S. Chen, C. Wang, L. Shan, Y. Li, X. Zhao, W. Xu, Revealing the Conditions of Bainitic Transformation in Quenching and Partitioning Steels, Metall. Mater. Trans. A Phys. Metall. Mater. Sci. 50 (2019) 4037–4046. https://doi.org/10.1007/s11661-019-05341-7.

[48] S. Matas, R.F. Hehemann, The Structure of Bainite in Hypoeutectoid Steels, Trans. Metall. Soc. AIME. 221 (1961) 179–185.

[49] J. Speer, D.K. Matlock, B.C. De Cooman, J.G. Schroth, Carbon partitioning into austenite after martensite transformation, Acta Mater. 51 (2003) 2611–2622.

https://doi.org/10.1016/S1359-6454(03)00059-4.

[50] A.Z. Hanzaki, S. Yue, P.D. Hodgson, The Influence of Bainite on Retained Austenite Characteristics in Si-Mn TRIP Steels, ISIJ Int. 35 (1995) 79–85. https://doi.org/10.2355/isijinternational.35.79.

[51] D.T. Pierce, D.R. Coughlin, D.L. Williamson, K.D. Clarke, A.J. Clarke, J.G. Speer, Characterization of transition carbides in quench and partitioned steel microstructures by Mossbauer spectroscopy and complementary techniques, Acta Mater. 90 (2015) 417–430. https://doi.org/10.1016/j.actamat.2015.01.024.

[52] F.G. Caballero, M.K. Miller, S.S. Babu, C. Garcia-Mateo, Atomic scale observations of bainite transformation in a high carbon high silicon steel, Acta Mater. 55 (2007) 381–390. https://doi.org/10.1016/j.actamat.2006.08.033.

[53] G.A. Thomas, F. Danoix, J.G. Speer, S.W. Thompson, F. Cuvilly, Carbon atom re-distribution during quenching and partitioning, ISIJ Int. 54 (2014) 2900–2906. https://doi.org/10.2355/isijinternational.54.2900.

[54] E.A. Ariza, J. Poplawsky, W. Guo, K. Unocic, A.J. Ramirez, A.P. Tschiptschin, S.S. Babu, Evaluation of Carbon Partitioning in New Generation of Quench and Partitioning (Q&P) Steels, Metall. Mater. Trans. A Phys. Metall. Mater. Sci. 49 (2018) 4809–4823. https://doi.org/10.1007/s11661-018-4743-8.

[55] G. Speich, R. Miller, Mechanical properties of ferrite-martensite steels., in: J.W. Morris, R. Kot (Eds.), Struct. Prop. Dual-Phase Steels, The metallurgical society of AIME, New Orleans, 1979: pp. 145–182.

[56] D. Matlock, G. Krauss, L. Ramos, G. Huppi, A correlation of processing variables with deformation behavior of Dual-Phase steels, in: J.W. Morris, R. Kot (Eds.), Struct. Prop. Dual-Phase Steels, The metallurgical society of AIME, New Orleans, 1979: pp. 62–90.

[57] A.H. Cottrell, B. Bilby, Dislocation Theory of Yielding and Strain Ageing of Iron, Proc. Phys. Soc. A. 62 (1949) 49–62.

[58] P. Chen, G.D. Wang, A. V. Ceguerra, A.J. Breen, S.P. Ringer, X.C. Xiong, Q. Lu, J.F. Wang, H.L. Yi, Yield Strength Enhancement by Carbon Trapping in Ferrite of the Quenching and Partitioning Steel, Metall. Mater. Trans. A Phys. Metall. Mater. Sci. 49 (2018) 235–240. https://doi.org/10.1007/s11661-017-4364-7.

[59] F. Alharbi, A.A. Gazder, A. Kostryzhev, B.C. De Cooman, E. V. Pereloma, The effect of processing parameters on the microstructure and mechanical properties of low-Si transformation-induced plasticity steels, J. Mater. Sci. 49 (2014) 2960–2974. https://doi.org/10.1007/s10853-013-8008-z.

[60] L. Wang, J.G. Speer, Quenching and Partitioning Steel Heat Treatment, Metallogr. Microstruct. Anal. 2 (2013) 268–281. https://doi.org/10.1007/s13632-013-0082-8.

[61] T. Waterschoot, S. Vandeputte, B.C. De Cooman, Static Strain Aging Phenomena in Cold-Rolled Dual-Phase Steels, Metall. Mater. Trans. A. 34A (2003) 781–791. https://doi.org/10.1007/s11661-003-0113-1.

[62] T. Swarr, G. Krauss, The effect of structure on the deformation of as-quenched and tempered martensite in an Fe-0.2 pct C alloy, Metall. Trans. A. 7 (1976) 41–48. https://doi.org/10.1007/BF02644037.

[63] G. Krauss, Tempering of Lath Martensite in Low and Medium Carbon Steels :

Assessment and Challenges, Steel Res. Int. 87 (2017) 1–18. https://doi.org/10.1002/srin.201700038.

[64] S. Ebner, C. Suppan, A. Stark, R. Schnitzer, C. Hofer, Austenite decomposition and carbon partitioning during quenching and partitioning heat treatments studied via in-situ X-ray diffraction, Mater. Des. 178 (2019) 107862. https://doi.org/10.1016/j.matdes.2019.107862.

[65] J. Rigsbee, P. VanderArend, Laboratory studies of microstructures and structure-property relationship in " Dual-Phase " HSLA steels, in: A. Davenport (Ed.), Formable HSLA Dual-Phase Steels, The metallurgical society of AIME, Chicago, 1977: pp. 56–86.

[66] S. Sangal, N. Goel, K. Tangri, A Theoretical Model for the Flow Behavior of Commercial Dual-Phase Steels Containing Metastable Retained Austenite: Part II. Calculation of Flow Curves, Metall. Trans. A. 16 (1985). https://doi.org/10.1007/BF02662403.

[67] A. Kumar, S.B. Singh, K.K. Ray, Influence of bainite/martensite-content on the tensile properties of low carbon dual-phase steels, Mater. Sci. Eng. A. 474 (2008) 270–282. https://doi.org/10.1016/j.msea.2007.05.007.

[68] I.B. Timokhina, P.D. Hodgson, E. V Pereloma, Effect of microstructure on the stability of retained austenite in Transformation-Induced-Plasticity steels, Metall. Mater. Trans. A. 35 (2004) 2331–2340. https://doi.org/10.1007/s11661-006-0213-9.

[69] N.C. Goel, S. Sangal, K. Tangri, A Theoretical Model for the Flow Behavior of Commercial Dual-Phase Steels Containing Metastable Retained Austenite: Part I. Derivation of Flow Curve Equations, Metall. Trans. A. 16 (1985) 2013–2021. https://doi.org/10.1007/BF02662402.

[70] J.H. Ryu, D. Kim, S. Kim, H.K.D.H. Bhadeshia, Strain partitioning and mechanical stability of retained austenite, Scr. Mater. 63 (2010) 297–299. https://doi.org/10.1016/j.scriptamat.2010.04.020.

[71] S.K. Paul, Real microstructure based micromechanical model to simulate microstructural level deformation behavior and failure initiation in DP 590 steel, J. Mater. 44 (2013) 397–406. https://doi.org/10.1016/j.matdes.2012.08.023.

[72] P. McKune, A. Khutorsky, K. Butala, Replacing Press Hardenable Steel with 980 MPa Generation 3 Steel for Automotive Pillars, SAE Tech. Pap. 2018-April (2018) 1–7. https://doi.org/10.4271/2018-01-0117.

[73] International Organization for Standardization (ISO), ISO 2566-1:1984. Steel-Conversion of elongation values - Part 1: Carbon and low alloy steels, Geneve, Switzerland, 1984.

[74] ASTM-International, E8/E8M-16a. Standard Test Methods for Tension Testing of Metallic Materials, Philadelphia, PA, 2020. https://doi.org/10.1520/E0008.

Chapter 8

General conclusions and future work

8.1 Summary of the conclusions

The results presented in this thesis focus on the evaluation of the microstructure and mechanical properties in AHSS annealed via ultrafast heating (UFH). Different steel grades were produced by combining ultrafast heating and different thermal pathways on steels with pre-selected chemical compositions. The most significant findings are summarized as follows:

In Chapter 4, an Fe-0.19C-1.87Mn-1.42Si (0.2C) and an Fe-0.19C-1.99Mn-1.43Si-0.32Mo-0.035Nb-0.020Ti (0.2CMoNbTi) steels were subjected to continuous heating in the range from 10 °C/s to 1000 °C/s, followed by direct fast cooling to room temperature. Two peak temperatures were used, 950 °C and the thermodynamically defined A_m temperature. It was found that increasing the heating rate from 10°C/s to 100 °C/s led to microstructural grain refinement in both steels. However, compared to the samples heated at 100 °C/s, raising the heating rate to 1000 °C/s did not cause a significant microstructural refinement. Additionally, the microstructural characterization revealed that the grain size variation in the microalloyed steel was less sensitive to the effect of the heating rate. This is the result of the Zener pinning effect created by undissolved Nb/Ti-rich carbides during the austenite grain boundary motion. When the A_m temperature was selected as peak temperature, incomplete proeutectoid ferrite dissolution was found to occur in high heating rate experiments, resulting in a higher fraction of ferrite after heat treating. Lower ferrite fractions and larger parent austenite grains were obtained by heating the samples above the estimated A_{C3} temperature. In addition, it was found that the additions of Mo, Nb and Ti effectively suppress the transformation of austenite to ferrite upon cooling, resulting in a fraction of martensite/bainite higher than the obtained in the 0.2C. The results indicate that the formation of banded microstructures and the presence of ferrite determine the mechanical behavior, leading to a decrease in strength and total elongation for the samples made of the 0.2C steel subjected to UFH. Contrarily, the overall mechanical behavior of the 0.2CMoNbTi steel remained unaltered despite the applied heat treatment.

In Chapter 5, the effect of the heating rate on the microstructure and mechanical properties of an Fe-0.28C-1.91Mn-1.44Si (0.3C) steel subjected to quenching and partitioning (Q&P) process was studied. The influence of the heating rate on the grain refinement is consistent with that observed in Chapter 4 for the 0.2C and 0.2CMoNbTi steels, where the parent austenite grain size distribution for the sample heated at 700 °C/s is marginally smaller than the one for the sample heated at

100 °C/s. After the Q&P process, the retained austenite volume fractions did not show a dependence on the prior heating rate, resulting in similar fractions for all heat-treated samples. The evaluation of the mechanical properties indicated that the mechanical behavior is not significantly affected by the microstructural modifications created after high heating rates. However, the uniform elongation improved slightly for the UFH steels compared to the steel heated at 10 °C/s. The studied steels display equivalent strain hardening behavior and mechanical properties. This is related to a comparable fraction and average composition of the retained austenite and the formation of a matrix composed mainly of tempered martensite.

Thermal cycling (TC) and rapid heating are known routes for refining the parent austenite grain size in steels, and consequently, the size of the transformation products obtained after heat treating. In Chapter 6, the Fe-0.28C-1.91Mn-1.44Si (0.3C) steel was subjected to conventional annealing (CA), TC and UFH followed by isothermal soaking at 400 °C for producing TRIP-aided bainitic steels. Similar morphology and size distributions of parent austenite grains and bainitic blocks were produced after TC and UFH, being both of them finer than the obtained for the CA steel. It was found that UFH led to the formation of a heterogeneous microstructure, and bands of ferrite were observed forming a microstructural pattern that resembled the initial deformed ferritic-pearlitic microstructure. Accordingly, the heterogeneous microstructure is proposed to be the result of chemical gradients in the parent austenite. Compared to CA and TC, UFH resulted in improved elongation and energy absorption capacity, possibly owing to an enhanced and prolonged TRIP effect.

Finally, in Chapter 7, an Fe-0.24C-1.39Mn-1.42Si (0.25C) steel was heated at 500 °C/s up to intercritical range and above the A_{C3} temperature followed by direct quenching (DQ) and Q&P processes. It was found that intercritical annealing produced microstructural banding along the rolling direction, where ferrite bands were separated by a mixture of martensite, retained austenite and undissolved carbides. Non-recrystallized ferrite grains were also observed as the result of the incomplete ferrite recrystallization due to the high heating rate applied. Instead, heating above the A_{C3} temperature, followed by rapid cooling, resulted in an even distribution of allotriomorphic ferritic grains in a martensitic matrix. After the Q&P process, bainite formation and tempering of martensite were produced.

Additionally, the occurrence of discontinuous yielding and enhancement of the yield point for the Q&P steels indicated that carbon trapping at dislocations took place during the partitioning step. The Q&P process also led to a decrease in the ultimate strength value compared to the DQ steels. However, the decrease in strength for the Q&P steels was accompanied by a significant improvement in elongation and energy absorption capacity. The evaluation of the strain hardening rate suggested that an improved strain-stress partitioning among microconstituents and prolonged TRIP

effect were obtained for the Q&P steels. Moreover, the ultimate strength and total elongation values of the Q&P steel heated above the A_{C3} temperature lie in the property window defined for the commercially produced Q&P-980MPa steel grade, classified as a 3rd generation AHSS.

In summary, the present research demonstrates that, under laboratory conditions, the tensile properties of steel grades subjected to ultrafast heating could be at least as good as those obtained in conventionally annealed cold-rolled low alloy AHSS. Microstructural characterization suggested that the grain refinement obtained after high heating rate experiments does not play a relevant role in the strength of cold-rolled steel grades with a martensitic or bainitic matrix. Instead, the formation of mixed microstructures is expected to be the main reason for the improved balance of strength and ductility. However, it is speculated that the enhanced mechanical response depends on the fraction and distribution of microconstituents, together with an effective strain-stress partitioning upon deformation.

Figure 8.1 summarizes the tensile properties (ε_{Total} and σ_{UTS}) obtained in this study, and the results are compared to those reported for different industrially produced AHSS for automotive applications. The tensile properties of martensitic (MS) [1], Dual-Phase (DP) [2,3], Complex-Phase (CP) [2], Q&P [4,5] and TRIP-aided bainitic ferritic steels (TBF) [2,6,7] are shown. The results presented in this thesis indicate that the combinations of ultrafast heating and low-temperature isothermal treatments, such as quenching and partitioning or austempering, lead to a strength-ductility balance in the range exhibited by the commercially available 3rd generation of AHSS. In addition, the 0.2C and 0.2CMoNbTi steels, with a microstructure mainly consisting of martensite obtained after continuous heating and direct cooling, also display a considerable high strength, which is required in the production of reinforcement parts for automotive components. The findings reported in this work provide new evidence for the effective applicability of the ultrafast heating of steel and give insight into the heat treatment design for future industrial implementations.

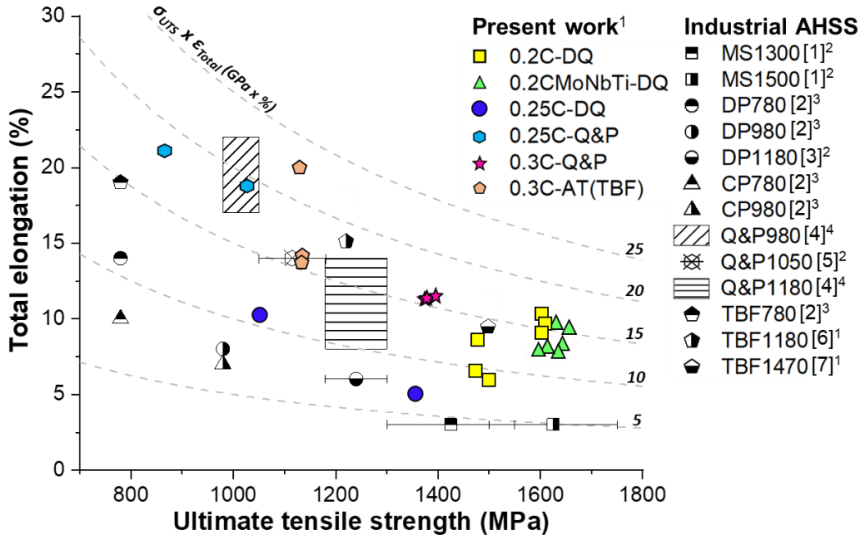

Figure 8.1: Total Elongation-Ultimate tensile strength diagram for the steel grades produced in this thesis and industrially produced AHSS. Notes: [1]Total elongation corrected according the methodology presented in the standard ISO 2566-1:1984 [8]; sample reference: ASTM E8/E8M (gauge length: 50 mm; width: 12.5 mm) [9]. [2]Minimum ε_{Total} after fracture using a specimen with a gauge length of 50 mm (ASTM E8/E8M). [3]Minumiun σ_{UTS} and minimum ε_{Total} according to standard ASTM A1088; specimen gauge length 50 mm (ASTM E8/E8M) [2]. [4]Tensile properties range for industrially produced Q&P steels reported in Ref. [4].

8.2 Prospect for the ultrafast heating of steels: Future work

Besides the insight into the combination of the ultrafast heating and low-temperature heat treatments presented in this thesis, the following topics could be further investigated for addressing the potential of the ultrafast heating process towards the new generation of AHSS:

- In this thesis, the formation of heterogeneous microstructures after ultrafast heating was discussed in terms of the local chemical heterogeneities in austenite. However, experimental evidence based on chemical characterization was not provided. Hence, characterization with advanced techniques such as Atom Probe Tomography (APT) could offer a quantitative elemental analysis at micro-scale. Such a chemical analysis could validate the discussions and conclusions focused on the local chemical heterogeneities in austenite produced under high heating rates.
- Modeling of austenite formation and decomposition in ultrafast heated experiments. Phase transformation and alloying redistribution upon heating and cooling could be described via Phase-Field modeling and coupled to chemical and microstructural characterizations of the heat-treated samples. This study could provide evidence for the mechanisms of austenite formation under ultrafast heating in steels.

- In order to further understand the strengthening mechanisms and the improved mechanical properties of ultrafast heated steels, it is suggested to perform in-situ testing using micro DIC and EBSD scans. These analyses could provide valuable information on the strain-stress partitioning among the mixed microstructures produced via ultrafast heating. Additionally, micro-strain localization and damage nucleation can be evaluated using these techniques, allowing to determine the role of the microstructural heterogeneities produced after ultrafast heating on the mechanical behavior.
- The heterogeneous microstructure produced after ultrafast heating could be a cause of the enhanced mechanical stability of retained austenite. The study of the kinetics of austenite transformation upon straining, evaluated via in-situ or ex-situ X-ray diffraction and EBSD, will provide quantitative information about the effect of the microstructures produced in ultrafast heating experiments on the austenite stability. Additionally, it is recommended to couple those analyses with the evaluation of local chemical composition in austenitic grains. Such a study could provide new experimental evidence for the kinetics of austenite transformation in heterogeneous steels.
- A quantitative study of the static aging phenomena in ultrafast heated cold-rolled steels. The formation of Cottrell atmospheres of carbon atoms at dislocations in non-recrystallized ferrite could provide further enhancement of the yield strength in low alloy bake hardenable steels. This analysis could also be extended to the study of the bake hardening behavior of Q&P, austempered and direct quenched peak annealed steels with a high fraction of non-recrystallized ferrite.
- Banded microstructures produced via ultrafast heating might cause anisotropy of the mechanical properties and poor forming capacity. A study on the anisotropy of mechanical properties will be beneficial to determine the role of the microstructural banding produced after ultrafast heating on the mechanical response of advanced high strength steel.
- The mechanical properties of ultrafast heated steels have been evaluated using uniaxial quasi-static tensile testing, which provides a first indication of the mechanical behavior. However, a complete description of the mechanical capabilities of ultrafast heated steels, designed to fulfill the demands of the automotive industry, requires the study of high strain-rate response and formability.
- Further experiments are required to determine the effect of the heating rate on the microstructure and mechanical properties of hot-rolled steel grades. Most of the results reported in the literature are focused on the study of cold-rolled low alloy steels subjected to ultrafast heating. This is greatly influenced by the technological restrictions related to reaching high heating rates during heating of thick plates.

References

[1] ArcelorMittal, MartINsite® steels. https://automotive.arcelormittal.com/products/flat/martensitic_steels/martinsite [Accessed June 2021].

[2] ASTM-International, A1088-13. Standard Specification for Steel, Sheet, Cold-Rolled, Complex Phase (CP), Dual Phase (DP) and Transformation Induced Plasticity (TRIP), Philadelphia, PA, 2019. https://doi.org/10.1520/A1088-13R19.2.

[3] ArcelorMittal, Dual phase steels. https://automotive.arcelormittal.com/products/flat/first_gen_AHSS/DP [Accessed June 2021].

[4] L. Wang, J.G. Speer, Quenching and Partitioning Steel Heat Treatment, Metallogr. Microstruct. Anal. 2 (2013) 268–281. https://doi.org/10.1007/s13632-013-0082-8.

[5] ArcelorMittal, Steels for cold stamping - Fortiform®. https://automotive.arcelormittal.com/products/flat/third_gen_AHSS/fortiform [Accessed June 2021].

[6] T. Murata, S. Hamamoto, Y. Utsumi, T. Yamano, Y. Futamura, Characteristics of 1180MPa Grade Cold-rolled Steel Sheets with Excellent Formability, KOBELCO Technol. Rev. 35 (2017) 45–49.

[7] Y. Mukai, The Development of New High-strength Steel Sheets for Automobiles, KOBELCO Technol. Rev. 26 (2005) 26–31.

[8] International Organization for Standardization (ISO), ISO 2566-1:1984. Steel-Conversion of elongation values - Part 1: Carbon and low alloy steels, Geneve, Switzerland, 1984.

[9] ASTM-International, E8/E8M-16a. Standard Test Methods for Tension Testing of Metallic Materials, Philadelphia, PA, 2020. https://doi.org/10.1520/E0008.

EBSD IPF and secondary electron micrograph of a Q&P steel.